ANL-86-40
I-28951CONF-8604116--

PROCEEDINGS OF THE INTERNATIONAL WORKSHOP ON HIGH-TEMPERATURE MOLTEN SALT BATTERIES

April 16-18, 1986
Argonne National Laboratory

Lithium Battery

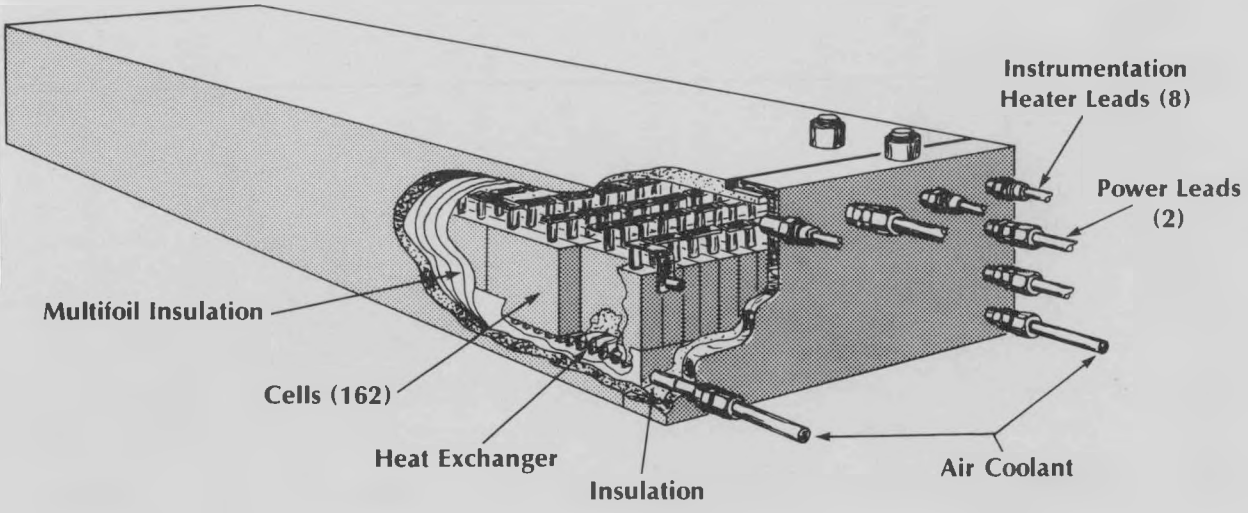

Sponsored by
DEPARTMENT OF ENERGY
ELECTRIC POWER RESEARCH INSTITUTE
ARGONNE NATIONAL LABORATORY

Argonne National Laboratory, with facilities in the states of Illinois and Idaho, is owned by the United States government, and operated by The University of Chicago under the provisions of a contract with the Department of Energy.

Printed in the United States of America
Available from
National Technical Information Service
U. S. Department of Commerce
5285 Port Royal Road
Springfield, VA 22161

NTIS price codes
Printed copy: A11
Microfiche copy: A01

Distribution Category:
Energy Storage--
Electrochemical (UC-94cb)

ANL--86-40

DE87 003297

ANL

ARGONNE NATI ABORATORY
9700 South Avenue
Argonne, 0439

PROCEEDINGS OF THE I IONAL WORKSHOP ON HIGH-TEMPERATURE SALT BATTERIES

April 1986

Spor by

Departm Energy
Electric Powe rch Institute
Argonne Na Laboratory

Co-Chairmen

Frank McLarnon — Lawrence Berkeley Laboratory/ University of California

Robert Weaver — Electric Power Research Institute

Donald R. Vissers — Argonne National Laboratory/ Chemical Technology Division

TABLE OF CONTENTS

TABLE OF CONTENTS (CONTD)

INTRODUCTION:

INTERNATIONAL WORKSHOP ON HIGH-TEMPERATURE MOLTEN SALT BATTERIES

A three-day workshop on high-temperature molten salt batteries sponsored by the U.S. Department of Energy (DOE), the Electric Power Research Institute (EPRI), and Argonne National Laboratory (ANL), was held at ANL on April 16-18, 1986. This was the first such workshop to be held at ANL for some 10 years, and it provided an excellent opportunity to bring together those who are actively involved in the research and development of rechargeable, molten salt battery systems.

Over the past 5 years, with only a fraction of the funding that had been available in the late 1970s, DOE, EPRI, and, most recently, the Tennessee Valley Authority (TVA), have been able to sustain a "critical mass" level of activity for both the LiAl/FeS and the LiAl/FeS_2 systems. The workshop provided an update of the advances which have been made during these past few years.

Twenty-six technical papers were presented, describing work on materials development; electrode kinetics; and cell and battery development by several private sector organizations (Gould Inc., General Motors Corp., EIC Labs. Inc., and Chemelectron Inc.), universities (Stanford University, Illinois Institute of Technology, Bowling Green State University, and University of California at Berkeley), and national laboratories (ANL and Lawrence Berkeley Laboratory).

Real progress was reported on improvements in the LiAl/FeS cell by Gould Inc. and ANL. Specific energy of 105 Wh/kg and specific power of 130 W/kg at 80% depth-of-discharge were obtained in engineering cells with a powder separator/immobilized electrolyte design, using negative-limited rather than positive-limited electrode capacities. Long life has still to be demonstrated with these cells. However, Gould believes that the change from positive- to negative-limited capacity at the top-of-charge should significantly reduce the formation of iron chloride and, therefore, minimize the precipitation of iron within the separator layer, which is the current life-limiting mechanism of the LiAl/FeS system.

Alternative methods for fabricating LiAl electrodes, to improve their mechanical stability when subjected to deep cycling, were described by ANL. These improvements should be particularly useful for application in the new high-power, negative-limited cell designs.

The successful operation and testing of two 12-volt battery modules fabricated by Gould was described by ANL. The tests showed that single-cell performance can be duplicated in a series array of cells, and also that the battery can continue to operate even with failed cells in the series string. This test program provided the first step in the electric-van demonstration program of EPRI/TVA. It will be followed by the in-vehicle testing of a battery subsystem at TVA's electric-vehicle test facility.

In parallel with the U.S. activities in the development of the LiAl/FeS system, work at Chemelectron Inc. in Canada has shown considerable progress in

the fabrication and use of low-cost boron nitride fibers as a separator material in flooded-electrolyte cells.

One of the key areas of progress reported at the workshop by ANL was the improved stability of the FeS_2 electrode, which was achieved when using a LiCl-LiBr-KBr electrolyte in place of the more commonly used LiCl-KCl or all-lithium-halide electrolyte. As a demonstration of this stability, a cell was operated for some 400 deep discharge cycles at 400°C without performance decline. It is not yet understood why the FeS_2 electrode has a greater stability in the bromide-containing electrolyte.

Argonne considers that performance levels of 200 Wh/kg, 200 W/kg, and 500 cycles should now be obtainable in engineering-size multiplate cells. These values were projected from results obtained on $LiAl/FeS_2$ bicells that incorporated the new electrolyte, together with electrodes of high capacity density.

If, as the test results indicate, the higher-performance FeS_2 electrode can be made to operate in a stable manner, a remaining problem in developing this system for commercial applications is the need for a low-cost positive current collector to replace pure molybdenum. At EIC Labs. Inc., the Illinois Institute of Technology, and ANL, various techniques such as electroplating from molten salt baths and chemical vapor deposition are being developed for producing thin coherent layers of molybdenum on low-cost substrates. However, such plated or coated materials have yet to be evaluated as candidate current collectors in practical $LiAl/FeS_2$ cells.

Other workshop topics included such areas as thermal management, the use of solid lithium-ion conductors for lithium-sulfur cells, and novel electrode materials for lower-temperature molten salt systems. The workshop was an excellent vehicle for exchanging information and ideas over a wide range of related technical topics.

The final presentation of the workshop was by Elton Cairns (Lawrence Berkeley Laboratory). He identified areas where he considered that emphasis is needed in the continued development of molten salt battery systems for energy-storage applications. These include (1) the need for new model approaches, on a macro-scale, to provide a better understanding of the operation of porous electrodes in molten salts, and (2) the development of new lower-cost materials (both "active" and "passive") for use with the disulfide system. He pointed out that the other advanced battery systems had not met their performance/cost targets and that a real "window of opportunity" now existed for the Li/MS system.

He further pointed out that interim markets for the system ought to be found, where cost is not the priority that it is for commercial energy-storage applications, but where there is a real need for the unique attributes of the molten salt battery. A system that meets the goals of 200 Wh/kg, 200 W/kg, and 500 cycles could, he felt, be demonstrated over the next 3-5 years. When combined with the other system properties, such as robustness, low volume, abuse resistance, safety, etc., there are likely to be customers for such a battery, even at high initial unit cost. What is now needed, he said, is a focused effort to develop such a battery and to identify these essential

interim markets. If this does not happen, the window of opportunity for the commercial application of this technology will probably disappear.

The papers presented at the workshop follow. The workshop was divided into three parts: basic properties of molten salt battery systems, engineering development of lithium-alloy/metal sulfide batteries, and research and development in molten salt systems. This format has been retained in the publication of the workshop papers, with each part having separate pagination.

Barry A. Askew
Los Altos, CA

SESSION A

BASIC PROPERTIES OF MOLTEN SALT BATTERY SYSTEMS

Morning, April 16, 1986
Chairman, Milton Blander
Vice Chairman, H. F. Gibbard

PREDICTION OF THERMODYNAMIC PROPERTIES OF MOLTEN SALT SOLUTIONS

Marie-Louise Saboungi and Milton Blander
Argonne National Laboratory
Argonne, Illinois 60439

Theoretical advances in the past decade permit one to make **a *priori*** calculations of thermodynamic properties of a variety of ionic solutions and to greatly minimize the number of measurements necessary to define the chemical properties of technologically important electrolytes. In this review, we discuss some examples of value for high–temperature molten salt batteries and fuel cells.

Prediction of Solubility of Dilute Species in Ionic Melts

Thermodynamic solution theories can be used to calculate, **a *priori***, solubility products of relatively insoluble substances in ionic solutions. We have shown that a simple cycle involving three chemical reactions provides an accurate evaluation of the solubility product of transition metal sulfides in a binary solvent, such as the LiCl–KCl or LiCl–LiF eutectics. The theory makes the study of the composition and temperature dependence of the solubility feasible with very few measurements. In addition, relative solubilities of different substances such as sulfides or oxides in the same solvent can be examined.

On Phase Diagrams and Thermochemical Properties of Multicomponent Solutions

Multicomponent molten salt solutions are most often used as liquid electrolytes in high–temperature batteries and fuel cells. Often, additives are sought to improve performance of molten salt cells and a primary question arises concerning the relation between chemical reactivities, liquidus temperatures and composition. Phase diagrams can be calculated from the conformal ionic solution theory for multicomponent additive or reciprocal systems using thermodynamic properties of lower order systems, e.g., binary subsystems and pure components. Similar analyses also provide the chemical potentials of all the components so that equilibria between the molten salt and a gas phase can be calculated. For example, in a carbonate fuel cell, theoretical analyses can provide the equilibrium electrolyte compositions for reactions with H_2O, CO_2, SO_2, and O_2 such as:

$$H_2O + K_2CO_3 \rightarrow 2KOH + CO_2$$

and

$$SO_2 + \frac{1}{2}O_2 + K_2CO_3 \rightarrow K_2SO_4 + CO_2$$

Current work is focused on extending this theoretical framework to ordered or "complex forming" systems such as silicates and chloroaluminates.

Acknowledgments

This work was supported by the Division of Materials Sciences, Office of Basic Energy Sciences, U.S. Department of Energy.

SPECTRAL METHODS IN THE CHARACTERIZATION OF MOLTEN SALTS

David S. Newman

Department of Chemistry and Center for Photochemical Sciences
Bowling Green State University
Bowling Green, Ohio 43403

ABSTRACT

Special problems associated with spectroscopy of the liquid state in general, and ionic liquids in particular, are described. The concepts of the radial distribution function and the partition function are introduced and their relationship to liquid structure is discussed. Diffraction spectroscopy, optical spectroscopy, and nuclear magnetic resonance spectroscopy are discussed together with the kinds of structural information available from these experimental techniques. Correlations between optical spectra and structure and between NMR spectra and structure of molten salts are emphasized and described in some detail.

INTRODUCTION

It is a fundamental principle of physical chemistry that structure determines chemical behavior so that if a system's structure is known, accurate predictions about its chemical and physical properties can be made. The preeminent experimental technique for obtaining structural information is spectroscopy, which can be conveniently divided into three different categories; scattering, optical and magnetic resonance.

In general, scattering experiments give structural information about the entire liquid phase. That is, they give both the long and the short range order of the system. For ionic melts, the only scattering technique that is useful is neutron diffraction because neutrons are scattered by nuclei whereas X-rays are scattered by core electrons and, as a result, yield inaccurate distribution functions. Therefore, only neutron diffraction will be discussed further. Optical spectrosocpy gives information about the short range order or local structure of the system, but can give some long range structural information if correlated with the other measurements. Magnetic resonance spectroscopy yields information about individual species present, but like optical spectroscopy, can be made to give some long range structural information. The kinds of information about molten salts obtainable using the various spectroscopic techniques are succinctly summarized in Table I.[1]

TABLE I - SPECTROSCOPIC METHODS

Technique	Effect	Measured Quantity	Information
A. Scattering			
Neutron diffraction	Neutrons scattered by nuclei; $\lambda = 1$ A, $\tau = 10^{-16}$ sec. (averaged over vibrational motions).	Angular distribution of the intensity of the scattered neutrons.	Radial distribution function [g(r)] of different isotopic species; internuclear distances; correlation length; number of neighbor atoms.
B. Optical			
Vibrational Raman	Inelastic scattering of light due to polarizability changes on vibration; λ = visible laser lines, $\tau = 10^{-14}$ sec.	Intensity of scattered light as function of energy (0 to 4000 cm^{-1}).	Energy and symmetry of Raman active vibrational states.
Absorption Spectra			
Vibrational infrared	Interaction of radiation with vibrating molecular dipoles; $\lambda = 10^{-1}$-10^{-4} cm^{-1}, $\tau = 10^{-13}$ sec.	Absorption (or emission) of radiation as a function of energy (0-4000 cm^{-1})	Energy of infrared active vibrational states.
Electronic absorption	Interaction of radiation with electronic states of the atoms; $3.10^3 > \lambda > 2.10^2$ A, $\tau = 10^{-15}$ sec.	Absorption of radiation as function of energy (4000-5000 cm^{-1}).	Electronic states of atoms. Mainly d-d ligand field transitions.
C. Magnetic Measurements			
NMR - Nuclear Magnetic Resonance	Interaction of radiation with nuclear spin states of an atom in a magnetic field; $10^7 > \lambda > 10^2$, $\tau = 10^{-9}$ sec.	Resonance absorption of radiofrequency in a variable magnetic field.	Nuclear spin states of atoms; relaxation processes.

IONIC LIQUIDS

In general, liquids have short range order, but no long range order. Solids, on the other hand, have both short and long range order and gases have no order at all. This simplifying concept is illustrated in Fig. 1 where the radial distribution function of an ionic crystal is compared with that of a fused salt.[2]

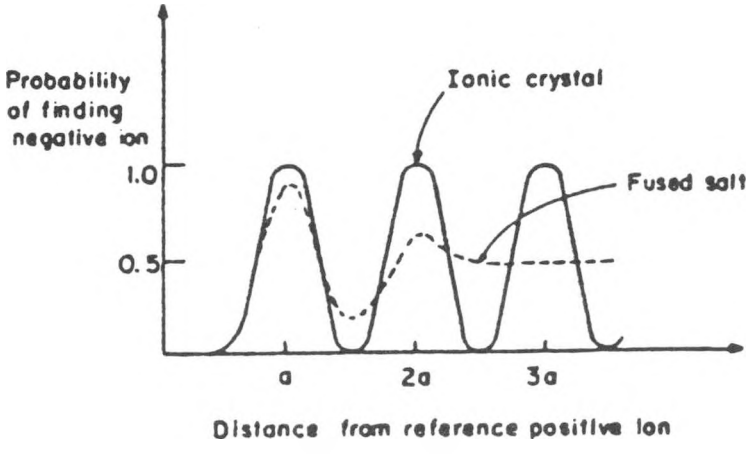

Fig. 1 Radial distribution functions for an ionic crystal and a fused salt

Molten salts are ionic liquids that are characterized by strong attractive forces and strong repulsive forces. The strong attractive forces (> kt) result in electrostrictions[3] of the melt, which increase short range order relative to the solid. This is illustrated by the data in Table II. It is obvious that the interionic radius in each melt is

TABLE II

Salt	Interionic Raddi(A) Crystal	Melt	Gas
LiCl	2.66	2.47	
LiBr	2.85	2.68	
KCl	3.26	3.15	
CsCl	3.50	3.46	3.00

smaller than the corresponding interionic radius in the crystal. These electrostrictions can be thought of as a pressure of several thousand

atmospheres on the melt. The idea of electrostrictions is one of the unifying concepts for understanding ionic liquids.

A phenomenon called charge compensation affects the structure of the melt and helps to distinguish further ionic liquids from molecular or metallic liquids. In a perfect crystal of a 1-1 salt, each positive ion would be surrounded by negative ions and vice-versa, which means the interactions are many bodied. Therefore, each positive charge will be partially compensated for by the negative charge of the surrounding ions (and vice versa) and the net Coulombic attraction between ions will appear to be less than the Coulombic attraction between the same two ions in the gaseous phase where there is no order and no charge compensation. For example, the internuclear distance in CsCl in the solid is 3.50 A, but in the gas is only 3.00 A. That is, there is a shrinkage of nearly half an angstrom in going from the crystal to the gas. On the other hand, there is a shrinkage of only 0.04 A in going from the crystal to the melt, which means much of the compensation is preserved. However, there is still a net reduction in the overall electrostatic charge compensation which is partially responsible for the electrostriction.

Molten salts, in common with electrolyte solutions, conduct an electric current using ions as the charge carriers. The major difference between the two classes of liquids is the screening between charges provided by the solvent. However, there is no sharp dividing line and the properties of very concentrated electrolyte solutions continuously approach those of molten salts as the solvent concentration diminishes.

Molten salts themselves may be conveniently divided into two classes, soft and hard.[4] The alkali metal halides are examples of hard salts. Soft salts are the pyridinium halides and the imidazolium halides, etc. Hard salts are characterized by high melting points (> 400°C) and high E_η/E_Λ ratios. Where E_η is the energy of activation for viscosity and E_Λ is the energy of activation for equivalent conductance in the Arrhenius equation, and expand quite a bit upon melting (usually between 10 and 20%). Moreover, on a microscopic scale, hard salts behave essentially like charged hard spheres. Soft salts are characterized by low melting points (<240°C), and low E_η/E_Λ ratios ($\sim$1.1 - 1.4), and expand relatively little upon melting.

NEUTRON DIFFRACTION SPECTROSCOPY

In neutron diffraction experiments, a molten salt sample is irradiated with neutrons with amplitudes around 1 A and the scattered beam analyzed. In order to extract useful information, an isotopic substitution technique must be used.[5] That is, for an AB molten salt such as $ZnCl_2$ there has to be three different measurements ($Zn^{35}Cl_2$, $Zn^{37}Cl_2$ and $Zn^{nat}Cl_2$) and for a binary mixture with no common ions there has to be ten independent measurements. To date, no true binary system has been completely characterized, but a "pseudo-binary," $LiAlCl_4$ has recently been characterized[6] by taking advantage of the fact that a mix-

ture of ^7Li and ^6Li is a "null" scatterer.

The principal piece of information available from neutron diffraction spectroscopy is the radial distribution function, g(r), which gives the probability of finding an ion at any distance, r, from a probe ion (see Fig. 1). Since all attempts at calculating g(r) from first principles have failed, neutron diffraciton remains the best method for obtaining this important function.

The reason g(r) is important theoretically is that it can be used to calculate the canonical partition function, Z, for the melt. Z has the form:

$$Z = (2\pi mkT/h^2)^{\frac{3N}{2}} Q_N \qquad (1)$$

where Q_N is the configurational partition function. For a monatomic gas, Q_N is given by the equation:

$$Q_N = (1/N!) \int_V \cdots \int_V e^{-U_{ij}/kT} \, d^3r_i \cdots d^3r_N \qquad (2)$$

Here U_{ij} is the sum of all pairwise interaction energies:

$$U_{ij} = (1/2) \sum_i \sum_j \varphi_{ij} \qquad (3)$$

and the other symbols have their usual meaning. Because of the strong attractions mentioned earlier, the distribution of the ions in a fused salt is far less uniform than is the distribution of atoms in a monatomic gas. Therefore, a correction to the random probability term, $(N/V)^2$, in Q_N is required in order to calculate U_{ij} for molten salts and to make this corrction, g(r) must be known. For a molten salt, Eq. (3) is rewritten as

$$U_{ij} = (2\pi N^2/V) \int_0^\infty \varphi_{ij}(r) g(r) r \, dr \qquad (4)$$

Eq. (4) is substituted back into Eq. (2) and then Z can be used to obtain all the equilibrium properties of the liquid. For example, the Helmholtz free energy, A, is given by the equation

$$A = - kT \ln Z \qquad (5)$$

In addition, the Boltzmann $\bar{H}$ theorem, where $\bar{\bar{H}}$ is any function of the coordinates of position and momentum, provides a mechanism for calculating the change in $\bar{\bar{H}}$ from one canonical distribution to another.[7] Therefore, nonequilibrium properties can be calculated in principle, but to my knowledge this has never been done for a molten salt.

Practically, g(r)'s are important because information extractable from them include interionic distances, coordination numbers, amount of penetration of like ions into first coordination shells, and the nature of species that exist in the melt.[5]

Neutron diffraction is potentially the most powerful tool for obtaining information about molten salts, because in effect, the diffraction pattern is a "snapshot," or time = 0 picture, of the melt. Unfortunately, neutron diffraction experiments are extremely expensive, difficult to interpret and tedious to perform. No true binary system has yet been studied by this technique, because of the ten isotopic substitutions required, and only a handful of facilities exist for neutron diffraction experiments. Therefore, other specroscopic techniques must also be relied upon for information about the structure of molten salts.

OPTICAL SPECTROSCOPY

Again, because of the strong electrostatic interactions, a molten salt is a highly associated liquid so that the relaxation time of the quasi-lattice that is the liquid as a whole is similar to the relaxation time of complex species extant in the melt. Therefore, the fundamental problem inherent in the interpretation of optical spectra of molten salts is how to distinguish kinetic complexes from the thermodynamic complex that is the whole melt.[8] A kinetic complex is defined as an entity with a lifetime that is long compared with the lifetime of a molecular vibration. For the purposes of this discussion, $\sim 10^{-7}$ sec, which is the observation time of an NMR experiment will be considered as the minimum lifetime for a complex species to qualify as a kinetic complex. Since the interactions are >kT, the entire system can be thought of as a "thermodynamic complex." That is, an ion in one part of the melt can be passing an oppositely charged ion, undergo a few vibrations and then pass on. These are called "quasi-lattice vibrations." As a result, the observation of a vibrational spectrum in a melt is not *prima facie* evidence for the existence of a kinetic complex unless the entitites responsible for quasi-lattice vibrations are themselves considered short-lived complexes.[9]

Two criteria for the existence of a kinetic complex are that it should exhibit a spectrum whose frequencies are relatively invariant to changing composition (Changes of 6% is a good rule of thumb here) and that it's spectrum will be different from those of the pure components of the melt. To illustrate these points, two sets of infrared absorption spectra obtained by Wilmshurst are reproduced[8] in Fig. 2 and Fig. 3. Fig. 2 shows the change in IR spectra as a function of composition for the LiCl-$CuCl_2$ system and Fig. 3 shows the same changes for

the KCl-$CuCl_2$ system. It is clear that by both stated criteria a kinetic complex exists in the KCl system, but not in the LiCl system.

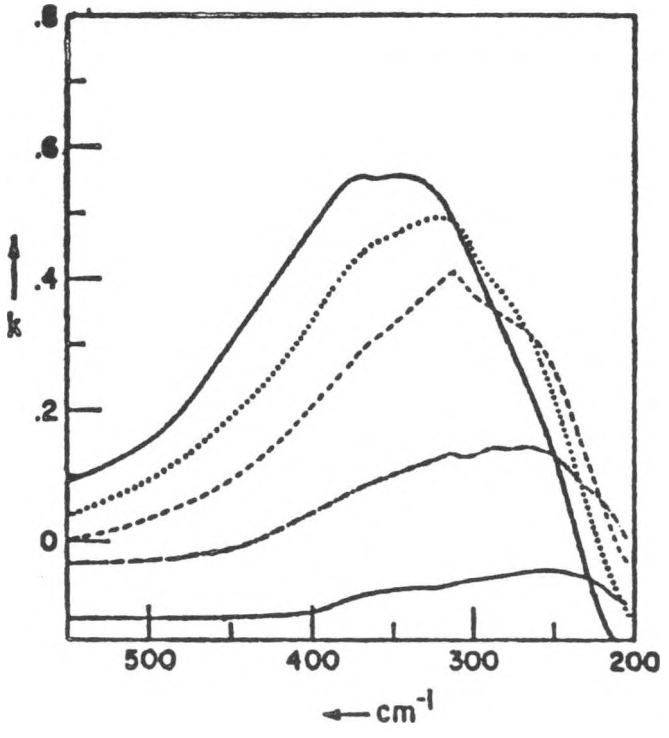

Fig. 2

Infrared absorption spectra for the system lithium chloride-cupric chloride.
_____ LiCl (695°C);
..... $3LiCl:CuCl_2$ (590°C);
- - - - $LiCl:CuCL_2$ (565°C);
-.-.-.- $LiCl:3CuCl_2$ (585°X);
$CuCl_3$ (565°C).

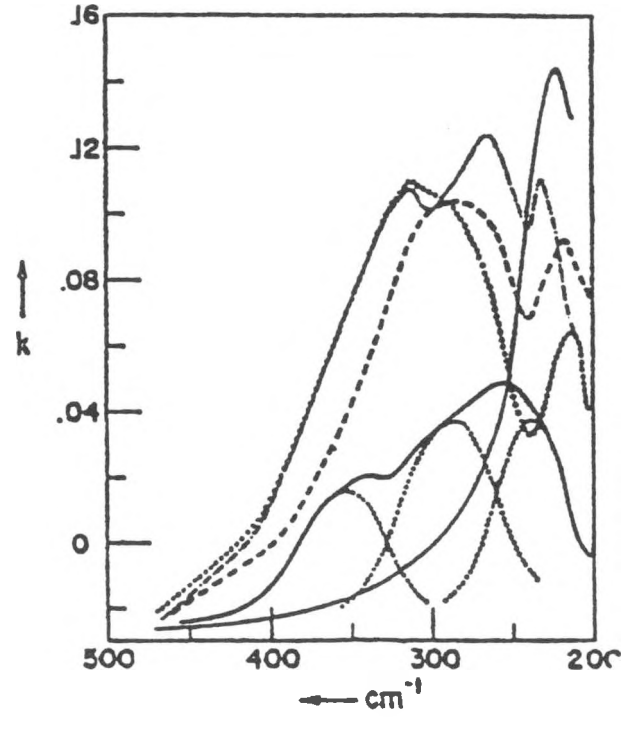

Fig. 3

Infrared absorption spectra for the system potassium chloride-cupric chloride.
_____ $CuCl_2$ (565°C);
.-.-.-.- $2CuCl_2:KCl$ (505°C);
° ° ° ° $CuCl_2:KCl$ (555°C);
- - - - $CuCl_2 2KCl$ (530°C);
KCl (830°C);
attempted resolution of the $CuCl_2$ spectrum

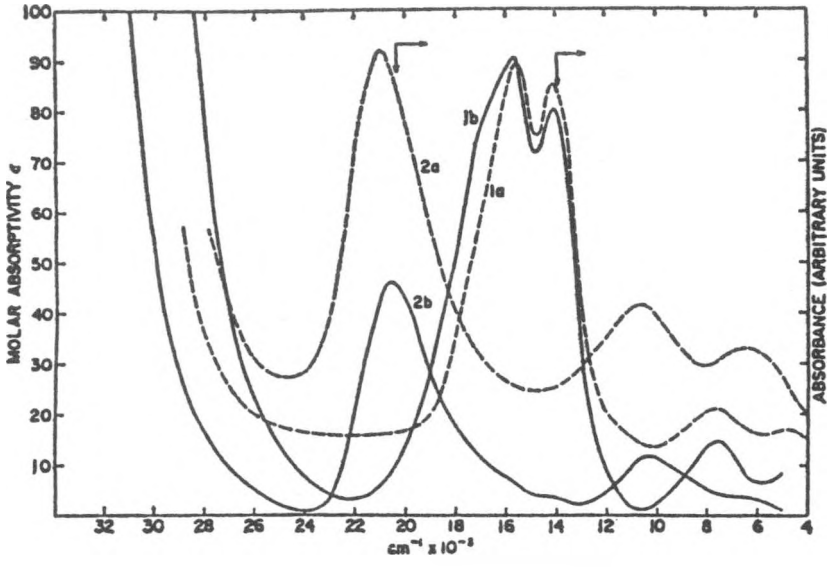

Fig. 4 **Comparison spectra of Ni(II) in melts and crystals. 1a and 2a are crystal spectra taken at 550° of Ni(II)-doped Cs_2MgCl_4 and $CsMgCl_3$, respectively. 1b and 2b are melt spectra in 68.4% KCl–31.6% $ZnCl_2$ at 550° and in 45.3% KCl–54.7% $ZnCl_2$ at 250°, respectively.**

The actual structure of these complexes cannot be specified without resort to other data, such as the IR spectrum of a species whose solid state X-ray diffraction pattern is known. Also it is necessary to have both Raman and IR data to determine the symmetry of a species, but even then there are possible ambiguities because of the long relaxation times, or short range order, of the melt itself.

These sorts of problems also exist in the interpretation of UV-visible spectra. For example, a transition metal ion may be passing by a structured region or "quasi-lattice site" in the melt with the same symmetry as a kinetic complex.

Gruen and coworkers[10-12] investigated the UV-visible absorption spectra of 3d transition metal ion-chloro-complexes in fused salts and avoided some of the difficulties mentioned above by, in effect, calibrating the melt spectra against the spectra of the complexes in host lattices with known structure. To illustrate the technique, a comparison between the spectra of Ni(II) complexes in KCl-$ZnCl_2$ melts and Ni(II) doped host lattices are shown in Fig. 4 which is reproduced from Ref. 12. In this figure, 1a and 2a are Ni(II) spectra taken at 550°C in Cs_2MgCl_4 and $CsMgCl_3$ host crystals respectively. In the Cs_2MgCl_4 crystal, the Ni ion is in an undistorted tetrahedral environment and in $CsMgCl_3$ the Ni is in an octahedral environment. Curve 1b is the spectrum of Ni(II) in a 68.4% KCl-31.6% $ZnCl_2$ melt at 550 °C and curve

2b is the spectrum of the same ion in a 45.3% KCl-54.7% $ZnCl_2$ melt at 250°C. It is clear that the melt spectrum at 550° matches the spectrum of Cs_2MgCl_4 and the melt spectrum at 250° matches the spectrum of $CsMgCl_3$ which means the Ni(II) ion is in an octahedral environment at the lower temperature and in a tetrahedral environment at the higher temperature and implies the existence of a temperature dependent octahedral - tetrahedral equilibrium in the melt:

$$NiCl_6^{-4} = NiCl_4^{-2} + 2Cl^-$$

Ti, and V, complexes also exhibit octahedral -tetrahedral equilibria, in molten salts with the tetrahedral species always being the most stable thermally. That is, as the temperature is raised, the concentration of the tetrahedral species increases at the expense of the octahedral species. This can be seen from the temperature dependence of the spectra of Ni(II) in 52.5% KCl-47.5% $ZnCl_2$ which is shown in Fig. 5. There is a sharp isosbestic point and a clear shift to the tetrahedral environment as the temperature is raised.

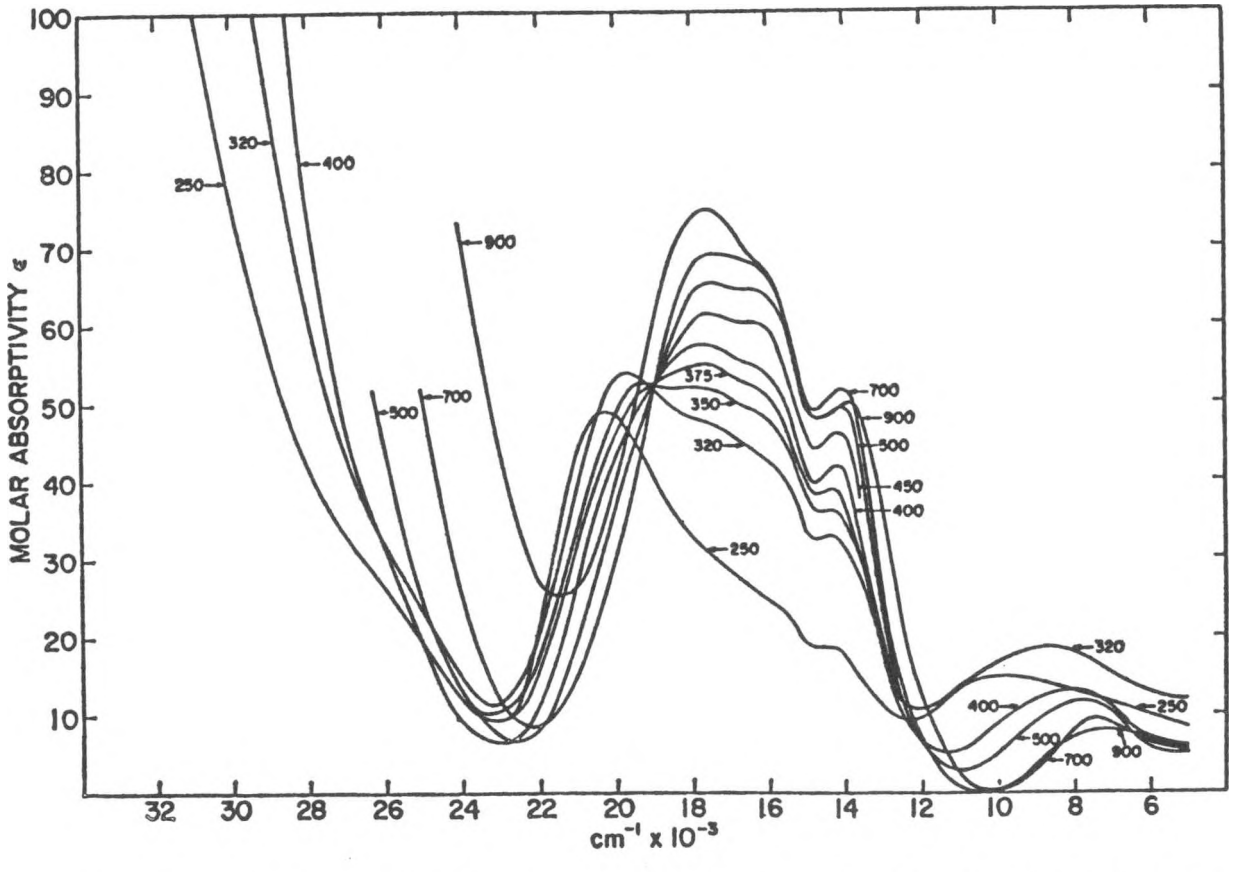

Fig. 5 **Spectra of Ni(II) in 52.5 mole % KCl–47.5 mole % $ZnCl_2$ melt as a function**

Another serious problem implicit in the measurement of the spectra of molten salts is the fact that most systems studied to date are liquids at elevated temperatures (another result of the strong electrostatic forces present) which means background radiation must be eliminated from the spectrum. Gruen solved this problem by reversing the sample and monochrometer so that his experimental design was: light source ---> chopper ---> sample ---> monochrometer ----> detector. This arrangement makes it possible to measure spectra at temperatures as high as 1000°C with accuracies similar to measurements made at ambient temperatures.

High resolution spectroscopy in the IR or "fingerprint" region of the spectrum have recently been brought to bear on the structure of molten salts by Ritter and coworkers who have developed a reflectance technique and used it to study the IR emission spectra of alkali-chloroaluminates.[13,14] The essential features of their technique were the production of sufficiently thin melt films to allow enough radiation to pass through to be detected, the use of diamond windows which are relatively inert, and the use of an opaque backplate to reflect radiation. This set-up minimizes background or black body radiation.

Fig. 6, reproduced from reference 13, shows the spectra of the alkali - chloroaluminate binaries in the acid region where the $Al_2Cl_7^-$ is

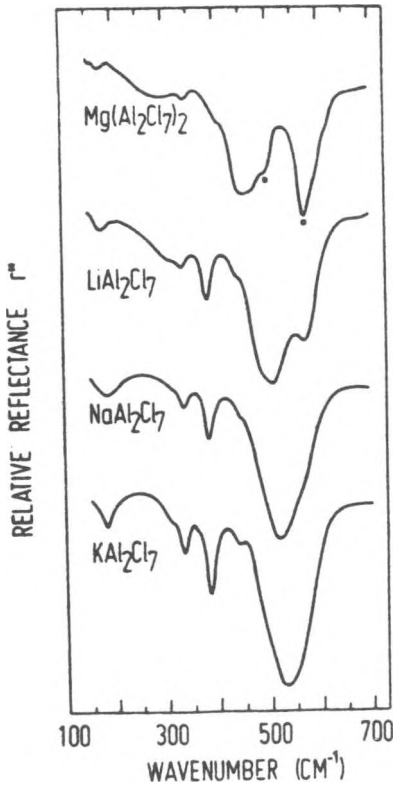

Fig. 6

IR spectra of molten $M(Al_2Cl_7)_n$.

the dominent negative species. It is clear form these spectra that there is a sharp splitting of the ν_{11} (E_u) band into two bands, one at 570 cm^{-1} and one at 514 cm^{-1}. These bands are not found in the spectra of the other melts and are not found in the spectrum of the $LiAlCl_4$ melt. This means that there probably is a kinetic complex in the lithium melt and not in the other melts. The postulated criteria for a kinetic complex have been more or less satisfied because the bands do not appear in the other spectra, but there is still some uncertainty and another measurement, such as an NMR spectrum, would have to be made to establish a minimum lifetime for the $LiAl_2Cl_7$ complex.

NUCLEAR MAGNETIC RESONANCE SPECTROSCOPY

During the last fifteen years or so, NMR spectroscopy has been used to help identify species present in soft molten salts such as the pyridinium halides and the imidazolium halides. These soft salts are particularly suitable for study by resonance techniques because their melting points are usually under 200°C, which in the upper limit of the variable temperature probe of most commercial spectrometers, they contain protons, and species identifiable in the NMR spectrum can be considered kinetic complexes. In addition, changes in the chemical shift with temperature and with composition can be correlated with the transport and thermodynamic properties so that a fairly decent picture of the melt's structure can be drawn.

For example, Newman and coworkers studied the HNMR spectra of a series of 4-methylpyridinium iodide isomers[4] and noted that the position of the downfield nitrogenic proton peak of the 2-methyl salt was temperature dependent, whereas the nitrogenic proton peaks of the other two isomers were not. More importantly, the area under this peak was only about half the area under the corresponding peak in the spectra of he other isomers. These observations, when coupled with analysis and transport measurements, lead to the conclusion that a μ species with the likely structure shown in Fig. 7, is present in the melt and that its lifetime is relatively long.

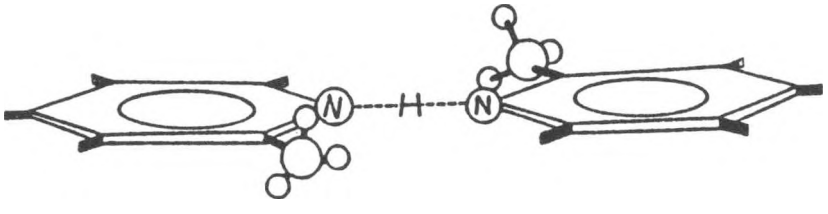

Fig. 7 **Structure of μ-hydrogenbis(2-methylpyridinium) cation**

NMR spectroscopy has been used exenstively to study the sructure of imidazolium-haloaluminate melts. For example, Wilkes and coworkers have observed a steady decrease in chemical shift of the hydrogen attached to the number 2 carbon of methylethylimidazolium chloride (Fig. 8), as the melt was made more acidic, beginning with a 66 mole % MeEtImCl -33% $AlCl_3$ until a 50-50 composition was reached. Then, virtually no further change in chemical shift occurred all the way to the 66% $AlCl_3$-33% MeEtImCl composition.[15] The reason for the change was the reduction in the concentration of oligomeric complexes which formed between the strongly polarizing Cl^- ion and the positively charged "soft" imidazo-

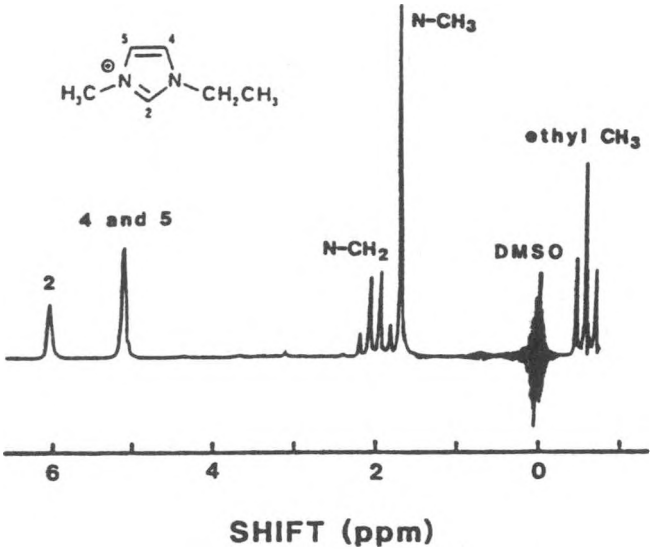

Fig. 8 **Proton NMR spectrum of neat 1-methyl-3-ethylimidazolium chloride–aluminum chloride melt at 30 °C**

lium ion. The formation of these complexes deshields the proton. As the melt becomes more basic, the concentration of free Cl^- ions decreases until at a 50-50 m% composition there are virtually no free Cl^- ions and the only species present are the imidazolium ions and the $AlCl_4^-$ ions. These hypotheses are corroborated by conductivity vs. composition data. The equivalent conductance increases linearly from 66 m% MeEtImCl-33 m% $AlCl_3$ until the 50-50 composition is reached and then no further change is observed.

NMR spectroscopy can also be used in conjunction with optical spectroscopy to identify species in molten salts and the two techniques complement each other. Maroni and Maciejewski measured the absorption spectra of transition metal ions dissolved in alkali metal carboxylates[16] and then used ^{13}CNMR spectroscopy to study the acetate

ion. They were able to distinguish between free and coordinate dcaetate ions only in the Ni(II) melt, suggesting that the lifetime of the Ni(II) acetate complex is fairly long and hence a kinetic complex.

CONCLUSION

The only way to unambiguously elucidate both the long range order and the short range order in molten salts is by means of spectroscopy. Neutron diffraction affords the most information, but its costs and difficulty take it out of the reach of most investigators. optical spectra, when carefully calibrated against solid or aqueous spectra of the same species give information about local structure but lifetimes of the entitites being studied are usually open to question. NMR spectroscopy, especially when correlated with other measurements is very useful because the observation time is long enough so that the species generating the spectra can be confidently considered to be kinetic complexes.

LIST OF REFERENCES

1. G.N. Papatheodorou, "Structure and Thermdoynamics of Molten Salts" in Comprehensive Treatise of Electrochemistry, vol. 5, Eds. Conway, Bockris, Yeager, Plenum, New York, 1983.

2. J. O'M Bockris, A.K.N. Reddy, Modern Electrochemistry, Plenum/Rosetta Edition, New Yori, 1970.

3. A.R. Ubblehode, in "Ionic Liquids", D. Inman, D. Lovering, Eds., Plenum, New York, 1981.

4. D.S. Newman, R.M. Stevens, J. Electrochem. Soc. 131, 1275 (1984).

5. S. Biggin, in "Proceedings of the Fourth International Symposium on Molten Salts," M. Blander, K.E. Johnson, M-L. Saboungi, D.S. Newman, Edtors, pp 44-57, The Electrochemical Society Softbound Proceedings Series, Pennington, N.J. 1984.

6. S. Biggin, S. Cummings, J.E. Enderby, M. Blander, in "Proceedings of the Fifth International Symposium on Molten Salts," M-L Saboungi, K.E. Johnson, D.S. Newman, D. Inman, Editors, pp 81-96, The Electrochemical Society Softbound Proceedings Series, Pennington, NJ 1986.

7. R.C. Tolman, The Principles of Statistical Mechanics, Oxford University Press, 1938, Chapter 6.

8. J.K. Wilmshurst, J. Chem. Phys. 39, 2545 (1963).

9. W. Bues, M. Atapour, G. Popperl, in "Proceedings of the Fourth International Symposium on Molten Salts" op. cit pp 217-224.

10. D.M. Gruen, R.L. McBeth, Pure and Appl. Chem. 6, 23 (1963).

11. D.M. Gruen, R.L. McBeth, J. Phys. Chem., 63, 3931 (1959).

12. C.A. Angell, D.M. Gruen, J. Phys. Chem., 70, 1601 (1966).

13. E. Ritter, in "Proceedings of the Fifth International Symposium on Molten Salts" op. cit. pp 275-288.

14. J. Hvistendahl, P. Klaeboe, E. Ritter, H.A. Oye, Inorg. Chem., 23, 7061 (1984).

15. A.A. Fannin, L.A. King, J.A. Levisky, J.S. Wilkes, J. Phys. Chem., 88, 2609 (1984).

16. V.A. Maroni, M.L. Maciejeswki, in "Proceedings of the Fourth International Symposium on Molten Salts" op. cit. pp 359-376.

AN OVERVIEW OF TRANSPORT MECHANISMS IN β-LITHIUM/ALUMINUM*

Sherman Susman, Torben O. Brun, and Kenneth J. Volin

Materials Science and Technology Division
Argonne National Laboratory
9700 S. Cass Avenue
Argonne, IL 60439 USA

ABSTRACT

A systematic study over a period of years has resulted in identifying (a) constitutional defects in β-LiAl at room temperature and (b) defects created at elevated temperatures. The relationship between these defects and charge and mass transport will be discussed. The results bear upon the use of LiAl as the negative electrode both in room-temperature and solid state batteries and in high-temperature, molten-salt electrochemical cells. The key to unravelling the Li-conduction mechanism has been the recognition that there is a critical composition within the β-phase domain corresponding to 50.7 atom% lithium. Free Li vacancies, bound Li vacancies, and reciprocal antisite defects contribute to the transport processes depending on temperature and composition. An understanding of these microscopic mechanisms has been used to remedy the loss of capacity with cycling of high temperature electrochemical cells.

The compound β-LiAl is a fast Li-ion conductor that is finding widespread use as the negative electrode in high-temperature molten salt batteries and in room-temperature solid state batteries. Despite the technological importance of this mixed electronic and ionic conductor, details of the microscopic mechanisms of charge and mass transport have been lacking. The picture is more complex than originally envisioned. No single, all-encompassing mechanism covers all temperatures and all compositions.

The conflicting phase diagrams for the Li-Al system have been reconciled by the work of Schurmann and Voss.[1] At room temperature, the β-phase domain, Li_xAl_{1-x}, extends from the lower phase boundary (LPB) at ~48 atom% Li to the upper phase boundary (UPB) at ~54 atom% Li. At 49 atom% Li, the compound melts congruently (T_m = 697°C). The β-phase crystallizes in the Zintl structure (B32 structure) which is built up of two interpenetrating diamond sublattices. This is a densely-packed structure with no obvious structural channels, interstitial sites or occupational parameters that can explain the fast Li diffusion.

*Work supported by the U. S. Department of Energy, BES-Materials Sciences, under Contract W-31-109- Eng-38.

For a number of years, we have had a program directed at understanding how β-LiAl could possibly be a superionic lithium conductor. Our experimental and theoretical approach for exploring the microscopic conduction mechanisms has been:

1. To establish the nature of the point defects at the technological temperatures of interest (25-50°C for ambient temperature batteries and 415°C and higher for molten salt batteries).

2. To determine the nature of more complex defects--if any. These may be pairs, triplets, etc., of point defects. (The use of the terms "defect aggregates or clusters" is deliberately avoided here as misleading.)

3. To determine the relationship between these defects and charge and mass transport not only in the stoichiometric compound, but also at the critically important upper and lower phase boundaries.

Partitioning the overall problem into room temperature and high temperature segments is appropriate both from consideration of the technology and from consideration of the defect physics in β-phase Li_xAl_{1-x}. The binding energy of a defect pair may be comparable to kT_{op}, where k is the Boltzmann constant and T_{op} is the temperature of battery operation. Defect concentrations will be governed by simple mass action considerations involving equilibria such as

$$D_i + D_j \rightleftharpoons D_{i-j} \ ,$$

and

$$K = \frac{[D_{i-j}]}{[D_i][D_j]} \ .$$

The equilibrium constant, K, is a function of temperature, D_i and D_j are point defects, D_{i-j} is a complex dimer defect, and all like and unlike combinations of i and j are allowed. In addition, at high temperatures, point defects with an energy of formation E_f, such that $E_f > kT_{room\ temp}$ may be generated which have no counterpart at room temperature.

The key to unravelling the Li-conduction mechanisms at any temperature has been the recognition that there is a critical composition within the β-phase domain corresponding to 50.7 atom% lithium (x = 0.507). This was first established by Tokuhiro and Susman[2] who called this composition the "magic composition." This critical composition has the effect of further partitioning the overall problem into four, more or less, discrete regions:

(1) Room temperature.....x < 0.507
(2) Room temperature.....x > 0.507
(3) High temperature.....x < 0.507
(4) High temperature.....x > 0.507

The point defects and dimeric defects necessary to account for the observed variations in Li diffusion have been determined for the first three regions. The fourth region is still unsettled, and it is the focus of current research interest.

ROOM TEMPERATURE

Region 1. The stoichiometric compound LiAl (x = 0.500) has a permanent population of constitutional lithium vacancies. This was first postulated by Schone and Knight[3] to interpret their NMR data. Precision density and X-ray lattice constant measurements[4] have confirmed their speculation and have led to a two-defect model. In this model, two types of point defects coexist over the entire β-phase field at room temperature. These defects are: (a) vacancies on the Li sublattice, V_{Li}, which are dominant in the Li-poor side of the phase field down to the LPB; and (b) Li antisite defects on the Al sublattice, Li_{Al}, which are the dominant defects in the Li-rich side up to the UPB. At room temperature, superionic diffusion of lithium[2,5] arises from the rapid motion of vacancies V_{Li} on the lithium sublattice. As $[V_{Li}]$ decreases going from the LPB to the UPB, the lithium tracer diffusion coefficient $D_o(Li)$ decreases. There is, however, an added complication that is discussed below.

Region 2. An NMR study shows that the temperature dependence of the spin-lattice relaxation time, T_1, varies strongly with composition.[2,6] More importantly, the minimum in T_1 is revealed as a double minimum with two distinct relaxation times.[2] Tokuhiro and Susman have explained this in terms of Li motion arising from two different kinds of vacancies; namely, free vacancies, V_{Li}; and vacancies bound to antisite Li defects, $V_{Li}\cdot Li_{Al}$ (see Fig. 1). They note that at the magic composition $[V_{Li}] = [Li_{Al}]$. For Li-rich compositions going from x = 0.507 to the UPB, there are no free vacancies. The lithium vacancy concentration not only diminishes, but all vacancies are trapped at Li_{Al} to form $V_{Li}\cdot Li_{Al}$ dimer defects.

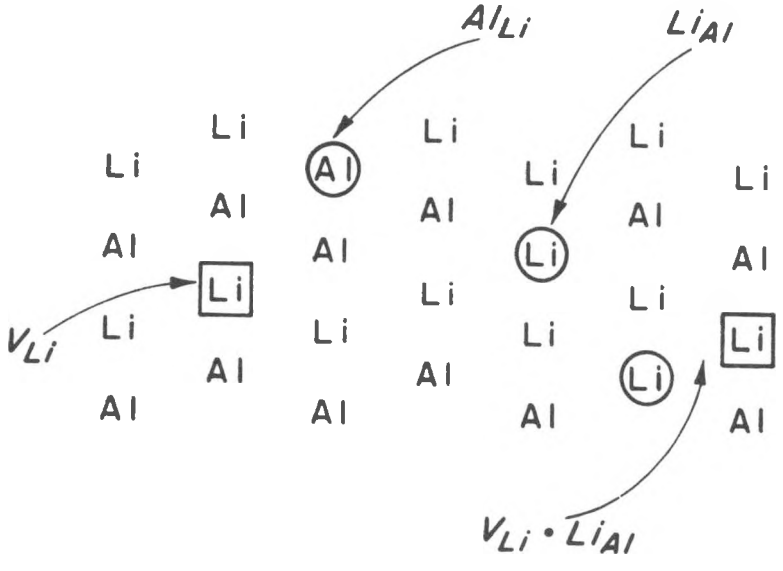

Fig. 1. Point defects and a dimer defect in in LiAl. This view is a {110} plane.

The concept of free vacancies and bound vacancies has been proven by measurements of electronic resistivity as a function of temperature (T < room temp) and composition in β-Li_xAl_{1-x}[7]. Singularities in the resistivity are observed at 100 K only for $x < 0.507$. The singularity is the signature of free vacancy ordering. Bound vacancies are, indeed, immobile at low temperatures. Neutron diffraction measurements by Brun and co-workers on a Li-poor crystal have established the structure of the ordered vacancies.[8]

To summarize for room temperature: In Region 1, superionic Li motion is determined by the motion of free V_{Li}. In Region 2, Li motion is determined by the motion of vacancies bound into the defect dimer $V_{Li} \cdot Li_{Al}$.

HIGH TEMPERATURE

Region 3. Wen and co-workers[9] have reported values for the lithium chemical diffusion $\tilde{D}(Li)$ at 415°C and at higher temperatures. Their coulometric titrations show that the lithium diffusivity diminishes by approximately two orders of magnitude upon going from the LPB towards the magic composition. Furthermore, the Li diffusivity is high and concentration-independent on the Li-rich side of the β-phase domain all the way to the UPB.

Brun and co-workers[10] have shown that for Li-poor compositions at high temperature, the mechanism of Li motion is, once again, very rapid diffusion of free constitutional vacancies V_{Li}; i.e., Region 3 and Region 1 are the same. Quasi-elastic neutron scattering data at 800 K were fit to a vacancy encounter model to give values of D(Li) consistent with those derived in Refs. 2 and 9.

Region 4. The mechanism of rapid Li transport at 415°C in Li-rich LiAl is not known. To be consistent with the $\tilde{D}(Li)$ values of Wen et al., the process must be composition-independent. Neutron diffraction experiments[11] have demonstrated that at molten-salt battery temperatures, reciprocal pairs of antisite defects, V_{Li} and Al_{Li}, are formed. These are in addition to the constitutional defects already present at room temperature. However, the formation of antisite defects at high temperatures is not due to any simple order-disorder transition.[12] The antisite defects are probably the dominant components in a complex defect that is thermally generated at high temperature. The relation between these antisite defects and Li motion is not known, but it may have already been observed in high temperature NMR measurements.[2] Various experimental probes including positron annihilation and γ-ray absorption are being used to explore Region 4.

To summarize for high temperatures: In Region 3, superionic Li motion is dominated by free vacancy motion on the Li sublattice. In Region 4, the mechanism is not known but may involve complex defects that have Li_{Al} and Al_{Li} antisite defects as their building blocks. Thermally-generated Schottky defects may also contribute.

An understanding of the microscopic mechanisms presented above has been used to remedy the loss of capacity with cycling of high temperature electrochemical cells. Such a loss is related to densification and/or void formation in the negative electrode structure. An understanding of the mechanisms has also provided a basis for the design of composite electrodes

in high-temperature cells and for negative electrodes in room-temperature cells.

References

1. E. Schurmann and H.-J. Voss, Giessereiforschung, 33, 39 (1981).
2. T. Tokuhiro and S. Susman, Solid State Ionics, 5, 421 (1981).
3. H. E. Schone and W. O. Knight, Acta Met, 11, 179 (1963).
4. K. Kishio and J. O. Brittain, J. Phys. Chem. Solids, 40, 933 (1979). S. Susman and T. O. Brun, Bull. Amer. Phys. Soc. 25, 414 (1980); Solid State Ionics, 1, 133 (1980).
5. J. R. Willhite, N. Karnezos, P. Cristea, and J. O. Brittain, J. Phys. Chem. Solids, 37, 1073 (1976).
6. T. Tokuhiro, S. Susman, T. O. Brun, and K. J. Volin, to be published.
7. L. N. Hall, T. O. Brun, G. W. Crabtree, J. E. Robinson, S. Susman, and T. Tokuhiro, Solid State Commun., 48, 547 (1983).
8. T. O. Brun, S. Susman, R. Dejus, B. Granéli, and K. Sköld, Solid State Comm., 45, 721 (1983).
9. C. J. Wen, B. A. Boukamp, R. A. Huggins, and W. Weppner, J. Electrochem. Soc., 126, 2258 (1979).
10. T. O. Brun, S. Susman, J. M. Rowe, and J. J. Rush, Solid State Ionics, 5, 417 (1981).
11. S. Susman and T. O. Brun, Solid State Ionics, 5, 413 (1981). T. O. Brun, J. D. Jorgensen, M. Misawa, F. J. Rotella, and S. Susman, J. Electrochem. Soc., 129, 2509 (1982).
12. J.-E. Jorgensen, S. Susman, T. O. Brun, K. J. Volin, and J. Faber, Jr., Solid State Ionics, to be published.

NEW NEGATIVE ELECTRODE MATERIALS FOR MOLTEN SALT BATTERIES

Robert A. Huggins

Department of Materials Science & Engineering
Stanford University
Stanford, CA 94305

ABSTRACT

The cycling behavior of electrochemical cells is often limited by negative electrode problems. These may include loss of capacity, increased impedance (which is observed as increased overvoltage), macroscopic shape change, dendrite growth, and a tendency for filamentary or whisker growth.

In some cases these problems can be reduced or eliminated by the use of alloys that undergo either displacement or insertion reactions at activities less than unity, instead of the pure elements, as electrode reactants. While providing enhanced cycling behavior, this approach involves some sacrifice of both cell voltage and specific energy.

The fundamental reasons for some of these problems with elemental electrodes are briefly discussed, and the basic background underlying the different behavior of alloys presented.

A considerable amount of information is now available concerning the thermodynamic and kinetic properties of binary alloys of potential interest for use in elevated temperature molten salt electrolyte lithium batteries. In addition, recent results have extended some of these results down to ambient temperatures, so that they can be considered for use with some of the new low temperature molten salt electrolyte systems. A number of alloys have been found to have quite rapid kinetics and attractive capacities, with relatively small voltage losses and weight penalties.

The all-solid mixed-conductor matrix concept will also be reviewed briefly. In this approach, the thermodynamic behavior of two different binary alloy systems can be combined to produce dense all-solid electrodes that have the kinetic properties of fine particle dispersions, as well as potentially attractive microstructural reversibility upon cycling.

INTRODUCTION

The cycling behavior of electrochemical cells, especially at lower temperatures, is often limited by negative electrode problems. These may include gradually increasing impedance, which is observed as increased electrode overvoltage. In some cases, there is macroscopic shape change. If

elemental electrodes are used (below their melting points), there may be dendrite growth, or a tendency for filamentary or whisker growth. This may lead to disconnection and electrical isolation of active material, resulting in loss of capacity. It may also result in electrical shorting between electrodes.

In the absence of a significant nucleation barrier, deposition of a species will tend to occur anywhere at which the electric potential is such that the element's chemical potential is at or above that corresponding to unit activity. This means that electrodeposition may take place upon current collectors and other parts of an electrochemical cell that are at the same potential as the negative electrode, as well as upon the electrode structure where it is actually desired. This was a significant problem during the period in which attempts were being made to use pure (molten) lithium as the negative electrode in high temperature molten salt cells. Another problem was the fact that alkali metals dissolve in their halides at elevated temperatures, leading to electronic conduction and self discharge.

In addition to these problems, the electrodeposition of a pure elemental negative electrode upon recharge can be inherently unstable on a microscopic scale, even in the presence of a chemically clean interface. It has been shown that electrodeposition can lead to an electrochemical analog of the constitutional supercooling that occurs during thermally-driven solidification[1,2]. This will be the case if the current density is such that solute depletion in the electrolyte near the electrode surface causes the local gradient of the element's chemical potential in the electrolyte immediately adjacent to the solid surface to be positive. Under such a condition, there will be a tendency for any protuberance upon the surface to grow at a faster rate than the rest of the interface. This leads to exaggerated surface roughness, and eventually to the formation of stable dendrites. In more extreme cases, it leads to the nucleation of solid particles in the liquid electrolyte ahead of the growing solid interface.

Further, the interface between the negative electrode and the adjacent electrolyte is often not clean. Instead, reaction between the electrode and species in the electrolyte can lead to the formation of reaction product layers. The properties of these layers can have significant effects upon the resultant behavior of the electrode. In some cases they may be useful solid electrolytes, and allow electrodeposition through them. But in many others they are ionically blocking, and thus can greatly increase the interfacial impedance. The presence of such layers, and the local nature of their electrical breakdown, generally related to defects in their structure that lead to spots of locally reduced impedance, often causes the formation of deleterious filamentary growths upon recharge. This is an endemic problem with the use of organic solvent electrolytes with lithium electrodes at ambient temperatures.

These problems can often be alleviated by the use of alloys, instead of elements, as negative electrode reactants. If the diffusion of the depositing species, e.g. Li, in the alloy is sufficiently fast that the activity at the surface remains less than unity, dendrite formation can be avoided. Deposition also occurs preferentially upon the desired electrode structure, rather than at other locations in the cell. In favorable cases, the formation of deleterious surface films may also be avoided.

However, the use of alloys with reduced activities implies reduced cell voltages, as well as increased weight. Therefore, possible increases in reversibility and cycle life of such electrodes are accompanied by reductions in the associated specific energy and energy density of cells in which they are employed.

Another potential problem in the use of alloy electrodes relates to the fact that there may be a significant volume or shape change involved in the electrode reaction. In some cases this will lead to mechanical deterioration of the electrode structure. In other cases, it is negligible.

EXPERIMENTAL RESULTS

A number of investigations have now been completed which have established the theoretical basis for understanding and predicting the potentials and capacities of both binary and ternary lithium alloys. These important practical parameters are directly related to the thermodynamic properties and compositional ranges of the pertinent phases in the respective phase diagrams.

In addition, measurements have been made of the chemical diffusion coefficient, which controls the kinetic behavior, in intermediate phases in a group of lithium alloy systems. Some of these have crystal structures that result in very high rates of lithium diffusion, indicating that they are good candidates for high rate cells.

There are three different types of reactions that can occur in electrodes, formation reactions, displacement reactions, and insertion reactions. In the first two of these, the number of phases present is equal to the number of components (under isothermal and isobaric conditions), so that, according to the Gibbs Phase Rule, all of the intensive parameters are independent of overall composition. This means that the electrode potential, under equilibrium or near-equilibrium conditions, is essentially constant. This leads to generally - desirable plateaus in discharge curves.

The length of these plateaus is determined by the extent of the two - phase regions in the related phase diagrams, in the case of binary alloys. In the ternary case, it is determined by the width of the three-phase constant - potential triangles.

Thermodynamic Data

Whereas, as pointed out above, it is possible to have insertion reactions in alloys, it has been found that these do not generally extend over appreciable compositional ranges in lithium - based alloy systems. For this reason, as well as the fact that such solid solution reactions produce potentials that vary with composition, rather than exhibiting constant - voltage plateaus, the bulk of the work to date has focussed upon materials that undergo displacement reactions.

An experimental arrangement employing the LiCl-KCl eutectic molten salt has been used in our laboratory at temperatures near 400 ^{o}C to study the phase diagrams and thermodynamic properties of alloys in the Li-Al, Li-Si, Li-Sb, Li-Bi, Li-Sn, Li-Pb, Li-In, Li-Ga and Li-Cd binary systems. The equilibrium potentials, as well as the stoichiometric ranges over which they are found, are presented in Table 1.

Table 1.
Thermodynamic Data For A Number of Binary Alloys

Voltage vs. Li	System	Range of y	Temp. (°C)	Reference
0.047	Li_ySi	3.25 - 4.4	400	(21-24)
0.058	Li_yCd	1.65 - 2.33	400	(25)
0.080	Li_yIn	2.08 - 2.67	400	(26)
0.089	Li_yPb	3.8 - 4.4	400	(27)
0.091	Li_yGa	1.53 - 1.93	400	(28)
0.122	Li_yGa	1.28 - 1.48	400	(28)
0.145	Li_yIn	1.74 - 1.92	400	(26)
0.156	Li_ySi	2.67 - 3.25	400	(21-24)
0.170	Li_ySn	3.5 - 4.4	400	(29)
0.237	Li_yPb	3.0 - 3.5	400	(27)
0.271	Li_yPb	2.67 - 3.0	400	(27)
0.283	Li_ySi	2 - 2.67	400	(21-24)
0.283	Li_ySn	2.6 - 3.5	400	(29)
0.300	Li_yAl	0.08 - 0.9	400	(30)
0.332	Li_ySi	0 - 2	400	(21-24)
0.373	Li_yCd	0.33 - 0.45	400	(25)
0.375	Li_yPb	1.1 - 2.67	400	(27)
0.387	Li_ySn	2.5 - 2.6	400	(29)
0.430	Li_ySn	2.33 - 2.5	400	(29)
0.455	Li_ySn	1.0 - 2.33	400	(29)
0.495	Li_yIn	1.2 - 0.86	400	(26)
0.507	Li_yPb	0 - 1.0	400	(27)
0.558	Li_yCd	0.12 - 0.21	400	(25)
0.565	Li_yGa	0.15 - 0.82	400	(28)
0.570	Li_ySn	0.57 - 1.0	400	(29)
0.750	Li_yBi	1.0 - 2.82	400	(31)
0.875	Li_ySb	2.0 - 3.0	400	(31)
0.910	Li_ySb	0 - 2.0	400	(31)

More recently, attention has been turned to the evaluation of such properties at lower temperatures. This has involved measurements[3] using $LiNO_3$-KNO_3 molten salts at about 150 °C, as well as experiments with organic solvent - based electrolytes at ambient temperatures[4,5].

Coulometric titration data were obtained over this wide temperature range for two alloy systems, Li-Sb and Li-Bi, each of which have two intermediate phases, in order to illustrate relevant principles. The temperature dependence

of the potentials of the two - phase equilibria in the Li-Sb system fell upon two straight lines, corresponding to the reactions 2 Li + Sb = Li_2Sb and Li + Li_2Sb = Li_3Sb, where Sb indicates the lithium - saturated terminal phase.

In the Li-Bi case, however, where the comparable reactions are Li + Bi = LiBi and 2 Li + LiBi = Li_3Bi, the temperature dependence is different. The data for the two reactions converge at high temperatures. Above about 420 °C, the phase LiBi is no longer stable, and there is only a single reaction, 3 Li + Bi = Li_3Bi.

In addition, the potentials of the second reaction fall along two straight line segments, depending upon the temperature range. There is a significant change in slope at about 210 °C, resulting in a negligible temperature dependence of the potential at low temperatures, due to the melting of bismuth.

From these temperature dependences, one can obtain values of the molar entropies of these several reactions. They are given in Table 2.

Table 2.
Thermodynamic Data For The Li-Sb and Li-Bi systems

Reaction	Molar Entropy of reaction (J/K · mol)	Temp. range (°C)
2Li + Sb --> Li_2Sb	-31.9	0 - 500
Li + Li_2Sb --> Li_3Sb	-46.5	0 - 600
Li + Bi --> LiBi	0	0 - 200
2LI + LiBi --> Li_3Bi	-36.4	0 - 400

In addition to the investigations at elevated temperatures, attention has been given to the ambient temperature properties of several alloy systems. Data on the potentials and stoichiometric ranges of the plateaus in the Li-Sb, Li-Bi, Li-Sn, Li-Pb, Li-Zn and Li-Cd systems at 25 °C are shown in Table 3.

The Li-Cd system is especially interesting, for it has a long plateau, spanning about 1.5 Li per mole, at a potential only about 50 mV above pure lithium.

Kinetic Data

As mentioned above, the kinetic properties of alloy electrodes are often determined by the rate at which solid state diffusion can occur through the outer phase of a two - phase microstructure. The pertinent basic parameter here is the chemical diffusion coefficient.

Several techniques have been developed whereby precise and reliable values of the chemical diffusion coefficient can be obtained by the use of molten salt

Table 3.
Plateau Potentials And Composition Ranges in Lithium Alloys at Low Temperatures

Voltage vs. Li	System	Range of y	Temp. (°C)	Reference
0.005	Li_yZn	1 - 1.5	25	(5)
0.055	Li_yCd	1.5 - 2.9	25	(5)
0.157	Li_yZn	0.67 - 1	25	(5)
0.219	Li_yZn	0.5 - 0.67	25	(5)
0.256	Li_yZn	0.4 - 0.5	25	(5)
0.292	Li_yPb	3.2 - 4.5	25	(5)
0.352	Li_yCd	0.3 - 0.6	25	(5)
0.374	Li_yPb	3.0 - 3.2	25	(5)
0.380	Li_ySn	3.5 - 4.4	25	(4)
0.420	Li_ySn	2.6 - 3.5	25	(4)
0.449	Li_yPb	1 - 3.0	25	(5)
0.485	Li_ySn	2.33 - 2.63	25	(4)
0.530	Li_ySn	0.7 - 2.33	25	(4)
0.601	Li_yPb	0 - 1	25	(5)
0.660	Li_ySn	0.4 - 0.7	25	(4)
0.680	Li_yCd	0 - 0.3	25	(5)
0.810	Li_yBi	1 - 3	25	(4)
0.828	Li_yBi	0 - 1	25	(4)
0.948	Li_ySb	2 - 3	25	(4)
0.956	Li_ySb	1 - 2	25	(4)

electrochemical cell techniques[6-10]. The physical arrangement can be closely related to that used for the thermodynamic measurements mentioned above.

The principles underlying the application of use of transient or relaxation electrochemical methods for the determination of the chemical diffusion coefficient in solids have been reviewed in a number of the places cited above, and thus will not be discussed here. One of the especially attractive features of this approach, compared to conventional methods, is the relative ease with which one can obtain data of high precision.

In addition to these methods, it was shown a few years ago[10-14] that a steady state ac method can also be used to obtain chemical diffusion data.

By the use of a combination of kinetic measurements and coulometric titration, which provides great compositional resolution, the variation of the diffusion coefficient with composition within phases, even if they have very narrow ranges of composition, can be readily obtained. This is particularly important in understanding the kinetics of polyphase electrode reactions.

As pointed out by Carl Wagner in an important paper[15] in 1953, the chemical diffusion coefficient can be very much greater than the self diffusion

coefficient in some materials. It is the latter quantity that has generally been measured in conventional radiotracer studies of diffusion in metals and alloys. This relationship is simply $D_c = D_s \cdot W$, where the quantity W is an enhancement factor, which can be written $W = d \ln a_i / d \ln c_i$, where a_i and c_i are the activity and concentration of electrically neutral species i, respectively. This enhancement factor has been discussed by Wagner[15,16], and was expressed in a somewhat different form by Darken[17], who called it the "thermodynamic factor". A general discussion of this factor, and its evaluation under various conditions relevant to electrochemical systems appeared[6] in 1977. By the use of the coulometric titration technique, the compositional variation of W can be experimentally determined.

These various techniques have been used to investigate chemical diffusion in a number of binary lithium alloys at elevated temperatures, and more recently, at ambient temperatures. Some of these data are included in Table 4. It can be seen that the value of W can be very large in some cases, and that this can lead to unusually high values of the chemical diffusion coefficient. This is indeed a fortunate circumstance, for it permits much faster electrode kinetics than would otherwise be the case.

Table 4
Data On Chemical Diffusion in Lithium Alloy Phases

Nominal Comp.	Range of Composition (% Li)	Max. Value of D_c (cm^2/sec)	Max. Value of W	Temp (^oC)	Reference
LiAl	16.4	1.2×10^{-4}	70	415	10,30
Li_3Sb	0.05	7.0×10^{-5}	70000	360	6
Li_3Bi	1.37	2.0×10^{-4}	370	380	32
$Li_{12}Si_7$	0.54	8.1×10^{-5}	160	415	24
Li_7Si_3	3.0	4.4×10^{-5}	111	415	24
$Li_{13}Si_4$	1.0	9.3×10^{-5}	325	415	24
$Li_{22}Si_5$	0.4	7.2×10^{-5}	232	415	24
LiSn	1.9	4.1×10^{-6}	185	415	33
Li_7Sn_3	0.5	4.1×10^{-5}	110	415	33
Li_5Sn_2	1.0	5.9×10^{-5}	99	415	33
$Li_{13}Sn_5$	0.5	7.6×10^{-4}	1150	415	33
Li_7Sn_2	1.4	7.8×10^{-5}	196	415	33
$Li_{22}Sn_5$	1.2	1.9×10^{-4}	335	415	33
LiGa	22.0	6.8×10^{-5}	56	415	28
LiIn	33.0	4.0×10^{-5}	52	415	26
LiCd	63.0	3.0×10^{-6}	7	415	25
Li_3Sn_4		$6\text{-}8 \times 10^{-8}$		25	4
Li_7Sn_3		$3\text{-}5 \times 10^{-7}$		25	4

The Mixed-Conductor Matrix Concept

In order to provide a high reactant surface area, and thus be able to achieve appreciable macroscopic current densities while maintaining low local microscopic charge and particle flux densities, many battery electrodes that are used in conjunction with liquid electrolytes are produced with porous microstructures containing very fine particles of the solid reactant materials. This porous structure is permeated with the electrolyte.

This porous fine-particle approach has several characteristic disadvantages. Among these are difficulties in producing uniform and reproducible microstructures, and limited mechanical strength when highly porous. In addition, they often suffer time - dependent changes in both microstructure and properties during cyclic operation.

A quite different approach was introduced a few years ago[18-20], in which a dense solid electrode is fabricated which has a composite microstructure in which particles of the reactant phase are finely dispersed within a solid mixed - conducting metallic matrix. This provides a large internal reactant/matrix interfacial area. If the matrix material has a high chemical diffusion rate for the electroactive species it can be rapidly transported through the solid matrix to this interfacial region, where it undergoes the chemical part of the electrode reaction. If the matrix material is also an electronic conductor, it acts as the electrode's current collector, and the electrochemical part of the reaction takes place on the outer surface of the composite electrode.

Upon discharge of such an electrode by deletion of the electroactive species, if a residual reactant particle does not interact with the surrounding matrix, it remains as a relic in the microstructure. This provides a fixed permanent location for the reaction to take place during following cycles. This provides a mechanism for the achievement of true microstructural reversibility.

There are several features of this situation that serve to illustrate and expand upon some of the principles discussed above. There are both thermodynamic and kinetic requirements that must be met.

The matrix and the reactant phase must be thermodynamically stable in contact with each other. One can evaluate this possibility if one has information about the relevant phase diagram - which typically involves a ternary system - as well as the titration curves of the component binary systems. In a ternary system, two materials must lie at the corners of the same constant - potential tie triangle in the isothermal ternary phase diagram in order to not interact. The potential of the tie triangle determines the electrode reaction potential. Therefore, an additional requirement is that the reactant material have two phases present in the tie triangle, but the matrix phase only one. This is another way of saying that the stability window of the matrix phase must span the reaction potential, but that the binary titration curve of the reactant material has a plateau at the tie triangle potential. One can evaluate the possibility that these conditions are met from knowledge of the binary titration curves, without having to do a large number of ternary experiments.

The kinetic requirements for a successful application of these concepts are also understandable. The primary issue is the chemical diffusion rate of the

electroactive species in the matrix phase. That can be determined by the various techniques discussed above.

An example has been demonstrated[18-20] that meets all of these requirements, the use of the phase with the nominal composition $Li_{13}Sn_5$ as the matrix, in conjunction with reactant phases in the lithium - silicon system at temperatures near 400 °C. This is an especially favorable case, due to the high chemical diffusion coefficient of lithium in the $Li_{13}Sn_5$ phase. There are surely other examples. We are currently investigating some possible combinations that might be useful at ambient temperatures in lithium systems.

One other obvious requirement is that the microstructure must have the ability to accommodate any volume changes that might result from the reaction that takes place internally. This can surely be taken care of by clever microstructural design and fabrication techniques.

ACKNOWLEDGEMENTS

The author gladly acknowledges that the results that are reported and discussed here are the fruits of the thought and labor of a number of his students and associates, to whom he is greatly indebted. Work in this area at Stanford University has been supported by the U. S. Department of Energy under Subcontract LBL 4519410.

REFERENCES

1. R. A. Huggins, J. Electrochem. Soc. 122, 90C (1975)
2. R. A. Huggins and D. Elwell, J. Crystal Growth 37, 159 (1977)
3. J. P. Doench and R. A. Huggins, J. Electrochem. Soc. 129, 341C (1982)
4. J. Wang, I. D. Raistrick and R. A. Huggins, J. Electrochem. Soc. 133, 457 (1986)
5. J. Wang, P. King and R. A. Huggins, to be published in Solid State Ionics
6. W. Weppner and R. A. Huggins, J. Electrochem. Soc. 124, 1569 (1977)
7. W. Weppner and R. A. Huggins, Z. f. Physik. Chem. NF 108, 105 (1977)
8. W. Weppner and R. A. Huggins, J. Solid State Chem. 22, 297 (1977)
9. W. Weppner and R. A. Huggins, in Annual Review of Materials Science, Vol 8, ed. by R. A. Huggins, Annual Reviews, Inc. (1978), p. 269
10. C. J. Wen, C. Ho, B. A. Boukamp, I. D. Raistrick, W. Weppner and R. A. Huggins, in International Metals Reviews 5, 253 (1981)
11. R. A. Huggins, in Chemical Metallurgy - A Tribute to Carl Wagner, ed. by N. A. Gokcen, A.I.M.E. (1982), p. 149
12. B. A. Boukamp, I. D. Raistrick and R. A. Huggins, in Fast Ion Transport in Solids, ed. by P. Vashishta, J. N. Mundy and G. K. Shenoy, North-Holland (1979), p. 177
13. C. Ho, I. D. Raistrick and R. A. Huggins, J. Electrochem. Soc. 127, 343 (1980)
14. C. Ho, Ph.D. Dissertation, Stanford University (1980)
15. C. Wagner, J. Chemical Physics 21, 1819 (1953)
16. C. Wagner, in Atom Movements, American Society for Metals (1951), p. 153
17. L. S. Darken, Trans. A.I.M.E. 175, 184 (1948)
18. B. A. Boukamp, G. C. Lesh and R. A. Huggins, J. Electrochem. Soc. 128, 725 (1981)

19. B. A. Boukamp, G. C. Lesh and R. A. Huggins, in Proceedings of the Symposium on Lithium Batteries, ed. by H. V. Venkatasetty, Electrochem. Soc. (1981), p. 467
20. R. A. Huggins and B. A. Boukamp, U. S. Patent 4,436,796 (1984)
21. L. R. McCoy and S. Lai, in Proc. of Symposium and Workshop on Advanced Battery Research and Design, Argonne Nat'l Lab. ANL-76-8 (1976), p. B-167.
22. S. Lai, J. Electrochem. Soc. 123, 1196 (1976).
23. R. A. Sharma and R. N. Seefurth, J. Electrochem. Soc. 123, 1763 (1976).
24. C. J. Wen and R. A. Huggins, J. Solid State Chem. 37, 271 (1981)
25. C. J. Wen, Ph.D. Dissertation, Stanford University (1980).
26. C. J. Wen and R. A. Huggins, Mat. Res. Bull. 15, 1225 (1980)
27. M. L. Saboungi, J.J. Marr, K. Anderson and D.R. Vissers, J. Electrochem. Soc. 126, 322C (1979)
28. C. J. Wen and R. A. Huggins, J. Electrochem. Soc. 128, 1636 (1981)
29. C. J. Wen and R. A. Huggins, J. Electrochem. Soc. 128, 1181 (1981)
30. C. J. Wen. B.A. Boukamp, R.A. Huggins and W. Weppner, J. Electrochem. Soc. 126, 2258 (1979).
31. W. Weppner and R.A. Huggins, J. Electrochem. Soc. 125, 7 (1978).
32. W. Weppner and R. A. Huggins, J. Solid State Chem. 22, 297 (1977)
33. C. J. Wen and R. A. Huggins, J. Solid State Chem. 35, 376 (1980)

SESSION B

ENGINEERING DEVELOPMENT OF LITHIUM-ALLOY/METAL SULFIDE BATTERIES

Afternoon, April 16, 1986
Chairman, John Dunning
Vice Chairman, Elton Cairns

Morning and Afternoon, April 17, 1986
Chairman, Robert Huggins
Vice Chairman, J. R. Selman

REVIEW OF CELL DEVELOPMENT FOR MOLTEN-SALT BATTERY

D. R. Vissers

Chemical Technology Division
Argonne National Laboratory
Argonne, IL 60439

ABSTRACT

In the early 1970s, transition metal sulfides (FeS, FeS_2 and Cu_2S) and Li alloys (Li-Al and Li-Si) were identified as attractive positive and negative electrode materials, respectively, for molten-salt battery cells. The development effort that followed in the 1970s and 1980s resulted in fabrication of a Li-alloy/FeS cell with high performance (>100 Wh/kg, 150 W/kg) and long cycle life (>1000 cycles). Recent studies conducted with upper-plateau Li-Al/FeS_2 cells indicate performance superior to that reported for Li-alloy/FeS cells. The paper reviews the engineering development of the Li-alloy/FeS_x cells and the cell chemistry research which assisted that development.

INTRODUCTION

In the late 1960s and early 1970s Argonne National Laboratory (ANL) and Rockwell International initiated efforts to develop long-lived Li/S cells, which have high theoretical specific energy, ~2600 Wh/kg. The inability to contain the active materials (lithium and sulfur) in the respective electrodes and the severe corrosion problems associated with these materials indicated that the goal of a long-lived Li/S cell would be difficult to achieve.[1,2] During the course of this work, however, insights, gained at both laboratories almost simultaneously, led to the selection of transition metal sulfides for the positive electrode materials (FeS, and FeS_2)[3,4] and Li alloy for the negative electrodes[5-9] (Li-Al and Li-Si). When these new electrode materials were coupled to form a cell with a molten-salt electrolyte, considerable improvements were observed in the cell cycle life.[10,11] These new electrode materials, however, resulted in a significant loss of specific energy, as indicated in Table 1.

The general reactions for the Li-Al/FeS and Li-Al/FeS_2 cells are as follows:

$$4\text{Li-Al} + FeS_2 \rightarrow 2Li_2S + Fe + 4Al \quad (1)$$

$$2\text{Li-Al} + FeS \rightarrow Li_2S + Fe + 2Al \quad (2)$$

These cells have an average open-circuit voltage of ~1.66 and 1.33 V, respectively. Cells with Li-Si negative electrodes have slightly higher voltage than the comparable cells with Li-Al alloy electrodes.

Table 1. Thermodynamic Characteristics of Selected Cell Couples

System	Theoretical Specific Energy, Wh/kg
Li/S	2555
Li/FeS_2	1326
$Li_{3.85}Si/FeS_2$	954
$Li-Al/FeS_2$	629
Li-Al/FeS	457
Pb/PbO_2	175

In the early 1970s, ANL inaugurated a research and development program on the lithium-alloy/metal sulfide cell. Throughout the course of this program, a major objective was to involve industrial organizations in the effort so that the technology could be transferred to them as it was developed.

Industrial participants included Gould Inc., Eagle-Picher Industries, Inc., and Catalyst Research Corp., and the Atomics International Division of Rockwell International.

In this paper, we will review the engineering development of the Li-alloy/metal sulfide cell and the research into cell chemistry and electrochemistry that assisted this development.

ENGINEERING DEVELOPMENT

The engineering development in this program was directed toward both the Li-alloy/FeS_2 and the Li-alloy/FeS cell systems. At first, the engineering efforts focused on the Li-alloy/FeS_2 cell because of its higher theoretic specific energy. However, as the problems of short cycle life and corrosion of current collector materials for the FeS_2 electrode became visible,[12,13] the effort shifted toward development of the Li-alloy/FeS cell system. After more than a decade of research and development, this system is near to "commercialization." For this reason, the Department of Energy decided to phase out the work on the Li-alloy/FeS battery in 1981.

Li-Alloy/FeS_2 Cells

The engineering cells built at ANL in 1974 were cylindrical and utilized a central positive electrode of FeS_2 with two facing Li-Al negative electrodes.[14,15] This cell design is depicted in Fig. 1. The cell case in

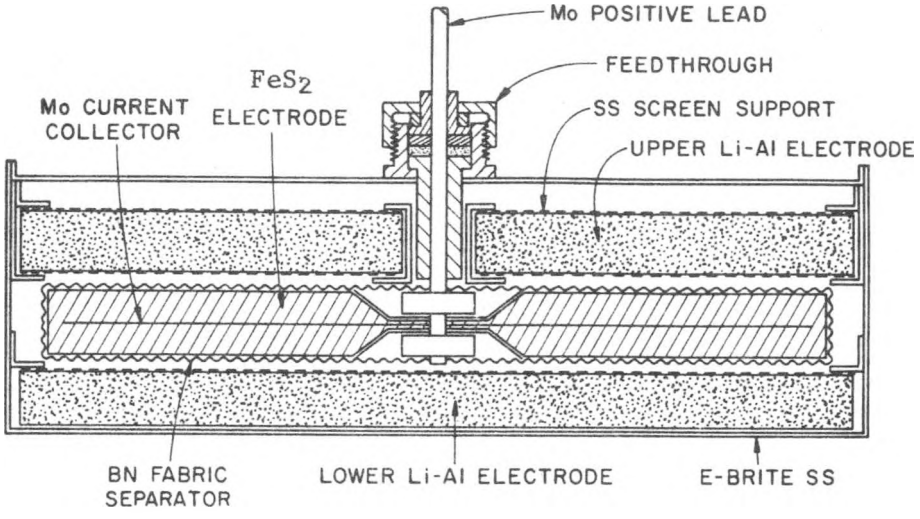

Fig. 1. Cylindrical Bicell Design

this design and all later designs operated at the negative electrode potential, thus requiring only one electrode feedthrough. This cell design was also used with the early Li-Al/FeS cells. These initial cells had capacities of ~150 Ah and specific energies of 75 to 100 Wh/kg.

The General Motors (GM) Research Laboratories developed a cell similar in design to the ANL cells.[11] These FeS_2 cells utilized Li-Si alloy negative electrodes and achieved excellent specific energies (~183 Wh/kg) at low specific power levels. At higher power levels, the high internal resistance of the cell reduced the specific energy significantly. Under low charging rates (~12 h), the GM Li-Si/FeS_2 cells demonstrated good cycle life (650 cycles) and excellent coulombic efficiencies (~99%).

During cycling tests of the cylindrical bicells, two serious problems were observed: (1) the electrodes swelled and became distorted, which led to short circuits caused by active material extrusion, and (2) the molybdenum welds on the current collector in the FeS_2 electrode sometimes broke and caused cell resistance to increase several fold. Better mechanical restraint could probably have solved the swelling problem; however, the current collector problem would require a collector redesign that would reduce the level of stress in the weld area.

Although the cylindrical cells gave excellent performance, stacking them to form a battery proved difficult. Efforts in recent years have, therefore, focused on the development of a prismatic bicell with vertically oriented electrodes. These cells can be stacked in a compact manner to form a high-performance battery. These cells are typically 13 x 13 cm or 13 x 18 cm and vary in thickness from 1 to 3 cm. The electrode arrangement is similar to that of the cylindrical bicells, with a central positive and two facing negative electrodes.

Prismatic Li-Al/FeS_2 bicells with capacities of 40 to 150 Ah were constructed by ANL[16,17] and three contractors: Eagle-Picher, Inc.,[18] Rockwell International,[18,19] and Gould.[18,19] In the development effort, several hundred prismatic bicells of varying designs were built and tested. Cell design parameters investigated in these studies included: (1) state of charge of cell during fabrication, (2) molybdenum current collector materials and fabrication methods, (3) feedthrough design, (4) design of electrode particle retainers, (5) positive-to-negative capacity ratio, (6) electrolyte composition, (7) loading density of active material (Ah/cm^3), (8) separator materials and separator wetting techniques, (9) composition of active materials, and (10) electrode construction.

Most of the Li-alloy/FeS_2 cells had excellent specific energy (~75-100 Wh/kg) and power (75-150 W/kg), but tended to lose capacity rapidly when they were charged at a 2- to 4-h rate. Until recently, the cycle life of these cells was usually 200 cycles or lower unless they were charged at a 12-h rate. The Li-Al/FeS_2 cells built with a LiCl-LiBr-KBr electrolye (rather than the usual LiCl-KCl) and operated on the upper-voltage plateau (reported in this proceedings by T. Kaun) appear not to have the cycle life problem associated with the earlier Li-Al/FeS_2 cell. Why these upper-plateau cells have excellent cycle life is not entirely understood. The long cycle life may, in part, result from the fact that the FeS_2 electrode is not deeply discharged, it has a very high loading density of active material, and it is operated at a slightly lower temperature with the LiCl-LiBr-KBr electrolyte instead of the LiCl-KCl.

Li-Alloy/FeS Cells

The specific energy of the Li-Al/FeS bicells fabricated by ANL, Gould, and Eagle-Picher varied between about 47 and 58 Wh/kg.[20] While these cells had longer cycle life than the Li-Al/FeS_2 cells (200-300 cycles), they did not have the specific energy needed for electric-vehicle applications. To improve the performance of the Li-Al/FeS cell, Gould and Eagle-Picher developed a multiplate cell design. This cell design contains two or three positive electrodes and three or four negative electrodes where each array of electrodes is connected in parallel. A schematic of the Eagle-Picher multiplate cell design (three positive electrodes) is shown in Fig. 2.[21] This multiplate is essentially the same as the electrodes of three bicells encased in a single cell housing, with appropriate changes in the positive and negative buses as well as feedthrough to accommodate the higher current. It is flooded with 68 mol % LiCl-KCl electrolyte and has a BN felt separator to electronically isolate the negative from the positive electrodes. The Gould cells are similar in design to those of Eagle-Picher, but they use a starved 22LiF-31LiCl-47LiBr (mol %) electrolyte and a pressed separator formed from fine MgO powder and electrolyte.

While various sizes and designs of multiplate cells were built by Eagle-Picher, the most recent design, developed for the U.S. Army Mobility Equipment and Research and Development Command (MERADCOM), had a capacity of 340 Ah (519 Wh) and weighed 3.7 kg. Five of these cells were fabricated and then tested at ANL. They achieved 93 Wh/kg at a 6-h discharge rate and an average of >1000 cycles in deep discharge cycling, with a mean time to failure of 1012 cycles.[22]

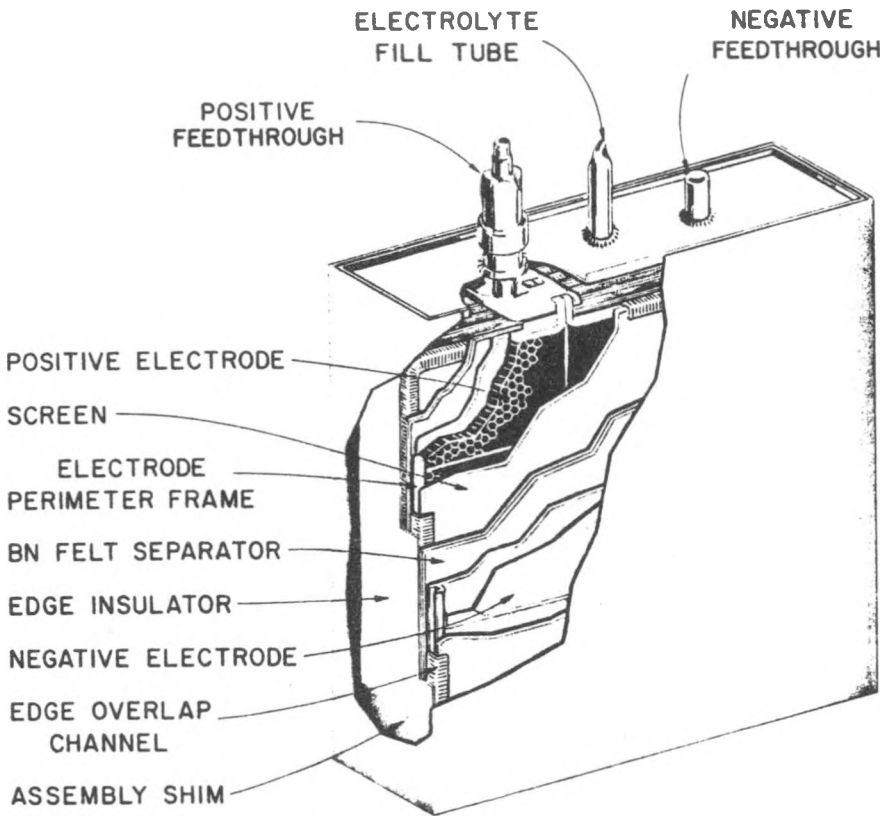

Fig. 2. Schematic of Multiplate Cell

The Gould multiplate cells are discussed in two other papers in this proceedings.[23,24] Unlike the Eagle-Picher cells, which are limited in capacity by the positive electrode, the most recent Gould cells use a negative-electrode-limited design. These latest 300-Ah cells have achieved a specific energy of 105 Wh/kg at a 3-h discharge rate and a cycle life of 200-300 cycles.[25] At the present time, only the Gould multiplate cells are being fabricated and tested. Battery modules with nine Gould cells are currently being tested at ANL. The cells in these modules are delivering ~90 Wh/kg.

CELL CHEMISTRY AND ELECTROCHEMISTRY

As part of the molten-salt battery program, a significant effort was devoted to understanding the chemistry and electrochemistry of the lithium alloys (Li-Al and Li-Si) and the metal sulfides (FeS and FeS_2). While the cell chemistry investigations on these materials were carried out primarily at ANL, studies were also done at the General Motors Research Laboratories, Stanford University, University of California at Berkeley, Rockwell International, and the Max-Planck Institute for Solid State Science (Stuttgart, West Germany).

Negative Electrode Materials

Two lithium alloys were developed as negative electrode materials. The first was the Li-Al alloy electrode, investigated and developed primarily at ANL, and the second was the Li-Si alloy electrode, which was investigated and developed primarily at General Motors and Rockwell International.

Li-Al Electrode. Because of some questions about the Li-Al phase diagram, it was redetermined. The diagram, given in Fig. 3,[26] indicates that at a cell operating temperature of 450°C, the solubility limit of lithium in aluminum is 10 at. %, which is the boundary of the α-Al phase field. The β-LiAl field has a composition width of 9 at. % (between 47 and 56 at. % lithium). The Li-Al electrode is usually cycled across the two-phase region between 10 and 47 at. % lithium, within which the emf of the electrode remains constant at 292 mV relative to elemental lithium.[5] If the lithium content is increased above 47 at. % into the β-LiAl phase, the potential decreases very rapidly and approaches that of lithium.[27] The theoretical capacity of Li-Al containing 47 at. % lithium, which has a density of 1.75 g/cm^3, is approximately 0.74 Ah/g or 1.3 Ah/cm^3 when the material is discharged to 10 at. % lithium.

Metallographic and scanning electron microscopic examinations showed that the Li-Al alloy, when cycled electrochemically, forms a porous, interconnected (skeletal) microstructure.[28] This type of microstructure is formed regardless of whether the starting material is Li-Al particles, Li-Al cast plates, or aluminum wire charged electrochemically with lithium. This

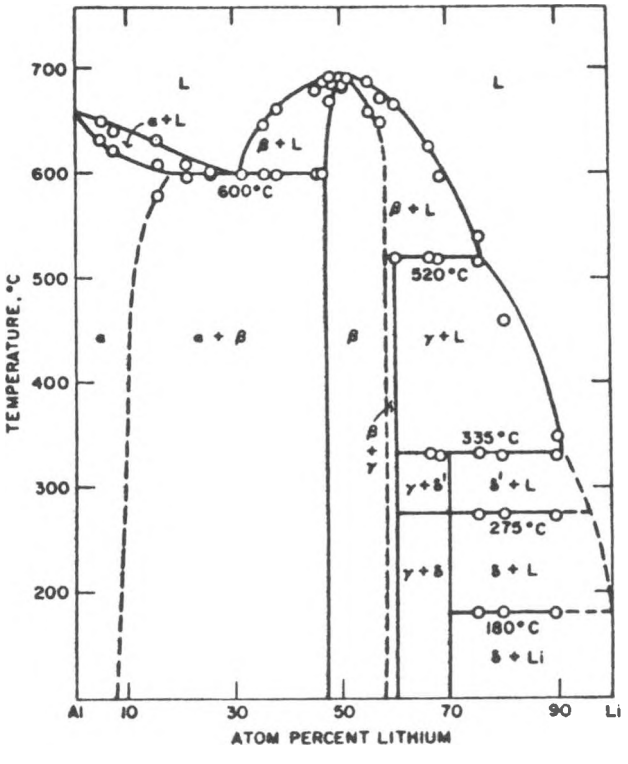

Fig. 3. Lithium-Aluminum Alloy Phase Diagram

porous microstructure appears to yield efficient electrodes that can be discharged at high rates. Under certain conditions (e.g., unfavorable electrode loadings), agglomeration of the active material can occur, with a resulting loss of cell capacity. This phenomenon is not observed, however, in well-designed Li-Al electrodes.

Kinetic studies of the Li-Al electrode were investigated by L. Redey et al.[29] to determine the voltage-loss characteristics of the electrode as a function of current density and electrode thickness. A specially designed compact cell with nearly perfect current collection was used in conjunction with a DC current-interruption, potential-relaxation technique to measure the voltage loss. The results of these studies[29] indicated that the voltage loss developed in Li-Al electrodes (0.30- to 0.50-cm thick) generated an area specific resistance (ASR) of less than 0.1 ohm·cm^2. For the Li-Al electrode, this value was found to be essentially independent of current density. The ASR value developed in this work is a useful engineering unit, since the resistance of an electrode can be derived simply by dividing the ASR value by the electrode area of the engineering cell being evaluated. The very low observed resistivity of the Li-Al electrode is probably associated with the high surface area of the skeletal electrode structure and the high chemical diffusibility of lithium in the α + β-LiAl.[27]

Li-Si Electrode. There is some question about the composition of the phases present in the Li-Si electrode at cell operating temperatures. Sharma and Seefurth[6] found the phases to be Li_2Si, $Li_{21}Si_8$, $Li_{15}Si_4$, and $Li_{22}Si_5$; while Lai,[7] and McCoy and Lai[8] concluded that the phases are Li_2Si, $Li_{2.8}Si$, $Li_{4.1}Si$, and Li_5Si. More recently, Schnering et al.[30] identified the phases to be $Li_{1.71}Si$, $Li_{2.33}Si$, $Li_{3.25}Si$, and $Li_{3.8-3.9}Si$; and Wen and Huggins[31] concluded that the phases are $Li_{1.731}Si$, $Li_{2.367}Si$, $Li_{3.317}S$, and $Li_{4.41}Si$.

Despite the disagreement over the composition of the phases in the Li-Si electrode, the various workers agree on the plateau emfs vs. lithium at cell operating temperature. These plateau values, which correspond to the respective two-phase regions, are 322, 288, 158, and 44 mV.

Polarization studies indicate that the voltage losses which develop in the electrode vary with the Li-Si composition.[29,32] For example, the power measured on three of the Li-Si voltage plateaus ($Li_{3.25}Si$-$Li_{2.33}Si$, $Li_{2.33}Si$-$Li_{1.71}Si$, and $Li_{1.71}Si$-Si) is quite good except for the $Li_{1.71}Si$-Si plateau. The poor power on this plateau probably results from the formation of elemental silicon on the surfaces of the $Li_{1.71}Si$ particles. The ASR values measured in this study for the Li-Si electrode during discharge was found to vary from 0.374 to 0.730 ohm cm^2 corresponding to a composition range of $Li_{3.17}Si$ to $Li_{0.95}Si$, respectively. These values are about a factor of three larger than those observed with the Li-Al electrode. The polarization values were again essentially independent of current density.

Since only a limited number of examinations have been made on cycled Li-Si electrodes, very little is known about the electrode morphology. However, based on the work of Fischer and Vissers,[33] it appears that the morphology of Li-Si electrodes is considerably different from that of Li-Al electrodes. The electrode morphology is more particulate in nature and does

not seem to form the interconnected skeletal structure found in the Li-Al electrode. Additional studies are required before definitive comments can be made on structural changes in this electrode.

FeS_2 Electrode. The first reported studies on the FeS_2 electrode indicated good electrochemical properties.[3] Since then, many studies have been performed to establish the phases formed and the phase progression as this electrode is discharged at cell operating temperatures.[34-42] Martin established the Li-Fe-S phase diagram that relates to the FeS and FeS_2 electrode phase transitions at 450°C (see Fig. 4).[43] The phases were identified in out-of-cell preparations examined by metallographic and x-ray diffraction techniques. Martin's phase diagram work indicates the phase progression sequence as

$$FeS_2 \rightarrow Li_3Fe_2S_4 \rightarrow Li_{2+x}Fe_{1-x}S_2 \ (x = 0.2) \qquad (3)$$

$$\text{and } Fe_{1-y}S \rightarrow Li_2FeS_2 \rightarrow Li_2S$$

Cycled FeS_2 electrodes examined by Tomczuk et al.[42] for phase identification indicated the following phases:

FeS_2, $KFeS_2$, $Li_3Fe_2S_4$, $Li_{2.33}Fe_{0.67}S_2$, $Fe_{1-x}S$, Li_2FeS_2 (X-phase),

$LiK_6Fe_{24}S_{26}Cl$ (J-phase), Li_2S, and Fe

The data of Tomczuk and Martin are in good agreement with the exception of the solid solution phase, $Li_{2+x}Fe_{1-x}S_2$, which was not detected because the phase decomposes on cooling to yield $Li_{2.33}Fe_{0.67}S_2$ and Li_2FeS_2 and the two potassium-containing phases. The potassium-containing phases are always minor phases in the FeS_2 electrode. Coulometry studies[42] of the FeS_2 electrode provided additional support for Martin's phase diagram, since breaks in the curve of voltage vs. depth of discharge were observed very near the composition values predicted by the phase diagram. The X-ray diffraction patterns for the respective phases were determined and have been published.[39]

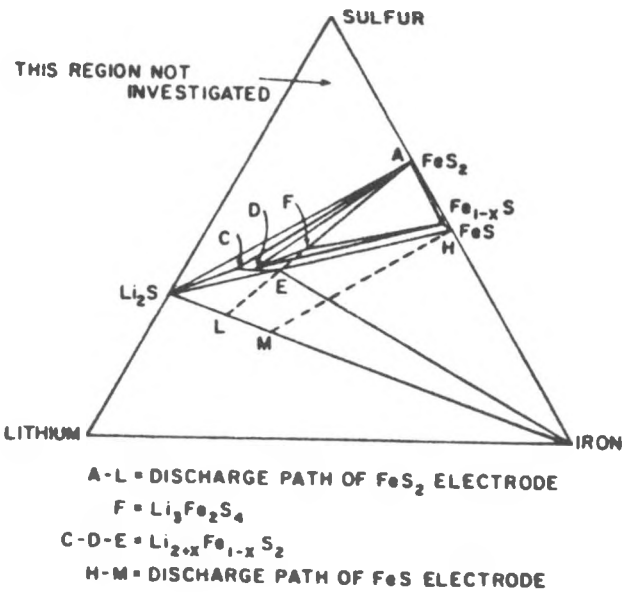

Fig. 4. Phases in the Li-Fe-S System at 450°C

The phase progression in cells charged at 18 mA/cm^2 to a preselected voltage and then constant-voltage charged at this value was consistent with the phase diagram data.[39] In these experiments, however, FeS_2 formation did not occur at the voltage at which it was observed when these cells were discharged, namely, 1.76 V at 400°C. Instead, complete formation of FeS_2 was not observed until a value of ~1.85 V was reached. Cyclic voltammetry experiments carried out by Preto et al.[43] also indicated a nucleation overpotential of 95 mV for the formation of FeS_2 at 400°C. They were able to show that the value of the nucleation overpotential depended on the degree of discharge. For example, when the FeS_2 electrode had been partially discharged to $Li_3Fe_2S_4$, with some FeS_2 still present in the electrode, the nucleation overpotential dropped to only 20 mV. Metallographic examinations on cycled electrodes[39] indicated that FeS_2 did not form on $Li_3Fe_2S_4$ but had formed on $Fe_{1-x}S$ particles. Since $Li_3Fe_2S_4$ particles were always observed on FeS_2 particles on discharge, these workers concluded that charge and discharge reactions were quite different in the $Li_3Fe_2S_4$ >FeS_2 transition region. Support for this conclusion was also obtained by Preto et al.,[43] who were able to show that a nonequilibrium species is formed in the region where $Li_3Fe_2S_4$ disappears and FeS_2 is formed. Although this species could not be conclusively identified, it was believed to be Li_2S_2. Earlier, Schmidt and Weppner,[44] in study of the kinetic properties of the ternary Li-Fe-S phases, also claimed that Li_2S_2 is formed in FeS_2 electrodes, but did not give any proof for this claim.

The results of these studies suggest that an upper-plateau FeS_2 electrode, which has a high solids loading in the charged states, many have much better cycle life than a two-plateau FeS_2 cell. This conclusion is based on the fact that an upper-plateau cell will be discharged to $Li_3Fe_2S_4$ and will probably still have FeS_2 present, thus a lower nucleation overpotential, and will have less electrolyte to transport from the electrode any soluble metal sulfide phases that form during charging.

The emf vs. temperature curves were determined by Tomczuk and Vissers[45] for the FeS_2 > $Li_3Fe_2S_4$, $Li_3Fe_2S_4$ > $Li_{2+x}Fe_{1-x}S_2$ + $Fe_{1-y}S$, and Li_2FeS_2 > Li_2S transitions in LiCl-KCl eutectic over the temperature range 382-455°C. The emf equations derived from these curves are presented in Table 2. The slopes for the first two transitions are positive, indicating that heat is adsorbed during these transitions; while the slope is negative for the last transition, indicating that heat is released. These data suggest that heat generation during discharge of an upper-plateau FeS_2 cell at a current density of 125 mA/cm^2 would be quite modest.[45]

Kinetic studies of a Li-Si/FeS_2 cell using nearly perfect current collection[46] indicate ASR values of 1 to 2 ohm cm^2 for an FeS_2 electrode with a loading of 1.1 Ah/cm^3 and a thickness of 0.6 cm. A sizable fraction of the observed ASR value was ohmic in nature, suggesting a large bed resistance and a need for dispersed current collection.

Table 2. Summary of Emf Results

Transition	Emf vs. Temperature Equation
FeS_2 > $Li_3Fe_2S_4$	E = 1.55580 + 0.0004785T (°C)
$Li_3Fe_2S_4 \longrightarrow Li_{2+x}Fe_{1-x}S_2 + Fe_{1-x}S$	E = 1.37902 + 0.0006666T (°C)
Li_2FeS_2 > Li_2S	E = 1.31999 - 0.000147T (°C)

FeS Electrode. The chemistry and electrochemistry of the FeS electrode have been investigated in detail,[39,42,47-58] and the results indicate that the electrode reactions are more complex than earlier thought. For example, the Li-Fe-S phase diagram (Fig. 4) suggests two reactions:

$$2FeS + 2Li\text{-}Al \longrightarrow Li_2FeS_2 + 2Al + Fe \quad (4)$$

$$Li_2FeS_2 + 2Li\text{-}Al \longrightarrow 2Li_2S + 2Al + Fe \quad (5)$$

These two reactions should appear essentially as one on the discharge voltage plateau, since the Gibbs energy of formation of Li_2FeS_2 from FeS and Li_2S is less than 1 kcal/mol.[42] However, microscopic examination of the phases present in the electrode after cycling indicated that the major voltage plateau corresponds to the formation of J-phase ($LiK_6Fe_{24}S_{26}Cl$).[42,48,59] The J-phase is formed in the electrode by an interaction of the electrolyte with the active materials in the FeS electrode. Thus, in addition to the above two reactions, three other electrochemical and four chemical reactions have been identified:[50]

Electrochemical Reactions

$$26FeS + 6KCl + 6LiAl \longrightarrow 2Fe + LiK_6Fe_{24}S_{26}Cl + 5LiCl + 6Al \quad (6)$$

$$LiK_6Fe_{24}S_{26}Cl + 5LiCl + 20LiAl \longrightarrow 13Li_2FeS_2 + 11Fe + 6KCl + 20Al \quad (7)$$

$$LiK_6Fe_{24}S_{26}Cl + 5LiCl + 46LiAl \longrightarrow 26Li_2S + 24Fe + 6KCl + 46Al \quad (8)$$

Chemical Reactions

$$23Li_2FeS_2 + Fe + 6KCl \longleftrightarrow LiK_6Fe_{24}S_{26}Cl + 20Li_2S + 5LiCl \quad (9)$$

$$3Li_2FeS_2 + 20FeS + Fe + 6KCl \longleftrightarrow LiK_6Fe_{24}S_{26}Cl + 5LiCl \quad (10)$$

$$23FeS + 3Li_2S + Fe + 6KCl \longleftrightarrow LiK_6Fe_{24}S_{26}Cl + 5LiCl \quad (11)$$

$$FeS + Li_2S \longleftrightarrow Li_2FeS_2 \quad (12)$$

The phase transition sequence and emf and thermodynamic information on these reactions were determined by Z. Tomczuk et al.[50]

During the development of the FeS cell, it became evident that the formation of $LiK_6Fe_{24}S_{26}Cl$ (J-phase), which occurs through reactions with the KCl in the LiCl-KCl electrolyte, hinders the kinetics of the FeS electrode. At one time, Cu_2S was added to the positive electrode to inhibit the formation of this phase, but subsequent post-test examinations of the cells indicated that this tended to cause early cell failures because the precipitation of metallic copper in the electrode separators resulted in short circuits.[60] Small-scale cell tests[61] and thermodynamic studies[5,54] indicated that the stability of this phase can be decreased either by increasing the LiCl content of the electrolyte (above the eutectic) or by raising the operating temperature of the cell. Saboungi and Martin[54] made a careful metallographic examination of the products of reactions (9) and (10) in eutectic and LiCl-saturated electrolyte to determine the temperature above which J-phase does not form. For reaction (9) the temperatures are 455°C for the eutectic electrolyte and 419°C for the LiCl-saturated electrolyte. The temperatures for reaction (10) are 623°C for the eutectic and 481°C for the LiCl-saturated electrolyte. Small-scale FeS cell tests by Vissers et al.[61] indicated that, as the LiCl content of the electrolyte was increased, the active material utilization of the FeS electrodes improved markedly and the effect of temperature on the electrode utilization decreased. From these studies, a LiCl-KCl electrolyte containing ~67 mol % LiCl seemed appropriate for Li-Al/FeS cell development.

The formation of $LiK_6Fe_{24}S_{26}Cl$ can be entirely avoided by the use of an electrolyte that contains only lithium cations, e.g., LiF-LiCl-LiBr. Although cell performance can be improved considerably by increasing the lithium ion content of the electrolyte (either by increasing the LiCl concentration or by the use of an all-lithium-cation electrolyte), this increased lithium content results in a higher liquidus temperature or melting point for the electrolyte. Consequently, the cell operating temperature must be raised above 450°C. Eagle-Picher and ANL used the LiCl-rich electrolyte (68 mol % LiCl-32 mol % KCl) in their cells, whereas Gould used the all-lithium cation electrolyte (22 mol % LiF-32 mol % LiCl-46 mol % LiBr).

Recent electrode kinetic studies on the porous FeS electrode have been conducted in specially designed prismatic bicells with one-dimensional current distribution. The current interruption, potential relaxation technique has been employed to determine ASR values for the FeS electrode. The ASR values for the FeS electrode[29] (thickness, 0.26 cm) were found to vary from 0.3 to 1.0 ohm cm^2, with the value rising rapidly at 60% depth of discharge. These results in conjunction with the ASR values for Li-Al clearly indicate that, at deep discharge levels, the performance of a lithium-limited cell would be superior to a sulfur-limited cell. That is to say the polarization characteristics of the LiAl electrode do not change as dramatically with depth of discharge as do those of the FeS electrode. The paper entitled "Development of the Lithium-Limited FeS Cell" by T. Kaun, presented in this proceedings, discusses the advantages of such a cell system.

Because low-carbon steel current collectors are used in engineering cells, the normal charge cutoff voltages employed are always less than 1.60 V vs. LiAl to minimize the oxidation of the current collector to $FeCl_2$. The soluble $FeCl_2$ tends to be reduced by the dissolved lithium metal in the electrolyte and results in metallic iron deposits in the separator. With time, short circuits are caused by these deposits and result in cell failure. Such deposits were the cause of the failure in most of the MERADCOM cells.

CONCLUSIONS

The development of the Li-alloy/FeS and Li-alloy FeS_2 cells has been unique in the field of battery technology. The electrode couples were identified almost simultaneously at Argonne National Laboratory and at Rockwell International. The bulk of the work on the electrochemistry and chemistry of the system was done at ANL, while significant efforts in the engineering development of the cell were conducted both at national laboratories (Argonne and Lawrence Berkeley) and at private industrial laboratories (Eagle-Picher, Gould, and General Motors).

While the efforts in electrochemistry and cell chemistry were probably about equally divided between the Li-alloy/FeS and Li-alloy/FeS_2 couples, the efforts in engineering cell development were focused on the Li-alloy/FeS couple. Recently, ten Li-Al/FeS cells connected in series and housed in a module were tested in preparation for construction of 30-kWh batteries. (See paper by A. A. Chilenskas, this proceedings.)

The Li-alloy/FeS_2 cells did not receive the same engineering development effort because of the cycle-life problems that the early cells exhibited. Recent work, however, by Kaun (see this proceedings) indicates that upper-plateau FeS_2 cells can achieve long cycle life and high specific energy and power. With this latest breakthrough, the potential of developing a Li-alloy/FeS_2 battery seems excellent.

Acknowledgment

This work was supported by the U.S. Department of Energy, Office of Energy Storage under Contract W-31-109-Eng-38.

References

1. R. K. Steunenberg, "Liquid Metal Electrodes in Secondary Batteries," in Proc. Int. Conf. Liquid Metal Technology in Energy Reduction, ERDA Report CONF-760503-P2, p. 485 (1977).

2. J. Birk and R. K. Steunenberg, "Chemical Investigations of Lithium-Sulfur Cells," in New Uses of Sulfur, J. R. West, Ed., Adv. Chem. Ser. 140, ACS, Washington, DC, pp. 186-202 (1975).

3. D. R. Vissers, Z. Tomczuk, and R. K. Steunenberg, J. Electrochem. Soc. 121, 655 (1974).

4. L. A. Heredy, S. Lai, L. McCoy, and R. Saunders, in New Uses of Sulfur, J. R. West, Ed., Adv. Chem. Ser. 140, ACS, Washington, DC, p. 203 (1975).

5. N. P. Yao, L. A. Heredy, and R. C. Saunders, J. Electrochem. Soc. **118**, 1039 (1971).

6. R. A. Sharma and R. N. Seefurth, J. Electrochem. Soc. **123**, 1763 (1976).

7. S. C. Lai, J. Electrochem. Soc. **123**, 1196 (1976).

8. L. R. McCoy and S. Lai, "Lithium-Silicon Electrode," Extended Abstracts of the Electrochem. Soc. Meeting, Vol. 75-2, p. 58 (1975)

9. D. R. Vissers et al., in High-Performance Batteries for Off-Peak Energy Storage and Electric Vehicle Propulsion: Progress Report for the Period of July-September 1976, Argonne National Laboratory Report ANL-76-98, p. 44 (1976).

10. W. W. Schertz et al., in Development of High-Specific-Energy Batteries for Electric Vehicles: Progress Report for the Period January 1974-August 1975, Argonne National Laboratory Report ANL-8058, p. 8 (June 1974).

11. E. J. Zietner, Jr., and J. S. Dunning, "High Performance Lithium/Iron Disulfide Cells," Proc. 13th IECEC, p. 697 (1978).

12. V. Kolba, G. W. Redding, J. L. Hamilton, High-Performance Batteries for Stationary Energy Storage and Electric Vehicle Propulsion: Progress Report for Period October-December 1976, Argonne National Laboratory Report ANL-77-17 (April 1977).

13. A. E. Martin and Z. Tomczuk, in High-Performance Batteries for Electric-Vehicle Propulsion and Stationary Energy Storage: Progress Report for the Period October 1978-March 1979, Argonne National Laboratory Report ANL-79-39, p. 71 (May 1979).

14. P. A. Nelson et al., Development of Lithium/Metal Sulfide Batteries at Argonne National Laboratory: Summary Report for 1975, Argonne National Laboratory Report ANL-76-45, p. 4 (March 1976).

15. P. A. Nelson et al., Development of Lithium/Metal Sulfide Batteries at Argonne National Laboratory: Summary Report for 1974, Argonne National Laboratory Report ANL-75-20, p. 8 (March 1975).

16. F. J. Martino, T. D. Kaun, H. Shimotake, and E. C. Gay, "Advances in the Development of Lithium-Aluminum/Metal Sulfide Cells for Electric-Vehicle Battery," Proc. 13th IECEC, p. 709 (1978).

17. H. Shimotake, in High-Performance Batteries for Stationary Energy Storage and Electric-Vehicle Propulsion: for Period January-March 1978, Argonne National Laboratory Report ANL-78-45, p. 35 (July 1978).

18. V. Kolba et al., in High-Performance Batteries for Electric-Vehicle Propulsion and Stationary Energy Storage: Progress Report October 1978-March 1979, Argonne National Laboratory Report ANL-79-39, p. 42 (May 1979).

19. P. A. Nelson et al., High-Performance Batteries for Electric-Vehicle Propulsion and Stationary Energy Storage: Progress Report October 1977-September 1978, Argonne National Laboratory Report ANL-78-94, p. 42 (November 1978).

20. E. C. Gay, in High-Performance Batteries for Electric Vehicle Propulsion and Stationary Energy Storage; Progress Report for the Period October 1978-September 1979, Argonne National Laboratory Report ANL-79-94, p. 98 (March 1980)

21. D. L. Barney et al., Lithium/Iron Sulfide Batteries for Electric-Vehicle Propulsion and Other Applications, Progress Report October 1980-September 1981, Argonne National Laboratory Report ANL-81-65, p. 62 (February 1982).

22. A. A. Chilenskas et al., Status of the Li-Al/FeS Battery Manufacturing Technology: Final Report November 1963, An Evaluation for the U.S. Army, Belvoir R&D Center, Argonne National Laboratory Report ANL-84-23 (August 1984).

23. G. Barlow, "The Development of a High Performance Lithium-Alloy/Metal Sulfide Cell for Electric Vehicle Propulsion," this proceedings.

24. A. A. Chilenskas, "Design and Test of Lithium-Alloy/Iron Monosulfide Batteries," this proceedings.

25. E. C. Gay et al., Li-Alloy/FeS Cell Design and Analysis Report, Argonne National Laboratory Report ANL-84-93 (July 1985).

26. J. L. Settle and K. M. Myles, The Lithium-Aluminum Phase Diagram, Argonne National Laboratory Report ANL-76-8, p. 42 (April 1976).

27. C. J. Wen, W. Weppner, R. A. Boukamp, and R. A. Huggins, J. Electrochem. Soc. 126, 2258 (1979).

28. J. E. Battles, F. C. Mrazek, and N. C. Otto, Post-Test Examinations of Li-Al/FeS_x Secondary Cells, Argonne National Laboratory Report ANL-80-130 (December 1980).

29. L. Redey, D. R. Vissers, J. Newman, and S. Higuchi, in Proc. Symp. Porous Electrodes: Theory and Practice, H. C. Maru and T. Katan, Eds., Electrochem. Soc. Proc. Vol. 84-8, p. 322 (1983).

30. H. G. V. Schnering, R. Nesper, K. F. Tebbe, and J. Curda, Z. Met. 71, 357 (1980).

31. C. J. Wen and R. A. Huggins, J. Solid State Chem. 37, 271 (1981).

32. D. R. Vissers, Z. Tomczuk, L. Redey, and J. E. Battles, "High Temperature Lithium-Alloy/Iron Sulfide Batteries," in Lithium: Current Applications in Science, Medicine and Technology, R. O. Bach, Ed., John Wiley and Sons, Inc., New York (1985).

33. A. K. Fischer and D. R. Vissers, "Microscopy of Electrodes Operating in Molten Salts," in Proceedings of the Symposium on Transport Processes in Electrochemical Systems, R. S. Yeo, T. Katan, and D. Chin, Eds., Proceedings Vol. 82-10, The Electrochemical Society, p. 141 (1982).

34. A. E. Martin, R. K. Steunenberg, and Z. Tomczuk, "Changes in the Composition of FeS_2 Electrodes of Li/LiCl-KCl/FeS_2 Cells During Cycling," Extended Abstracts of the Electrochem. Soc. Meeting, Vol. 74-2, p. 132 (1974).

35. R. Sharma, J. Electrochem. Soc. **123**, 448 (1976).

36. K. Abe and T. Chiku, J. Electrochem. Soc. **122**, 1322 (1975).

37. R. Brec and A. Dugast, Mater. Res. Bull. **15**, 619 (1980).

38. A. E. Martin and Z. Tomczuk, in High-Performance Batteries for Electric-Vehicle Propulsion and Stationary Energy Storage, Argonne National Laboratory Report ANL-79-39, p. 71 (1979).

39. Z. Tomczuk, B. Tani, N. C. Otto, M. F. Roche, and D. R. Vissers, J. Electrochem. Soc. **129**, 925 (1982).

40. A. E. Martin, in High-Performance Batteries for Electric-Vehicle Propulsion and Stationary Energy Storage, Argonne National Laboratory Report ANL-78-84, p. 167 (1980).

41. R. Pollard and J. Newman, J. Electrochem. Soc. **126**, 1713 (1979).

42. Z. Tomczuk, M. F. Roche, and D. R. Vissers, J. Electrochem. Soc. **128**, 2255 (1981).

43. S. K. Preto, Z. Tomczuk, S. von Winbush, and M. F. Roche, J. Electrochem. Soc. **130**, 264 (1983).

44. J. A. Schmidt and W. Weppner, "Kinetics of Compositional Variations in the Ternary System Li-Fe-S," Extended Abstracts of the Electrochem. Soc. Meeting, Vol. 82-1, p. 562 (1982).

45. Z. Tomczuk and D. R. Vissers, J. Electrochem. Soc. (in press).

46. L. Redey, in Lithium/Iron Sulfide Batteries for Electric Vehicle Applications: Progress Report for October 1981-September 1982, Argonne National Laboratory Report ANL-83-62, p. 17 (September 1983).

47. Z. Tomczuk, A. E. Martin, and R. K. Steunenberg, "Chemistry of the FeS Electrode of Li/FeS Cells," Extended Abstracts of the Electrochem. Soc. Meeting, Vol. 76-2, p. 131 (1976).

48. B. Tani, Am. Mineral. **62**, 819 (1977).

49. C. Melendres and B. Tani, J. Phys. Chem. **82**, 2850 (1978).

50. Z. Tomczuk, S. K. Preto, and M. F. Roche, J. Electrochem. Soc. **128**, 760 (1981).

51. R. Pollard and J. Newman, J. Electrochem. Soc. **128**, 491 (1981).

52. R. Pollard and J. Newman, J. Electrochem. Soc. **128**, 503 (1981).

53. M. L. Saboungi, J. J. Marr, and M. Blander, J. Electrochem. Soc. **125**, 1567 (1978).

54. M. L. Saboungi and A. E. Martin, "Electrochemical and Metallographic Investigations of the Stability of the J ($LiK_6Fe_{24}S_{26}Cl$) Phase in Several Molten Salt Mixtures," Extended Abstracts of the Electrochem. Soc. Meeting, Vol. 78-2, p. 919 (1978).

55. C. E. Vallet and J. Braunstein, J. Electrochem. Soc. **125**, 1193 (1978).

56. R. Sharma, J. Electrochem. Soc. **123**, 448 (1976).

57. H. F. Gibbard, J. Electrochem. Soc. **125**, 353 (1978).

58. D. M. Chen and H. F. Gibbard, J. Electrochem. Soc. **130**, 1975 (1983).

59. F. C. Mrazek and J. E. Battles, J. Electrochem. Soc. **124**, 1556 (1977).

60. N. C. Otto and J. E. Battles, in High-Performance Batteries for Electric-Vehicle Propulsion and Stationary Energy Storage, Argonne National Laboratory Report ANL-79-39, p. 49 (May 1979).

61. D. R. Vissers, K. E. Anderson, C. K. Ho, and H. Shimotake, Proc. of the Symp. on Battery Design and Optimization, S. Gross, Ed., Electrochem. Soc. Proc. Vol. 79-1, 416 (1979).

ELECTROCHEMICAL METHODS IN THE ANALYSIS OF HIGH-TEMPERATURE BATTERY PROCESSES

J.Robert Selman
Department of Chemical Engineering
I.I.T.
Chicago, IL 60616

The charge and discharge processes taking place in high-temperature batteries such as the lithium-alloy/metal sulfide and sodium/sulfur batteries are characterized by the coexistence of solid and liquid phases, which may transform into each other via very complex reactions. Whereas the electrode-kinetic and mass transfer rates are usually rapid in molten salts, the phase transformation kinetics are often slow. These conditions require modification of the traditional techniques for studying electrode processes. In addition, the help of mathematical modeling is required if one wants to interpret the results of basic techniques such as potential step and potential sweep, or chronopotentiometry, quantitatively.

INTRODUCTION

This contribution consists of two parts. First, a cursory overview is presented of basic electrochemical techniques. Most of these have been developed for the study of electrode processes in solution at ambient temperature. It is shown by several examples that they can also be applied to high-temperature processes, if the processes are relatively simple.

Typical high-temperature battery processes are complex and have multi-step, multi-phase, mechanisms which are often only partially understood. In the second part of this review this is illustrated by examples taken from the FeS electrode of the LiAl/FeS battery and from the polysulfide electrode of the Na/S battery. In both cases cyclic voltammetry has been employed to gain deeper insight in the reaction mechanism and the rate processes involved. The obstacles which prevent a simple quantitative interpretation of the results, by applying classical CV solutions, are discussed. Mathematical modeling can be helpful in such a situation if sufficient and accurate input information is available, and if the objectives are clearly defined.

ELECTROCHEMICAL TECHNIQUES

During the last three decades there has been a remarkable growth in the number and sophistication of techniques for the study of electrochemical processes. Here we are only surveying briefly a few of those techniques that are experimentally rather simple; a more extensive discussion is given in standard works.[1]

The oldest electrochemical techniques are electroanalytical techniques. Their practical objective is to determine reactant concentration from the limiting current density. The limiting current is defined as the maximum current due to a specific reactant. It is identified experimentally by a plateau or inflection of the current in the current-overpotential plot. (Fig. 1a) When the limiting current condition is reached, the reactant concentration has become very small (Fig. 1b); further increase of the current is only possible when the electrode potential becomes so negative (if it concerns a cathode) that another electrode reaction can take place.

At the limiting current, the current density is simply related to the bulk reactant concentration by the expression

$$i_{lim} = Dc_b nF/\delta_N \qquad (1)$$

Here δ_N stands for the Nernst diffusion layer thickness, which is an effective quantity and somewhat smaller than the real extent of the diffusion layer, δ (Fig. 1b). The essential condition for meaningful measurements is the reproducibility of the diffusion situation, or equivalently of δ_N. This implies either diffusion under stagnant conditions or a well-defined type of convection.

In polarography a dropping mercury electrode (DME, Fig. 2a) is used to generate essentially stagnant diffusion at an expanding drop. The limiting or diffusion current satisfies in first approximation the equation

$$I = 3.57c_b nF(D^{1/2}m^{2/3}\tau^{1/6}) \qquad (2)$$

where m is the mercury flow rate in cm^3/sec, and I is the current in A.

When the electrolyte is flowing or the electrode is moving in a reproducible well-defined manner, the limiting current is determined by well-defined convective diffusion. This technique is sometimes termed hydrodynamic voltammetry. The limiting current may be formally expressed in terms of a mass-transfer coefficient, k, as follows:

$$i_{lim} = kc_b nF \qquad (3)$$

The mass transfer coefficient is correlated with convection characteristics and with transport parameters of the electrolyte. For the well-known case of a rotating disk (RDE, Fig. 2b) in laminar flow the correlation is:

$$i_{lim} = 0.621c_b nF\,{}^{1/2}D^{2/3}\nu^{-1/6} \qquad (4)$$

ELECTRODE-KINETIC TECHNIQUES

Electroanalytical techniques usually involve the recording of a current-potential (voltammetric) curve. Such curves in principle contain information about the electrode kinetics of the reaction in question, However, techniques which are aimed at elucidation of the electrode kinetics must allow a clear separation of the kinetic contribution to the polarization (surface or activation overpotential) from the mass transfer contribution (concentration or diffusion overpotential). Following Newman[2] these quantities are designated by η_s and η_c, respectively:

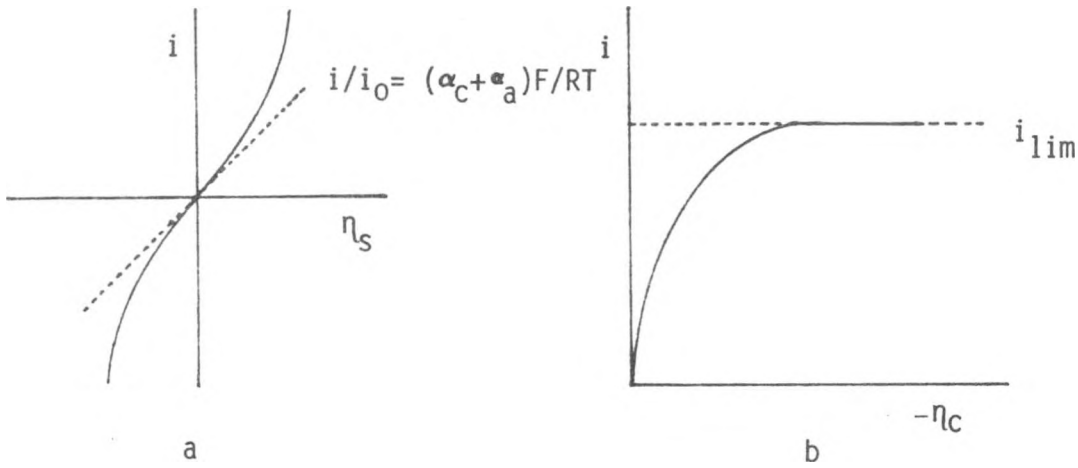

Figure 3. Surface polarization curve (a) and the concentration polarization curve (b).

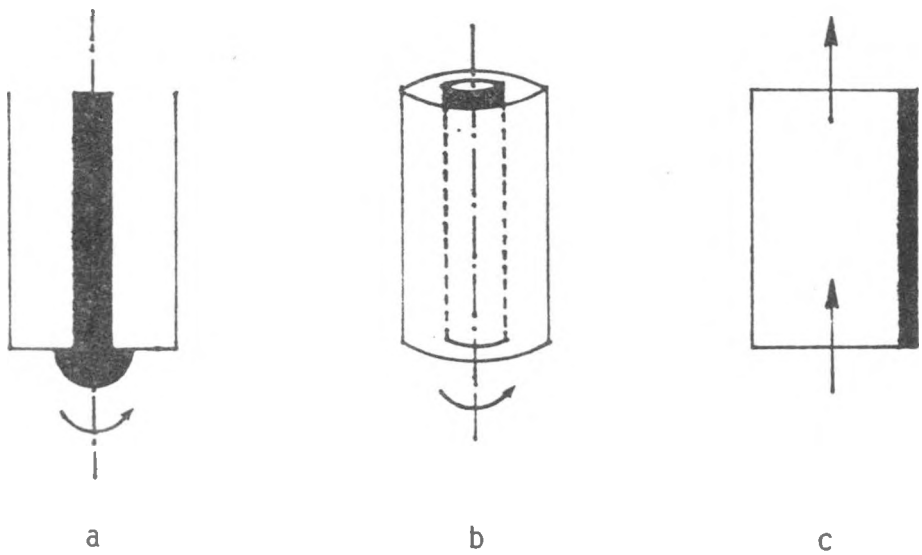

Figure 4. Rotating hemispherical electrode - RHE (a), the rotating concentric cylinder electrode - RCCE (b) and the parallel plate flow channel electrode (c).

techniques, e.g., double-pulse methods and other programmed perturbations, are often more powerful for relatively simple mechanisms; in particular, when it comes to determining the rate constants of very fast reactions, such programming may be necessary. However, when the reaction mechanism is complex (multi-step and multi-phase) and the results must be interpreted by numerical simulation, simple boundary conditions have a definite advantage.[4]

If one deals with a molten-salt high-temperature system, transient techniques as a group also have an advantage over hydrodynamic methods from an experimental viewpoint. It is usually very difficult to construct, for example, a rotating disk or channel flow electrode of sufficient dimensional stability in such a very corrosive environment. A transient technique applied at a simple sheathed-wire electrode is then attractive.

Potential Step Technique

In this method, originated by Gerischer and Vielstich, one applies a potential step to the electrode (Fig. 5a) and analyzes the current response. In the absence of double-layer charging the ideal response is schematically as shown in Fig. 5b. For a simple (one-step redox) reaction:

$$Ox + ne^- \longrightarrow Red \qquad (10)$$

the current response near zero decays proportionally with the square root of time:

$$i = i_{kin}[1 - 2Q(t/\pi)^{1/2}] \qquad (11)$$

The slope contains information about the forward and backward reaction rate constants, k_f and k_b, as well as the diffusion coefficients of reactant and product. In the case of a small potential step, and again assuming a one-step redox reaction:

$$Q = k_f/D_{Ox}^{1/2} + k_b/D_{Red}^{1/2} \qquad (12)$$

The extrapolation of the response with $t^{1/2}$, back to time zero, yields the kinetic current corresponding to the applied overpotential. (Fig. 5c) The kinetic currents thus obtained may be correlated with the overpotentials according to the Butler-Volmer equation, to extract the kinetic parameters. The upper limit of the rate constant which can accurately be determined according to this simple procedure is approximatively k = 0.2 cm/s.

Fig. 6 shows an example of potential-step response for an apparently simple high-temperature electrode process: the cathodic reduction of oxygen at a smooth (nonporous) gold electrode submerged in molten carbonate, at 650°C.[5] Only the response over the time period 0.3 - 0.8 ms is used for the extrapolation[6]. The remainder of the curve contains mainly information about the mass-transfer processes taking place near the electrode.

Fig. 7 illustrates the correlation of the kinetic currents by means of a so-called Allen-Hickling plot, i.e., a special version of the Butler-Volmer equation in which the sum of the cathodic and anodic transfer coefficients is assigned an a priori value (in this case, 2). This plot, combined with others for different gas compositions, indicates that the standard exchange-current density for oxygen reduction is 26.3 mA/cm^2, or the standard rate constant 0.25 cm/s.[5]

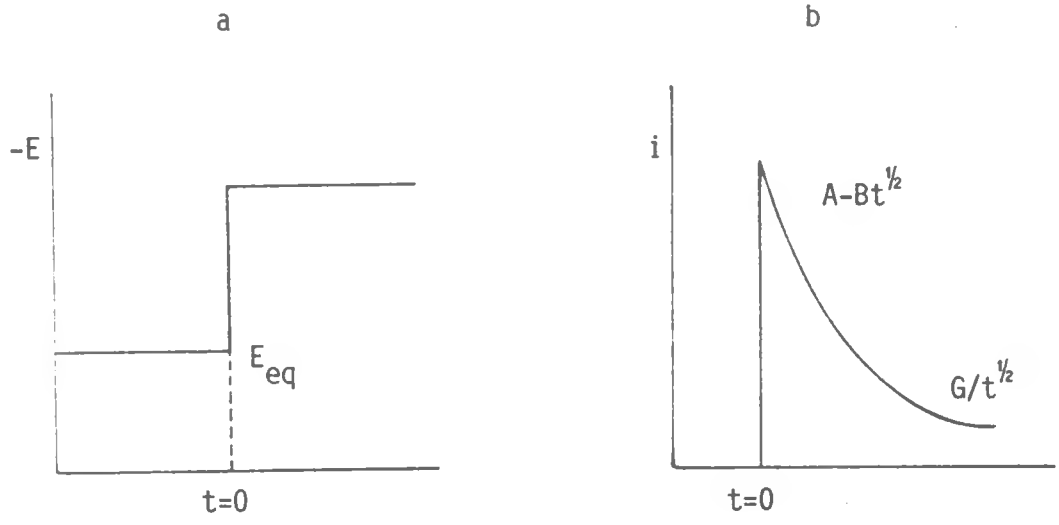

Figure 5. Potential step signal (a) and the current response (b).

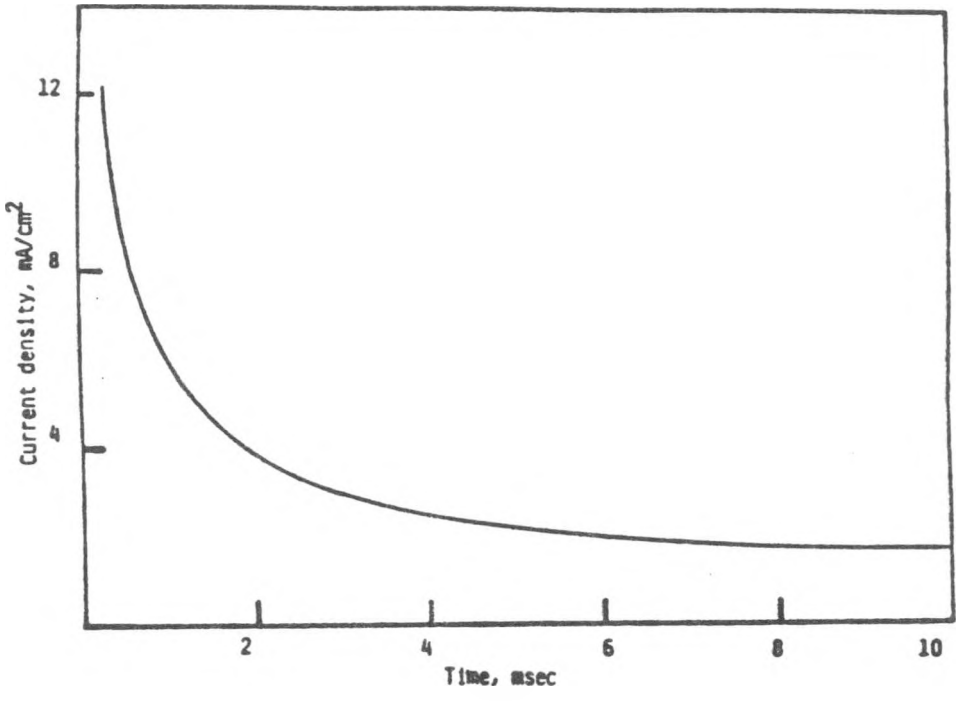

Figure 6. Current response following a potential step of -100 mV at the oxygen electrode in molten carbonate at 650°C. (Ref. 5)

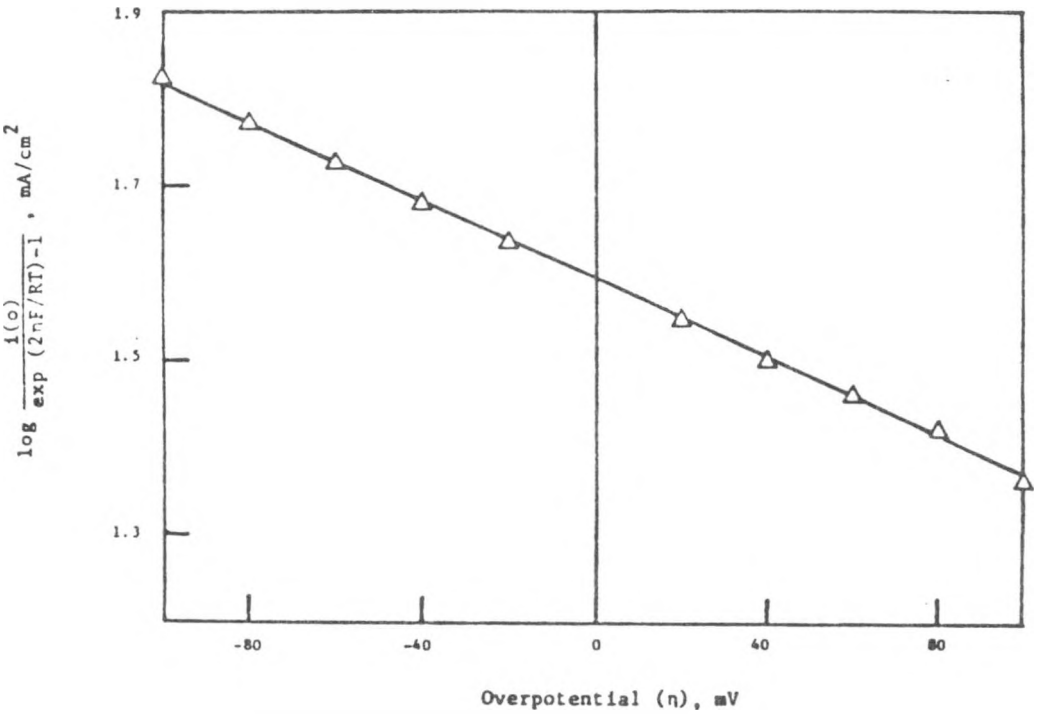

Figure 7. Allen-Hickling plot for oxygen reduction as in Figure 6.

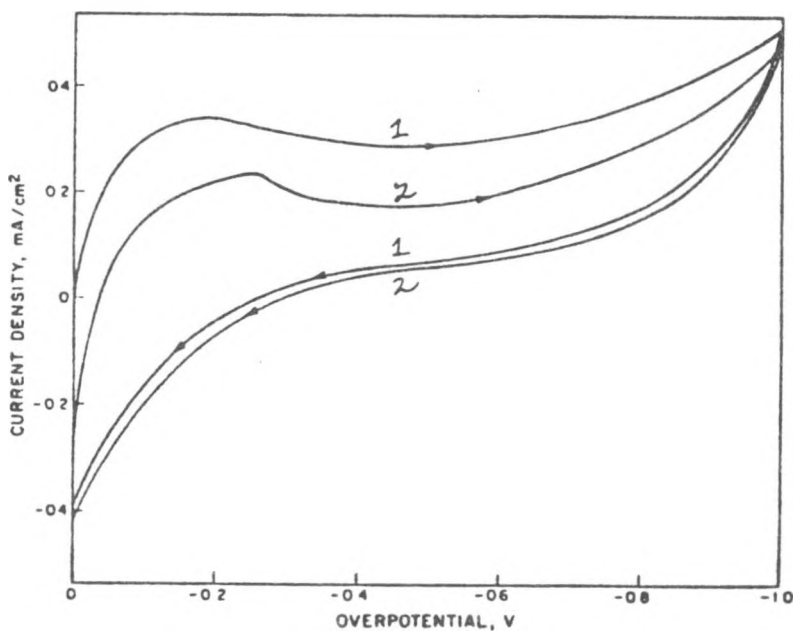

Figure 8. Linear sweep voltammograms (cycle 1 and 2) for oxygen reduction as in Figure 6.

However, when a different technique is used to determine the kinetic parameters of oxygen reduction, e.g., linear scan voltammetry (to be discussed below), the resulting values of i_o turn out to be almost two orders of magnitude smaller then the value quoted above.[5,7]. The reason for this anomaly appears to be the complex reaction mechanism. In pure lithium carbonate the reaction mechanism is probably:

$$0.5\ O_2 + CO_3^{2-} \longrightarrow O_2^{2-} + CO_2 \qquad (13)$$

$$O_2 + 2e^- \longrightarrow 2O^{2-} \qquad (14)$$

$$2[\ O^{2-} + CO_2 \longrightarrow CO_3^{2-}\ ] \qquad (15)$$

Here the last reaction, the chemical recombination of oxide ions with dissolved CO_2 to form carbonate ions, is apparently slow, for reasons that are at present not completely understood. This may be inferred from the strong hysteresis of the first cathodic sweeps of a linear sweep voltammogram (Fig. 8): the oxygen/oxide equilibrium potential is negatively displaced as a result of oxide accumulation near the electrode.[8] Under these conditions the "normal" interpretation of the linear potential sweep response, assuming first-order kinetics for the rate determining electrochemical step, is not valid; this explains the implausibly small values for the kinetic rate constant.

Current Step Method and Chronopotentiometry

In this method the potential response to a current step (Fig. 9a) is analyzed. In the short term the potential response is as shown in Fig. 9b and, for a simple redox reaction, satifies the Sand-Karaoglanoff equation. Assuming linear kinetics, this is

$$\eta = (RT/nF)i[2N(t/\pi)^{1/2} + 1/i_o] \qquad (16)$$

where the slope of the E-vs-square-root-of-t line is given by

$$N = (1/nF)[1/C_{o,Ox}(D_{Ox})^{1/2} + 1/C_{o,Red}(D_{Red})^{1/2}] \qquad (17)$$

while the intercept yields the value of i_o.

In reality the short-time response of the potential is complicated by the presence of the electric double layer, of capacity C_d. Berzins and Delahay have derived a more complete expression, again for a simple redox reaction, as follows:

$$\eta = (RT/nF)i[2N(t/\pi)^{1/2} - RTN^2C_d/nF + 1/i_o] \qquad (18)$$

Therefore, if C_d is known with some accuracy from other measurements, i_o can still be determined from the intercept. The upper limit on the value of the standard rate constant by this method is approximativelly 1 cm/s . However, it is clear that the charging current limits the application of the method in many important cases, e.g., when the reactant is very dilute, or when porous electrodes are used.

The long time response of the potential to a current step contains mainly mass-transfer information. An inflection in the potential-vs-time curve (Fig.10b) marks the time at which a limiting current condition is reached with

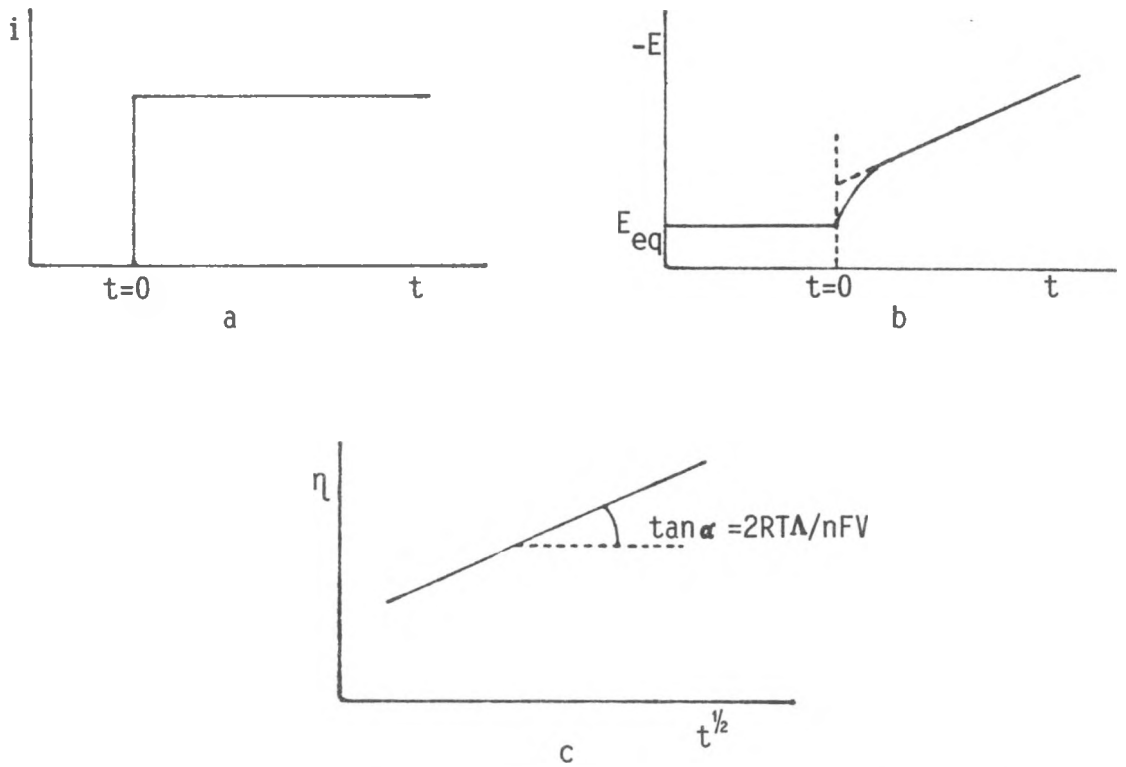

Figure 9. Current step signal - short time (a),potential response (b) and the characteristic slope (c).

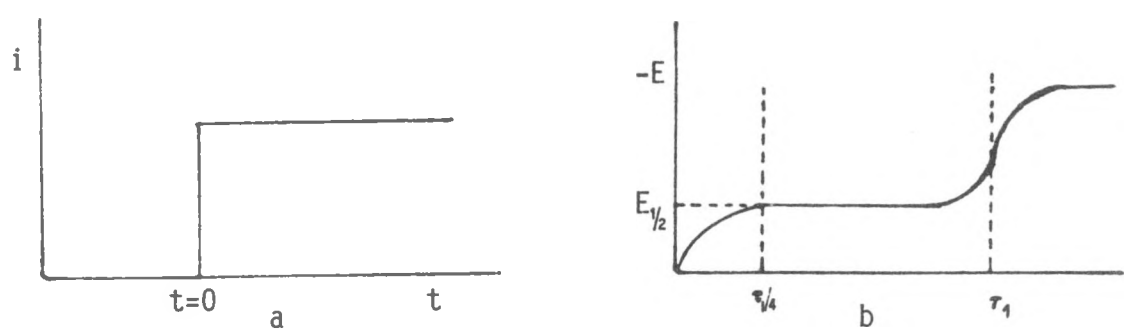

Figure 10. Current step signal - long time (a) and the potential response (b).

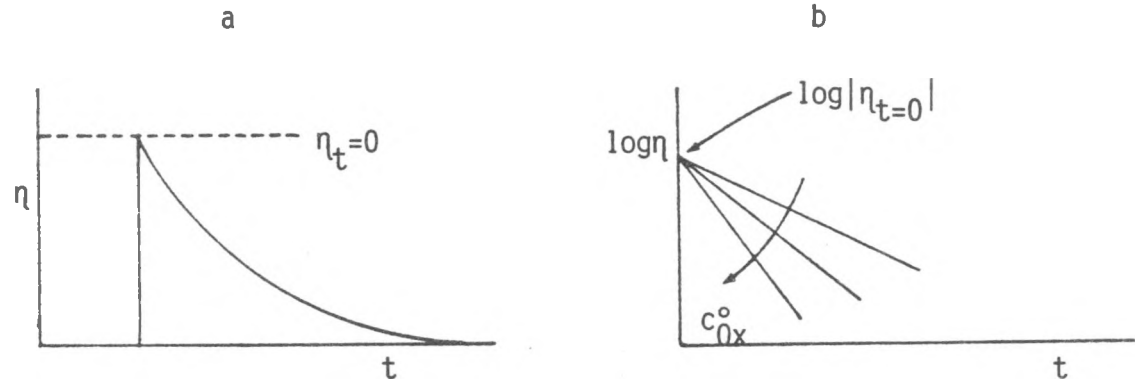

Figure 12. Coulostatic potential response (a) and the characteristic slope (b).

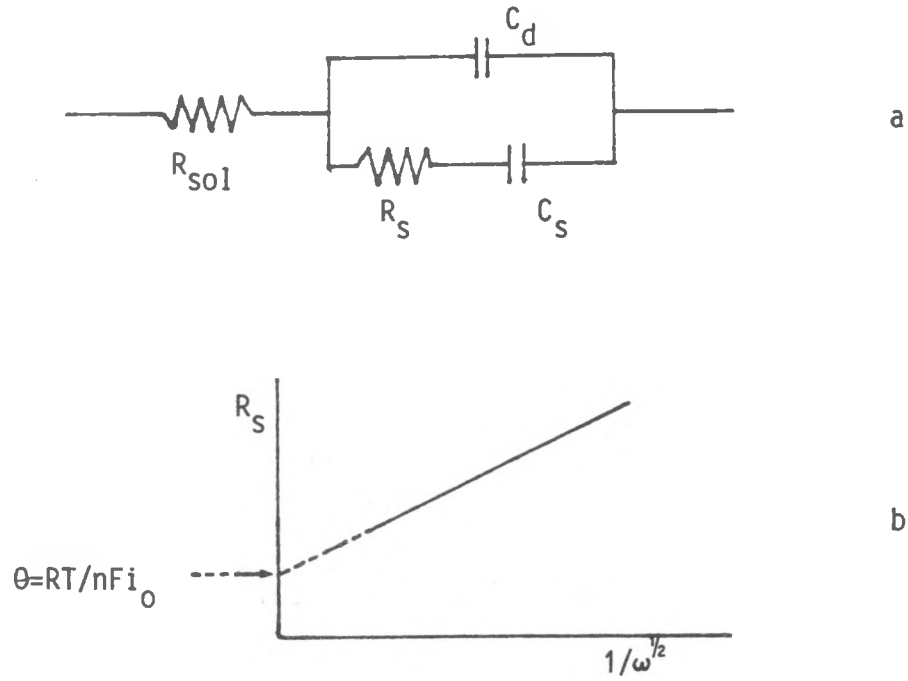

Figure 13. Series RC circuit for AC impedance (a) and the evaluation of AC impedance results (b).

$$C_s = (\sigma\omega^{1/2})^{-1} \quad (25)$$

$$\sigma = (2^{1/2}nF)^{-1}[\beta_{Ox}/(D_{Ox})^{1/2} - \beta_{Red}/(D_{Red})^{1/2}] \quad (26)$$

$$\beta = dE/dc_i \quad (27)$$

Figure 13b shows the theoretical dependence of R_s on the inverse square root of frequency (Randles plot). Extrapolation to very high frequency allows to extract i_o; however, it is clear that the value of C_d must be known with considerable accuracy.

An alternative way to present the results is in the form of a real-vs-imaginary-component plot of the impedance in parallel with C_d (Cole-Cole plot). For a one-step redox reaction this plot reflects quite clearly the relative importance of electrode kinetic limitations vs mass-transfer limitations (Fig. 14a vs Fig. 14b). The frequency appears as a continuous parameter on these plots.

The interpretation of AC impedance plots becomes quite difficult when complex reaction mechanisms are involved, or when the electrodes are porous. In such cases AC impedance plots may be of greater value as qualitative tools than as quantitative approach to electrode kinetics. Nevertheless, mathematical modeling in conjunction with empirical osbervations may be helpful. When porous electrodes operate under mixed kinetic-mass transfer control, their imaginary-vs-real-resistance plots are overall similar to those for simpler systems and their dependence on reactant and product concentration can give valuable insight.

This is illustrated in Figs. 16 and 17 for the oxygen reduction reaction in a porous molten carbonate fuel cell electrode.[10]. The kinetic half-circles, similar to those in Fig. 13a, can be used to infer that the reaction order of oxygen is 0.85 but that of CO_2 -0.45 under the working conditions of such electrodes.

Linear Sweep and Cyclic Voltammetry

These techniques are by far the most popular methods of exploring the characteristics of an electrode process qualitatively and making inferences about the reaction mechanism. However, linear sweep voltammetry (Fig. 15a.) is also suitable for quantitative determination of the electrode-kinetic parameters.

From the viewpoint of analysis, it is a "simple" technique, similar to potential step, since it involves only a single parameter (sweep rate). The current response (Fig. 15b) shows a peak which is essentially due to mass-transfer limitations but whose locus may be affected by kinetics. The analysis for a reversible reaction (fast kinetics) indicates that the peak current is proportional with the square root of the sweep rate, but that the peak potential is independent of the sweep rate.

If the electrode reaction is a single-step redox reaction, the peak current is given by:

$$i_p = 0.446c_{b,Ox}(D_{Ox}a)^{1/2}nF \quad (28)$$

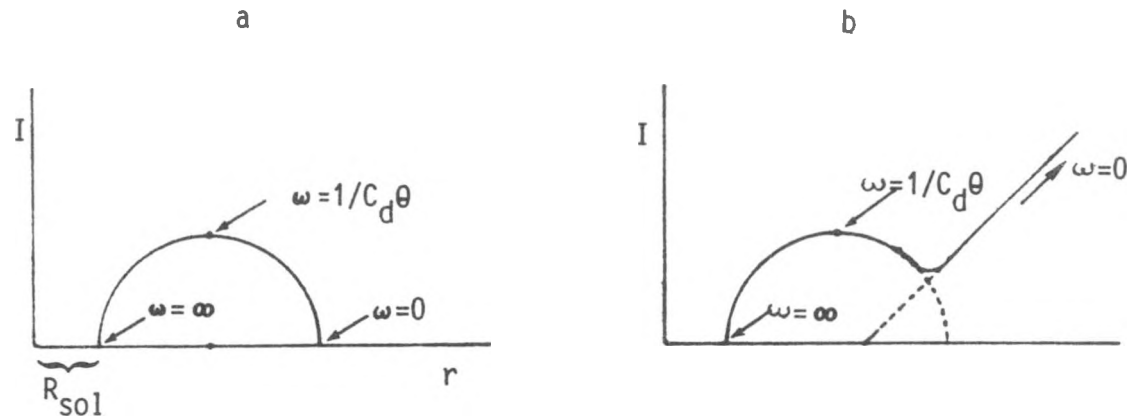

Figure 14. Real-vs-imaginary resistance plots for schematic of Fig. 12: (a) very slow reaction; (b) fast reaction with mass transfer resistance.

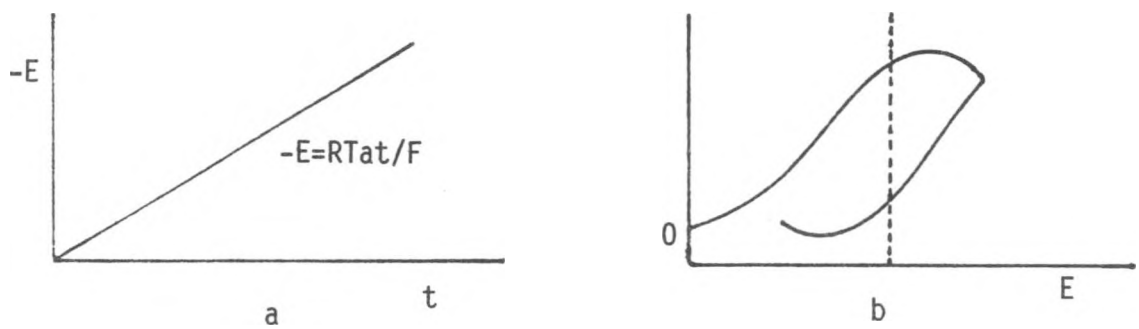

Figure 15. Linear sweep voltammtery signal (a) and the current response for signal and reversal (b).

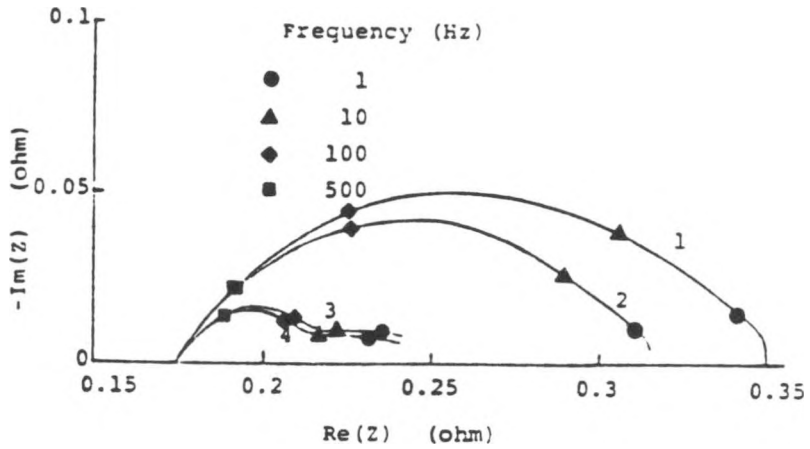

Figure 16. Effect of p_{O_2} on the impedance of a porous cathode in molten carbonate. (Ref. 9)

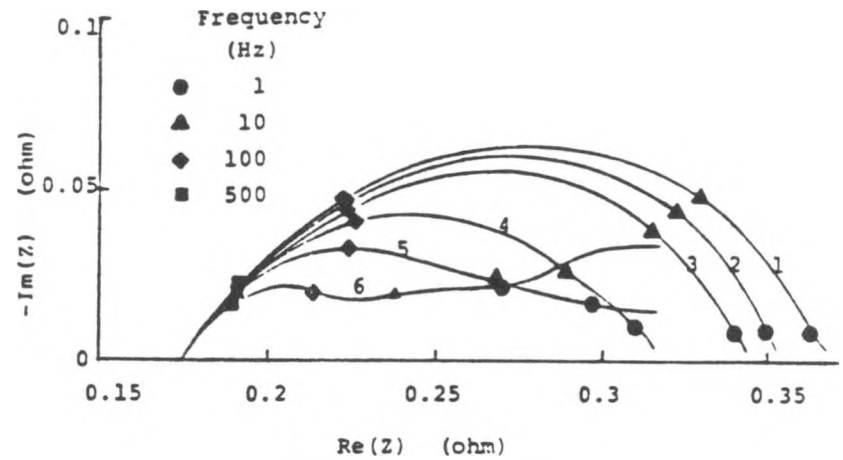

Figure 17. Effect of p_{CO_2} on the impedance of a porous cathode in molten carbonate. (Ref. 9)

and the peak potential by:

$$E_p = E^\circ - (RT/nF)[\ln(D_{Ox}/D_{Red})^{1/2} - 1.109] \qquad (29)$$

Similar simple theoretical relationships may be derived for the case of a reversible deposition reaction.

For single-step redox reactions the "peak separation" upon reversal of the sweep, i.e., the potential difference between, for example, the cathodic and anodic (reverse) peak, is independent of sweep rate and the reversal potential:

$$\Delta E_p = 2.218(RT/nF) \qquad (30)$$

The peak potential and the peak separation therefore give information about the number of electrons involved in the reaction. However, this is only strictly true for fast ("reversible") reactions.

Irreversible reactions, i.e.,

$$Ox + ne^- \xrightarrow{k_f} Red \qquad (31)$$

in which kinetic resistance is appreciable, also show a dependence of peak current on the square root of the sweep rate but the proportionality constant will involve kinetic characteristics as well as diffusivities. Usually the peak potential and the peak separation upon current reversal are a more convenient indicator of the extent of "irreversibility". If the reaction is "totally irreversible", no anodic wave will arise upon current reversal.

When the reaction mechanism is more complicated, the LSV response is still often informative, and much theoretical work has been done to catalogue the response characteristics systematically. Three "diagnostics" can be used to characterize the LSV response: the peak current dependence on sweep rate, the peak separation dependence on sweep rate, and the variation of the ratio of anodic to cathodic peak currents with sweep rate.[11]

Cyclic voltammetry is an extension of the LSV-with-sweep-reversal concept to continuous back-and-forth (triangular) sweeping over a specified "potential window". Cyclic voltammograms are often recorded after a cyclic steady state is established with respect to the diffusion of reactants and products toward and from the electrode. The analysis of such a voltammogram in exact quantitative terms is very difficult when the reaction involves more than a single step, and especially if diffusing intermediates occur. As illustrated above, even for the comparatively simple single-LSV the available analysis according to linear kinetics leads to incorrect conclusions, when applied to a two-step electron tranfer followed by chemical reaction when diffusing intermediates occur.

The difficulties inherent in the interpretation of cyclic voltammograms are further illustrated with results for the FeS electrode in LiCl-KCl and the sulfur/polysulfide electrode in NaS_x.

THE FeS ELECTRODE OF THE LiAl/FeS CELL

This electrode, in a LiCl-KCl melt at temperatures between 425 and 475°C, has been studied intensively by various electrochemical techniques, but especially by cyclic voltammetry. This work is closely identified with the work of a number of Argonne National Laboratory researchers, a.o., Martin, Steunenberg, Tomczuk, Vissers, Preto and Roche. It has been reviewed a.o. by Vissers et al.[11] and by Selman and Sabougi[12].

The factors which complicate the interpretation of cyclic voltammograms in this system are:

* the occurence of multiple reaction paths;
* the occurence of two sulfide phases in all reaction paths;
* the coexistence of two and often three phases during an actual cell discharge;
* the accumulation of K^+ and Li^+ ions at the electrode due to migrational separation.

The multiple reaction paths are illustrated in Fig. 18, which show also the intermediate phases that can occur during the overall reaction:

$$FeS + 2Li^+ \longrightarrow Li_2S + Fe \qquad (32)$$

These intermediate phases are the X-phase, of composition $Li_2S.FeS$, and the J-phase, of composition $LiK_6Fe_{24}S_{26}Cl$.

The normal mechanism of discharge, at 450°C, is by the sequence

$$(a) \quad FeS \longrightarrow J \qquad (33)$$
$$(c) \quad J \longrightarrow Li_2S, Fe; \qquad (34)$$

that of charge is different:

$$(f) \quad Li_2S, Fe \longrightarrow X^* \qquad (35)$$
$$(b) \quad X^*, Fe \longrightarrow J, Fe \qquad (36)$$
$$(c) \quad J, Fe \longrightarrow FeS \qquad (37)$$

Here X* is a nonequilibrium X-phase.

These "normal" sequences, combined with detailed thermodynamic information obtained independently, suffice to explain the quasi-equilibrium discharge and charge curves for very low current density (Fig. 19). However, at higher discharge and charge rates various transport resistances will start complicating the picture. Thus, the discharge of an electrode containing large FeS particles will take place by parallel paths:

$$FeS \text{ (surface)} \longrightarrow J, Fe \qquad (38)$$
$$FeS \text{ (core)} \longrightarrow H, Fe \qquad (39)$$

$$X \text{ (core)} \longrightarrow Li_2S, Fe \qquad (40)$$
$$J \text{ (surface)} \longrightarrow Li_2S, Fe \qquad (41)$$

Reactions (39) and (40) are completed rapidly, before (41), since the latter needs Li^+ ions which have to diffuse through the J-phase. Thus, three phases are commonly coexisting and the corresponding phase transformation is slow. It should also be noted that reaction (38) requires K^+ ions; consequently,

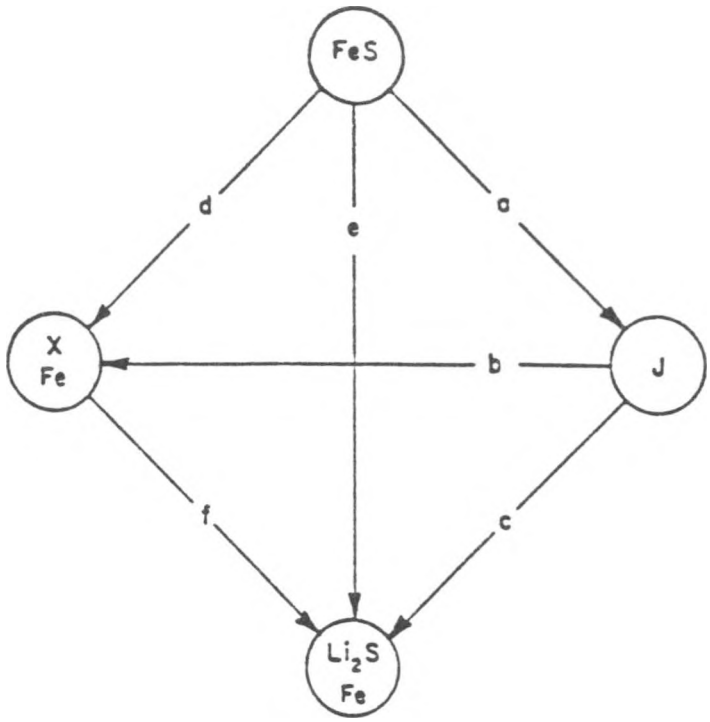

Figure 18. Electrochemical reactions of the FeS electrode. (Ref. 12)

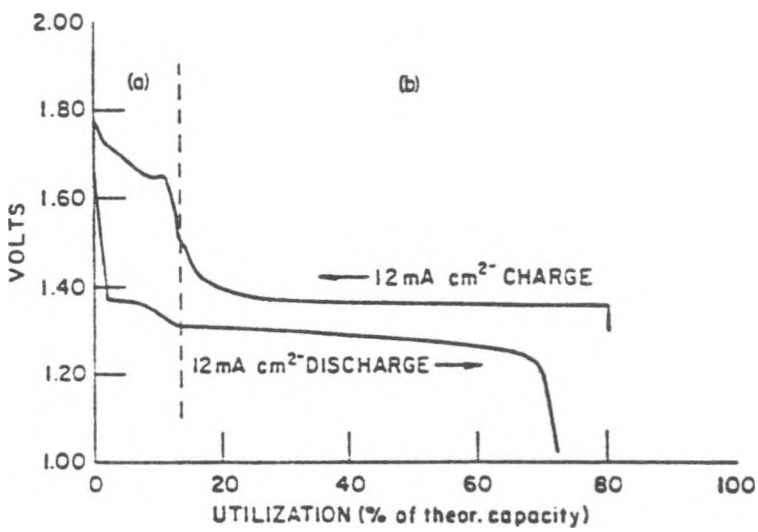

Figure 19. Voltage curves for LiAl/FeS cell at 716 K and low c.d.(0.45 A.hr capacity). (Ref. 12)

this reaction may become diffusion-limited, especially if Li^+ is enriched and K^+ depleted atthe electrode by the overall ion movements due to concentration gradients and the electric field (migrational separation).

When these "normal" discharge and charge sequences are compared with the evidence from cyclic voltammograms, it is found that the discharge path is more complicated than thermodynamics suggest, but that the charge path is simpler. This is illustrated in Fig. 20. The peaks identified by number are associated with reactions as followed:

Discharge:

I_D FeS $\rightarrow$ J

II_D FeS $\rightarrow$ X and X $\rightarrow$ J

III_D J $\rightarrow$ X

IV_D X $\rightarrow$ Li_2S

V_D J $\rightarrow$ Li_2S

Note: At higher temperature or higher Li-concentration (bottom CV) mergers occur

Charge:

I_C $Li_2S \rightarrow$ X

II_C X $\rightarrow$ FeS

and also:

X $\rightarrow$ J + Li_2S

X + FeS $\rightarrow$ J

III_C J $\rightarrow$ FeS

Note: The first two peaks correspond to reactions (35) and (36), the third one to (37).

These detailed assignments could be made only after extensive exploration of the CV characteristics and comparison of peak potentials with thermodynamic data obtained independently. The determination of kinetic characteristics of individual steps is obviously out of the question; however, modeling of the cyclic voltammetric response of a system of reactions resembling those of the FeS electrode might give further insight in the relative slowness of some steps compared to others.

THE Na-POLYSULFIDE ELECTRODE OF THE Na/S CELL

The electrochemistry of this electrode has been investigated extensively by researchers from Ford Motor Co., Rensselaer Polytechnic Institute, Southampton University, and Lawrence Berkeley Laboratory. (Ludwig, Tischer, Aikens, Cleaver, Dobson, McLarnon and Cairns). Most of this work has been thoroughly reviewed by Tischer and Ludwig[13] and by Aikens[14].

Cyclic voltammetry again made a major contribution to unraveling the complications of the electrode process and understanding the reaction mechanism, although some aspects remain poorly understood. The complicating factors here are the following:

* the absence of a supporting electrolyte, leading to significant migration fluxes (due to the electric field) in addition to

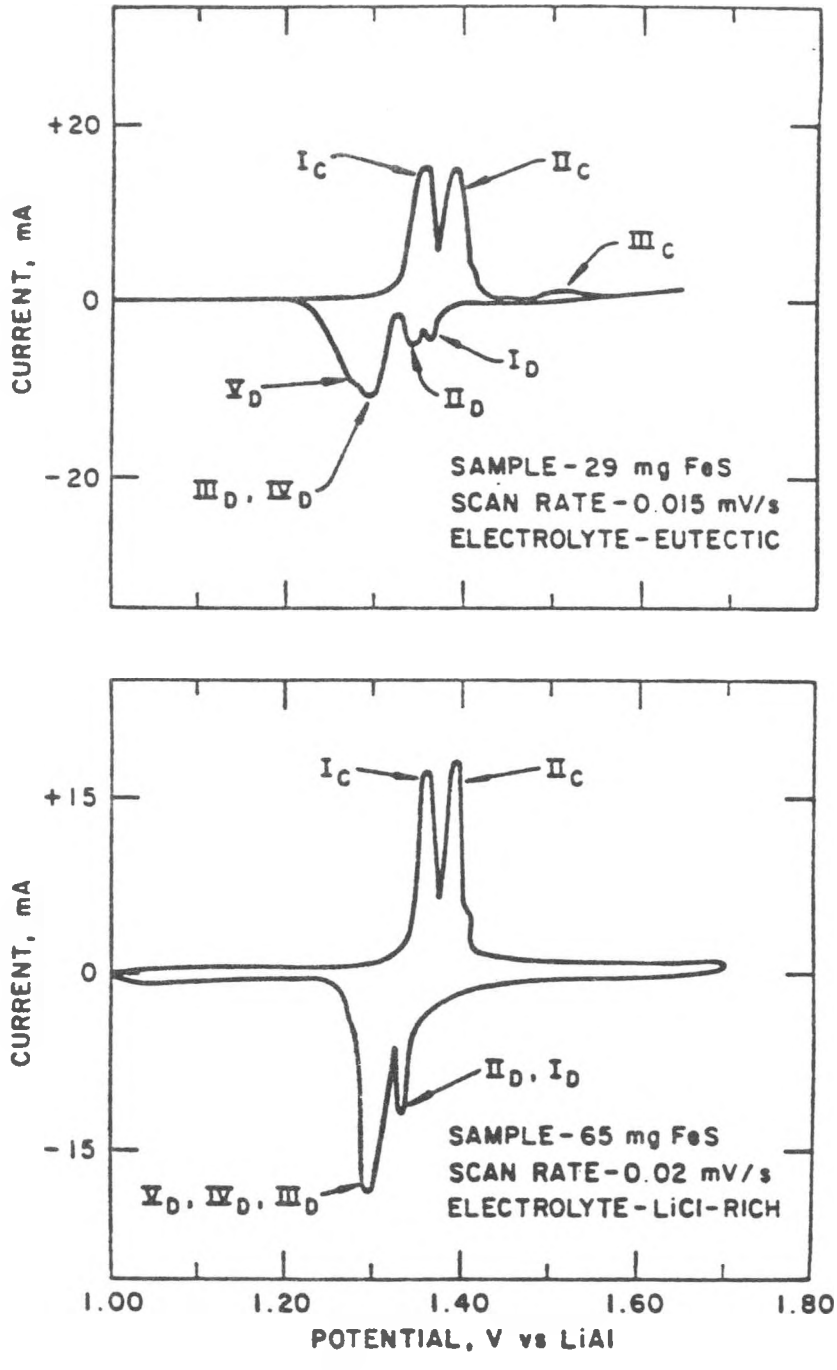

Figure 20. Cyclic voltammograms for FeS electrode in eutectic and LiCl-rich electrolyte at 445°C. (Ref. 12)

diffusion;
* lack of clear insight in the local composition of the melt near the electrode, in part due to the complicated transport picture;
* film formation occuring at the electrode, either due to elemental sulfur (anodic) or Na_2S_2 (cathodic).

The sodium-polysulfide electrode is, like the FeS electrode, also complicated by the coexistence of phases, although the situation here is much simpler. The phase diagram, as potential vs. composition at 300°C, is shown in Fig. 21. A single liquid phase exists only between the compositions Na_2S_5 and Na_2S_3. Upon further charging two liquid phases form, of which one is practically pure sulfur, the other Na_2S_5. Further discharge leads to the formation of solid Na_2S_2 coexisting with liquid Na_2S_5.

The LSV shows a characteristic cathodic peak whose magnitude depends on the melt stoichiometry at the start (Fig. 22). The peak would appear to be due to the reaction:

$$S_4^{2-} + 2e^- \longrightarrow 2S_2^{2-} \qquad (42)$$

and it shows catalytic characteristics due to the rapid equilibrium reaction, e.g., with S_5^{2-} :

$$2S_5^{2-} + S_2^{2-} \longrightarrow 3S_4^{2-} \qquad (43)$$

Recent work has shown that the peak is actually not one peak but two, corresponding to two closely spaced electron-transfer reactions. The peak is eventually followed by a "pasive" region due to coverage by a layer of Na_2S_2.

Upon anodic sweep the cyclic voltammogram (Fig. 23) shows clearly a perturbation at the point where the passivating layer has completely disappeared (D in Fig. 22). This is followed by a step anodic rise. The slope of this rise, and the maximum reached, depend on the sulfur content of the bulk melt.(Fig. 24) Here also a catalytic reaction mechanism is a work. The initial electrode reaction is discharge of S^{2-}, which would passivate the electrode; however, a rapid equilibrium reaction with, e.g., Na_2S_4 leads to back formation of Na_2S_5. Once the melt has become of that composition, the anodic rise is very modest and a type of passivation sets in, as illustrated in Fig. 24 for $Na_2S_{5.2}$.

It would be worthwhile to model the behavior of an electrode under the conditions discussed above, to simulate the CV response. This would yield greater insight in "passivation" phenomena and the local composition of the melt near the electrode; it could give guidance in the design of the positive electrode compartment of a Na/S cell.

CONCLUSION

The presence of multiple liquid phases and solid phases, often as a film on the current collector, complicates the interpretation of classical electrode-kinetic responses in high-temperature molten-salt systems. For reasons of experimental convenience, transient methods are often used. The simplest transient methods, e.g., potential or current step, LSV and AC impedance, are often attractive because they require minimal instrumental effort. They also allow interpretation by mathematical modeling more easily than

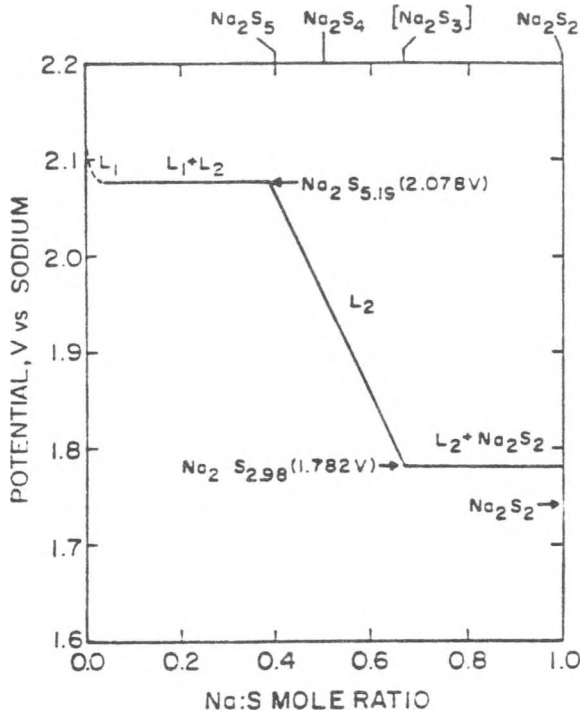

Figure 21. Potential-vs-composition diagram for Na-S at 300°C.

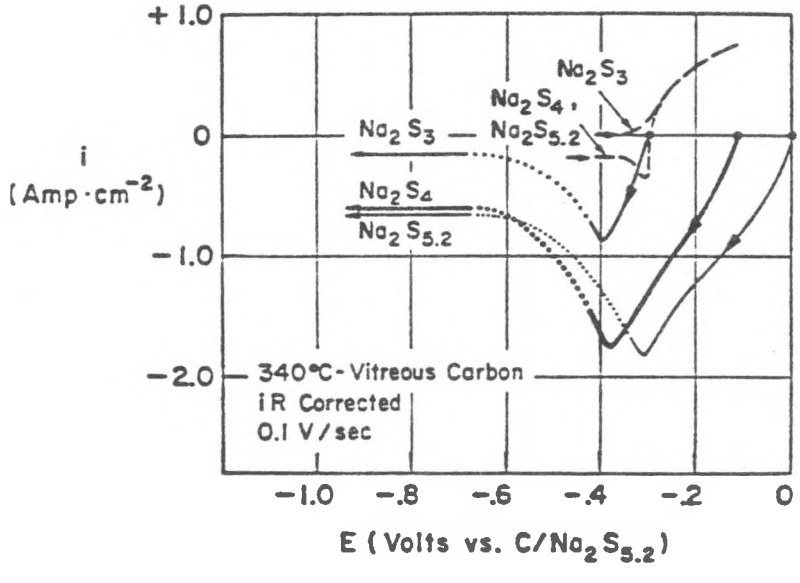

Figure 22. LSV response of sulfur electrode in various polysulfide melts. (Ref. 13)

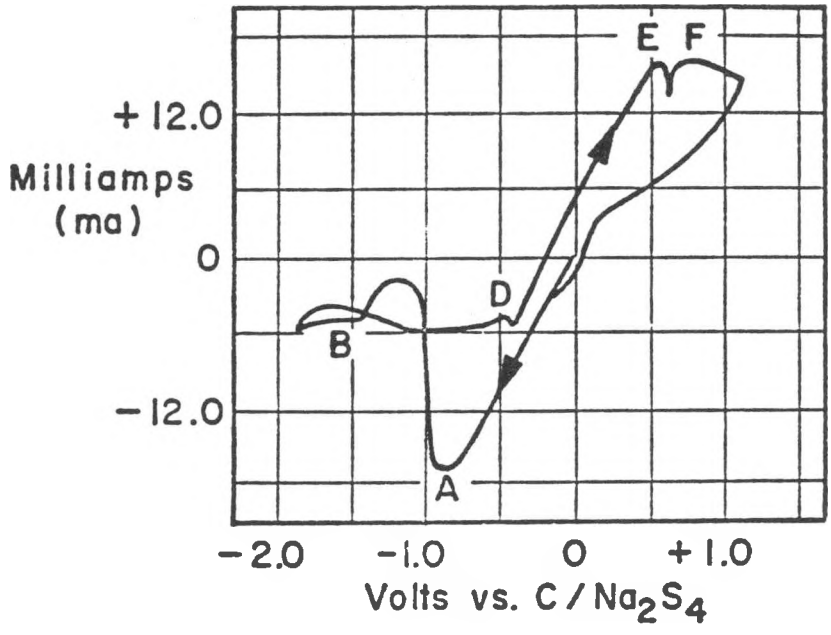

Figure 23. Cyclic voltammogram for sulfur electrode in Na_2S_4. (Ref. 13)

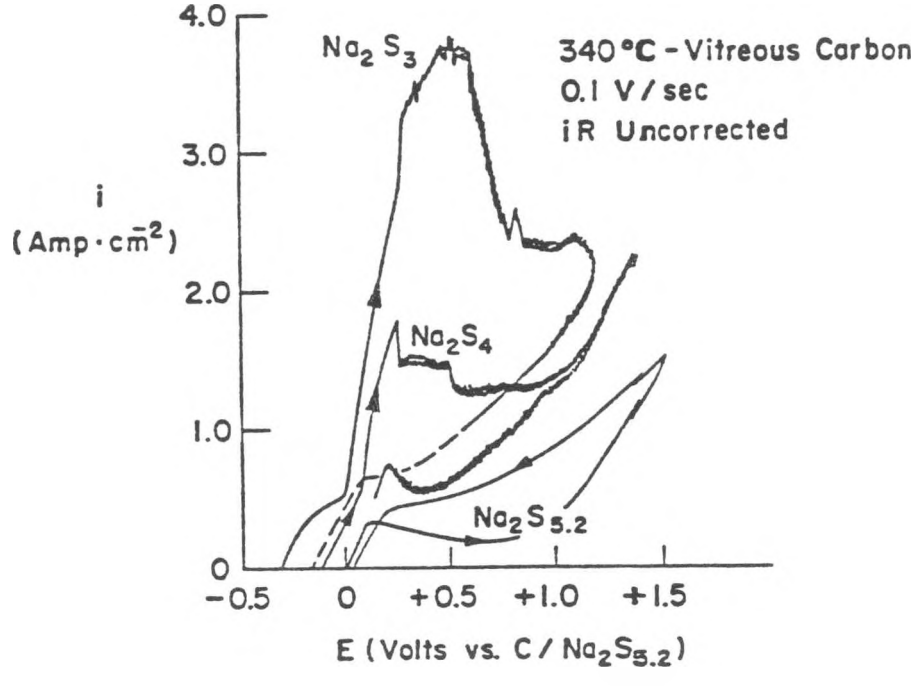

Figure 24. Anodic current rise in various polysulfide melts. (Ref. 13)

techniques with special current or potential programs. Nevertheless, in practically important systems such as the FeS electrode of the LiAl/FeS battery and the Na-polysulfide electrode of the Na/S battery, much analysis by modeling still remains to be done; this would be especially fruitful if focused on the simulation of responses to simple electrode-kinetic techniques.

Acknowledgment

This work was supported by the U.S. Department of Energy, through the Berkeley Electrochemical Research Center (Project #4529210).

REFERENCES

1. A.J. Bard and L.R. Faulkner, "Electrochemical Methods", Wiley, N.Y.,(1980)
2. J. Newman, "Electrochemical Systems", Prentice Hall (1973)
3. J.R. Selman and C.W. Tobias, Adv.Chem.Eng. 10(1978)211
4. Z. Nagy, Electrochimica Acta, 25(1980)575
5. S.H. Lu, "Electrode Kinetics of Fuel Oxidation and Oxygen Reduction in Molten Carbonate", Ph.D. Thesis, I.I.T., Chicago, IL (1985)
6. S.H. Lu and J.R. Selman, J.Electrochem.Soc.,131(1984)2827
7. A.J. Appleby and S.B. Nicholson, J.Electroanal.Chem.,112(1980)71
8. W.Weppner, R.A. Huggins, J.C. Wen and B.A. Baukamp,J.Electrochem.Soc., 126(1979)2258
9. C.Y. Yuh, "Potential Relaxation and AC Impedance of Porous Electrodes", Ph.D. Thesis, I.I.T., Chicago, IL (1985)
10. D.D. McDonald, "Transient Techniques in Electrochemistry", Plenum (1977)
11. D.R. Vissers, Z. Tomczuk, L. Redey and J. Battles, "High-Tempearture Lithium-Alloy/Iron Sulfide Batteries", in "Lithium: Current Applications in Science, Medecine and Technology" (R.O. Bach, Ed.), Wiley (1985)
12 J.R. Selman and M.L. Saboungi, "Electrochemistry of Sulfur in Halide Melts", in: "The Sulfur Electrode: Fused Salts and Solid Electrolytes" (R.P. Tishcer, Ed.), Ac. Press (1983)
13 R.P. Tischer and F.A. Ludwig, in: "Advances in Electrochemistry and Electrochemical Engineering" (H. Gerischer and C.W. Tobias, Eds.) Vol. 10, Wiley (1977)
14 D.A. Aikens, in: "The Sulfur Electrode: Fused Salts and Solid Electrolytes" (R.P. Tischer Ed.) Ac. Press (1983), Chap.4.

MODELING OF POROUS ELECTRODES IN MOLTEN-SALT SYSTEMS

John Newman

Materials and Molecular Research Division,
Lawrence Berkeley Laboratory, and
Department of Chemical Engineering,
University of California, Berkeley

Abstract

Porous electrodes are used for many batteries because they permit the reactants to be close to the site of the electrochemical reaction. The basis for a nonuniform reaction distribution in such electrodes is reviewed, and some results are discussed for lithium alloy, iron sulfide cells. Discrepancies between model and experimental results can be attributed to poor approximations to the effective conductivity of packed-bed electrodes and to inadequate treatment of the precipitation of KCl.

Here we want to go over, by way of background, some of the fundamentals of porous-electrode theory and expected behavior. This will be further illustrated by the modeling of molten-salt cells, including some problems and possibilities for improvement.

Figure 1 illustrates the concept of a porous electrode, in which reactants are embedded in an electronically conducting matrix which is permeated by an electrolyte. In this example, current enters the electrode through an electronic current from the left into the matrix. Somewhere within the volume of the porous electode, an electrochemical reaction occurs, and the current emerges at the right as ionic current within the electrolyte. An obvious advantage of porous electrodes is the high interfacial area, which can minimize the surface overpotential associated with the electrochemical reaction. A second major advantage for battery applications is the possibility to store reactants close to the reaction site. These can include insoluble reactants, such as iron sulfide, soluble reactants, such as sulfuric acid in a lead-acid cell, or gaseous reactants, such as in fuel cells. Porous electrodes find uses in primary and secondary batteries, flow redox energy storage systems, and in flow-through electordes for metal ion removal by plating or ion adsorption.

The modeling of porous electrodes involves establishing a number of unknowns which one needs to determine and a set of governing equations. In this application, these equations are likely to include transport processes, such as Ohm's law in the matrix and the description of migration, diffusion, and convection in the solution, material balances on liquid and solid phases, and reaction kinetics for electrochemical reactions. The distributed resistor network in figure 2 illustrates why the reaction is nonuniform and distributed throughout the volume of the porous electrode. The circle at the left can represent the current collector, and the upper resistor series the electronically conducting matrix. The circle at the right can represent the

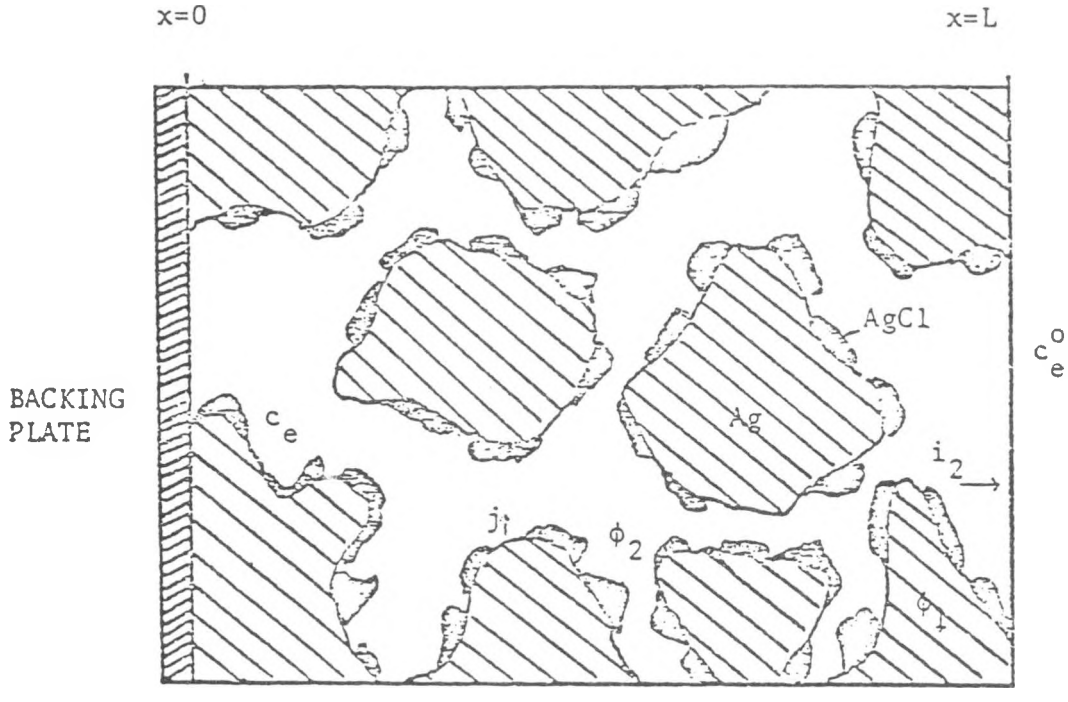

Figure 1. Schematic of a porous electrode, showing solution and matrix phases and a solid reactant. The current collector is at the left, and the separator and counterelectrode are at the right.

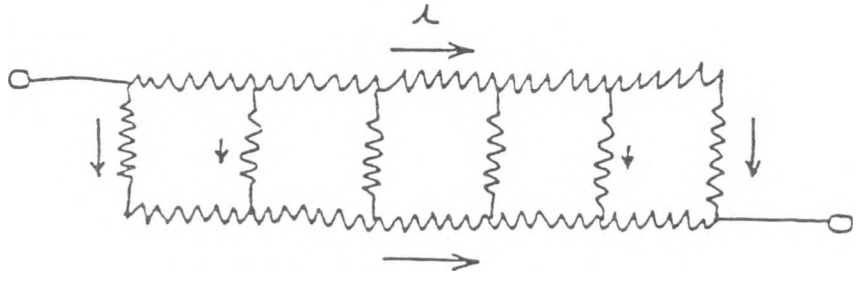

Figure 2. Resistor network illustrating the mechanism of the distribution of current in a porous electrode.

separator, and the lower resistor series the ionically conducting pore solution. The vertical resistors represent the electrochemical reaction whereby charge is transferred from the matrix to the solution. Charge flowing from left to right must react within the network, and it will try to distribute itself between the matrix and the solution (that is, between the upper and the lower resistor series) in inverse relation to their resistivities. Thus, the reaction has a tendency to occur near the left or the right and to be relatively absent within the middle of the electrode. If the resistance of the electrochemical reaction is high, the distribution will tend to be uniform. A low resistivity for the matrix phase tends to shift the reaction towards the right, towards the separator.

Figure 3 shows the cell sandwich which represents a molten-salt cell designed to form part of a high-power battery. The current that we had been following in the single-electrode system now continues through the separator and into the positive electrode where a cathodic reaction results in the current flow now being in the electonically conducting matrix and thence to the positive current collector. Electrode reactions are indicated for a negative made of LiAl and for one of the reactions of an iron sulfide positive. At the temperatures of molten salts, the electrode kinetics tend to be relatively fast. As an alternative to the reaction of FeS to Li_2FeS_2 (also called "*X*" phase), the reaction can go through a complex compound called "*J*" phase (which is $LiK_6Fe_{24}S_{26}Cl$) according to the following scheme:

$$26\ FeS + Li^+ + Cl^- + 6\ K^+ + 6\ e^- \rightarrow LiK_6Fe_{24}S_{26}Cl + 2\ Fe$$

followed by the reaction of *J* phase to other compounds, such as

$$J + 25\ Li^+ + 20\ e^- \rightarrow 13\ Li_2FeS_2 + 11\ Fe + 6\ K^+ + Cl^-.$$

Figure 4 shows concentration profiles for a LiAl/FeS cell discharging through the Li_2FeS_2 ("*X*" phase) mechanism. At short times, the concentration profiles reflect the stoichiometry of the electrode reactions. In the negative, Li^+ ions are injected into the electrolyte, thus raising the mole fraction of LiCl, while in the positive, Li^+ ions are extracted from the melt, thus lowering the mole fraction of LiCl. The figure shows that the reactions occur relatively close to the separator, since the locations of injection and extraction occur close to the separator, and one can see the regions moving into the depth of the electrodes as time progresses. The negative electrode is opening up as the reaction occurs, and the concentration profiles are not very sharp there, while in the positive electrode, the porosity is small after the first reaction, and the progress of the reaction front through the electrode is clearly visible. The reaction front is also less distinct in the negative electrode because this is an alloy electrode, and changes in the composition of the LiAl alloy result in concentration overpotentials which tend to spread out the reaction region over the depth of the electrode. After 2.5 hours, a second reaction front is visible in the positive, before the first reaction front has reached the back of the electrode. The second reaction (of Li_2FeS_2 to Fe and Li_2S) also produces an even smaller porosity, and concentration gradients become even more pronounced in the positive. This eventually leads to precipitation of KCl in the positive, and in the model this causes the cell potential to drop drastically if the precipitate blocks the pore cross-section.

Figure 5 shows contrasting concentration profiles predicted for the reaction through the *J* phase. Here the mole fraction rises in the positive as well as the negative in the early stages of discharge because K^+ ions are extracted in greater numbers than Li^+ ions. However, the following reaction in the positive brings the mole fraction down again, and more drastically than in the *X* phase mechanism, because no Li^+ ions were transferred during the early stages of the discharge.

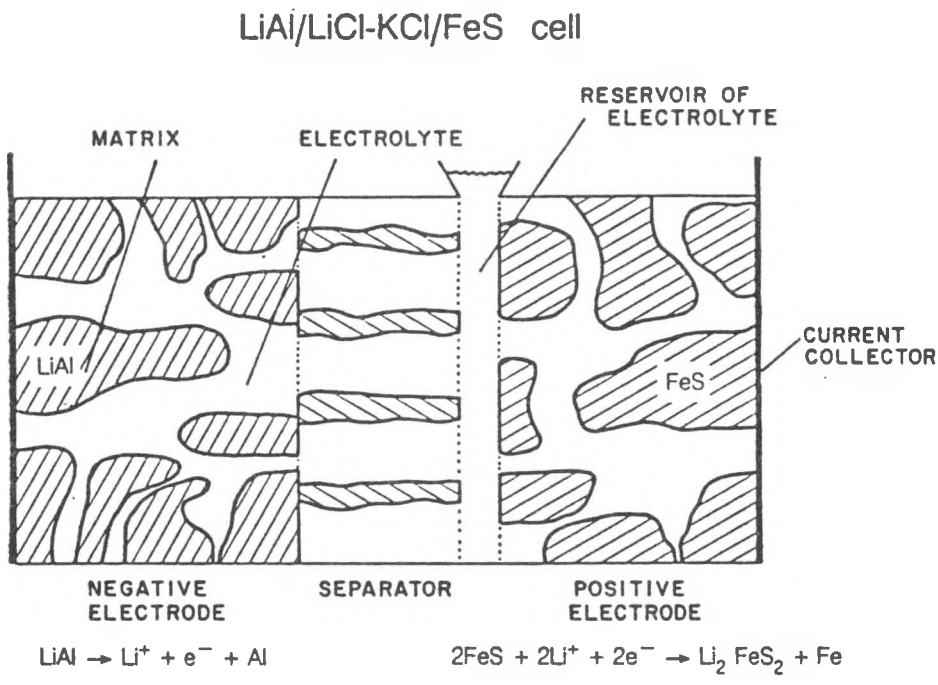

Figure 3. Schematic diagram of the LiAl/FeS cell.

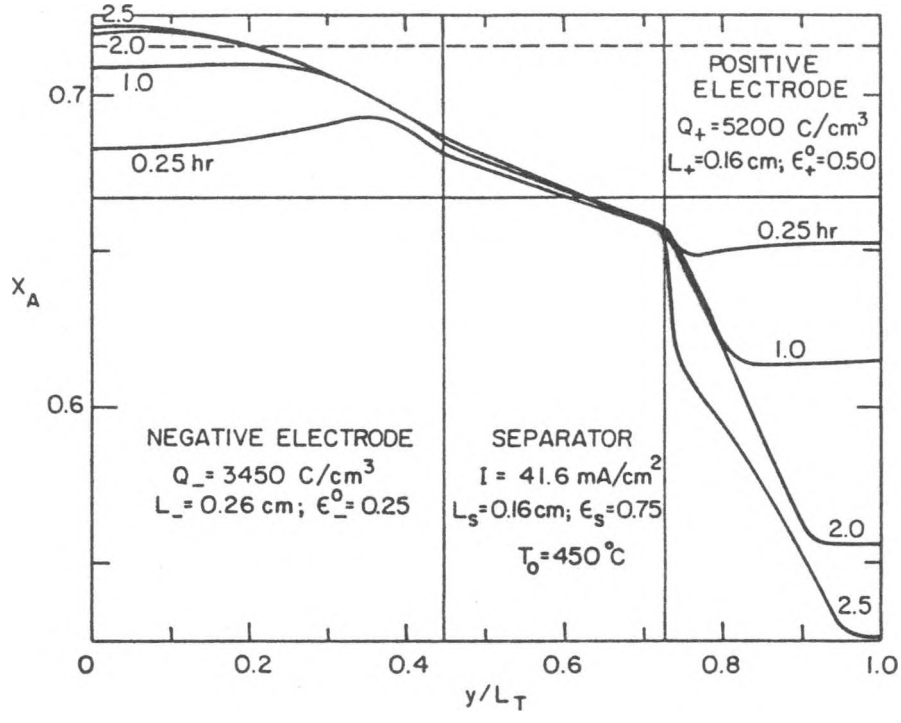

Figure 4. Position dependence of mole fraction of LiCl at different discharge times. Dashed line represents saturation limit for LiCl at 450°C.

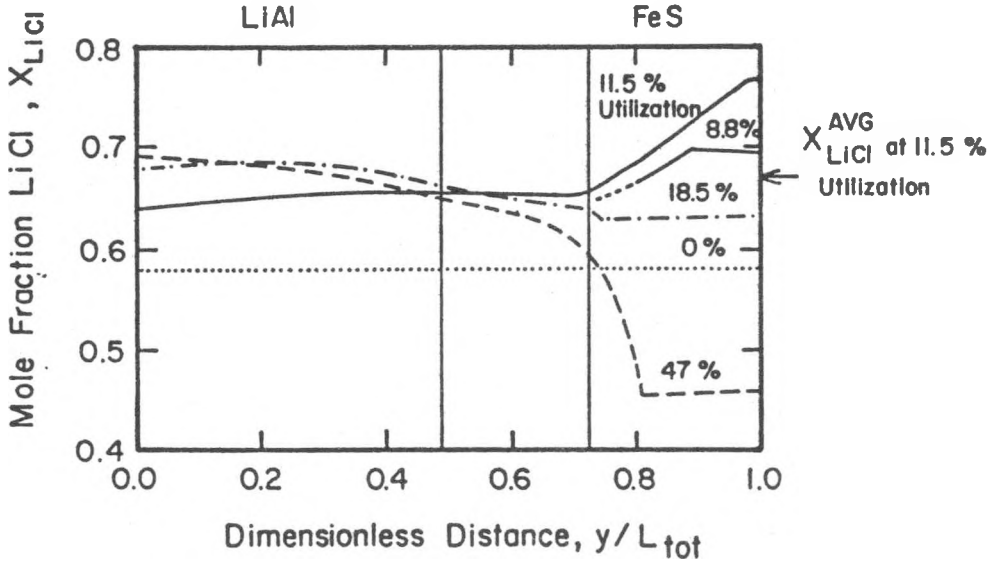

Figure 5. Position dependence of the mole fraction of LiCl at different states of discharge for the *J*-phase mechanism.

Figure 6 shows predicted discharge curves (for the X-phase mechanism) contrasted with experimental cell-potential data. The model results follow the experimental results reasonably well in the latter part of the discharge if precipitation of KCl is precluded in the model. The curves labeled A and B indicate the early termination of the discharge if precipitation is allowed to occur.

Figure 7 shows predicted and experimental results for the discharge of a $LiAl/FeS_2$ cell. The top curve (with several line segments) corresponds to a reversible discharge and is based on thermodynamic cell potentials. The model calculations lie slightly below the reversible curve, and the experimental results lie below that. All three curves reflect the reaction sequence believed to apply to the FeS_2 electrode. In the early stages of discharge, the model results do not show as much polarization as the experimental curve, indicating that resistances within the electrodes are not properly accounted for. Also, the model results show an end of discharge, due to precipitation, much earlier than the experimental curve. This illustrates the two major discrepancies between the model and the experiment: there is too little voltage loss and too much precipitation.

Figure 8 shows volume fractions of various phases at a point in the discharge of the FeS electrode by means of the X-phase mechanism. Here both reaction fronts can be seen; the front for the first reaction is at about 0.077 cm, and that for the second reaction is at about 0.01 cm. The initial porosity is about 0.5, and this is reduced to about 0.29 after the first reaction and to about 0.06 after the second reaction. However, at the reaction front for the first reaction, the porosity drops sharply to a small value over a very small distance. This is due to the calculated precipitation of KCl in the positive electrode, and this causes the discharge potential to drop considerably, eventually leading to the prediction of the end of discharge.

There are several things that one can try in order to improve the agreement with experiment and to enhance our understanding of the discharge process in these systems:

1. Improve the representation of the conductivity of composite solids, such as form the positive electrode of these cells.

2. Try to account for the swelling of the positive electrode on discharge.

3. Investigate whether convection could produce better mixing and thus delay precipitation of KCl.

Figure 9 shows the observed swelling of the positive electrode during cycling, as a percent above its constructed thickness. At the right one sees that the electrode is expanded beyond the fabrication thickness even at full charge. This is taken into account in the model because the thicknesses of the electrodes and the separator are chosen to represent the values after the cell has gone through several "break-in" cycles. The positive electrode expands during discharge, exerting pressure on the separator and thence on the negative, so that the negative and the separator decrease in thickness during discharge. This behavior will tend to discourage precipitation of KCl in the positive.

In order to get an idea of the magnitude of this effect, we have run the FeS model with several, constant values of the positive-electrode porosity and have recorded the predicted utilization of the electrode, before precipitation terminates the discharge. We have translated these different initial porosites into amounts of electrode expansion and represented the results in figure 10. These results are for the J-phase mechanism. One can infer the additional capacity that might be predicted with expansion amounts corresponding to the end of discharge (where the precipitation problem is most acute) and to the middle of discharge.

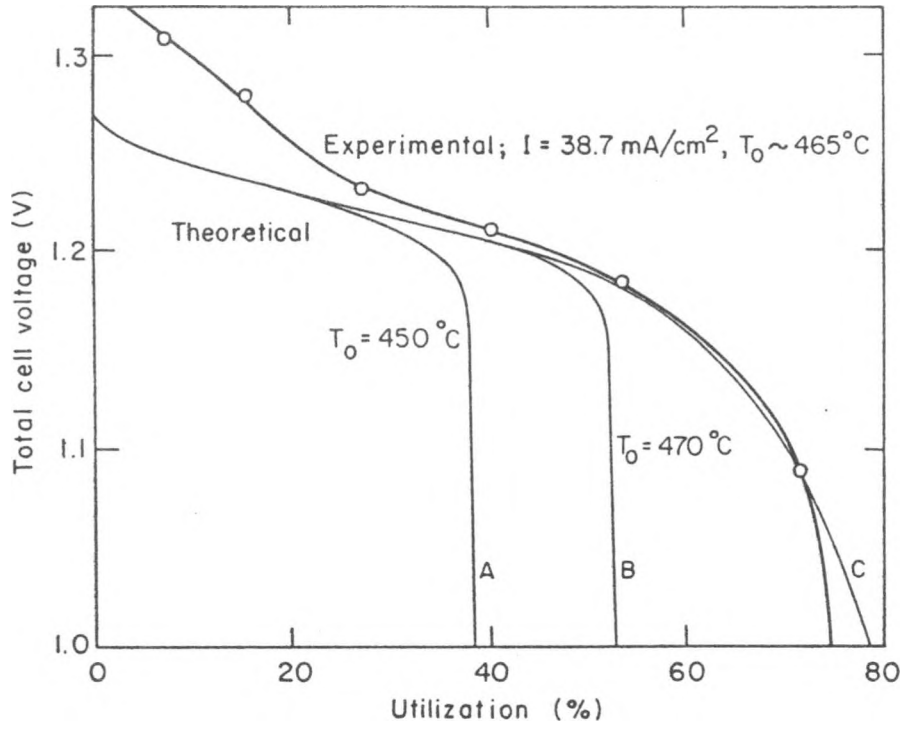

Figure 6. Comparison of theoretical and experimental discharge curves for the X-phase mechanism.

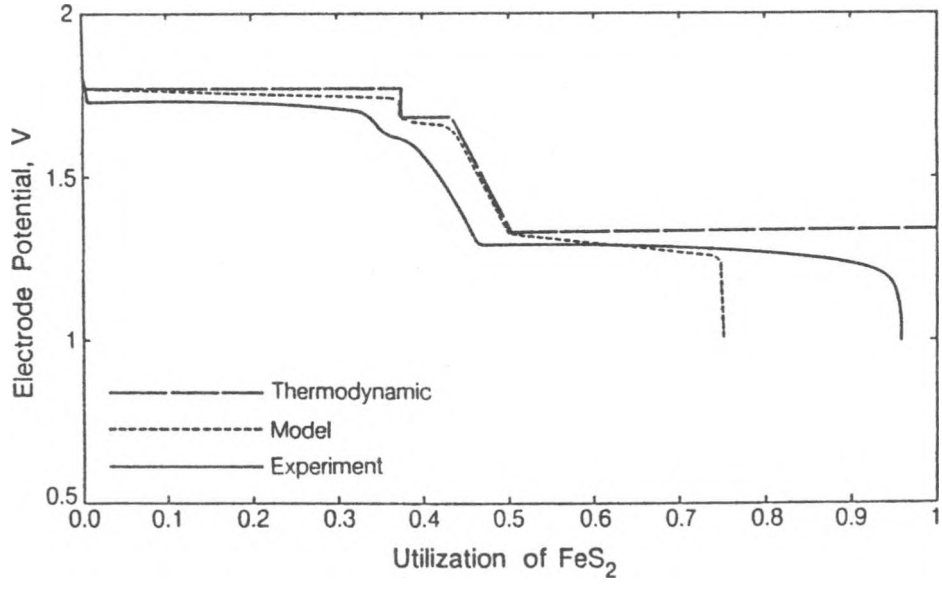

Figure 7. Comparison of model and experimental results for the voltage of the FeS_2 electrode in a LiAl/FeS_2 cell, relative to a LiAl (α–β) reference electrode (450°C, 50 mA/cm^2, x^0_{LiCl} = 0.68). The reversible, thermodynamic potential is also shown in order to display more clearly the losses of the system.

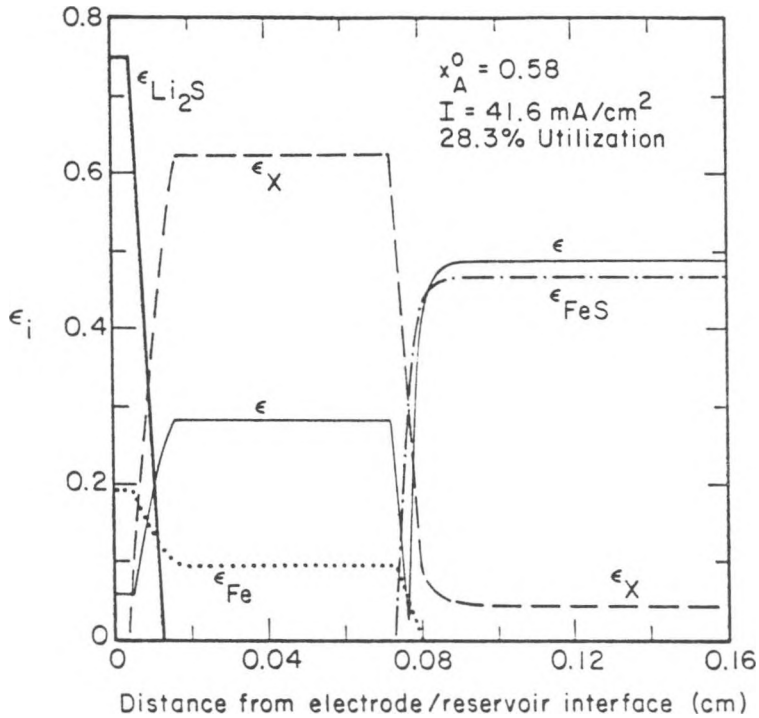

Figure 8. Volume fractions of solid phases and electrolyte in the positive electrode of a LiAl/FeS cell discharging by the *X*-phase mechanism.

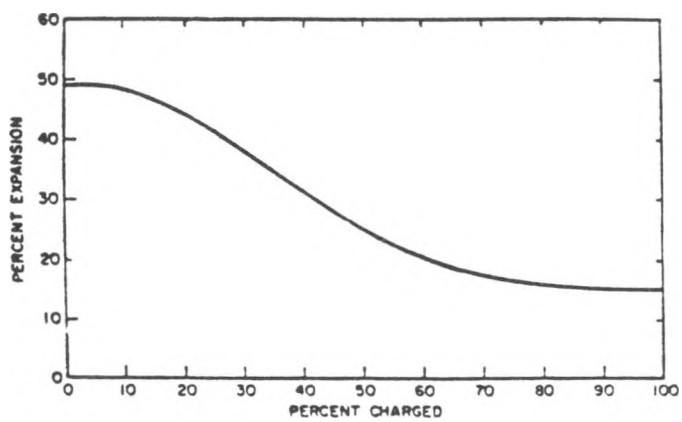

Figure 9. Average positive-electrode expansion of a series of experimental cells as a function of state of charge.

In summary, let us emphasize that models of batteries with porous electrodes can predict polarization characteristics, as well as temperature changes. They can also give details of the what is going on inside, such as composition profiles, precipitation of electrolyte, and reaction and porosity distributions, which would be difficult to determine experimentally. These details, as well as attempts to reconcile results with experiments, can enhance our understanding of how such systems operate.

ACKNOWLEDGMENT

This work was supported by the Assistant Secretary of Conservation and Renewable Energy, Office of Energy Systems Research, Energy Storage Division of the United States Department of Energy under Contract Number DE-AC03-76SF00098.

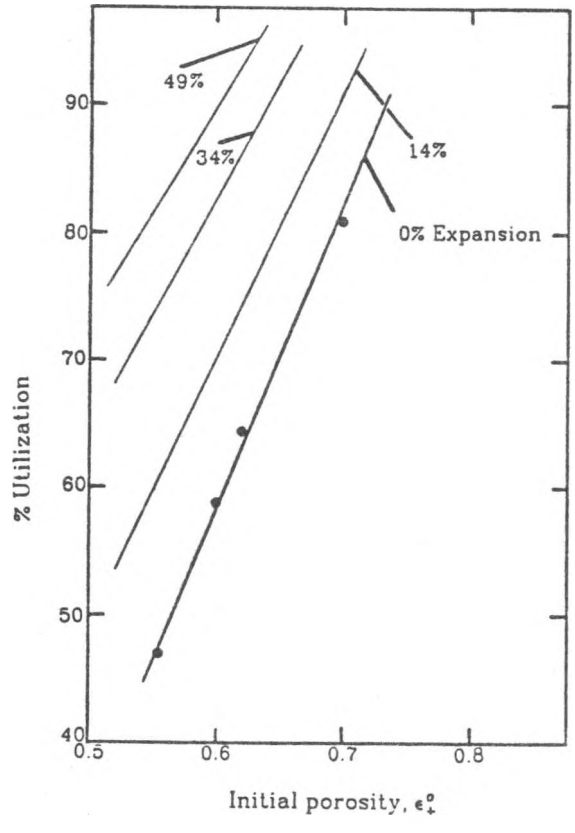

Figure 10. Maximum positive electrode utilization as a function of ϵ_+^0. The points are simulation results.

THE DEVELOPMENT OF A HIGH PERFORMANCE LITHIUM-ALLOY/METAL SULFIDE CELL FOR ELECTRIC VEHICLE PROPULSION

G. Barlow

Gould Inc.,
40 Gould Center,
Rolling Meadows,
Illinois 60008

ABSTRACT

Lithium-alloy/metal sulfide molten salt rechargeable batteries have been under development for electric vehicle propulsion for about ten years. During this time a practical multi-plate monopolar cell design has been developed based on the lithium-alloy/iron monosulfide electrochemical couple. The state-of-the-art cell is a seven plate, negative electrode limited design with a theoretical capacity of 300 Ah (based on lithium) and a negative:positive capacity ratio of 0.95. Cells of this type have specific energies of approximately 105 Wh/kg and 235 Wh/l at a C/3 discharge rate, a (15 sec.) peak power of approximately 130 W/kg at 80% depth of discharge and a cycle life of about 200 cycles.

The peak power of the negative-limited cell is greatly improved over that of the earlier positive-limited cell design without any significant change in the specific energy. The life of the negative-limited cells is presently somewhat lower than the 1000 cycles that has been achieved in the best positive-limited cells. However, there is no reason why comparable cycle life cannot be attained in negative-limited cells once the defective welds joining the positive-electrode particle-retainer baskets are rectified.

The mechanism identified in both positive-limited and negative-limited cells which leads to the majority of cell failures is the deposition of metallic iron in the separator. The deposited iron particles advance from the face of the positive electrode towards the negative electrode and this eventually leads to a short. It is postulated that the cell life could be greatly extended by employing constant potential charging and lowering the charge cut-off voltage, since this would minimize the formation of soluble iron species in the positive electrode which subsequently can be redeposited as metallic iron elsewhere in the cell.

Cells of the design discussed in this paper recently have been incorporated into 9-cell battery modules and tested extensively at NBTL in Argonne National Laboratory. The results of these battery tests are given in a companion paper presented by A. Chilenskas of ANL at this Workshop.

DESIGN AND TEST OF LITHIUM-ALLOY/IRON MONOSULFIDE BATTERIES

A. A. Chilenskas, R. L. Biwer, and W. H. DeLuca

Argonne National Laboratory
9700 South Cass Avenue
Argonne, IL 60439-4837

ABSTRACT

A program has been initiated by the Electric Power Research Institute to examine the feasibility of using the Li-alloy/FeS battery for electric-vehicle propulsion. In the first phase of the program, a joint effort between Argonne National Laboratory and Gould Research Center resulted in the design, fabrication, and testing of two full-scale 12-V modules and related battery components at Argonne's National Battery Test Laboratory. The design of the module and battery components was based upon a van battery design study supported by the U.S. Department of Energy. The objective of the Phase I program was to provide test data to the battery developers applicable to cell and module development, insulated case design, heating/cooling subsystem design, and charger development.

BATTERY DESIGN STUDIES

Performance requirements for the electric van were based upon an Electric Power Research Institute (EPRI) study.[1] The principal requirements are given in Table 1. The power-train limits were taken from a power-train development program sponsored by DOE,[2] and the performance coefficients for battery energy and power for an electric van were based upon an electric van study performed by Toyota Motors.[3]

Table 1. Electric Van Requirements

Parameter	Specification
Range	60-100 mi
Acceleration	0-30 mph in 14 s
Payload	1000 lb

The shape of the battery was based upon the maximum space available under the deck of a Chrysler van, i.e., 12 x 30 x 75 in. The battery arrangement consists of 18 series-connected modules. Each module consists of nine cells connected in series. The modules are secured to the heat exchanger, which also serves as a load-supporting tray.

The main components of the battery case consist of the jacket and the plug. The jacket is a rectangular box that is open on one end and has outer dimensions of 12 x 30 x 75 in. The material of construction is 0.015-in. stainless steel sheet, with one inch of Linde insulation sandwiched between outer and inner shells. To obtain the low thermal conductivity necessary for high efficiency battery operation, the Linde insulation must operate in a vacuum of about 10^{-2} to 10^{-3} torr.

12-VOLT MODULE TEST RESULTS

Energy

The two 12-V modules (nine cells each) fabricated by Gould Research Center (GRC) were tested at the ANL National Battery Test Laboratory. Weight parameters used in the module performance assessment are given in Table 2.

Table 2. Weights of the 12-Volt Modules

Module Number	Cell N/P Ratio[a]	Cell Weight, kg	Module Weight, kg
1	1.3	2.74	30.04
2	0.95	2.80	28.81

[a]N/P is the negative-to-positive capacity.

The specific energies achieved by modules #1 and #2 and the projected specific energy for a future module are shown in Fig. 1. The specific

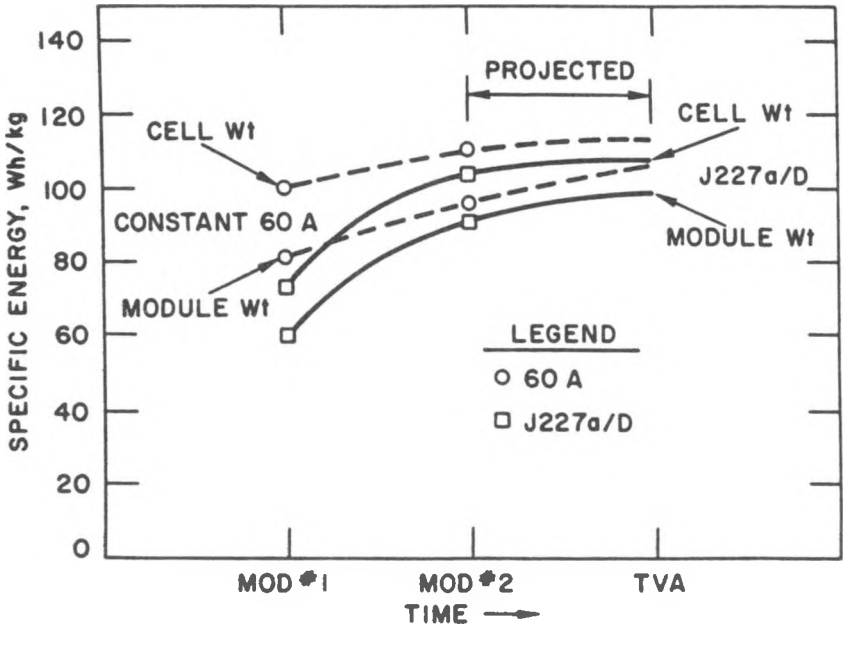

Fig. 1. Specific Energy of Li-Alloy/FeS Modules

energies are given on a cell-weight and module-weight basis. Values are shown for the two types of tests that were performed, a 60-A constant-current discharge and a driving load employing the SAE J227a/D profile. The 60-A and J227a/D tests resulted in an average power delivery of 26-28 W/kg (cell-weight basis). A comparison of the energy outputs of the two tests shows a decrease in energy delivered by the module under the driving load, as expected, because the discharge is terminated by a cell-voltage cutoff. The voltage cutoff is reached sooner during the driving-profile test because of the current surge that is required during the acceleration phase. The figure shows the significant improvements made in the energy delivery capability of Li-Al/FeS modules. The most advanced module, module #2, delivered 91 Wh/kg (module-weight basis) under the J227a/D test regime, exceeding the design target set in the EPRI program by about 8%.

Module #2 was tested at several constant-current discharge levels. The results are summarized in Table 3.

Table 3. Constant-Current Discharge Performance of Module #2

Discharge Current, A	Average Specific Power, W/kg	Energy Output, kWh	Specific Energy,[a] Wh/kg
60	26	2.77	110
30	14	2.93	116
15	7	3.02	120

[a]Cell-weight basis.

The specific energies achieved are record highs for engineering-scale lithium-alloy/iron monosulfide cells. The 110 Wh/kg achieved at a discharge current of 60 A represents a 22% increase in the specific energy of the same type of cells that were tested individually at GRC at the same average power output. The improvement is due to the added incremental storage provided by the ANL charger-equalizer, which employs a stepped-current taper charge and a constant 3-A equalization period following a constant-current charge.

Power

Several power tests with module #2 were performed at a constant 300-A discharge to determine power capability as a function of DOD. The results of these tests are given in Table 4.

The power production of module #2 when tested under the J227a/D profile proved to be satisfactory, as evidenced by the high specific energy (104 Wh/kg, cell-weight basis) and number of "D" cycles (109) achieved per discharge.

Table 4. Module #2 Power Output as Function of Depth of Discharge[a]

Ah Discharged	DOD, %	Specific Power, W/kg
25	10	107
125	50	97

[a]Basis: Constant 300 A for 28 s.

Cycle Life

Testing of module #1 began at the ANL National Battery Test Laboratory (NBTL) on April 12, 1985 and was completed on August 27, 1985 (4-1/2 mo). Module #2 was tested from September 25, 1985 to December 12, 1985 (2-1/2 mo). A summary of cycle life performance is given in Table 5.

The cycle lifetimes achieved for modules #1 and #2 were limited due to internal cell shorts caused by defective welds on the positive-electrode containment structure. This failure mechanism was discovered at GRC after cycling and examining similar cells. The cell design has since been modified by GRC to correct this failure mode.

Table 5. Cycle Life Performance Summary

Module Number	Cycle Number	Test Regime	Energy Output, kWh	Specific Energy,[a] Wh/kg	"D" Cycles per Discharge[b]
1	1-20	60-A discharge	2.45	100	--
	20-29	J227a/D (100% DOD)	1.73	70	73
	30-111	J227a/D (80% DOD)	1.43	58	59
	144	J227a/D (voltage reversed)	1.00	41	25
	151	Testing discontinued			
2	1-14	(see Table 3)	--	--	--
	15-19	J227a/D (100% DOD)	2.62	104	109
	20-114	J227a/D (60 mi)	1.46	58	60
	115-125	J227a/D (voltage reversed)	-	--	36-48

[a]Cell-weight basis.

[b]Each "D" cycle equals a driving range of about 1 mi.

REFERENCES

1. B. A. Askew and P. C. Symons, Battery Options for Meeting the Performance Requirements of a Fleet Electric Vehicle, Proc. EV Council Expo '83, Detroit, MI, October 4-6, 1983.

2. K. C. Winters, Military - Public Electronic Systems, Chrysler Corporation, Huntsville, AL, private communication, March 1983.

3. A. A. Chilenskas et al., Design Considerations for a Li-Al/FeS Battery for an Electric Van, Proc. 1st Congress & Exposition, Detroit, MI, February 28-March 4, 1983 (SAE publication SP-541, Feb. 1983).

ACKNOWLEDGMENT

Support for this work was provided by the Electric Transportation Program of the Electric Power Research Institute under Contract No. RP-2415-2. The cognizant Program and Project Managers at the Electric Power Research Institute are D. L. Douglas and R. Weaver. The tests were conducted at the National Battery Test Laboratory, at Argonne National Laboratory, which is operated under the auspices of the U.S. Department of Energy.

Support for the battery design studies was provided by U.S. Department of Energy, Assistant Secretary for Conservation and Renewable Energy, Office of Transportation Systems.

FAILURE ANALYSIS OF LITHIUM-ALUMINUM/IRON SULFIDE CELLS

James E. Battles
Argonne National Laboratory
Chemical Technology Division
9700 South Cass Avenue
Argonne, IL 60439

INTRODUCTION

Post-test examinations were an integral part of the Li-alloy/FeS battery development program at Argonne National Laboratory. Important functions of post-test examinations were to determine the causes of cell failure and to provide recommendations on cell design and assembly techniques that would eliminate these failure modes. Cell failure was generally indicated by a sharp decline in the coulombic efficiency, which is the manifestation of an electrical short circuit between the positive and negative electrodes. Combinations of macroscopic and microscopic examinations were utilized to identify the source and cause of the short circuits. A special metallographic glovebox facility with a helium atmosphere was constructed for these examinations.[1]

Cell failure analysis was conducted on bicells (<100-Ah capacity) from the early cell development program and on multiplate cells (about 200- and 400-Ah capacity) from the Mark IA and Mark II battery development programs. A description of the design for these cells can be found in Ref. 2. The results of the cell failure analysis for the bicell (~163 cells) and for the Mark IA multiplate cells were discussed in detail in a previous report,[1] and are briefly summarized here.

RESULTS OF FAILURE ANALYSIS

The principal causes of cell failures for the bicells from the early development program were short circuits formed by (1) extrusion of active material from the edge of one electrode, because of inadequate mechanical restraint in the design or a mechanical defect, and subsequent contact of that material with the opposite electrode or the cell can, (2) cutting of electrode separators by the honeycomb current collector of the positive electrode, and (3) formation of metallic copper deposits across the separator from the Cu_2S added to the positive electrode for improved conductivity. In addition, difficulties in cell assembly such as misaligned electrodes resulted in cell failure. Failures caused by metallic copper deposits and cut separators were eliminated by removal of the Cu_2S additive to the positive electrode and by the addition of a retainer screen to both the positive and negative electrodes. Improvements in the quality assurance procedures decreased the number of cell failures caused by assembly difficulties.

For the Mark IA multiplate cells, the leading causes of failures were (1) extrusion of active material from the positive electrode through a rupture in the retainer screen at the edge and the overlapping BN fabric cups (the separator) and subsequent contact of the active material with the cell can or the negative electrode and (2) the development of short circuits in the electrical feedthroughs because of a metallic bridge caused by corrosion initiated by electrolyte leakage through the BN powder seal.

In the Mark II program, progress in the fabrication and development of cells was determined by tests at ANL for groups of 12 or more cells[3] of identical design, called "status cells." Post-test analyses was completed on four groups of status cells fabricated by Eagle-Picher Industries, Inc. (Group I, III, VI, and IX) and two groups by Gould Inc. The Eagle-Picher cells contained BN-felt separators, and the Gould cells contained MgO-powder separators.

Two major failure modes were identified for the Eagle-Picher cells.[2,3] The first is the formation of Li-Al protrusions that penetrate the BN-felt separator and contact the positive electrode. A typical example of this type of failure is shown in Fig. 1. The protrusions exhibited the porous microstructure typical of the Li-Al negative electrode. This failure mode

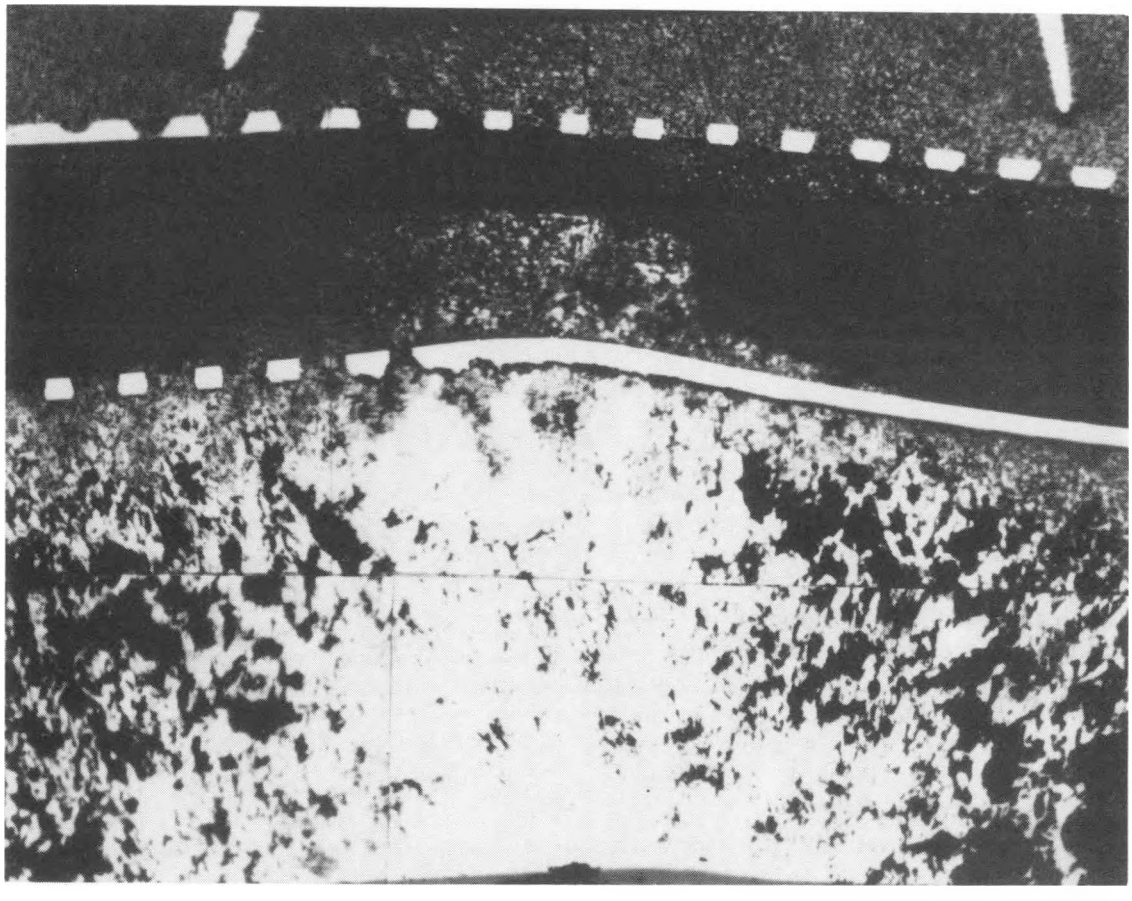

Fig. 1. Penetration of BN-Felt Separator by a Li-Al Protrusion.

was especially prevalent in the Group III, VI, and IX cells (23 of 36 cells failed by this mode). The second major cause of short-circuit failures in Eagle-Picher status cells was the extrusion of active material at the edge of the electrodes as shown in Fig. 2. This failure mode, which was caused by inadequate mechanical restraint at the electrode edges, was the predominant cause of short-circuit failures in Group I cells (9 of the 14 cells in this group failed by this mode). No additional extrusion failures occurred after a U-shaped channel was added to reinforce the mechanical restraint at the edges of both electrodes in the Group III cells.

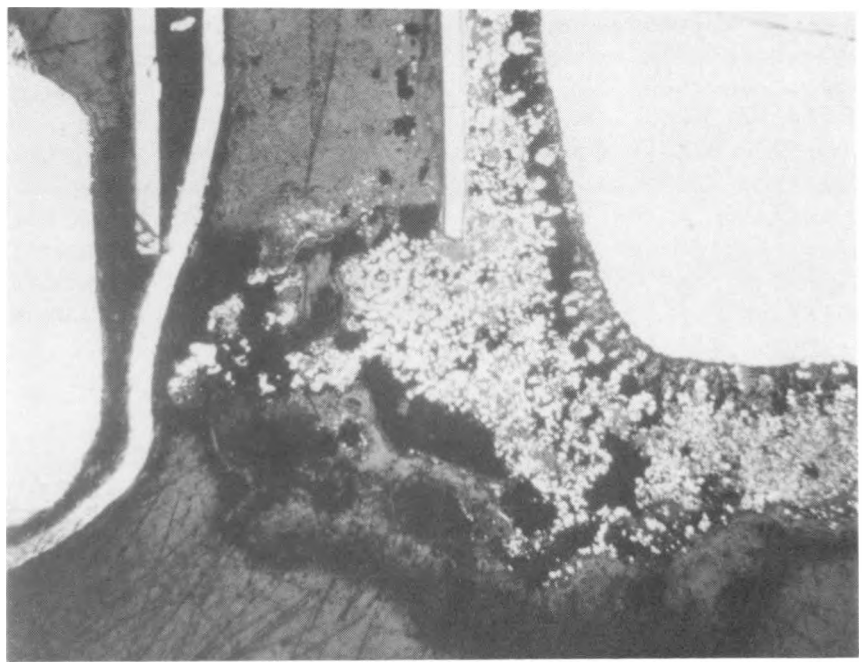

Fig. 2. Example of Cell Failure Caused by Extrusion of Positive Material through a Rupture in the Electrode Retainer.

Post-test analysis was also done on five Li-Al/FeS multiplate cells (Group X) that were fabricated by Eagle-Picher for the U.S. Army MERADCOM and tested at ANL[4]. The mean time to failure (i.e., until 20% loss of capacity or operation at <95% coulombic efficiency) for the five cells was 1023 cycles (range: 849-1319 cycles). These cells had a fine mesh screen (200 mesh) in support of the normal electrode retainer to prevent the formation of Li-Al protrusions across the BN felt electrode separators. Metallographic examination confirmed that the addition of the fine mesh screen had effectively prevented the formation of Li-Al protrusions. In this group of five cells, the failure mechanism was the deposition of metallic iron in the electrode separator. The iron eventually bridged the space between the electrodes. Iron deposition, which had been observed in previous examinations of cells that had been overcharged, is known to be dependent on the charge cutoff voltage. Solutions to this failure mechanism are to reduce the charge cutoff voltage, to increase the electrode separation, and to add overcharge protection to the positive electrode.

The extensive cell failure results discussed above indicate that the short-circuit failures are of mechanical origin. Appropriate changes have been made in the cell designs to correct those mechanical deficiencies.

Post-test examination of the two groups of Gould status cells (MgO-powder separators) showed a single mechanism for the internal short-circuit failures.[5] Although all of the cells in the first group and most of the cells in the second group failed because of capacity loss, cell operation was continued to the point of short-circuit failure (coulombic efficiency decline) except for two cells in the first group. Electrolyte leakage was observed in the feedthroughs of all cells, and two cell failures were caused by short circuits in the electrical feedthroughs. However, in the cells from these two groups, the predominant failure mode was internal short circuits caused by complete penetration of the MgO-powder separator by active material from the positive electrode. This failure mode is shown in Fig. 3. The material from the positive electrode compressed the MgO powder, and its irregular advance resulted in numerous localized penetrations, which eventually contacted the negative electrode (at 300-500 cycles). This failure mode occurs because the mechanical properties of the present MgO-powder separators are inadequate for the containment of the positive electrode material. Elimination of this failure mechanism requires substantial improvements in the mechanical properties of the powder separator/retainer system.

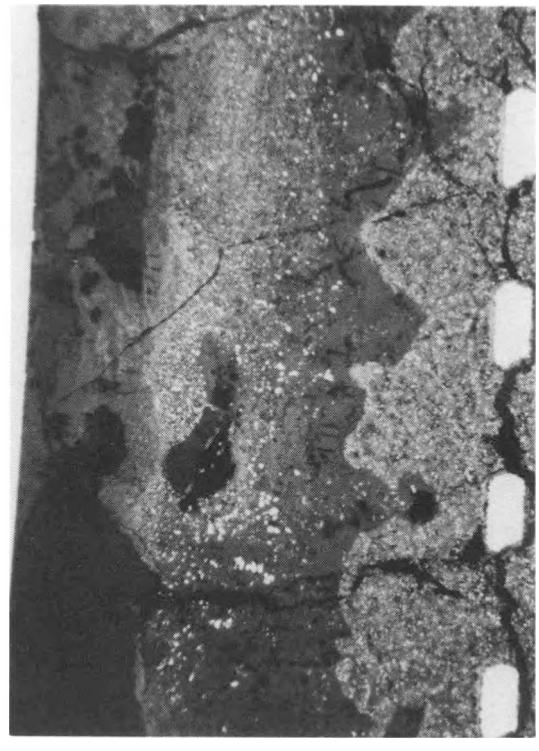

Fig. 3. Penetration of MgO-Powder Separator by Active Material from the Positive Electrode.

ELECTRODE EXPANSION

Electrode expansion has been observed in the post-test examinations of all bicells and multiplate cells. The electrode expansion within a given cell can be divided into three classes:

1. Negative electrode expansion and positive electrode compression,

2. Positive electrode expansion and negative electrode compression, and

3. Expansion of both electrodes.

Class three behavior is most common; class one behavior occurs next most frequently. Class two is a rare occurrence and appears to be associated with porous negative electrodes such as those fabricated from pressed aluminum wire and lithium foil. Obviously, the amount of electrode expansion depends upon a number of factors; however, the most important factors appear to be the as-fabricated electrode loading density (Ah/cm^3 or volume fraction of active material), percent utilization of the active electrode material, compressibility of the separator, and the degree of cell restraint used during its operation.

Engineering-scale cells have been examined to obtain quantitative data on the expansion of the electrodes. The data are summarized in Table I for Li-Al/FeS multiplate cells fabricated by Eagle-Picher for the Group I cells. The state of charge for each cell is indicated by the phases present in the positive electrode (Li_2S + Fe for full discharge and FeS for full charge). The electrode expansion is reported as percent increase in thickness over the as-fabricated thickness for the positive electrodes, the inner negative electrodes, and the outer negative electrodes (which are normally one-half the thickness of the inner negative electrodes). The cells listed in Table I showed reasonable uniformity in electrode thicknesses. The data show that more expansion occurred in the outer negative electrodes than in the inner electrodes. This finding is consistent with the metallographic observation that the outer negative electrodes show less agglomeration than do the inner negative electrodes. This difference may be related to the fact that the outer electrodes are in contact with the cell can; consequently, they have better current collection. The data show a trend in the electrode expansion according to the state of charge; this is to be expected since the volume of the active material increases by almost a factor of two when the positive electrode discharges from FeS to Li_2S + Fe. Similarly, the volume of the negative-electrode active material decreases during discharges. The data have been normalized, and the results are presented graphically in Fig. 4. The electrodes of the Eagle-Picher multiplate cells exhibited class three behavior, i.e., both the positive and negative electrodes expanded.

A similar analysis of the electrode expansion data for the twelve multiplate cells fabricated by Gould Inc. (D-series) showed that the electrodes exhibited class one behavior. These cells had BN-felt separators and were assembled in the half-charged state with a high capacity loading density in the negative electrodes (~1.3 Ah/cm^3). The positive electrodes

Table I. Summary of Electrode Expansion and Cause of Failure in Eagle-Picher Group I Multiplate Cells

Mark II Cell No.	Cycles	Cause of Failure	Separator Thickness, mm,[a]	Electrode Expansion						State at Termination of Operation
				Outer Neg.		Inner Neg.		Positive		
				cm,[b]	%	cm,[b]	%	cm,[b]	%	
-032	238	Protrusion	1.6	0.40	25	0.83	30	0.32	3	Charged
-033	696	Extrusion	1.5	0.38	19	0.69	8	0.43	39	Discharged
-036	1031	Iron sulfides across separator	1.3	0.50	56	0.82	28	0.38	23	Charged
-037	292	Protrusion	1.3	0.42	31	0.72	13	0.41	32	Discharged
-038	356	Extrusion	1.6	0.42	31	0.73	14	0.42	35	Discharged
-039	263	Extrusion	1.6	0.40	25	0.71	11	0.41	32	Discharged
-040	508	Extrusion	1.2	0.40	25	0.78	22	0.42	35	Semicharged
-041	804	Extrusion	1.4	0.41	28	0.86	34	0.36	16	Charged
-043	323	Extrusion	1.6	0.42	31	0.84	31	0.34	10	Semicharged
-046	559	Wrinkle in corner of electrode frame that cut separator	1.4	0.39	22	0.81	25	0.40	29	Charged
-049	263	Extrusion	1.5	0.41	28	0.72	13	0.40	29	Semicharged

[a]The separators were compressed to a 2.5-mm thickness in the as-assembled cell.
[b]The reported thickness is an average of the measured minimum and maximum thicknesses. As-fabricated thicknesses are: outer negative, 0.32 cm; inner negative, 0.64 cm; positive, 0.31 cm.

showed a slight compression at full charge, but the negative electrodes exhibited severe expansion (60-70%). This electrode expansion was accommodated by the compression of the BN-felt separators. Post-test examinations indicated that the electrode expansion is related to the loading density of the as-fabricated electrode. For example, the Gould cells with the high loading density (1.32 Ah/cm^3, near 100% solids at full charge) exhibited excessive expansion (60-80%), whereas the Eagle-Picher cells with a lower loading density (~0.92 Ah/cm^3) exhibited moderate expansion (20-30%).

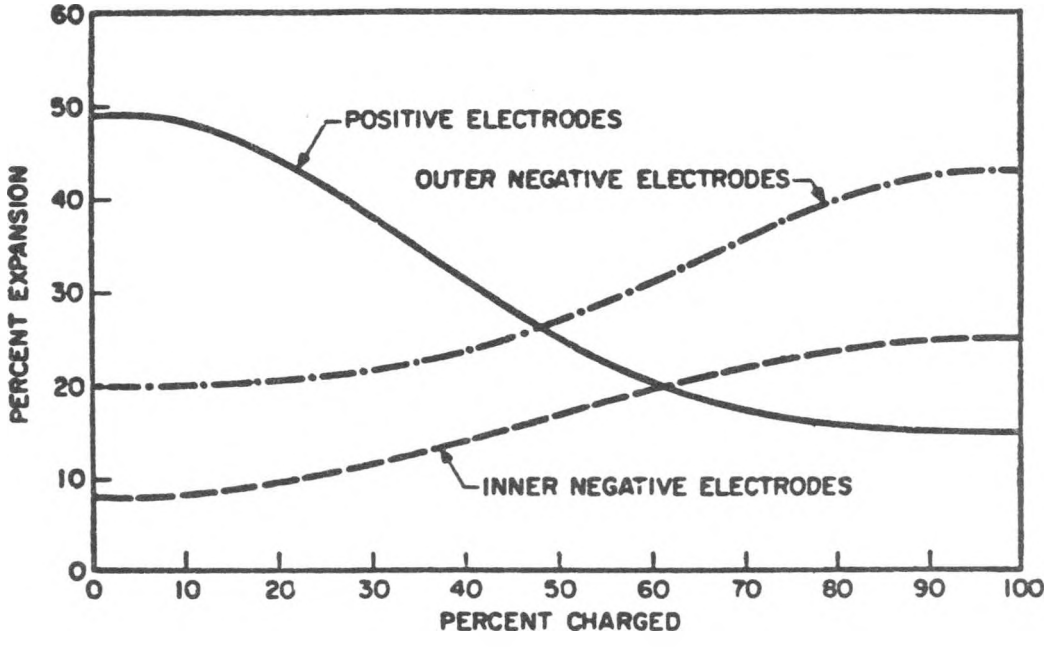

Fig. 4. Electrode Expansion as a Function of Depth of Discharge for Eagle-Picher Group I Cells.

CONCLUSION

In conclusion, the data from the post-test examinations of both the Eagle-Picher and Gould cells showed that the failure mechanisms are mechanical in origin and can be easily corrected by design changes. Further, the microscopic examinations of the Li-Al and FeS electrodes from long-lived cells have shown that the electrode microstructures are stable with cycle life and that corrosion of the current collector materials is not a serious problem.[2] Most important, these examinations have shown no indication of intrinsic behavior that would be expected to limit the cycle life of Li-Al/FeS cells.

ACKNOWLEDGMENT

This work was supported by the U. S. Department of Energy, Office of Energy Storage, under Contract W-31-109-Eng-38.

REFERENCES

1. J. E. Battles, F. C. Mrazek, and N. C. Otto, Post-Test Examinations of Li-Al/FeS_x Secondary Cells, Argonne National Laboratory Report ANL-80-130 (December 1980).

2. E. C. Gay et al., Li-Alloy/FeS Cell Design and Analysis Report, Argonne National Laboratory Report ANL-84-93 (July 1985).

3. E. C. Gay, J. E. Battles, and W. E. Miller, J. Electrochem. Soc., 130, 1646 (1983).

4. E. C. Gay, J. E. Battles, A. A. Chilenskas, W. E. Miller, R. F. Malecha, and J. D. Arntzen, Extended Abstracts, 166th Electrochem. Soc. Meeting, New Orleans, LA, October 7-12, 1984, Vol. 84-2, pp. 166-167 (1984).

5. E. C. Gay, J. E. Battles, and W. E. Miller, Extended Abstracts, 162nd Electrochem. Soc. Meeting, Vol. 82-2, pp. 74-75 (1982).

Molten Salt Research and Development in Japan

Yasuhiko Ito
Department of Nuclear Engineering
Kyoto University
Kyoto, Japan
and
Hiroshi Shimotake
Amoco Research Center
Amoco Corporation
Naperville, Illinois, U.S.A.

ABSTRACT

There is growing interest in the molten salt technology in Japan. New processes are being developed to produce a semiconductor material, aluminum and other materials. The government is pursuing the development of molten carbonate fuel cell systems. This paper describes the recent status and activities of these efforts in Japan.

INTRODUCTION

This paper reviews several highlights of recent research and development activities on molten-salt technologies in Japan. It is not intended to give complete coverage to all aspects of the technologies. Molten salt technology has been always an important branch of the Japanese technology. In 1960, Molten Salt Technology Committee was formed in the Electrochemical Society of Japan as a place of communication between industrial and academic communities. Today, the Committee has 42 corporate and 120 private members. More recently, the Society of Molten Salt Thermal Technology was organized with 12 corporate and 40 private members. The numbers of papers on the molten salt technology submitted in their journals as well as presented in their meetings are increasing. Particularly, since the development program of molten carbonate fuel cells, sponsored by the Ministry of International Trade and Industry (MITI) was initiated in 1981, an exponential increase in the number of publications and patents has occurred.

Japanese are also active in the effort to exchange information with foreign laboratories, particularly with the U.S. In the past, the direction of information flow tended to be one-sided, partly due to the language and cultural barriers. Japanese are trying to rectify this. For example, in January 1986, International Symposium on Fuel Cell and Advanced Battery was held in Toyko by the Institute of Applied Energy (a MITI's organization). Several key U. S. technologists were invited to the symposium and participated in the workshops. Furthermore, the visitors were invited to the laboratories and plants. In 1987, the International Joint Symposium on Molten Salt will be held jointly with the U.S. and Japan in Hawaii. In 1989, the International

Society of Electrochemistry will be held in Kyoto. Through these international society meetings as well as the governmental programs, the "open-door policy" is expected to continue. It should be pointed out that, special funds have been set up by the Japanese government to invite foreign scientists and technologists for an extended stay in Japanese national laboratories or universities, usually three months to one year. Such arrangements would allow the scientists and technologists to accomplish a great deal more than technical information exchange.

TECHNICAL HIGHLIGHTS

1) Production of Monosilane

The use of monosilane has been increasing as a base material of silicon semiconductor, amorphous silicon, and other semiconductor devices. The process developed by Komatsu Electronic Metals Co., Ltd.[1] is based on the following reactions:

$$4LiCl \rightarrow 4Li + 2Cl_2 \text{ (molten salt electrolysis)}$$
$$4Li + 2H_2 \rightarrow 4LiH$$
$$4LiH + SiCl_4 \rightarrow 4LiCl + SiH_4$$
$$\underline{2Cl_2 + Si \rightarrow SiCl_4}$$
$$Si + 2H_2 \rightarrow SiH_4$$

This process is energy-efficient and has been adopted as part of Japanese National project "Sunshine Project".

2) Production of NF_3 [2]

NF_3 is widely used in the plasma etching of LSI, the surface treatment of optical fiber, cleaning of CVD and plasma processes. However, the production of NF_3 has been inefficient and costly. A new process developed by Central Glass Company involves a reaction between ammonium salt of a metal halide and F_2 which is obtained by electrolysis of molten KH_2F_3. Another method developed by Showa Denko Company based on Professor N. Watanabe, et al, (Kyoto University) uses a direct electrolysis of NH_4F - nHF (n=1-2) to obtain NF_3. These examples show the potential production of functional gases by molten salt processes.

3) Production of Misch Metal

Another interesting development by Japanese is the production of misch metal (40-50% Ce-20-40% La), which is used as an alloy additive and other industrial uses. The original concept was developed in the U.S.A. in 1951, but was never adopted in a full scale production. Santoku Metal Industry Co. Ltd.[3] has succeeded in commercialization of the process, which uses a large-scale electrolytic bath for the production.

4) Production of γ-$Li_2V_2O_5$

Vanadium bronze is becoming an important catalyst, but availablity of this material is still limited. Professor H. Kojima, et al, (Yamanashi University) have developed a new process to synthesize needle-like crystals of γ-LiV_2O_5 by the following reaction:[4]

$$(V_2O_3)_2(SO_4)_3 + 4Li_2O = 2LiV_2O_5 + 3Li_2SO_4$$

An important observation was made in this process that by adjusting the mole ratio of V_2O_5 and Li_2O to 4:1, β-$Li_{0.3}V_2O_5$ could be obtained. Therefore, a vanadium bronze containing mixed valences can be produced by this process.

5) Production of Aluminum

Aluminum production by the electrolysis of a chloride bath at 700-800°C was developed by Professor T. Ishikawa (Hokkaido University)[5]. This process involving a bath containing several mole % of $AlCl_3$ is highly energy efficient.

6) Production of Na, NaOH and HCl

The production of these materials by electrolysis was developed by Professor S. Yoshizawa and Y. Ito (Kyoto University).[6] The process uses β-alumina solid electrolyte and a mixed salt bath containing NaCl-$AlCl_3$ and NaCl-$ZnCl_2$. A low production cost is predicted.

7) Electrodeposition of Refractory Metals

Professor K. Koyama, et al, (Himeji Institute of Technology)[7] has successfully developed a method to deposit tungsten from a mixed salt bath by electrolysis. The salt systems KF-$Na_2B_4O_7$-K_2WO_4, and KF-$K_2B_4O_7$-K_2WO_4, having melting points near 700°C, were used. The deposited surface is smooth and free of dendrite.

8) Development of Molten Carbonate Fuel Cells

A 7-year program started in 1981 to develop 10-kW molten carbonate fuel cells is underway as part of the Moonlight Project, sponsored by the New Energy Development Organization, which is a part of Ministry of International Trade and Industry. Five industrial corporations (Toshiba, Hitachi, Mitsubishi, Fuji, and IHI), a utility laboratory (Central Research Institute of Electric Power Industry), and a national laboratory (Government Industrial Research Institute, Osaka), are participating in the program. Since this topic has been reported extensively elsewhere[8], we will not discuss it here.

9) Development of High Temperature Molten Salt Batteries

Research is being conducted by several industrial organizations on both primary and secondary molten salt batteries as exemplified by

disclosures made in patents. However, the efforts are still limited in laboratory scale cells.

Japan Storage Battery Co., Ltd. has been engaged in the development of a rechargeable LiAl/FeS_x cell battery since 1981.[9] To date their effort is limited to single cells. They have successfully developed a unique method of applying MgO powder separator in the molten salt cell system. Professor N. Koura (Tokyo University of Science) et al, have been developing Al/$AlCl_3$-NaCl-KCl/FeS_2.[10] This rechargeable cell system is unique in that Al is used as the negative material while operating at a temperature below 200°C. However, the cell size is still limited to a laboratory scale. Professor M. Hiroi (Kobe University of Mercantile Marine)[11] has been conducting basic research on LiAl/FeS_{2x} cells. His research made a contribution in the resistance mechanism of the positive electrode.

SUMMARY

We have pointed out that Japanese consider the molten salt technology as an important branch of their technology, which they use as an efficient tool to produce new and old materials to modify the material and to convert and store energy. Although we did not cover in this paper, there are also extensive efforts under way on basic research in molten salt systems. A great deal of interest also exists in the area of nuclear reactor technology. We would hope that this paper helped to shed light on some of the Japanese activities in this important technology.

REFERENCE

[1] K. Seto, et al, Yoyuen (Molten Salt), 25, 63, (1982).

[2] A. Tasaka, Yoyuen, 28, 284, (1985).

[3] K. Yamamoto, Yoyuen, 28, 296, (1985).

[4] H. Kojma et al, Yoyuen, 28, 280, (1985).

[5] T. Ishikawa, Yoyuen, 28, 197, (1985).

[6] Y. Ito, et al, Advances in Molten Salt Chemistry and Technology, Vol. 4, pp 391-435, Plenum Press (1981).

[7] K. Koyana, et al, Denki Kagaku, 54, 40, (1986).

[8] Proceedings of IAE International Symposium on Fuel Cell and Advanced Battery, January 21 and 22, 1986, Tokyo, Japan, The Institute of Applied Energy (1986).

[9] Private communication (1986).

[10] N. Koura, et al, Kenki Kagaku, 53, 674, (1985).

[11] M. Hiroi, et al, Proc. 25th Battery Discussion Meeting, Electrochem Soc. of Japan, November 13-14, 1984, Nagoya (1984).

MATERIALS SELECTION FOR MOLTEN SALT BATTERY COMPONENTS

John A. Smaga
Argonne National Laboratory
9700 South Cass Avenue
Argonne, IL 60439

ABSTRACT

Candidate materials for the hardware used in Li-alloy/FeS_x ($x = 1,2$) cells are reviewed in this paper. Intermetallic layer formation on negative electrode components is discussed, and methods to alleviate this deleterious reaction are examined. For the FeS electrode, the relative merits of current collectors made with low-carbon steel or nickel are compared. The FeS_2 electrode imposes the most stringent requirements for current collectors, but the development of ceramic-coated substrates may overcome some of the limitations of currently used materials, such as molybdenum. Both BN-felt and MgO-powder separators have demonstrated successful performance in operating cells, but advances in the fabrication of ceramic structures have not been fully applied to separator development. Similarly, alternative feedthrough designs may offer improvements over the compression-type feedthroughs that are currently used.

INTRODUCTION

In secondary batteries, selection of cell hardware materials neccesitates trade-offs among criteria which include compatibility, cost, fabricability, and the physical and mechanical properties of these materials. The intended function of each hardware component imposes a different mix of these requirements. Development work on the lithium/metal sulfide battery has generated a wealth of information on the suitability of candidate materials for the various hardware components of this system. A review of this information reveals areas where the selection criteria have been met and other areas that are open to further investigation.

NEGATIVE ELECTRODE HARDWARE

The selection criteria for metallic components in contact with the negative electrode include: (1) adequate mechanical strength at elevated temperatures, (2) ease of fabrication into the desired component structures, (3) low electrical resistivity for current-carrying components, and (4) compatibility with the active materials in this electrode. To varying degrees, most iron and nickel-base materials satisfy the physical and mechanical requirements, and low-carbon steel is commonly used because of its cost advantage. However, these materials are susceptible to a galvanic reaction.[1-3] The brittleness of the resulting intermetallic layers undermines the structural integrity of the components, and the high electrical resistivity of these layers impairs cell performance. The galvanic reaction

has been well characterized, and several approaches to minimize it have been investigated.

Galvanic Reaction Mechanism

For Li-Al electrodes, the galvanic reaction becomes activated when the electrode is in or near the discharged state. Aluminum ions are generated within the electrode, transported by the electrolyte, and deposited on the components. Measurements of the iron aluminide layers formed on the collectors from similar cells operated within the 435 to 450°C range determined that layer growth was dependent on the square root of time.[4] This finding indicated that the rate of reaction was controlled by a diffusional process.

The compositions of the reaction layers formed on iron- and nickel-based alloys were established in a series of experiments that used unalloyed aluminum as one-half of a bi-metal couple.[3] This study found that $FeAl_2$ is the predominant compound formed on low-carbon steel (AISI 1008 or 1010) and that Ni_2Al_3 is the main compound formed on nickel. For austenitic and ferritic stainless steels, commonly used materials for electrode retainers and cell housings, the reaction layer is composed of an inner layer of the form MeAl and an outer layer of $MeAl_2$, where Me stands for a mixture of Fe, Ni, and Cr.

The growth of the reaction layer has been studied most extensively for low-carbon steel.[5] The process involves first the deposition of aluminum onto the steel substrate followed by diffusion into this substrate. As seen in Fig. 1, aluminum deposition obeys an Arrhenius dependence on temperature for bi-metal couples. The deposition rate, DR, can be expressed as:

$$DR = DR_o \exp(-Q/RT) \qquad (1)$$

where the activation energy, Q, is 21.4 $kcal \cdot mol^{-1}$ and the rate constant, DR_o, is 1.65×10^{-2} $g \cdot cm^{-2} \cdot s^{-1}$. The thickness, x, of the deposited layer, allowing for conversion to the iron aluminide, can be expressed as:

$$x = 1.67\,(DR/\rho)t \qquad (2)$$

where t is the time in seconds, ρ is the density of the iron aluminide, and 1.67 is a combination of conversion constants. At 475°C, Eq. (1) predicts a deposition rate of 9.1×10^{-9} $g \cdot cm^{-2} \cdot s^{-1}$, and Eq. (2) becomes:

$$x = 4.05 \times 10^{-9} t \qquad (3)$$

The linear dependence on time is valid only during the initial stage of layer formation. Beyond a certain transition time, layer growth becomes diffusion controlled and shows a square-root dependence on time:

$$x^2 = Dt \qquad (4)$$

where the diffusion coefficient, D, was measured to be 2.7×10^{-11} $cm^2 \cdot s^{-1}$ at 475°C. Solving Eqs. (3) and (4) gives a value of 19.1 days for the transition time at 475°C.

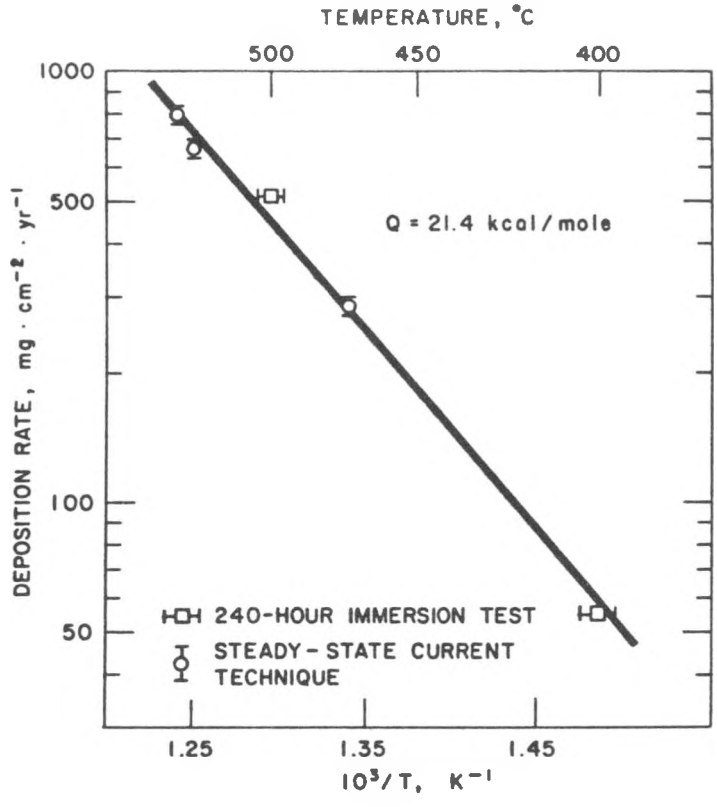

Fig. 1. Arrhenius Temperature Dependence for Aluminum Deposition with Couples of Al/LiCl-KCl/AISI 1008 Steel.

This analysis is based on out-of-cell tests, which do not reflect complicating factors in operating cells, such as the actual ratio of collector surface area to active material surface area and the varying composition of the negative electrode. Nevertheless, the treatment should be qualitatively correct, and as previously noted,[4] the finding that diffusion ultimately controls the rate of layer growth has been confirmed by post-test examinations.

Diffusion-Resistant Coatings

Coatings applied to the hardware substrate may provide a feasible method of preventing serious impairment in component performance. The need for coatings obviously is dependent on the initial component thickness and the desired cycle life. If the use of coatings is warranted, the coating must satisfy these requirements: (1) act as a barrier to the diffusion of aluminum into the substrate, (2) be easily applied to sometimes complex geometries, (3) be compatible with β-LiAl, (4) be adherent to the substrate without appreciable diffusion of the coating into the substrate, and (5) have sufficient electrical conductivity for the intended application. A number of coatings have been evaluated, and coating performance was found to be dependent on both the coating composition and the method of application.[6]

Thin, conductive ceramic coatings of TiC and TiN/TiC applied by chemical vapor deposition (CVD) hold the most promise.[7] These coatings are compatible with β-LiAl and are highly effective barriers to aluminum diffusion, preventing $FeAl_2$ formation for a diffusion couple tested at 475°C for 1000 h. These coatings remain adherent to low-carbon steel in spite of the tendency to develop fine cracks through the full thickness (10-20 μm) of the coating.

Galvanic Reaction in the Li-Si Electrode

The galvanic reaction is not restricted to the Li-Al electrode. Investigators of the Li-Si electrode report that metallic silicides form at an even faster rate than metallic aluminides and have the same detrimental consequences.[8] Two approaches have been used to control the reaction. First, additions of $FeSi_2$ to the negative electrode can reduce the reaction rate observed in cells. Alternatively, coatings can again be used as a protective barrier. Titanium coatings have been cited by the same investigators as one promising method.

POSITIVE ELECTRODE HARDWARE

The materials used for the positive electrode (FeS or FeS_2) hardware have the same mechanical and conductivity requirements as their counterparts in the negative electrode. However, their compatibility requirements are markedly different. The metals used in the positive electrode must be resistant to sulfidation by the various sulfides formed in this electrode. Additionally, candidate materials are required to have an oxidation potential (the onset of rapid anodic dissolution in pure electrolyte) safely above the charge cut-off voltage.

Materials for FeS Electrodes

Accelerated corrosion tests conducted in mixtures of FeS and electrolyte have identified commercially pure metals (Ni, Nb, Mo), iron-base alloys, and nickel-base alloys that have acceptably low corrosion rates over the 400 to 500°C range.[9] Measurements made for most of these alloys also indicate that they have sufficiently noble oxidation potentials in LiCl-KCl eutectic electrolyte.[10,11] The presence of Li_2S in the electrolyte is known to dramatically lower the oxidation potentials of metals and alloys because metal sulfides can now form.[12,13] Fortunately, in an actual positive electrode, the formation of Li_2S always occurs in conjunction with fine iron particles, and the overwhelming surface area of these particles shields the hardware components from significant attack.

The majority of FeS-type cells have used AISI 1010 current collectors, in spite of the marginal compatibility.[14] This material is favored because the electrical resistivity (52 μΩ·cm at 450°C) is 50 to 70% lower than that of highly alloyed materials.[15] Post-test measurements made on collectors fabricated into a honeycomb structure determined that corrosion was nonuniform and greatest near the interface.[4] Initially, the corrosion was characterized by intergranular penetration and subsequent grain fallout. The initial penetration rate averaged 90 μm/yr per side, but declined with time. Perforation of the 125-μm honeycomb ribs of the current collectors began in

less than 225 days. After approximately 250 days, the corrosion rate declined to 5-10 μm/yr, and little additional intergranular corrosion occurred.

An electrode modification has been developed to suppress the initial stage of rapid corrosion.[16] Excess iron powder was added to the active material mix used to form the positive electrode. The optimum concentration, as determined by the accelerated corrosion tests shown in Fig. 2, is 30 mol %, provided the powder size is less than 150 μm. Small test cells with low-carbon-steel collectors and retainers were operated for two months to test this modification. The results showed a 70 to 75% reduction in corrosion with the excess iron powder addition.

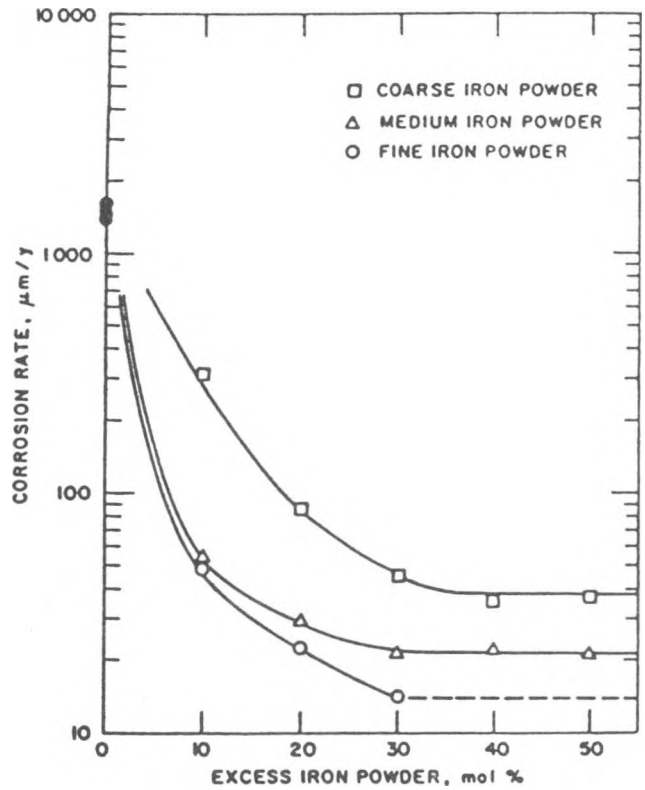

Fig. 2. Corrosion of Low-Carbon Steel Tested for 500 h at 450°C in a Mixture of FeS and LiCl-KCl Eutectic Modified with Different Concentrations of Iron Powder.

In engineering-scale cells, Type 304 stainless steel (in perforated sheet or woven-screen form) is commonly used for the FeS-electrode retainer. In addition to possessing the necessary corrosion resistance, stainless steel retainers, when properly welded, also have the mechanical strength required for this application. The need for mechanical strength should not be underestimated; extrusion of positive active material was a frequent cause of failure in early developmental cells.[4]

Nickel has also been used for positive electrode hardware. With an electrical resistivity of 38 μΩ·cm at 450°C, nickel offers a further improvement in conductivity for current collectors, but at this temperature nickel is relatively soft and not well suited for use as an electrode retainer. The in-cell corrosion resistance of this material can be highly dependent on the as-assembled state of charge.[17] Figure 3 contrasts the appearance of collectors from cells assembled in the fully charged (only FeS) and semicharged states. Negligible corrosion is typical for components from cells built in the fully charged condition. The major reaction is deposition of iron to a typical thickness of 4 to 6 μm. Intergranular corrosion occurs in cells assembled in the semicharged or uncharged condition if coarse (>100 μm) iron powder is used in the positive electrode mix.

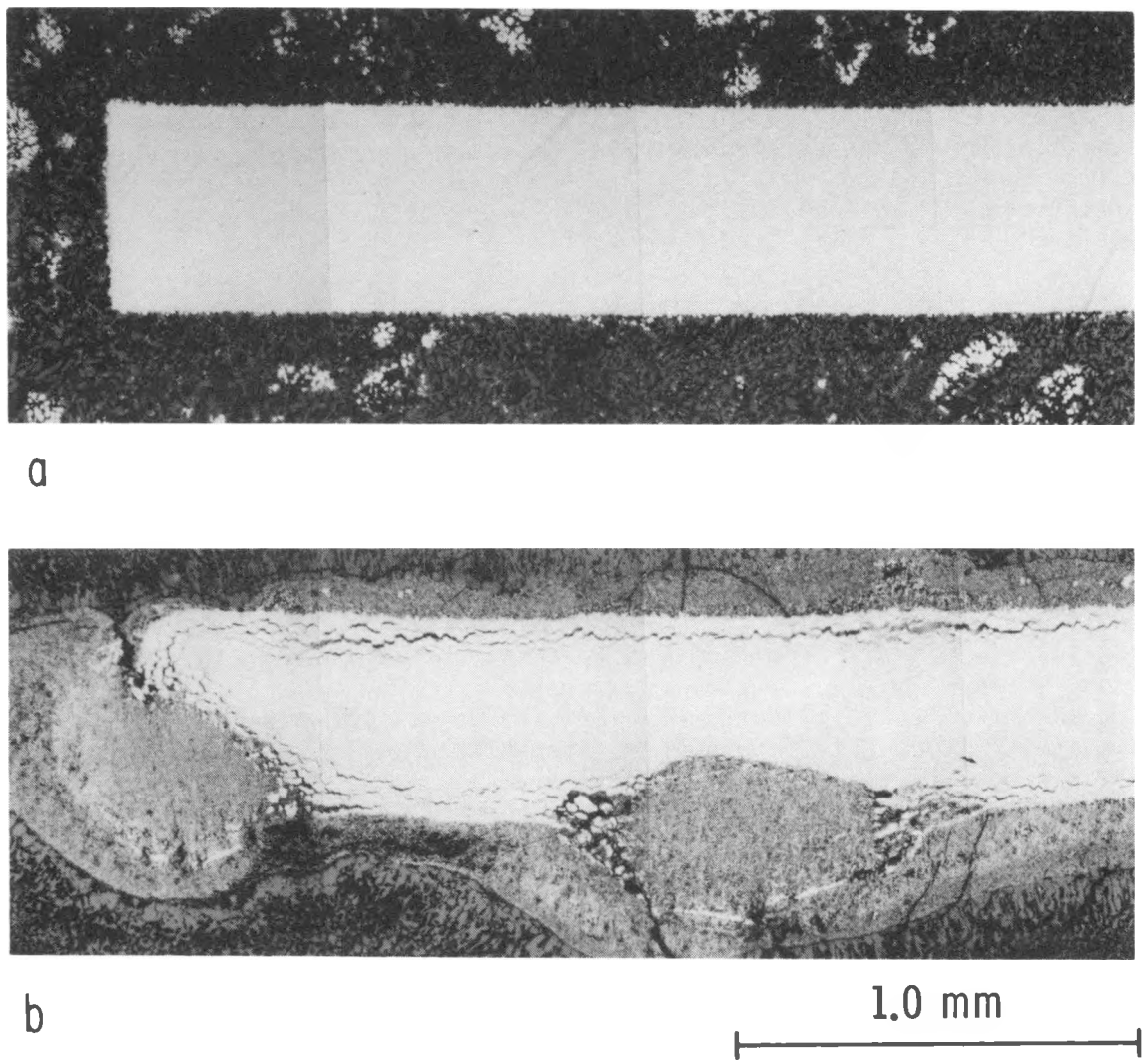

Fig. 3. Photomicrograph Composites of Two Nickel Current Collectors: (a) Fine Iron Particles Deposited on the Collector Surface from a Cell Built in the Charged State, (b) Intergranular Corrosion of a Collector from a Cell Built in the Semicharged State.

The intergranular attack occurs during the early charge cycles, when the nickel components serve as a partial substitute for the slowly reacting, large iron particles in the cell redox process. Fortunately, this detrimental reaction is avoided through the use of fine iron particles that more closely approximate the less than 5-μm diameter particles that normally form during discharge of an FeS electrode. The use of fine iron particles improves iron distribution within the electrode and greatly increases the surface area of iron.

Low-carbon-steel components plated with nickel offer a lower-cost, corrosion-resistant alternative to nickel. Both electroless and electroplated Ni coatings have been evaluated, and the latter technique was judged superior in providing substrate protection.[18] In-cell testing of electroplated components, however, did result in substrate attack.[19] For 25-μm coatings as much as 20% of the component surface, primarily the retainer framing, was pitted. Nickel-plated copper current collectors have also been tested as a means of further reducing internal cell resistance. One cell, which completed more than 500 cycles, indicated that this coating-substrate combination may prove satisfactory.[20]

Materials for FeS_2 Electrodes

The high sulfur activity of the FeS_2 electrode places more severe compatibility requirements on the hardware materials. In addition, the oxidation potential must be safely above the 2.0-V cutoff (vs. β-LiAl) typically used for these cells. The limited list of materials that have demonstrated acceptable compatibility in static immersion or in-cell tests is molybdenum, tungsten, carbon, and graphite.[14] However, component design is restricted by difficulties in fabrication and joining. Molybdenum has been used extensively in FeS_2-type cells and has shown excellent corrosion resistance. In-cell corrosion rates were found to be less than 4 μm/yr.[21] Some alloys, such as Hastelloy B (Ni-28Mo-5Fe-1Cr), could serve as a retainer material in low-temperature cells (~400°C), but show excessive corrosion at higher temperatures.[21] The high electrical resistivities of highly alloyed nickel-base alloys make them unattractive for use as current collectors.

Conductive ceramic coatings applied to low-carbon steel may prove to be a worthwhile alternative. Several metal borides, carbides, and nitrides have reasonable resistivities (10-100 μΩ·cm) and the technology for their application is well established.[22] Thermodynamic calculations indicate that TiB_2, TiN, TiC, TaC, and niobium carbides should be stable in the FeS_2 environment.[23,24] The oxidation potentials for TiN and TiC were also measured and found to be safely above the charge cutoff voltage.[23] Ceramic coatings were the subject of one extensive study[25] which determined that: (1) TiN and TiC are inherently stable in the FeS_2-type cell environment, (2) CVD coatings provide better protection of the substrate than rf-sputtered coatings, and (3) fractures in CVD coatings occurred at the sample edges because of the high residual stresses imparted to these coatings during the deposition process. Additional tests determined that current collectors fabricated from monolithic (hot-pressed) TiN and TiN-coated AISI 304 stainless steel were completely stable in test cells operated for 20 to 30 days.[25]

ELECTRODE SEPARATORS

The requirements for electrode separators include the following: compatibility with both the positive and negative electrodes, maintenance of electrical insulation between electrodes that are closely spaced together, high but uniform porosity, and good wettability by the electrolyte.

Candidate Ceramics

Compatibility with the β-LiAl electrode places severe restrictions on the selection of candidate ceramic materials. Among the nonradioactive and nonhygroscopic oxides, only MgO, Y_2O_3, CaO, and BeO have the required thermodynamic stability.[26] Similarly, the only nonconductive, commercially available nitrides that are more stable than LiN are AlN, BN, and Si_3N_4.[27] Boron nitride, however, can react to form lithium borides and Li_3N at potentials within 100 mV of liquid lithium,[28] and these potentials can be encountered with Li-Si electrodes. Because of the reduced activity of lithium in β-LiAl, other ceramics with marginal stability have been considered. However, ceramics such as $CaZrO_3$, $MgAl_2O_4$, or SiC-2AlN become electrically conductive, disintegrate, or fragment after test exposures.[21,29]

Impurities often reduce the corrosion resistance of a supposedly stable material. Weight losses for hot-pressed MgO samples are directly related to the concentration of SiO_2 present in the sample.[21] The preferential attack of impurities concentrated at the grain boundaries in Si_3N_4 bodies leads to intergranular cracking. Hot-pressed BeO has excellent long-term resistance to lithium attack, provided that the concentrations of both silicon and sulfur are kept below 30 ppm.[30] Beryllia, however, is toxic in its powdered form. While Y_2O_3 is compatible with lithium, use of this material in cells has been discontinued because yttria reacts with the positive electrode to form conductive Y_2O_2S.[31,32] For these reasons, the developmental effort has concentrated on the use of BN and MgO as separator materials. Different separator concepts have evolved because of the differences in the physical properties and available form (powder or fiber) of these two materials.

Boron-Nitride Felt Separators

Boron-nitride felts, prepared under a proprietary process by the Kennecott Copper Co., are formed by the conversion of spun B_2O_3 fibers through a high-temperature reaction with ammonia. Additional B_2O_3 fibers are mixed throughout the BN fibers prior to a second treatment at 1700°C in nitrogen that forms the BN bonds between the individual fibers. No more than 0.5 wt % B_2O_3 can remain after the conversion, or lithium reduction of B_2O_3 results in a conductive separator.[29] The typical diameter of a fiber is 6-8 μm, and the average size of the openings in the felt is 25 μm. The felt thickness can be varied from 1 to 3 mm. A typical 2-mm-thick felt averages 35 mg/cm^2 in basis weight, 4.5 kPa/mm in burst strength, and 92% in porosity.[33] Electrode expansion during cell operation compresses the felt to about one-half of its original thickness.

A major difficulty with the BN separator was its nonwettability by the electrolyte.[34] Several wetting treatments were developed to overcome this difficulty. The more successful treatments depend upon the incorporation of MgO within the felt. Both Gould Inc. and Eagle-Picher Industries, Inc. have

worked on a magnesium acetate wetting treatment.[35] The felt is immersed in an organic solution containing $Mg(C_2H_3O_2)_2$. A subsequent heating step evaporates the solvent and ultimately decomposes the acetate to form a thin coating of MgO on the BN fibers. This coating stiffens the separator and enhances its wettability. Eagle-Picher has since developed a similar treatment which uses magnesium nitrate as the wetting agent. The $Mg(NO_3)_2$ process takes less than half the time and produces a separator that is considered more uniform in its wettability.[36] Another wetting treatment involves the direct incorporation of fine MgO powder into the BN felt during its fabrication.[37] The BN fibers and MgO powder are slurried together in kerosene before the felt is laid down and the BN bonds are formed. Felts with 0.3 g of MgO per square centimeter of felt showed improved wetting characteristics in initial tests.

Powder Separators

For powder separators the other cell components confine a loose bed of insulating powder.[38] A wider selection of lower-cost candidate ceramics is feasible with this concept, since most thermodynamically stable ceramics are available in a suitable powdered form. Furthermore, the structural integrity of this type of separator cannot be compromised by impurities in an inherently stable material. The MgO powder used in the first cell to successfully demonstrate this concept had a purity of only 94%. Magnesia has been used extensively in cells built at ANL, Rockwell International, and Gould, but other ceramics have also been tested. At Rockwell International, AlN and Si_3N_4 powders have been used because these ceramics are stable when in contact with Li_xSi electrodes.[39]

Vibratory compaction and various pressing techniques are used to form powder separators. With vibratory compaction, screen retainers are used on the faces of both electrodes to maintain a uniform electrode-separator interface during cell assembly. For one pressing technique, the separator is formed by hot pressing a blended mix of powdered ceramic and electrolyte directly onto a prepressed positive electrode plaque. This method eliminates the positive electrode retainers in cell designs where interfacial current collection is not critical. Comparison tests of these two methods of fabrication showed that they have little, if any, effect on cell performance.[40] Gould has used cold pressing to fabricate rigid, free-standing separators out of powdered MgO and electrolyte mixtures.[41]

The thickness of powder separators is typically 2 to 3 mm, and the porosity ranges from 30 to 50%. The greater thickness and lower porosity in comparison to BN-felt separators result in higher internal resistances for cells with powder separators. Cell performance is diminished because of the lower porosity, especially at high current densities, as is illustrated in Fig. 4. The findings for the powder separator cells of Gould indicate that improvements in the current collection system minimize this problem.[41] Work on the optimum size distribution and volume fraction of powder in the separator is incomplete, but indicates that powder which is too coarse (+100 mesh) or too fine (-250 mesh) fails to maintain active material separation.[42] Mixtures of fine and coarse powders reduce this tendency but also substantially lessen separator porosity.

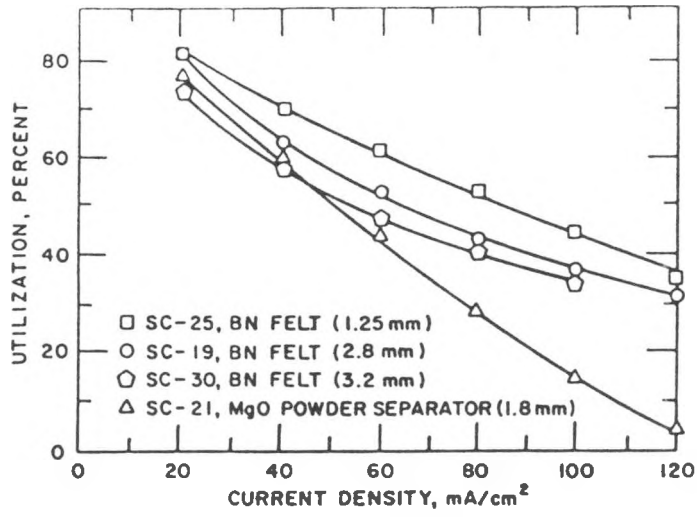

Fig. 4. Positive Electrode Utilization for Cells with BN Felt and MgO Powder Separators.

Porous-Plate Separators

Sintered ceramic plates have been tested as separator structures and found to facilitate cell assembly, maintain uniform spacing between electrodes, and minimize the movement of active materials into the separator region. Different ceramic powders have been fabricated into rigid separators, and these candidates have cost and/or wettability advantages over BN felt. Rockwell International has built cells with AlN and Si_3N_4 plates.[43] These separator plates are approximately 2 mm in thickness and range from 45 to 50% in porosity.

Alternative presintering procedures can increase the porosity of rigid separators. Much of this work was done with Y_2O_3 powder prior to the discovery of yttria's in-cell reaction. Ceramic foams were made from aqueous suspensions of an oxide powder, foaming agents, and organic binders. Cured Y_2O_3 foams have porosities of 63 to 90%, depending on the processing parameters.[44] In another technique, cast plasters are made by mixing an oxide powder into a dilute nitric acid solution. Yttria separators prepared in this manner range in porosity from 55 to 70%, depending on the sintering treatment.[45] The Y_2O_3-HNO_3 plaster technique produces stronger plates, which have more uniform pores of smaller diameter (<5 μm) than those produced by the foaming method. However, severe shrinkage during firing results in serious warpage. Acceptably strong and flat plates have been formed by crushing ceramic structures prepared by these two methods and then calcining the powder prior to sintering new plates.

Both Y_2O_3 and MgO separators formed by the calcination/sintering treatment have been used successfully in small test cells.[32] The MgO plates prepared in this manner are typically 40% porous, but porosities as high as 60% are believed to be achievable. Further optimization of strength, porosity, and pore size is required, and the fabrication of flat, full-sized separator structures remains to be demonstrated. Sintered separators possess two advantages over felt and powder separators: resistance to compressional

stresses that develop in a cell due to electrode expansion and excellent electrode particle retention because of the extremely small pore size.[46] A possible disadvantage of this concept is separator fractures caused by non-uniform electrode expansion and subsequent electrical shorting through these fractures.

ELECTRICAL FEEDTHROUGHS

The electrical feedthrough insulates the positive-electrode terminal rod from the cell can and completes the seal of the cell. This hardware component requires the use of compatible materials in leak-tight, lightweight, compact, and inexpensive designs. The feedthrough used in the construction of most cells relies on the mechanical compression of a powder to form the insulating seal. An alternative concept that depends on a metallurgical bond to form the seal has also been investigated.

Mechanical Feedthroughs

Mechanical feedthroughs, such as the one shown in Fig. 5, rely on the compaction of a layer of BN powder to form the seal. The compressive load is maintained by a number of methods, such as the engagement of a retainer ring in a groove in the feedthrough housing. Maximum leak-tightness in air is approximately 10^{-6} Pa·m^3/s and is achieved with a pressure of about 100,000 kPa. Secondary glass seals can be used to reduce the leak rate by an additional four orders of magnitude.[47] The BN powder is sandwiched between two insulators. Beryllia is used as the lower insulator because of its superior combination of corrosion resistance, thermal shock resistance, and mechanical strength. A copper-cored steel terminal can be used to lower the IR loss associated with this component. A further reduction in cell resistance is possible by enlarging the feedthrough to accommodate a larger terminal. However, there is concern that increasing the terminal diameter from the present 6.4 mm to 12.7 mm will reduce the reliability of the seal.[48]

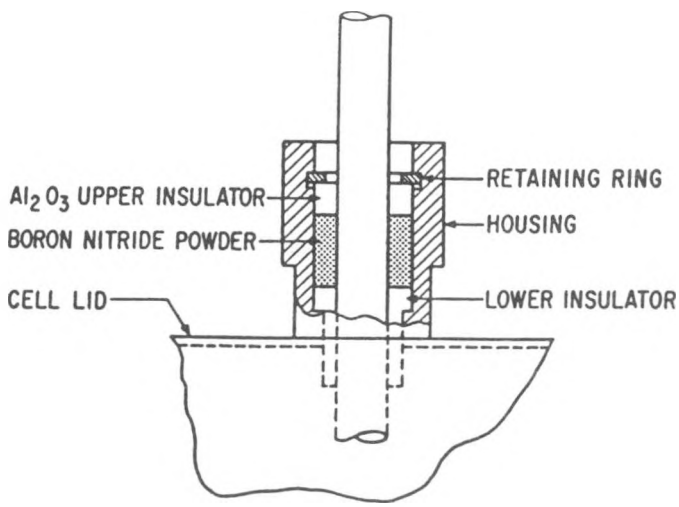

Fig. 5. Schematic of the ANL Mechanical Feedthrough

This feedthrough has generally proven effective when properly assembled, and variations of this design have been used in recent generations of engineering cells. The mechanical feedthrough is easy to assemble, more compact (<25 mm), and lighter in weight than earlier designs based on this concept.[49] Failures have occurred, however, when poor sealing allowed electrolyte penetration of the powder sealant to occur and established an electrochemical couple between the feedthrough housing and the positive terminal. The resultant anodic dissolution of the terminal rod and subsequent metallic deposition near the housing forms a metallic bridge across the insulator.[50]

Brazed Feedthroughs

A successful brazed feedthrough would allow the use of lightweight, inexpensive, stamped-metal parts instead of the machined parts used in the mechanical design. This cost advantage and the pretested hermetic seal are major advantages of the brazed feedthrough. The principal problem encountered with this type of feedthrough is that most brazes for metal-to-ceramic bonds have relatively low oxidation potentials. Brazed feedthroughs were tested by applying a constant potential across a sealed Li-Al/LiCl-KCl half cell. Failures due to the dissolution of the braze (or one of its constituents) and subsequent deposition as a metallic bridge occurred in comparatively short time periods when the applied potentials ranged from 1.8 to 2.0 V.[51] These results indicate that brazed feedthroughs are not suited for FeS_2-type cells; however, use in FeS-type cells should not be ruled out. Several braze compositions should have adequate resistance to dissolution at lower potentials. Among the more promising candidates are nickel-base brazes applied to BeO insulators and nickel terminals.

CONCLUSION

Advances in cell performance have often stemmed from design changes made possible by new materials for cell hardware. Materials studies have delineated the performance limits of commonly used materials for positive and negative hardware and have identified methods of extending the usable lifetime of low-carbon steel collectors for FeS and Li-alloy electrodes. Effective wetting treatments for BN felts have eliminated a serious drawback formerly associated with this separator. Commendable progress has also been made on lower-cost alternatives, such as the powder- and plate-type separators.

Two key components, however, would benefit from continued research. For FeS_2 electrodes, acceptable substitutes are needed to end the design limitations imposed by molybdenum current collectors. The development of effective ways to coat or clad molybdenum onto readily fabricable substrates is a possibility. Another approach is further development of corrosion-resistant collectors based on alternative materials, such as the conductive ceramics described earlier. The basic design of the mechanical feedthrough has undergone only relatively minor refinements over the last ten years. Effort directed towards its improvement or the development of the brazed feedthrough could produce substantial savings in cost and weight.

ACKNOWLEDGMENT

This work was supported by the U. S. Department of Energy, Office of Energy Storage, under Contract W-31-109-Eng-38.

REFERENCES

1. F. C. Mrazek and J. E. Battles, Simulated Cell Tests, Argonne National Laboratory Report ANL-8109, pp. 70-73 (January 1975).

2. F. C. Mrazek and J. E. Battles, Postoperative Cell Examinations, Argonne National Laboratory Report ANL-75-36, pp. 65-74 (March 1976).

3. K. M. Myles, F. C. Mrazek, J. A. Smaga, and J. L. Settle, Materials Development in the Lithium-Aluminum/Metal Sulfide Battery, Proc. of the Symp. and Workshop on Advanced Battery Research and Design, Argonne National Laboratory Report ANL-76-8, pp. B50-73 (1976).

4. J. E. Battles, F. C. Mrazek, and N. C. Otto, Post-Test Examinations of Li-Al/FeS_x Secondary Cells, Argonne National Laboratory Report ANL-80-130 (December 1980).

5. J. A. Smaga and J. E. Battles, Materials Research, Argonne National Laboratory Report ANL-83-62, p. 46 (September 1983).

6. J. A. Smaga, Current-Collector Coatings for Li-Al Electrodes, Argonne National Laboratory Report ANL-80-128, pp. 147-149 (February 1981).

7. J. A. Smaga and B. T. Warner, Current-Collector Coatings for Li-Al Electrodes, Argonne National Laboratory Report ANL-81-65, pp. 35-36 (February 1982).

8. Li-Si/FeS Cell and Battery Development--Atomics International, Argonne National Laboratory Report ANL-77-68, p. 54 (October 1977).

9. E. C. Gay et al., Li-Alloy/FeS Cell Design and Analysis Report, Argonne National Laboratory Report ANL-84-93 (July 1985).

10. J. A. Smaga, Current Collector Materials for FeS Electrodes, Argonne National Laboratory Report ANL-79-39, pp. 83-84 (May 1979).

11. J. A. Smaga et al., Oxidation Potentials of Alloys, Argonne National Laboratory Report ANL-78-94, pp. 140-141 (November 1978).

12. C. A. Melendres, C. C. Sy, and B. Tani, J. Electrochem. Soc. 124, 1060 (1977).

13. D. O. Raleigh, J. T. White, and C. A. Ogden, J. Electrochem. Soc. 126, 1093 (1979).

14. J. E. Battles, J. A. Smaga, and K. M. Myles, Metall. Trans. 9A, 183 (1978).

15. J. A. Smaga, Resistivity Measurements of Candidate Collector Materials, Argonne National Laboratory Report ANL-79-94, pp. 161-162 (March 1980).

16. J. A. Smaga and J. E. Battles, Electrode Modification for Corrosion Control in FeS Electrodes, Extended Abstracts, 163rd Electrochem. Soc. Meeting, San Francisco, CA, May 8-13, 1983, Vol. 83-1, p. 131 (1983).

17. J. A. Smaga and J. E. Battles, J. Electrochem. Soc. 129, 496 (1982).

18. J. A. Smaga and B. T. Warner, Characterization of Nickel-Coated Substrates, Argonne National Laboratory Report ANL-81-65, p. 30 (February 1982).

19. J. A. Smaga and B. T. Warner, In-Cell Testing, Argonne National Laboratory Report ANL-81-65, p. 34 (February 1982).

20. R. C. Saunders and L. R. McCoy, Electric-Vehicle Cells, Argonne National Laboratory Report ANL-79-94, pp. 51-52 (March 1980).

21. J. A. Smaga, F. C. Mrazek, K. M. Myles, and J. E. Battles, Materials Requirements in LiAl/LiCl-KCl/FeS_x Secondary Batteries, in Materials Considerations in Liquid Metals Systems in Power Generation, eds., N. J. Hoffman and G. A. Whitlow, NACE, Houston, TX, pp. 52-67 (1978).

22. J. L. Pentecost, High Temperature Inorganic Coatings, ed. J. Hamirik, Jr., Reinhold Publishing Corp., New York, NY, pp. 10-109 (1963).

23. N. Kuora, J. E. Kincinus, and N. P. Yao, J. Electrochem. Soc. Jpn. 46, 395 (1978).

24. T. D. Claar and J. T. Dusek, Ceramic Coatings for Positive Current Collectors, Argonne National Laboratory Report ANL-78-21, pp. 44-45 (March 1978).

25. G. Bandyopadhyay, J. Electrochem. Soc. 128, 2545 (1981).

26. J. E. Battles, Materials for High-Temperature Li-Al/FeS_x Secondary Batteries, in Critical Materials Problems in Energy Production, ed., C. Stein, Academic Press, New York, p. 769 (1976).

27. R. N. Singh, J. Am. Ceram. Soc. 59, 112 (1976).

28. R. A. Sharma and T. G. Bradley, J. Electrochem. Soc. 128, 1835 (1981).

29. J. E. Battles, F. C. Mrazek, W. D. Tuohig, and K. M. Myles, Materials Corrosion in Molten-Salt Lithium/Sulfur Cells, in Corrosion Problems in Energy Conversion and Generation, ed., C. S. Tedmon, Jr., The Electrochem. Soc., Princeton, NJ, pp. 20-30 (1974).

30. J. A. Smaga, Corrosion Rates of Candidate Ceramics for Cell Components, Argonne National Laboratory Report ANL-79-94, p. 158 (March 1980).

31. F. C. Mrazek, N. C. Otto, and J. E. Battles, Formation of Y_2O_2S in Y_2O_3 Separators, Argonne National Laboratory Report ANL-78-21, p. 49 (March 1978).

32. C. Bandyopadhyay, J. T. Dusek, and T. M. Galvin, Ceramurgia Int. 5, 95 (1979).

33. R. B. Swaroop and J. E. Battles, J. Electrochem. Soc. 128, 1873 (1981).

34. J. G. Eberhart, The Wetting Behavior of Molten-Chloride Electrolytes: Capillary Effects in Lithium-Aluminum/Metal Sulfide Batteries, Argonne National Laboratory Report ANL-79-34 (1979).

35. J. Buchanan et al. (p. 32) and B. A. Askew (pp. 42-44), Separator Development, Argonne National Laboratory Report ANL-80-128 (February 1981).

36. Eagle-Picher Industries, Inc., Separator Investigation, Argonne National Laboratory Report ANL-81-65, pp. 68-69 (February 1982).

37. S. Sudar, L. R. McCoy, and R. C. Saunders, Evaluation of BN-Felt Separators, Argonne National Laboratory Report ANL-80-128, pp. 180-185 (February 1981).

38. J. P. Mathers, C. W. Boquist, and T. W. Olszanski, J. Electrochem. Soc. 125, 1913 (1978).

39. H. M. Lee, Ceramic Separator Development, Argonne National Laboratory Report ANL-78-94, pp. 68-72 (November 1978).

40. T. W. Olszanski and G. B. Tuson, Development of Powder Separators, Argonne National Laboratory Report ANL-78-94, pp. 134-137 (November 1978).

41. Gould Inc., Engineering Cell Development, Argonne National Laboratory Report ANL-81-65, pp. 77-83 (February 1982).

42. S. Sudar, L. R. McCoy, and R. C. Saunders, Evaluation of MgO Powder Separators, Argonne National Laboratory Report ANL-80-128, pp. 185-190 (February 1981).

43. Li-Si/FeS Cell and Battery Development--Atomics International, Argonne National Laboratory Report ANL-77-17, p. 55 (April 1977).

44. W. D. Tuohig and J. T. Dusek, Ceramic Materials Development, Argonne National Laboratory Report ANL-77-17, pp. 34-37 (April 1977).

45. T. D. Claar and J. T. Dusek, Porous, Rigid Separators, Argonne National Laboratory Report ANL-78-21, pp. 43-44 (March 1978).

46. G. Bandyopadhyay, R. B. Swaroop, and J. E. Battles, J. Electrochem. Soc. 129, 2187 (1982).

47. K. M. Myles and J. L. Settle, Electrical Feedthrough Development, Argonne National Laboratory Report ANL-77-17, pp. 32-33 (April 1977).

48. Eagle-Picher Industries, Inc., Feedthrough (Terminal Seals) Experimentation, Argonne National Laboratory Report ANL-81-65, pp. 70-71 (February 1982).

49. K. M. Myles and J. L. Settle, Electrical Feedthrough, Argonne National Laboratory Report ANL-77-75, pp. 32-33 (January 1976).

50. F. C. Mrazek and N. C. Otto, Multiplate Cells, Argonne National Laboratory Report ANL-79-94, pp. 101-102 (March 1980).

51. K. M. Myles and J. L. Settle, Electrical Feedthrough Development, Argonne National Laboratory Report ANL-76-35, p. 17 (May 1976).

STATUS OF LiAl/FeS CELLS BASED ON BN SEPARATORS

S. Das Gupta, D. Ghosh, J.K. Jacobs and M. Machler

The Electrofuel Manufacturing Company
9 Hanna Avenue, Toronto, Ont. M6K 1W8 Canada.

ABSTRACT

For the last three years an engineering development program has been carried out on the LiAl/FeS cells. At the start of the development program it was decided that a low cost process was necessary for producing good quality Boron Nitride fibres. A research and development program was launched and good quality BN fibres and felts are now commercially available from Electrofuel. The BN fibres are about 4 microns in diameter and are available as tows or felts. The engineering development program for the LiAl/FeS cells has concentrated in attempting to make reliable cells which can be manufactured through standard production practices. Hence attempts have been made to use non exotic materials, duplicate large scale production methodology and give low priority to cell performance. It was felt that the performance potential of the technology was well established and needed no further demonstration. As a result of this development work it appears that the manufacture of the LiAl/FeS cells can be both technically feasible and cost effective. Presently a battery development program has been initiated.

INTRODUCTION

Secondary batteries with high specific power and high specific energy have been under development over the last few decades. The LiAl/FeS system appears to be a potential candidate for such a battery. The work at Argonne National Laboratory has demonstrated the major attractions of the system. It is safe, robust, can undergo any number of thermal cycles, has excellent volumetric energy density and high specific power. All components of the system are essentially low cost items and it was felt that they were amenable to standard production methodology. Hence an engineering development program was started on the system about three years ago.

SEPARATOR

The separator in a LiAl/FeS cell has been a continual stumbling block in the design of reliable and cost effective cells. While in many other batteries the cell lifetime and performance is determined by electrode deterioration, the life and performance of a LiAl/FeS cell seems invariably to be related to separator deficiencies. Even where failure results from electrode morphological irregularities, these seem to have separator deficiencies as their root cause. Recent data suggest that with negative electrode protrusion through the separator prevented and positive electrode extrusion

eliminated, cells will consistently last for 1000 cycles. The data from ANL work had suggested that better performance and lifetime was expected from separators using Boron Nitride felts. The Carborundum process was expensive and it was decided at the start of the program that a development program was necessary to produce a low cost acceptable Boron Nitride based separator. A three year research program was initiated and presently Electrofuel can supply commercially BN fibres and felts for battery and any other potential application.

Figure 1 shows the X-ray data of the fibres produced at Electrofuel. The fibres are turbostratic as compared to the hexagonal BN formed at very high temperatures. Figure 2 shows a SEM microphotograph of a BN felt. It was realised that the wettability of the BN separators was a major consideration for the cells and attempts were made to change the fibre diameter to improve wettability. Fibre diameter of 10, 7, 4 and 2 microns were produced. Above 7 microns the fibres were rather brittle and difficult to handle. Below 4 microns the fibres are more difficult to wet. The surface properties of the fibres can be changed by etching, similar to the carbon fibre technology. For good wettability the fibres are coated with MgO. Coating load depends on fibre diameter for the same basis weight. Various coating loads from 4 to 20 mg/cm^2 was used. For 4 micron fibre, good wetting by the LiCl/KCl electrolyte was found with 10 mg/cm^2 of MgO loading. Etching of the fibres substantially improved the adhesion characteristics of the coating. The compressive strength of the felt without the MgO coating was about 78 psi, while with the MgO loading it decreased to about 70 psi, well above the design requirement of 60 psi.

Along with the BN separator, there was a requirement for high strength BN solids for certain insulation requirement inside the cell. The BN solids from both standard commercial sources had good room temperature strength (15,000 psi) but at high temperatures the strength dropped dramatically to about 2,500 psi. It was assumed that this was due to the solids being bonded by the boric oxide. BN being a very covalent compound, is difficult to diffusion bond, as the diffusion rate at even $2000^{o}C$ is extremely slow. A new grade of BN solid was produced at Electrofuel which has a room temperature flexural strength of 6,000 psi but which increases with temperature such that at $800^{o}C$ it is 9,000 psi. This BN material is now being utilised inside the cell as a insulator.

ELECTRODES

The electrode materials in both the positive and the negative are essentially the same composition as optimised by previous work at ANL and elsewhere. The major effort at Electrofuel was to carryout production methodology experimentation. For that objective attempts were made to produce electrodes through an injection molding process using elevated temperatures and electrolyte mixed with the electroactive species. Because the major fraction of cell resistance is in the positive electrode, the design of the electrode

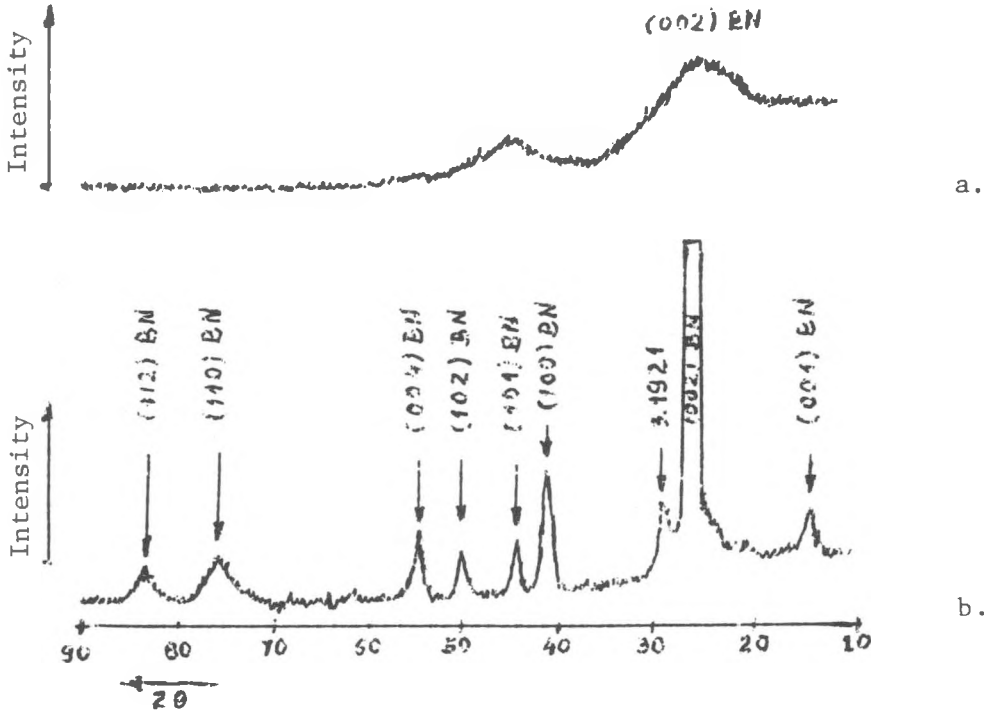

Fig.1 X-ray diffraction pattern for: a. BN fibres b. hot-pressed BN

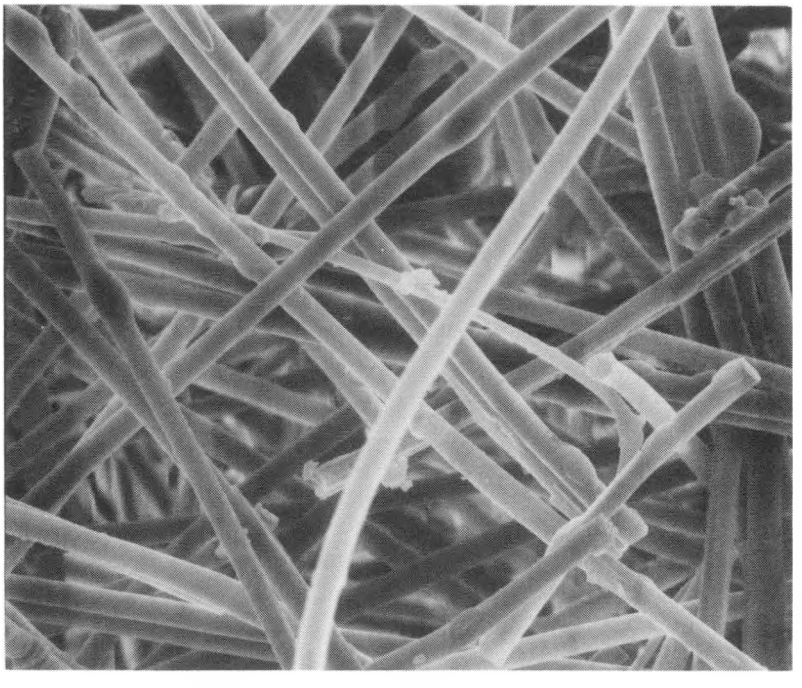

Fig.2 SEM microphotograph of BN felt

including the current collector and the centre post was substantially changed. Use was made of low cost pressed metal internal structures to provide increased reliability at lower cost. The design of cell internal structures was somewhat modified such that the dimensional stability of the electrodes were improved. The objective was to produce cells where the expansion of one cell will not affect adjacent cells in a battery.

ELECTROLYTE

All cells produced by Electrofuel utilised low cost technical grade salt as the electrolyte. The electrolyte in the cells were lithium rich mixture of LiCl/KCl. A method was devised where the technical grade salts could be utilised. This was important as an engineering objective as the cost of the technical grade was approximately 1% of the laboratory grade salts. To date we have had no problems using this grade of electrolyte and no failures were noticed which could be attributed to electrolyte problems.

PERFORMANCE

The cell cycling system at Electrofuel is rather rudimentary and no attempts were made to demonstrate performance such as power density with depth of discharge. It was felt that the performance characteristics of the LiAl/FeS technology has been well demonstrated and one can predict the performance such as power densities relatively accurately from considerations such as electrode bed thickness, separator resistance, packing densities and overall resistance calculations of cell components. Hence no attempts were made to develop a sophisticated cell cycling system. From the cell design it is expected that the cell performance should be similar to the Meradcom cells produced by Eagle-Picher or a slight improvement. The cell cycling at Electrofuel was carried out to provide lifetime data as well as quick and dirty design data for certain of the cell component changes. The latter included ratio of electroactive species, different utilization rates, varying separator thickness etc. Cells were made with energy densities from 75 to 105 watt hr./kgm. A semi-bipolar design was developed which is expected to be the building block for the batteries. The module has a voltage of 2.6 volts and nominal 300 amp.hr. capacity. The semi-bipolar module is expected to be self containing with respect to mechanical stability and electrolyte leakages. The volume of that module is 3.2 litres and weight being about 6.5 kgms. At 80% utilisation, this approximates to 96 watthr./kgm and 200 watt.hr/litre. Further testing of this module is expected to be carried out late in 1986.

Presently a battery development program has been initiated at Electrofuel and work has started on general design, thermal management, cell and module interactions. The aim is to produce batteries of good reliability and cost and it is not the objective to produce maximum performance this technology has the capability to produce. The objective is to get into early commercialisation with high value applications.

ACKNOWLEDGMENTS

The authors wish to acknowledge the financial support from the National Research Council of Canada and the Department of Energy, Mines and Resources.

REFERENCE-ELECTRODE SYSTEMS AND THEIR APPLICATION IN Li/MS_x BATTERY RESEARCH

Laszlo Redey
Argonne National Laboratory
9700 S. Cass Ave.
Argonne, IL 60439

ABSTRACT

Three reference electrode systems, $Li\text{-}Al|Li^+$, $Ni|Ni_3S_2|S^{2-}$, and $Ag|Ag^+$, are described briefly and evaluated on the basis of experience gained during about 200,000 test hours. The $Li\text{-}Al|Li^+$ system has been selected as the primary standard because of the convenience of in situ calibration and the availability of a technique that unmistakably manifests the standard condition of the electrode. The $Ni|Ni_3S_2$ reference electrode is extremely stable, with slow potential shift of no more than $\pm$2-3 mV during thousands of hours of operation. The short-range stability (less than 100 hours) is $\pm$0.1 mV. Advantages of the $Ag|Ag^+$ membrane electrode system are the perfect chemical isolation from the rest of the cell and the possibility of miniaturization by means of 0.5- to 1.0-mm-OD Pyrex capillaries.

INTRODUCTION

Three reference electrode systems, $Li\text{-}Al|Li^+$, $Ni|Ni_3S_2|S^{2-}$, and $Ag|Ag^+$, are being used for various types of investigations being done on the Li/MS_x cells and electrodes at Argonne National Laboratory (ANL). The $Li\text{-}Al|Li^+$ system has been selected as the primary standard because of the convenience of in situ calibration and the availability of a technique that unmistakably manifests the standard condition of the electrode.

On the basis of experience gained during about 200,000 test hours, these reference electrode systems can be reliably evaluated. Our reliability criteria include, in addition to $\pm$3-mV reproducibility and precision, the long-range stability of the reference potential over several thousands of hours. Each of the electrode systems has certain advantages (as well as disadvantages) in any of the routine investigation techniques requiring reference electrodes. Investigations performed at ANL include measurements of energy and power performance of model electrodes (0.1- to 2-Ah capacity) and compact engineering cells (10- to 350-Ah capacity), study of electrochemically induced phase changes, and resistance and impedance measurements on high-performance electrodes and other cell components.

Li-Al PRIMARY STANDARD REFERENCE ELECTRODE SYSTEM

Of the alloy phases that constitute the Li-Al phase diagram [1] (Fig. 1), the α-Al and the β-LiAl phases are the most important for reference electrode construction. There is a wide composition range of the alloy,

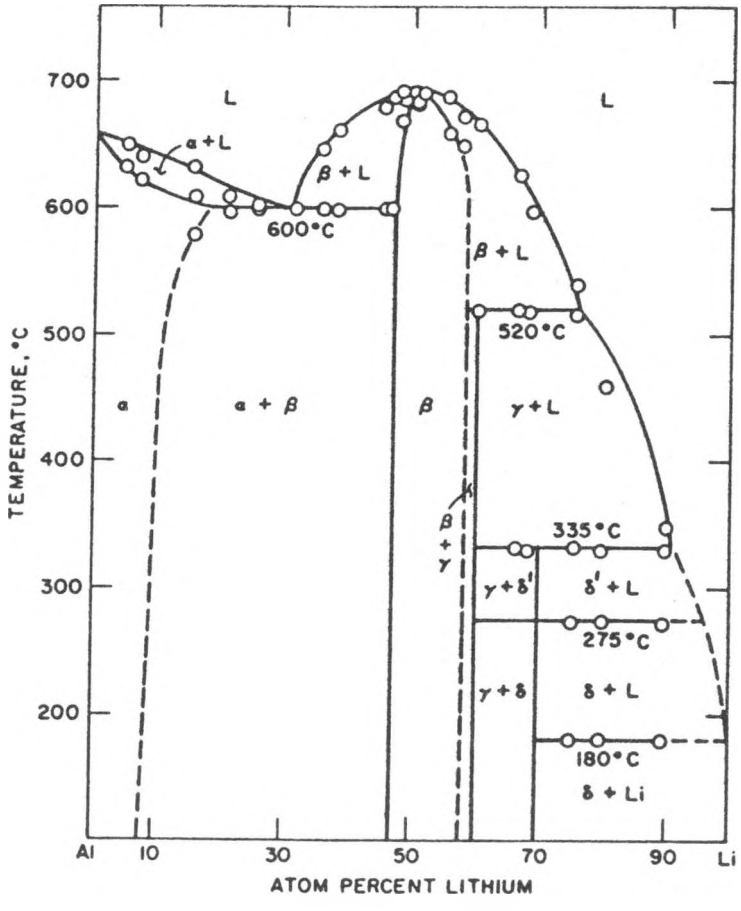

Fig. 1. Phase Diagram of the Lithium-Aluminum System [1].

between approximately 8 and 48 at. % Li content, in which these two phases coexist, and the alloy shows constant, stable electrode potential in Li^+-ion containing electrolytes. The alloy in this composition range is designated for reference electrode applications as "Li-Al."

The potential of the Li-Al electrode has been related to a lithium electrode in several studies using the cell

$$Li \,|\, Li^+\text{-ion-containing electrolyte} \,|\, Li\text{-}Al \qquad \text{Cell 1}$$

This cell measures the Li activity in the alloy ($a_{Li\ alloy}$) relative to that of the pure lithium (a_{Li}), but is practically independent of the Li^+-ion activity of the electrolyte melt (Eq. 1). The emf for this cell is represented by

$$E = -\frac{RT}{F} \ln a_{(Li\ alloy)} \qquad \text{Eq. 1}$$

However, the lithium electrode cannot serve as a thermodynamic standard reference system. The lithium electrode in a cell is not in thermodynamic equilibrium because of the displacement reaction with other cations, e.g., with K^+ ion in a LiCl-KCl electrolyte:

$$Li_{(dissolved)} + KCl \leftrightarrows K_{(vapor)} + LiCl \qquad \text{Eq. 2}$$

and because of the relatively high solubility of the lithium metal in the molten electrolyte.

These effects explain the observed emf instability in Cell 1 and the differences between the Li-Al electrode potential values reported by different authors. The displacement reaction between Li and K (Eq. 2) produces a non-negligible concentration of potassium metal in the melt and results in an appreciable partial pressure of potassium at the melt temperatures [2] (0.95 mbar at 450°C in equilibrium with lithium). Consequently, the displacement reaction can proceed to a considerable extent and create unstable conditions on the electrode surface in an open cell; it also tends to decrease the KCl content of the electrolyte in the long run. In an all-Li^+-cation electrolyte, the displacement reaction is not relevant, but the lithium solubility and the resulting significant electronic conductivity of the electrolyte [3] cause problems.

An acceptable reference electrode must minimize the effects of the displacement reaction and lithium dissolution in the electrolyte, as well as those of the electronic conductivity. These effects become less important when the activity of lithium is decreased by alloying with aluminum. In the γ-phase region, only ± 2 mV instability has been observed [4]. At even lower lithium activity, such as that of the α-Al + β-LiAl two-phase alloy ($a_{Li} = 0.007$ at 427°C), the potential of the alloy electrode is very stable. The Li-Al electrode may be considered in quasi-thermodynamic equilibrium with the electrolyte.

The Li-Al reference-electrode system is defined by the electrode diagram:

$$(Mo)Li\text{-}Al \,|\, Li^+$$

where (Mo) is an electrochemically inert voltage lead. A 20 to 40 at. % Li content in the Li-Al alloy is a safe working range within the α-Al + β-LiAl two-phase region of 8 to 48 at. % Li composition. The standard state of the reference electrode is defined by this two-phase composition. Standard conditions of the temperature and electrolyte composition are optional as long as they are precisely defined and the lithium-salt content is more than 5 mol % and there are no cations present that could significantly alloy the Li-Al as a result of displacement reactions with lithium. They are selected according to the needs of the particular investigation.

The standard state of the electrode can be produced easily and reproducibly by electrochemical means in situ by intermittent charging of Li into an Al wire [5]. Figure 2-A shows the potential variation of an aluminum wire charged with lithium intermittently with a constant current density of approximately 0.5-5 mA/cm^2. Duration of the current-interruption period is

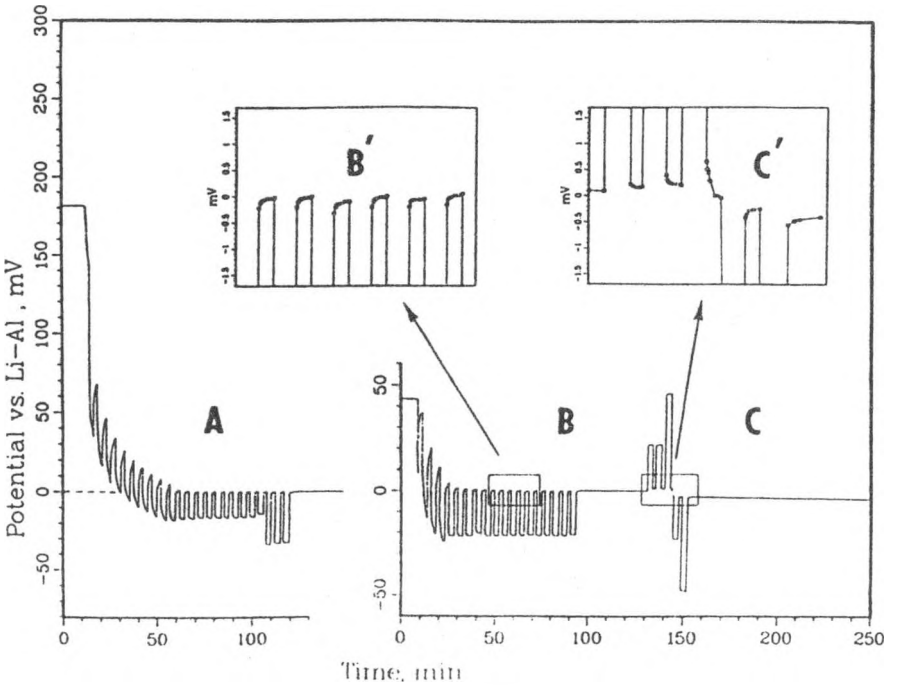

Fig. 2. Intermittent Coulometric Titration Curve of Li-Al Formation as Recorded on an Analog Chart Recorder.

constant within the course of this intermittent coulometric titration and is usually between one and three minutes. After current interruption, the potential relaxes toward a steady value, which is determined by the alloy composition. The envelope curve that connects the open-circuit potentials recorded just prior to the next charging period shows a characteristic shape. The long plateau of the envelope curve (shown in the figure by a broken line, which is an extrapolation of the actually measured plateau values to the horizontal axis of the diagram) indicates that the standard alloy composition is present. This phenomenon has a great practical importance; the standard state of the reference electrode is apparent and does not require knowledge of the concentration of the electroactive species, as is the case for the silver reference electrode. The standard state condition and, consequently, the standard potential can be reproduced within at least ±1 mV precision under most experimental circumstances going from either the undercharged or the overcharged condition of the Li-Al alloy. Furthermore, an aged reference electrode, which has been gradually exhausted by the measuring current or other effects and has higher potential than the standard, can be reconditioned in situ in the test cell by this technique (Fig. 2-B). Any other electrode of the test cell that has a stable potential during the procedure and is not influenced by the titrating current can serve as a counter electrode for the conditioning of the reference electrode. A reversibility test of the reference electrode (e.g., a micro-polarization test) is a part of the technique (Fig. 2-C). Because of the reliability of this technique, the Li-Al reference electrode can be used as a "primary" standard for calibration of other reference electrodes in molten lithium-halogenide electrolyte systems. The high potential excursions observed during the

application of 100- and 200-μA cathodic or anodic currents, as seen on Fig. 2-C, are caused by the high resistance of the diffusion barrier that was used in the construction of the tested Li-Al reference electrode. Because of the fast electrode kinetics [6], the polarization resistance of the Li-Al electrode is low. Reproducibility of the electrode is ±1 mV. Its stability over several days in Li-sink type environments (e.g., in metal-sulfide electrode testing) is not very good, but the electrochemical reconditioning technique is available.

Construction of the Li-Al reference electrode is similar to the Ni/Ni_3S_2 electrode described in the next section.

$Ni|Ni_3S_2$ REFERENCE ELECTRODE

The $Ni|Ni_3S_2$ reference electrode is based on the equilibrium

$$3\ Ni + 2\ S^{2-} \leftrightarrows Ni_3S_2 + 4\ e^- \qquad \text{Eq. 3}$$

The reversible properties of the electrode were first attributed to the Ni|NiS couple [7]. Later, however, X-ray diffraction examinations revealed [8] that Ni_3S_2 is the first stable phase formed during anodic sulfidization of the nickel electrode in Li_2S-containing LiCl-KCl electrolytes. The $Ni|Ni_3S_2$ electrode can serve as an excellent reference electrode.

The electrochemical properties of the $Ni|Ni_3S_2$ electrode were investigated in a Li_2S formation cell [5], which utilized the overall cell reaction

$$4LiAl + Ni_3S_2 = 2Li_2S + 3Ni + 4Al \qquad \text{Eq. 4}$$

The cell was constructed as shown in the following cell diagram:

$$\underset{T_1\ T_2}{Cu|Ni}|Li\text{-}Al|LiCl,KCl,Li_2S_{(s)}|Ni_3S_2|\underset{T_2\ T_1}{Ni|Cu} \qquad \text{Cell 2}$$

where T_1 is the temperature of instrumentation, and T_2 is that of the cell. According to the primary standard concept, the potential of the Li-Al electrode is defined as zero at any temperature in order that this alloy serve as a thermodynamic reference state in any chemically compatible electrolyte. Equation 5 describes the emf of Cell 2 and the potential of the Li_2S-saturated $Ni|Ni_3S_2$ reference electrode on the Li-Al potential scale in millivolts as a function of temperature:

$$E = 1369.7 + 0.097(T - 450), \qquad T \text{ in } °C \qquad \text{Eq. 5}$$

Thermal cycling between 360 and 500°C caused no hysteresis and indicated excellent reproducibility. In other than eutectic compositions of the LiCl-KCl mixture and in an LiF-LiCl-LiBr (22-31-47 mol%) electrolyte, the same emf values and temperature coefficients have been observed [8].

The Nernstian response of the emf of the Li_2S concentration cell

$$Ni|Ni_3S_2|LiCl,KCl,Li_2S_{(s)} \quad LiCl,KCl,Li_2S_{(N)}|Ni_3S_2|Ni \qquad \text{Cell 3}$$

showed that the $Ni|Ni_3S_2$ electrode acts as an electrode of the second kind in responding to the S^{2-} ion fraction (N) of the electrolyte [9]. The low solubility of the Li_2S in the tested electrolytes ensures constant S^{2-} ion fraction at a constant temperature when solid Li_2S is present. Solubilities of Li_2S in several molten electrolytes have been measured [10] and found to be in agreement with the calculated values [11]; solubility is in the range of 500 to 8000 ppm, depending on the temperature and composition of the electrolyte. Adjustment of the Li_2S saturation to a new temperature is reasonably fast. The very low Ni^{2+}-ion activity in Li_2S-saturated electrolytes ($\sim 10^{-12}$) emphasizes the merits of this reference electrode of the second kind.

Figure 3 depicts typical construction of the Li_2S-saturated $Ni|Ni_3S_2$ reference electrode [12]. This electrode utilizes a high-density alumina

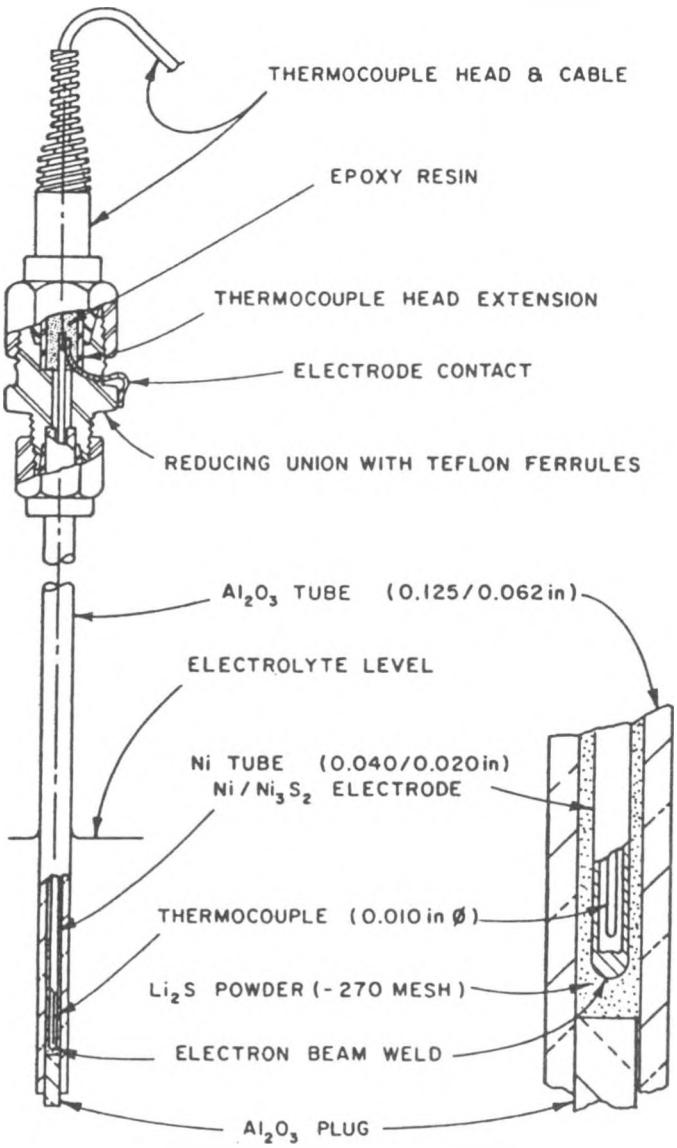

Fig. 3. Design Details of a Li_2S-Saturated $Ni|Ni_3S_2$ Reference Electrode.

tube (3.2-mm OD, 1.6-mm ID) of the required length (long enough that the upper end is at room temperature) and a Ni tube with its lower end closed by electron-beam welding. This nickel tube serves as sheathing for a 0.25-mm OD chromel-alumel thermocouple and, at the same time, as the base metal for anodic formation of Ni_3S_2. The diffusion barrier is made by inserting a 10- to 15-mm-long solid piece of alumina rod into the alumina tube. End sections of both the rod and the tube are polished to make a near perfect fit. Friction holds this plug in place, and the narrow gap between the two pieces forms a fine capillary that creates an excellent liquid junction with high resistance and thus a very low diffusion rate. The resistance of the diffusion barrier is adjustable between 0.2 and 5 kohm. The electrodes are assembled "dry" in a high-purity helium-atmosphere glove box and are activated by allowing molten electrolyte to penetrate through the diffusion barrier. Because of the small masses of its active components and housing, the device responds rapidly to temperature changes. A typical response time for 90% of the total temperature change (starting from electrode temperatures below the melting point of the electrolyte) is 12 s; the potential approaches the final mean value to within 1 mV in 50 s.

The $Ni|Ni_3S_2$ reference electrode is extremely stable, with a very slow potential shift or variation of $\leq$ 2-3 mV during thousands of hours of operation. The short-range stability (<100 h) is $\pm$0.1 mV. Reproducibility of the potential is better than $\pm$1 mV. Both the chemical and the constructional stability of the electrode are excellent. The construction of the electrode is insensitive to freeze-thaw cycles.

$Ag|Ag^+$ MEMBRANE REFERENCE ELECTRODE

Of the two basic types (liquid-junction and membrane-junction construction) of the $Ag|Ag^+$ reference electrodes, only the membrane-junction construction is acceptable for cell/electrode testing. This type prevents a change of the concentration of the silver salt and silver precipitation on the test electrode. The electrode consists of a silver wire (99.99% or higher purity) dipped into the reference electrolyte. This latter is a solution of a precisely known AgCl concentration; usually a mole fraction of 10^{-3} to 6×10^{-2} N AgCl in LiCl-KCl eutectic is applied. Because of the high solubility of silver chloride in molten alkali halides, the silver|silver chloride electrode is a reference electrode of the first kind in these melts. The reference electrolyte and the silver wire are placed within a closed-end Pyrex capillary. The electrochemistry of this reference electrode works similarly to the one described in Ref. 13.

The emf of the $Ag|Ag^+$ electrode versus the Li-Al reference electrode as a function of temperature is shown in Fig. 4. Measured by comparing identically prepared electrodes, the potential has a reproducibility of $\pm$10 mV. Potential variation of an $Ag|Ag^+$ electrode is not more than $\pm$1 mV during a few hours of operation; after this period a gradual potential shift occurs, caused supposedly by glass degradation. Also, the mechanical stability of the reference electrode is not very good; thin capillaries are sensitive to mechanical stress and break easily.

Important advantages of the silver-membrane electrode system are the perfect chemical isolation from the rest of the test cell and the possibility of miniaturization by means of 0.5- to 1.0-mm-OD Pyrex capillaries.

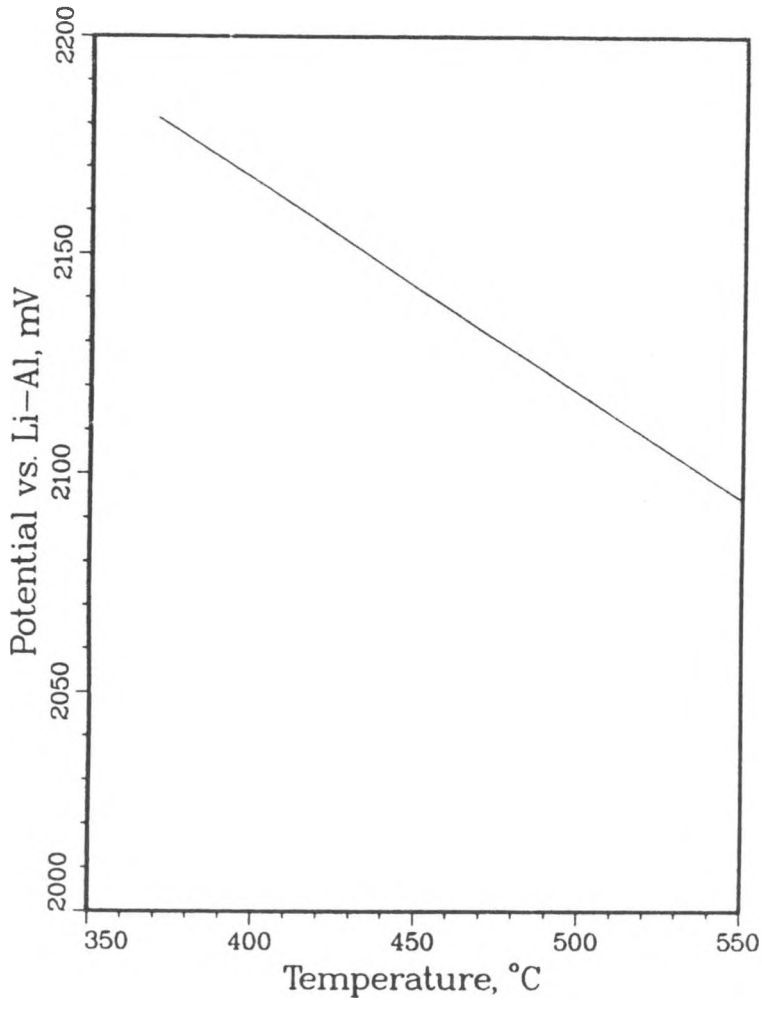

Fig. 4. Potential of a $Ag|Ag^+$ Pyrex-Membrane Electrode vs. Li-Al Reference Electrode. Electrolyte: AgCl (0.0055 Mole Fraction) in LiCl-KCl Eutectic.

ACKNOWLEDGMENT

This work was supported by the U. S. Department of Energy, Office of Energy Storage under Contract W-31-109-Eng-38.

REFERENCES

1. K. M. Myles, F. C. Mrazek, J. A. Smaga, and J. L. Settle, in Proc. of Symp. and Workshop on Adv. Battery R&D, March 1976, U. S. ERDA Report No. ANL-76-8, p. B-50.

2. R. N. Seefurth and R. A. Sharma, J. Electrochem. Soc., 122, 1049 (1975).

3. G. J. Reynolds, M. C. Y. Lee, and R. A. Huggin, in Proc. of 4th International Symp. on Molten Salts, Vol. 84-2, Eds. M. Blander et al., The Electrochem. Soc., Pennington, NJ (1984) p. 519.

4. J. R. Selman, D. K. DeNuccio, C. Sy, and R. K. Steunenberg, Electrochem. Soc., 124, 1160 (1977).

5. L. Redey and D. R. Vissers, J. Electrochem. Soc., 128, 2703 (1981)

6. C. A. Melendres, J. Electrochem. Soc., 124, 650 (1977).

7. C. H. Liu, A. J. Zielen, and D. M. Gruen, J. Electrochem. Soc., 120, 67 (1973).

8. Z. Tomczuk, L. Redey, and D. R. Vissers, J. Electrochem. Soc., 130, 1074 (1983).

9. L. Redey and D. R. Vissers, Extended Abstracts, Meeting of The Electrochem. Soc., Denver, CO, Vol. 81-2, The Electrochem. Soc., Pennington, NJ (1981) p. 1412.

10. D. Warin, Z. Tomczuk, and D. R. Vissers, J. Electrochem. Soc., 130, 64 (1983).

11. Z. Tomczuk, D. R. Vissers, and M-L. Saboungi, in Proc. of 4th International Symp. on Molten Salts, Vol. 84-2, Eds., M. Blander et al., The Electrochem. Soc., Pennington, NJ (1984) p. 352.

12. L. Redey and D. R. Vissers, J. Electrochem. Soc., 130, 231 (1983).

13. J. O'M. Bockris, G. J. Hills, D. Inman and L. Young, J. Sci. Instrum., 33, 438 (1956).

DEVELOPMENT OF THE LITHIUM-LIMITED FeS CELL

Thomas D. Kaun
Argonne National Laboratory
9700 S. Cass Avenue
Argonne, IL 60439

ABSTRACT

The lithium-limited FeS cell (having excess FeS electrode capacity) was the culmination of insights into the operation of Li-Al electrodes and into the performance limitations of the Li-Al/FeS couple. This paper will review the development of this molten-electrolyte cell (54 wt % LiCl-KCl at 450-470°C).

Earlier, we had identified a problem with the thin, cold-pressed Li-Al electrodes of the Li-Al/FeS multiplate cells that led to cell-capacity decline rates of 0.1-0.25 percent per cycle. A change in cell design to reduce the Li-Al capacity utilization to $\leq$60% mitigated the capacity decline phenomenon of the Li-Al electrode. Subsequently, deep-cyclable Li-Al electrodes having 82% utilization of theoretical capacity (85% is considered to be complete utilization of available lithium capacity) were developed with $\leq$0.02 percent per cycle of capacity-decline rates. The improved Li-Al electrode provided a stepping stone for the development of a lithium-limited FeS cell design. An investigation of power limitations for the Li-Al/FeS cell revealed a greater than 100% increase in FeS electrode resistivity beyond 60% utilization of its theoretical capacity, which significantly diminished cell power capability. The lithium-limited FeS cell demonstrated an approximate doubling of specific power (100 W/kg) at 80% depth of discharge (DOD) compared with a FeS-limited cell and expanded its usable capacity from 50% to 80% DOD for power-demanding applications. Simultaneously, specific energy was increased about 15% to 100 Wh/kg at a 3-h discharge rate.

INTRODUCTION

Development of the Li-Al/FeS battery at Argonne National Laboratory (ANL) is directed toward applications demanding high specific energy and power, such as electric vehicles. In addition, sufficient power output throughout the battery's discharge capacity is desired. As will be discussed, the electrode capacity ratio (positive vs. negative electrode capacity) strongly influences the specific energy and power of a LiAl/FeS cell.

Earlier Li-Al/FeS cells contained 20-35% excess Li-Al capacity. This excess Li-Al capacity was deemed necessary to provide stable cell capacity (1). Initially lithium-aluminum electrode utilizations of 65% or more of the theoretical capacity did not meet cell stability goals of $\leq$0.02% capacity decline per cycle. Recent improvements in the Li-Al electrode, however, have resulted in higher utilization (80%) and a low capacity decline rate (2).

These Li-Al electrodes are fabricated by a slurry method, whereas conventional Li-Al electrodes are cold-pressed.

This paper will also describe additions to the Li-Al electrode that increase utilization of available lithium and maintain stable capacity. (An 85% utilization of lithium in Li-Al is considered to be complete utilization of lithium available in the $\alpha+\beta$ region of the lithium-aluminum phase relation.) The porous Li-Al electrodes were modified with one of three additives: MgO, which provides insulative properties; carbon, which is semiconductive; AlFe, which is conductive. A further objective of this investigation was to maintain, if not improve, the capacity density of the Li-Al electrodes. A loading density of 0.9-1.0 $A \cdot h/cm^3$ was found to be desirable for specific energy development.

When the FeS electrode limits the cell capacity, the cell power capability is closely linked with the FeS electrode characteristics. Multiplate cell diagnostic work by Kaun et al. (3) indicated significant increases in cell resistances after 50% depth of discharge due to the FeS electrode. Extensive work by Redey et al. (4) refined and automated voltage-loss measurements of Li-alloy/metal sulfide cells. With an improved Li-Al electrode, it became feasible to design a cell with excess FeS electrode capacity. This paper describes the performance characteristics of a cell design in which the Li-Al electrode limits the cell capacity.

BACKGROUND

The cells (5) of the first development battery, Mark IA,* contained three positive electrodes of FeS with Cu_2S additive and four Li-Al (46 at. % Li) electrodes in LiCl-KCl eutectic electrolyte. The multiple thin electrodes enabled greater cell capacity per unit of cell hardware weight compared to earlier "bicells," which had a central positive electrode and facing negative electrodes. The Mark IA cells, with 3.2-mm-thick positive electrodes and electrode dimensions of 17.5 x 17.5 cm, also provided high active material utilization (80-95%) for both electrodes. Unfortunately, they exhibited appreciable capacity decline rates, 0.1-0.25% per cycle, particularly during the initial 50-100 cycles.

Investigations by Kaun et al. (6) indicated that the negative electrode utilization is a factor in the capacity decline of multiplate cells. Additionally, some of the 50 Mark IA cells tested for capacity stability were cycled with limited depth of discharge. The rate of capacity decline was correlated to the depth of charge--or more directly to the percent utilization of the negative electrode. Beyond 60% utilization of the Li-Al (46 at. % Li) electrode, the rate of capacity decline increased significantly, to 0.25% per cycle, as shown in Fig. 1. Therefore, a direct approach to reducing the rate of capacity decline in multiplate cells was to increase the relative Li-Al electrode capacity to the positive electrode so that its percent utilization was limited. Increasing the negative-to-positive capacity ratio from approximately 1.0 for Mark IA cells to 1.3

*Fabricated by Eagle-Picher Industries, Inc., of Joplin, MO, under a sub-contract to Argonne National Laboratory.

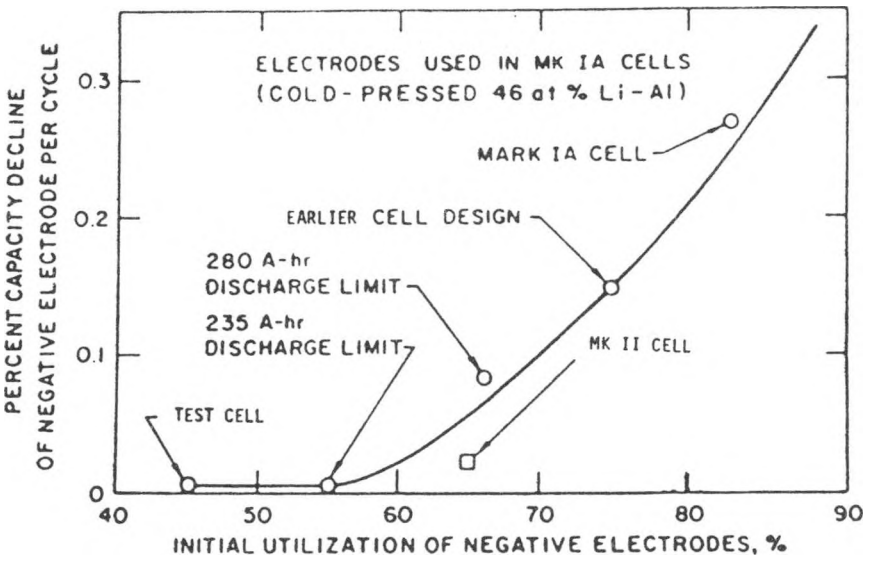

Fig. 1. Cell Capacity Decline Rate as Function of Depth of Discharge of Li-Al Electrode for Mark IA Cell

produced this change. The next-generation multiplate cells, Mark II, were designed with a 30% increase in Li-Al electrode capacity, which yielded a negative-to-positive capacity ratio of 1.3. Consequently, the rate of capacity decline for the Mark II cell was an acceptable, $\leq$0.02% per cycle, as shown in Fig. 2. With contributions from other modifications (i.e., use of LiCl-rich electrolyte rather than eutectic and an increase from 46 to 50 at. % Li), as well as reduced negative utilization, the negative electrode of Mark II cells exhibited acceptable capacity stability for utilizations up to 65% of the theoretical capacity of the Li-Al electrode.

Metallographic examinations showed that some degree of Li-Al agglomeration occurred in multiplate cells of 150 to 400 Ah capacity. These Li-Al electrodes had typically exhibited high lithium utilizations, of >60%. The agglomeration was classified according to the appearance of the microstructure. Typically, the center portion of the electrode densified and became depleted of lithium. As reported by Battles et al. (7) the initial loading density of Li-Al in the electrode was hypothesized to be a factor in electrode agglomeration. Out-of-cell experiments by Bandyopadhyay et al. to initiate sintering in β-LiAl were unsuccessful (8). Microscopic examinations showed significant sintering in an aluminum sample, but only a minor amount of sintering for a sample containing a two-phase (α-Al plus β-LiAl) material.

It was further hypothesized by this author that insufficient current distribution within the porous Li-Al electrode provided an environment for electrode agglomeration. The porous Li-Al electrodes formed by pressing have interconnected Li-Al particles. Consequently, the electronic conductivity network of these porous electrodes is much greater than its Li-ion conductivity network (See Fig. 3, Case I). Therefore, during recharge of the Li-Al network, there is less propensity for Li ions to migrate into the porous Li-Al electrode before depositing. The surface of the porous Li-Al electrode

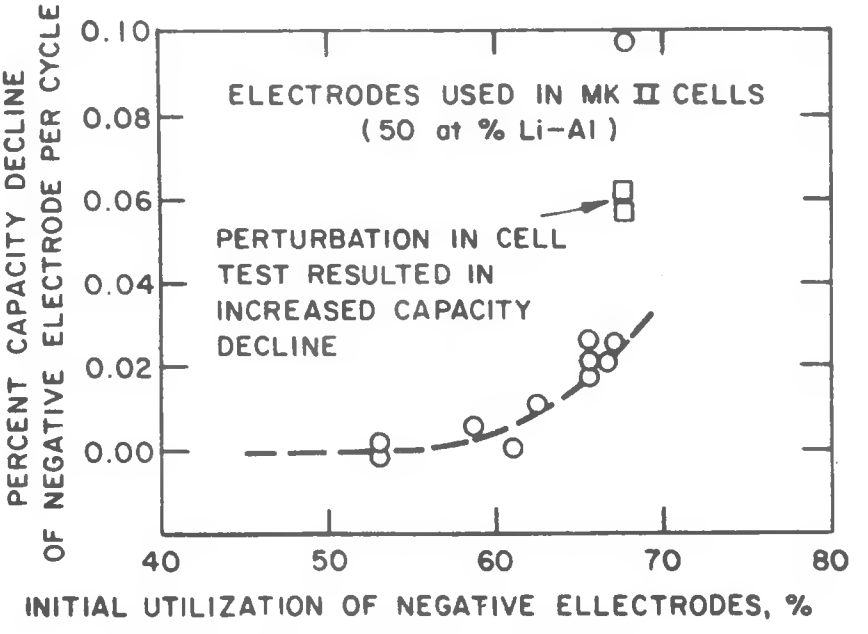

Fig. 2. Cell Capacity Decline Rate as Function of Depth of Discharge of Li-Al Reduced Negative (Li-Al) Electrode for Mark II Cell.

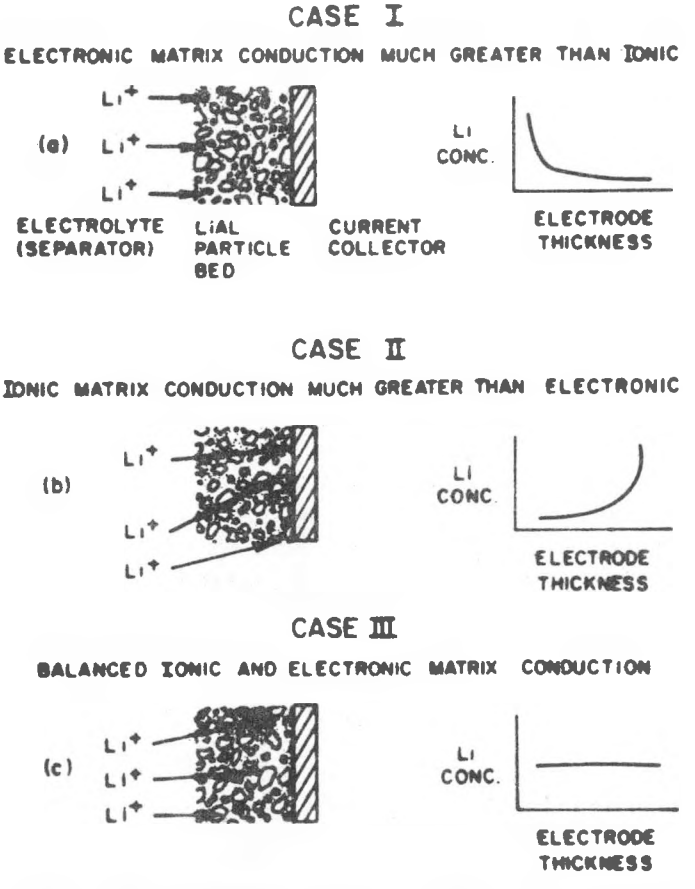

Fig. 3. Porous Electrode Models: Distribution of Lithium Deposition Upon Recharge of the Lithium-Alloy Electrode.

attains full charge before its central (or inner) portion. With repeated deep cycling, the central portion of the Li-Al electrode becomes depleted of lithium to αAl(Li). The αAl(Li) would sinter (agglomerate) under these conditions.

IMPROVED LiAl ELECTRODES

Experimental

Conventional Li-Al electrodes have been fabricated by cold-pressing (at 83 MPa) a powder mixture of Li-Al and LiCl/KCl. These electrodes attained ~0.9 $A \cdot h/cm^3$ or 70 vol % of 46 at. % Li-Al. The additive to this electrode was either MgO (Cerac), carbon (E Coke Flour, Great Lakes Carbon), or AlFe (Alfa). A slurry method of Li-Al electrode fabrication facilitated inclusion of the additive powders without pressing. (Powder pressing with carbon additive was unsuccessful.) The Li-Al (149-420 μm dia particles) and additive powders (about 75 μm dia particles and 3.5% of electrode volume) were slurried in an organic solvent, which was removed by vacuum before the electrode was assembled into a test cell. In cold pressing, interparticle friction-bonding forms the Li-Al into a porous plaque. The slurry fabrication method bypasses the Li-Al particle interconnecting and is capable of providing a denser electrode (70-75 vol % Li-Al) than loose powder packing (50-55 vol % Li-Al).

The test cell design submitted the Li-Al electrodes to harsh operation. A 65-Ah Li-Al electrode (area, 12.5 x 12.5 cm; thickness, 0.5 cm) was operated versus a 120-Ah FeS electrode (Fig. 4). Therefore, the Li-Al electrode received the major portion of cell polarization at the end of discharge and charge. Reference electrodes indicated that the Li-Al electrode polarized about 150 mV at the end of discharge. Earlier examination of the Li-Al capacity decline phenomenon associated it with heavy electrode polarization (6). Also, post-operative examination of multiplate cells revealed greater agglomeration of the inner Li-Al electrodes, which are acted upon from both sides. In our tests, the bicells had a centrally located negative electrode with facing positive electrodes as a simulation of inner Li-Al electrodes in multiplate cells. The electrode materials were contained in steel perforated sheet (0.45-mm thick, 45% open area) enclosures, which also served as the current collector (9). The test bicells were assembled with BN-felt separators (Kennecott Corp.). Molten salt electrolyte (54 wt % LiCl-KCl, Anderson Physics Lab.) was introduced by vacuum infiltration in a helium atmosphere glovebox.

Cells were tested at 465-475°C. Cycling at 20-A discharge (75 mA/cm^2) and 10-A charge (37 mA/cm^2) was controlled between 1.6 V and 1.0 V cutoffs. A Ni/Ni_2S_3 reference electrode (10) indicated changes in the Li-Al electrode potential versus capacity with cycling. Typical cell coulombic efficiency was 98+%. Cell discharge capacity was about 50 Ah, with 1.25 V average.

Results

The additive and loading density for the test cells are listed in Table 1. Two test cells (WR-1 and WR-2) contained Li-Al electrodes fabricated by the conventional pressing method, while the subsequent test

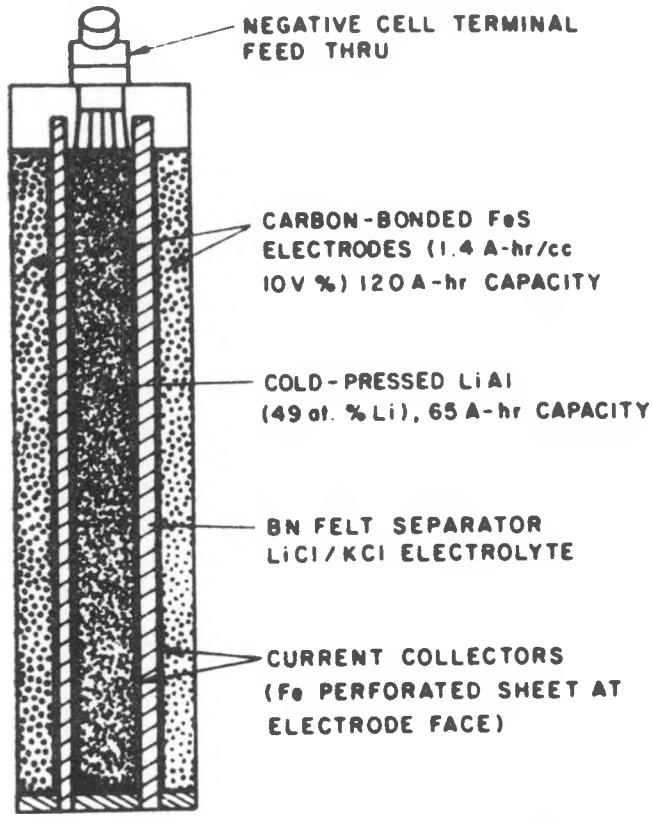

Fig. 4. Test-Cell Design for Evaluation of Improved Li-Al Electrode

Table 1. Lithium-Aluminum Electrode Additive Tests

Cell Name	Additive, vol. %	Loading Density Ahr/cm^3	Utilization % theo. cap.	Decline Rate %/cycle	Cycles Operated
WR-1 cold-pressed	None	0.90	69	0.093	292
WR-2	AlFe/10	0.90	58	0.014	672
WR-3 Slurry-formed	Carbon/3.3	0.78	82	0.016	186
WR-5	Carbon/5.0	0.73	77	Negligible	170
WR-6	None	0.72	80	0.005	313
WR-8	Carbon/3.0	0.80	65	0.002	363
WR-9	None	0.90	76	0.037	>200
WR-10	Carbon/3.0	0.90	78	0.014	>150
WR-11	MgO/5	0.90	77	0.012	>150

cells utilized the slurry fabrication method. Cell WR-1 exhibited Li-Al electrode characteristics analogous to earlier multiplate cells, i.e., a 0.093% decline rate with an initial 69% utilization. In Cell WR-2 (AlFe additive), lithium utilization was suppressed and stable capacity resulted. The lithium utilization and capacity stability for the Li-Al electrodes with carbon addition showed some sensitivity to the level of carbon addition, as shown in Table 1.

Strict control of loading density to 0.9 Ah/cm^3 for WR-9 through WR-11 provided evidence of the improvements made by the MgO and carbon additives. The additives are effective in maintaining stable capacity and high utilization in the closer Li-Al particle packing with the slurry fabrication method, as depicted in Fig. 5. At lower loading densities (0.7-0.8 Ah/cm^3), the carbon additive cells (WR-3 and WR-5) did not demonstrate a clear improvement over the cell with no additives(WR-6).

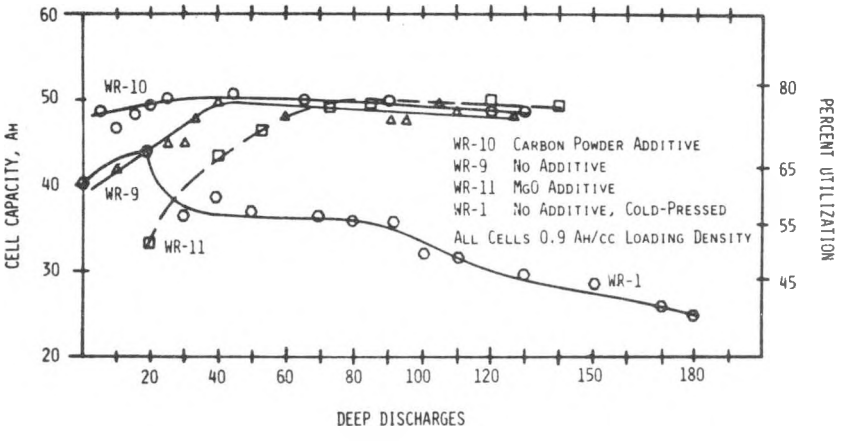

Fig. 5. Capacity Stability with Cycling for Improved Li-Al Electrodes Compared with Conventional (Cold-Pressed) Li-Al Electrode

The slurry-formed Li-Al electrode with 3 vol % carbon additive has been tested in a number of developmental cells, where capacity has been limited by the FeS electrode polarization. All have shown stable capacity, $\leq$0.02% decline/cycle. A bicell test (electrode area, 12.5 x 17.5 cm; capacity for 110 Ah) was designed to require a lithium utilization of 75%, where 65% is typical. The Li-Al with carbon additive reduced the volume and weight of the Li-Al electrode necessary for a given capacity Li-Al/FeS cell. Specific energy was thereby improved from 90 to 98 Wh/kg at a 4-h discharge rate.

The experimental results indicate that improved performance for the porous Li-Al electrode occurs through reduced particle-particle contact of the slurry-fabricated Li-Al electrode, as proposed in Fig. 3, Case III. Also, the slurry fabrication method (11) demonstrated itself as a viable option to cold-pressed Li-Al electrode fabrication. For Li-Al electrode loading densities of $\geq$0.9 Ah/cm^3, powder additions of MgO and carbon in 3-5 vol % amounts suppressed capacity decline rates to <0.02% per cycle, with lithium utilization approaching 80% (or 94% of available lithium). This

performance was demonstrated in harsh operating conditions of high polarization and central negative-electrode operation. In development cells, the improved Li-Al electrode demonstrated stable cell capacity and its higher utilization yielded a 9% increase in specific energy.

THE LITHIUM-LIMITED FeS CELL

Experimental

Prismatic test cells were fabricated with electrodes having an area of 12.5 cm x 17.5 cm and a thickness of 0.7-1.4 cm. The active materials were contained within steel perforated sheet (0.45-mm thick, 45% open area) enclosures. As an example, the Li-Al electrodes were fabricated by spreading a mixture of Li-Al (149-420 μm dia particles) and carbon powder additive (3.5% of electrode volume) slurried with an organic solvent (e.g., petroleum ether, toluene) into the current collector. The solvent was removed by vacuum before cell assembly. Electrode capacity-densities were 0.9 Ah/cm^3 for the Li-Al and 1.4 Ah/cm^3 for the FeS. These electrodes were assembled into cells with BN-felt separators (Kennecott Corp.). Molten salt electrolyte (54 wt % LiCl-KCl, Anderson Physics Lab.) was introduced by vacuum infiltration in a helium-atmosphere glovebox.

An advanced cell design (12) was devised to use positive electrode expansion to aid in electrode confinement. During discharge, the volumetric change of FeS is greater than that of Li-Al. As seen in Fig. 6, the multiplate cell hardware configuration, LCMP-17, provides compartments in which the FeS electrode is free to expand around a central prismatic Li-Al electrode. The FeS electrode expansion is intended to confine the Li-Al electrode and BN separator within their enclosures. Expansion of the FeS electrode uniformly supports the separator layer and reduces dependence upon metal enclosures to confine the slurry-like electrode materials. Therefore, the weight contribution of the hardware components was reduced such that electrode materials accounted for 36% of the cell weight, in comparison to 24-29% for earlier cell designs; about a one-third increase in capacity per unit cell weight was achieved.

Cells were tested at 465-475°C. Typical cycling at 8-h charge (37 mA/cm^2) and 3-h discharge (100 mA/cm^2) rates was controlled between 1.6 V and 0.9 V cutoffs. A Ni/Ni_3S_2 reference electrode placed through an electrolyte reservoir at the top of the cell indicated working electrode potentials during cycling. Current interruptions of one-second duration were used to evaluate electrode and cell resistances. Power measurements were derived from integrating constant-current pulses (100-300 A) of 15-s duration. Resistance mapping was conducted for some cells by removing the tops of the cell housings and attaching potential leads to the interelectrode connections. Potential (IR) measurements were taken at constant current. Typical cell coulombic efficiency was 99%. Cell discharge capacity was about 125 Ah for bicells and about 250 Ah for multiplate cells, with a 1.2-V average voltage.

Results

Extending high power capability to 80% depth of discharge (13) is a principal objective in evaluating the effect of excess FeS electrode capacity

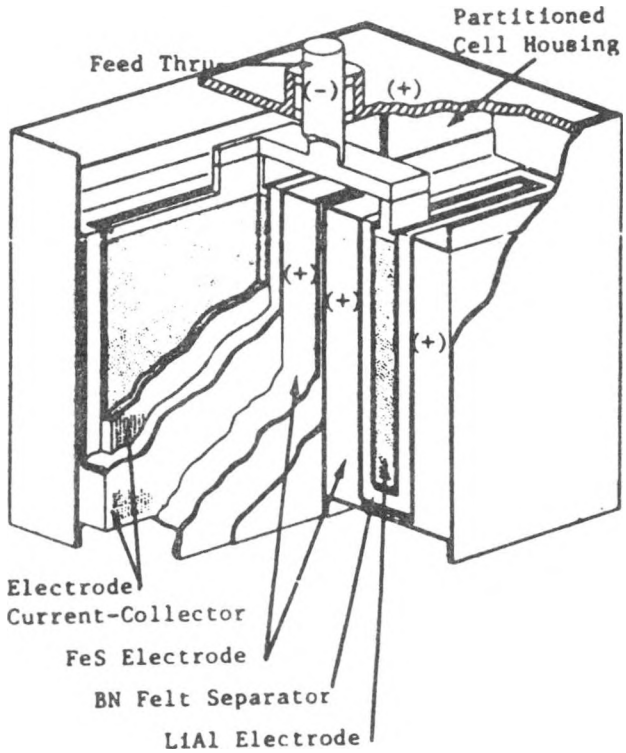

Cell Design LCMP-17

Fig. 6. Positive-Electrode Grounded Cell Design

in the Li-Al/FeS cell design. Cell resistance is a dominating factor in determining specific power. Cell resistance as a function of depth of discharge (DOD) is presented in Fig. 7 for three prototype battery cells. Cell EP-111 (a MKII design developed by Eagle-Picher Industries, Inc.) and Cell LCMP-16 (an ANL design) have 30% excess Li-Al capacity, while Cell LCMP-17 (also an ANL design) has 19% excess FeS capacity. Our resistivity investigations gave guidance to the electrode capacity matching of the lithium-limited cell such that the FeS electrode utilization was about 65%.

Cell EP-111 is a seven-plate cell of 1800-cm^2 separator area and has the conventional honeycomb current collectors. Figure 8 presents data on electrode-to-electrode resistance for Cell EP-111, with the terminal effects (from resistance mapping investigations) subtracted. Terminal effects accounted for 40% of EP-111 cell resistance and less than 10% for the LCMP cells. Cell EP-111 (512 Ah FeS vs. 396 Ah Li-Al) exhibits nearly constant resistance to 50% DOD, but the resistance increases from 1.3 ohm-cm^2 to 2.0 ohm-cm^2 for 50% to 80% DOD. Power at 50% DOD is only 0.185 W/cm^2. Measurements using a Ni/Ni_3S_2 reference electrode reveal that an increase in cell resistance at 50% DOD is due chiefly to the FeS electrode.

Cell LCMP-16 (260 Ah FeS vs. 340 Ah Li-Al) exhibits a resistance as a function of DOD that is quite similar to that of Cell EP-111, but is reduced

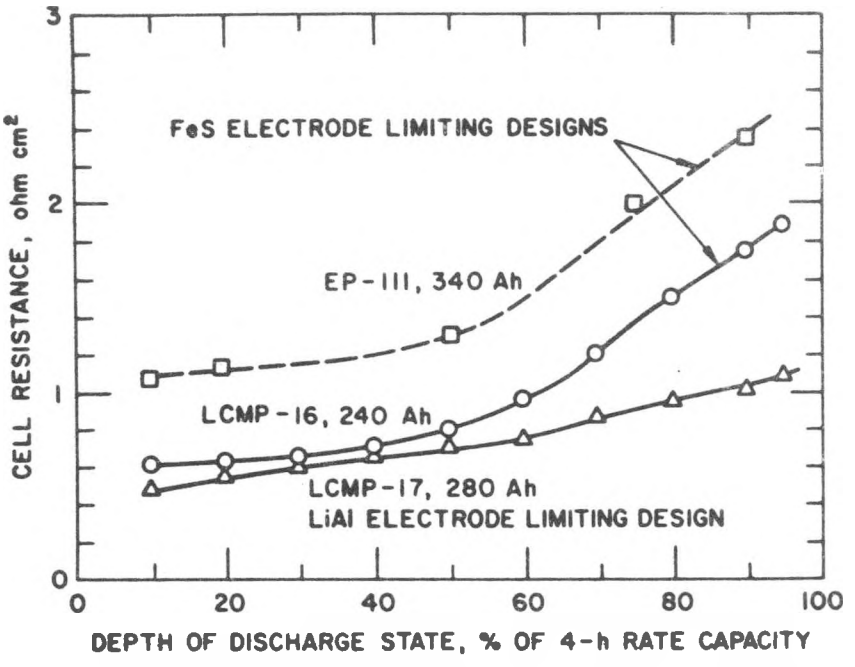

Fig. 7. Cell Resistance as a Function of Depth of Discharge for Lithium-Limited and FeS-Limited Cell

0.5 ohm-cm^2 throughout the discharge (Fig. 7). The improved current collector design (perforated sheet) of Cell LCMP-16, along with a low-resistance terminal, results in a power of 0.5 W/cm^2 at 50% DOD. Cell LCMP-17 (a lithium-limited cell) has cell hardware identical to that of LCMP-16, but the thicker electrodes (440 Ah FeS vs. 370 Ah Li-Al) provide 15% greater discharge capacity--280 Ah. The LCMP-17 cell resistance as a function of DOD does not exhibit the extreme rise at 50% DOD. In this "lithium-limiting" design (or excess FeS capacity), the cell performance characteristics change to resemble those of the Li-Al electrode. Resistance increase for 50% to 80% DOD is less dramatic, 0.7 ohm-cm^2 to 0.9 ohm-cm^2. As shown in Fig. 9, this change has improved the cell power at 80% DOD by 70%, from 0.22 W/cm^2 for LCMP-16 to 0.38 W/cm^2 for LCMP-17.

The hardware weight reduction of cell LCMP-17 was not detrimental to its resistance. This cell's resistance was nearly half that of earlier cell designs (0.7 ohm-cm^2 vs. 1.3 ohm-cm^2 at 50% DOD). Unlike earlier cell designs, the cell housing serves as the FeS electrode current collector. Applying the greater portion of hardware weight (i.e., cell housing) to the FeS electrode, instead of the Li-Al electrode, resulted in an overall 15% reduction of internal cell resistance. The electrode and cell terminal connections account for under 10% of the overall cell resistance, compared to almost 40% for earlier cells.

Due to the change to a "lithium-limited" design, specific energy of Cell LCMP-17 was increased about 15% along with improved power. Cell LCMP-17 specific energy at a 3-h rate is 101 Wh/kg, compared with 87 Wh/kg for LCMP-16. In particular, higher specific energy was accomplished through the thicker electrodes building more capacity into the cell without proportionally

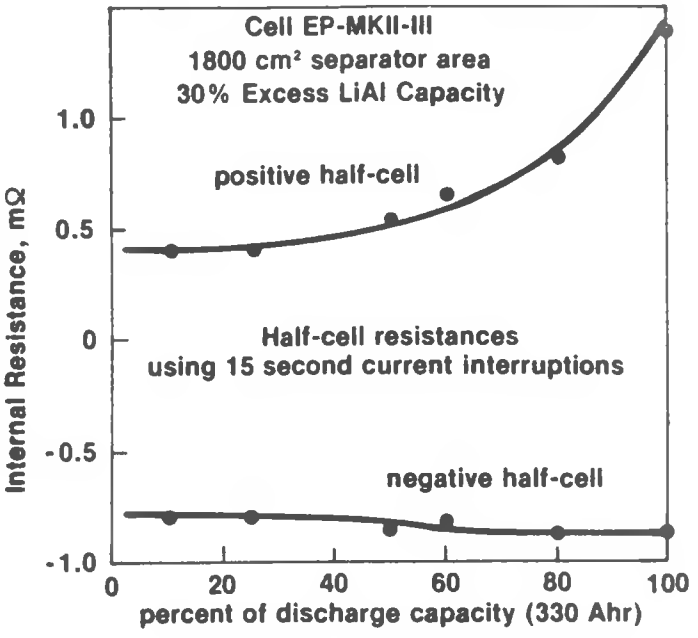

Fig. 8. Half-Cell Resistance of Mark II Cell as a Function of Depth of Discharge

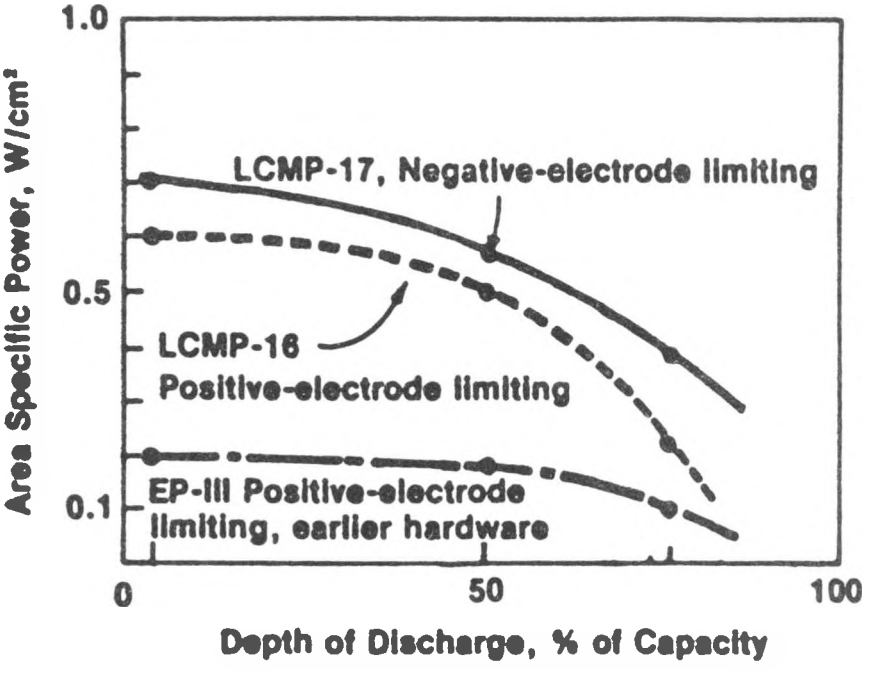

Fig. 9. Area-Specific Power as a Function of Depth of Discharge for Lithium Limited and FeS-Limited Cell

increasing cell weight. An equally important factor is the tradeoff in electrode thickness (available capacity) and the reduced utilization from higher operating current density.

Two bicells, LC-20 and LC-22, illustrate the differing effect of current density upon utilization for the FeS- and lithium-limiting designs, respectively. Figure 10 shows the voltage/capacity functions at two current densities, 75 mA/cm^2 and 100 mA/cm^2. Cell LC-20 exhibits a 15% capacity reduction with an increase of current density from 75 to 100 mA/cm^2, whereas the capacity of LC-22, the lithium-limiting design, is reduced by less than 4%. The improved discharge kinetics of Cell LC-22 provides a basis for designing cells with high specific energy and high specific power. High utilization of 75% is obtained from Li-Al electrodes of more than 1.0-cm thickness (0.9 Ah/cm^2) at current density of 100 mA/cm^2, while FeS utilization is less than 65% and thereby does not impart a resistive hindrance to high power capability.

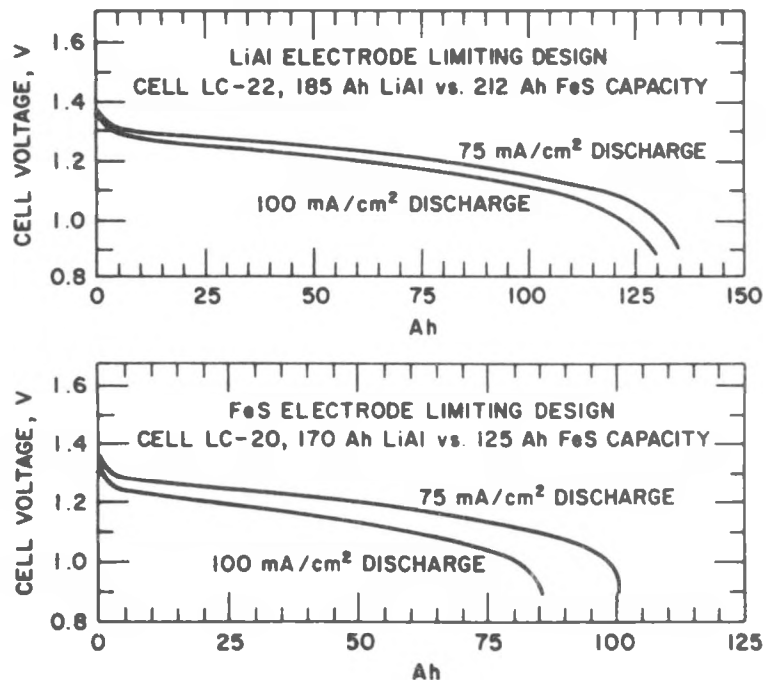

Fig. 10. Cell Voltage vs. Capacity at Two Discharge Rates for a Lithium-Limited and a FeS-Limited Cell

CONCLUSIONS

Both the FeS electrode and the improved Li-Al electrode (slurry formed) at thicknesses of ~1 cm tend to decline linearly in capacity utilization with discharge current density (DCD). Although FeS utilization is quite high at low DCD (90% at 25 mA/cm^2), it declines rapidly to 65% at 100 mA/cm^2. On the other hand, the slurry-formed Li-Al electrode, which has an 80% utilization of total Li at 25 mA/cm^2, is still 76% at 100 mA/cm^2. The cell capacity decline, a result of deep discharging the Li-Al electrode, has been resolved by using the new method of electrode fabrication. With an FeS-

limiting cell design, electrode resistance as a function of depth of discharge (DOD) differs markedly for FeS and Li-Al electrodes. The FeS resistance more than doubles beyond 60% capacity utilization, whereas the Li-Al has a nearly negligible increase in resistance during discharge.

With a lithium-limiting FeS cell (14), the undesirable increase in cell resistance from the FeS electrode is eliminated. As a consequence, area-specific power of the lithium-limiting couple at 80% DOD (0.38 W/cm^2) is 70% greater than that of an FeS-limiting couple (0.22 W/cm^2). Stable capacity utilization of a lithium-limiting electrode couple at discharge rates (such as 75-100 mA/cm^2) was demonstrated.

The cell with a lithium-limited design (LCMP-17) has demonstrated specific energy of 101 Wh/kg at a 3-h rate and specific power of 152 W/kg at 50% DOD, both of which are an improvement of about 25% over earlier FeS cells with LiCl-KCl electrolyte. These earlier cells were FeS limited and fabricated by Eagle-Picher (7-plate cell) and Gould Inc. (5-plate cell). The performance for these cells (Fig. 11) represented a tradeoff in specific energy and power, in spite of a number of differences in cell design.

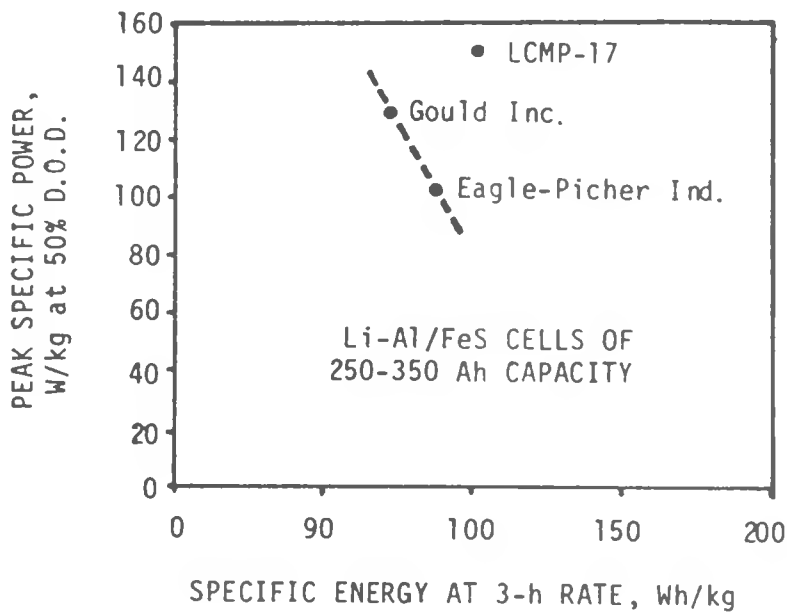

Fig. 11. Ragone Plot of the Lithium-Limited Cell and Contractor-Fabricated FeS-Limited Cells

Enhanced capabilities were also identified. Cell LCMP-17 has improved discharge kinetics, which results in stable capacity at a 3-h discharge rate (a 4-h rate was typical for earlier cells) and also yields a substantially improved specific power at 80% DOD (100 W/kg). In power-demanding applications such as electric vehicles, test results suggest that the LCMP-17 design extends useful cell capacity beyond 50%, to 80% DOD. Recently, Gould, Inc. has adopted the lithium-limited cell design for its FeS (LiCl-LiBr-LiF electrolyte) battery development and reports similar increases in cell performance (15).

ACKNOWLEDGMENT

The author is grateful for the support of E. C. Gay and W. E. Miller during the course of this work. The assistance of M. Anderson, W. Reder, A. Jackson, and Y. Jeanneret as student researchers was highly valued. This work was supported by the U.S. Department of Energy, Office of Energy Storage under Contract W-31-109-Eng. 38.

REFERENCES

1. E. C. Gay et al., Argonne National Laboratory Report ANL-84-93 (July 1985).

2. Thomas D. Kaun and William G. Reder, "Improving the Performance of the LiAl Secondary Electrode," Extended Abstracts of the Electrochem. Soc., Vol. 82-1, pp. 563-464 (1982).

3. P. A. Nelson et al., Argonne National Laboratory Report ANL-81-65, p. 15 (1982).

4. L. Redey, "Reference Electrode Systems and Their Applications for High Temperature Lithium/Metal Sulfide Cell Testing", This Symposium.

5. P. A. Nelson et al., Argonne National Laboratory Report ANL-78-94, pp. 20-29 (1978).

6. T. D. Kaun, W. E. Miller, L. Redey, and J. D. Arntzen, "Designing Stable Capacity for LiAl/FeS Multiplate Cells," in Symposium on Lithium Batteries, H. V. Venkatasety, Ed., pp. 421-428, The Electrochem. Soc. (1980).

7. J. E. Battles, F. C. Mrazek, and N. C. Otto, Argonne National Laboratory Report, ANL-80-130 (December 1980).

8. G. Bandyopadhyay and J. E. Battles. J. Electrochem. Soc. 129, 2265-2267 (1982).

9. T. Kaun, P. Eshman, and W. Miller, "New Approach to Electrode Current Collection for LiAl/Iron Sulfide Cells," Proc. of the 15th Intersoc. Ener. Conv. Engin. Con. (1980).

10. L. Redey and D. R. Vissers, J. Electrochem. Soc. 130, 231 (1983).

11. T. Kaun, U.S. Patent 4,358,513 (1982).

12. T. Kaun, U.S. Patent 4,540,642 (1985).

13. T. Kaun, "Changing the LiAl/FeS Cell to Include Excess FeS Capacity", Extended Abstracts of the Electrochem. Soc., Vol. 83-1, p.67-68 (1983).

14. T. Kaun, U.S. Patent 4,446,212 (1984).

15. G. Barlow, "Development of High Performance Lithium-Alloy/Metal Sulfide Battery Cells for Electric Vehicle Propulsion," This Symposium.

ELECTROCHEMICAL STUDIES OF IRON ELECTRODES IN SULFIDE-CONTAINING MOLTEN SALTS

S. S. Wang

Electrochemistry Department
General Motors Research Laboratories
Warren, Michigan 48090-9055

ABSTRACT

During testing of a Li-Si/FeS_2 cell, 75% of the cell resistance was detected in the porous FeS_2 electrode. A planar iron electrode was designed to investigate this observation. A molybdenum sleeve, fusion bonded to the iron electrode, was used in combination with boron nitride insulators to provide a uniform primary current distribution. Cyclic voltammetry was conducted on planar iron electrodes in two electrolytes, LiCl-KCl eutectic and potassium-free LiF-LiCl-LiBr. The electrolytes were saturated with Li_2S. Electrochemical reactions with high overpotential, which are responsible for the high resistance of Li/FeS_2 cells, were identified in these electrolytes. It was found that the overpotential of the electrochemical reactions is inversely proportional to the activity of lithium ion in the electrolytes. Some iron-containing compounds, electrochemically formed on the iron electrodes in the potassium-free electrolyte, were found highly soluble in the electrolyte.

INTRODUCTION

During testing of compact Li-Si/LiCl-KCl eutectic/FeS_2 cells (60 Ah capacity) for electric vehicle application, high internal resistance has been observed.[1] A small test cell[2] (0.6 Ah capacity) with a porous FeS_2 working electrode, a Li-Si counter electrode, and two Li-Al reference electrodes, was designed to study the contributions to the internal resistance of various cell components. The results[2] indicated that 75% of the overall resistance was in the FeS_2 electrode.

In the past, porous FeS_2 electrodes were employed[2-4] for studies on Li/FeS_2 cells. However, the current and potential distributions in a porous electrode are nonuniform. Therefore, a planar FeS_2 electrode, with more uniform current and potential distributions than a porous electrode, is needed in studying high internal resistance of Li/FeS_2 cells.

The approach taken in this work was to fabricate a planar Fe electrode and then electrochemically converted it to FeS, FeS_2, etc. The planar Fe electrode was fusion bonded to a molybdenum sleeve, believed nonreactive in the Li/FeS_2 cell environment, to prevent the electrolyte leakage.

In this research work, cyclic voltammetry and galvanostatic charge-discharge experiments were conducted on the planar iron electrodes in two electrolyte, LiCl-KCl eutectic and potassium-free LiF-LiCl-LiBr. Cathodic-anodic pairs with high overpotential were identified.

EXPERIMENTAL

Cell Configuration

The configuration of the test cell is shown in Fig. 1. The geometric areas of the planar iron working electrode and the Li-Si counter electrode were made the same to help achieve uniform current density on the working electrode.

The distance between the capillary opening of the reference electrode and the working electrode was 0.7 mm. Therefore, the electrolytic resistance between the working and the reference electrodes was 0.16 Ω based on the reported[5] electrical conductance of pure LiCl-KCl eutectic electrolyte. Since the total current passed through the cell was in the milliampere range, the ohmic loss between the working and the reference electrodes was negligible.

Planar Iron Working Electrode

For the planar Fe electrode, a 4.83 mm diameter iron disk (99.999% pure) was fusion bonded to a 7.94 mm o.d. molybdenum sleeve. The fusion bonding process consisted of melting the iron disk under the inert atmosphere inside a helium-filled glove box using a welding torch. The temperature was measured by an optical pyrometer and was maintained at about 1600°C to minimize molybdenum diffusion into the iron. The electrode was polished using a 1 μm alumina polishing wheel.

A scanning electron micrograph of the planar Fe electrode is shown in Fig. 2. Complete bonding between iron and molybdenum was observed.

Figure 2 also shows a dendritic phase at the edge of the planar Fe electrode, indicating the possibility of molybdenum diffusion into iron electrode during fusion bonding. A microprobe study of the electrode, shown in Fig. 3, implied that the molybdenum diffusion front was only 50 μm from the iron-molybdenum boundary. Thus, the electrode would closely approximate the behavior of pure iron.

Counter Electrode

The counter electrode was compacted from a mixture of pyrometallurgically formed 37% lithium-in-silicon alloy (Foote Mineral Co.) and eutectic LiCl-KCl interspersed throughout a nickel foamed matrix. The eutectic LiCl-KCl electrolyte was prepared by mixing LiCl of 99.6% purity and KCl of 99.9%

purity. This mixture was purified by bubbling chlorine through the melt at 775°K for four hours, and subsequently removing the chlorine by bubbling with helium for one hour. Two layers of this prepared counter electrode were embedded in a stainless steel holder with a 400 mesh size stainless steel screen as a particle retainer.

Reference Electrode

A Li-Al reference electrode, electrochemically impregnated to 45 atomic percent (a/o) lithium-in-aluminum, was located in the hole on top of the boron-nitride fixture.

Cell Assembly and Operating

The test cell was assembled inside a stainless steel beaker, which was contained inside a pyrex glass closure. The cells were impregnated with two different electrolytes saturated with Li_2S (98.0% pure). They were: (a) LiCl-KCl eutectic electrolyte and (b) potassium-free (K-free) electrolyte 22 mole percent (m/o) LiF, 31 m/o LiCl, and 47 m/o LiBr.

The cell was assembled and operated inside a helium atmosphere glove box. Operating temperatures measured by a thermocouple located inside an aluminum thermal mass surrounding the stainless steel beaker, were kept at 430°C, 470°C, 510°, and 550°C.

Cyclic Voltammetry and Galvanostatic Studies

Cyclic voltammetric experiments were conducted by scanning potential, measured between the working and the reference electrodes, from 1.0 V at a rate of 0.1 mV/sec. Potential scan was controlled by a PAR 175 universal programmer and a PAR 173 potentiostat/galvanostat. Galvanostatic studies were conducted by applying a constant current of 0.7 mA using a PAR 173 potentiostat/galvanostat for both charge and discharge. The potential was also measured between the working and the reference electrodes.

RESULTS AND DISCUSSION

LiCl-KCl Eutectic Electrolyte

The open circuit potential for the planar Fe electrode in the eutectic electrolyte was measured to be 1.3 V versus the Li-Al reference electrode. A cyclic voltammogram obtained from the planar Fe electrode at 430°C is shown in Fig. 4. The scan rate was 0.1 mV/sec.

The upper and the lower limits of potential scans for the planar Fe electrode were changed at 510°C, see Fig. 5, and the cathodic peaks were associated with

the anodic peaks. Five cathodic-anodic reaction pairs, i.e., (I_c, I_a), (II_c, II_a), (III_c, III_a), (IV_c, IV_a), (V_c, V_a), and a singular cathodic peak VI_c were thus matched and labeled in Figs. 4 and 5. The planar Fe electrode was also studied at various temperatures, i.e., 470°C, 510°C, and 550°C. The cyclic voltammograms obtained at a scan rate of 0.1 mV/sec are also shown in Fig. 4.

It was found that at 510°C the singular cathodic peak VI_c would not appear unless the upper limit of the potential scan went above 1.3 V, see Fig. 5. Meanwhile, as shown in Fig. 5, the magnitude of this peak was proportional to the upper limit of potential scan. Therefore, it is believed that this singular cathodic peak VI_c is associated with a reactant, which is chemically formed along with anodic reactions II_a, III_a, and IV_a.

The temperature effect shown in Fig. 4 indicated that the chemical reaction was favored, while cathodic peak III_c was retarded at higher operating temperature. It was reported[6] that the discharge of J-phase[6] to Li_2S and Fe appeared at around 1.28 V at a scan rate of 0.015 mV/sec. Although cathodic peak III_c appeared at a lower potential, 1.20 V, our scanning rate was also much faster, i.e., 0.1 mV/sec. Furthermore, it was reported[6] that the formation of J-phase could be suppressed by increasing the operating temperature. Therefore, it is believed that the cathodic peak III_c is indeed the discharge of J-phase to form Li_2S and Fe.

The causes of poorer resolution for anodic peak I_a and II_a, and the further broadening of cathodic peak II_c at higher temperature are unknown at present. Nevertheless, the broadened cathodic peak II_c observed at 550°C is certainly not desirable for battery applications. Since cathodic peak II_c is one of the major discharge peaks for Li/FeS_2 cells, the operating temperature should be kept below 550°C to narrow the potential range for cathodic reaction II_c.

Galvanostatic studies were then conducted on the same planar Fe electrode at 430°C. The charge-discharge curves obtained at a constant current of 0.7 mA are shown in Fig. 6. As compared to the cyclic voltammograms, two more reactions, occurring at 1.31 V and 1.34 V, were observed in Fig. 6. The galvanostatic charge-discharge curves obtained from a pure molybdenum electrode are also shown in Fig. 6(A). Comparing Fig. 6 to 6(A), it is obvious that the two reactions were occurring on the surface of the molybdenum sleeve for the planar Fe electrode. It was also found that the molybdenum sleeve became passivated and the two plateaus disappeared in the subsequent cycles. This observation implied little or no interference from the molybdenum sleeve during testing of the planar Fe electrode.

Extremely low coulombic efficiency was observed for reaction V_c and V_a (Fig. 6), indicating the charge product of V_a either self corroded or became passivated. Coulombic efficiencies higher than 95% were obtained from porous FeS_2 electrodes[2]. Thus, this low efficiency is believed specific to the configuration of the test electrode employed in this work.

The peak separations for cathodic-anodic reaction pairs in Fig. 4 at 470°C were measured and summarized in Table I. It was seen that, with the exception of reactions (II_c, II_a) and (V_c, V_a), all other electrochemical reactions are fairly irreversible.

K-Free Electrolyte. The cyclic voltammogram obtained from a planar iron electrode dipped in the K-free molten salt electrolyte at 470°C is shown in Fig. 7. Fewer peaks were observed, as compared to the cyclic voltammograms obtained from the LiCl-KCl eutectic electrolyte at 470°C (Fig. 4). The cathodic peaks were associated with the anodic peaks by changing the upper and the lower limits of potential scans for the planar Fe electrode. Anodic-cathodic couples were thus matched and labeled in Fig. 7. Anodic-cathodic couples (I_a, I_c), (III_a, III_c), (IV_a, IV_c) did not appear in the K-free electrolyte.

The peak separation for cathodic-anodic reaction couples was estimated from the cyclic voltammograms (Table I). Table I shows that the peak separation of cathodic-anodic couples (II_a, II_c) was less in the K-free than in the eutectic electrolyte. Also, the less reversible couples, such as (I_a, I_c) and (III_a, III_c), did not appear in the K-free electrolyte, indicating that the reactions occurring on the planar iron electrode is more reversible in the K-free electrolyte. However, the planar iron electrode lasted only for two cyclic voltammetric runs before a short circuit developed between the working and the counter electrodes.

Although the chemical analysis of reaction products was not conducted in this work, electrochemical reactions associated with peaks observed on the cyclic voltammograms can be analyzeed based on information reported previously.[3,4,7] It was believed that couple (II_a, II_c), part of the lower plateau, is associated with X-phase:

$$Li_2FeS_2 \text{ (X-phase)} + 2Li^+ + 2e^- \rightleftarrows 2Li_2S + Fe \qquad (1)$$

It was mentioned earlier that the couple (III_a, III_c), also part of the lower plateau, is associated with the reactions involving the J-phase, $LiK_6Fe_{24}S_{26}Cl$. Since the J-phase cannot be formed in the absence of potassium ion, the absence of couple (III_a, III_c) in the K-free electrolyte supports the conclusion that peaks III_a and III_c are indeed associated with the J-phase. In addition, the reaction responsible for couple (V_a, V_c), the upper plateau, is believed to be[4,7]

$$2FeS_2 + 3Li^+ + 3e^- \rightleftarrows Li_3Fe_2S_4 \qquad (2)$$

A discharge path of the FeS_2 electrode was proposed (7) as

$$FeS_2 \rightleftarrows Li_3Fe_2S_4 \rightleftarrows Li_{2+x}Fe_{1-x}S_2^{(x=0.2)}$$

$$+ Fe_{1-x}S \rightleftarrows Li_2FeS_2 \rightleftarrows Li_2S + Fe \qquad (3)$$

CONCLUSION

Excellent resolution on cyclic voltammograms and galvanostatic charge-discharge curves were obtained from planar iron electrodes in Li/FeS_2 cells. Cathodic-anodic reaction pairs with high overpotential were identified, which may be responsible for high resistance. More understanding about the origination of this high overpotential is necessary. The planar iron electrode, worked well in this study, and will be employed to continue research in these areas.

REFERENCES

1. E. J. Zeitner, Jr. and J. S. Dunning, "High-Performance Lithium/Iron Disulfide Cells," General Motors Research Laboratories, Warren, Mich., Research Publication GMR-2724, May 16, 1978.

2. S-C. S. Wang, "Internal Resistance in Li-Si/LiCl-KCl/FeS_2 Cells," General Motors Research Laboratories, Warren, Mich., Research Publication GMR-3568, March 10, 1981.

3. Z. Tomczuk, S. K. Preto, and M. F. Roche, "Reactions of FeS Electrodes in LiCl-KCl Electrolyte," J. Electrochem. Soc., 128 (4), 760,1981.

4. S. K. Preto, Z. Tomczuk, and M. F. Roche, "Reactions of FeS_2, CoS_2, and NiS_2 Electrodes in Molten LiCl-KCl Electrolytes," J. Electrochem. Soc., 130 (2), 264, 1983.

5. E. R. Van Artsdalen and I. S. Yaffe, "Electrical Conductance and Density of Molten Salt Systems: KCl-LiCl, KCl-NaCl and KCl-KI," J. Phys. Chem., 59, 118 (1955).

6. "Annual DOE Review of the Lithium/Iron Sulfide Battery Program Volume II," Argonne National Laboratory Chemical Engineering Division, June 25-26, 1980.

7. Z. Tomczuk, B. Tani, N. C. Otto, M. F. Roche, and D. R. Vissers, "Phase Relationships in Positive Electrodes of High Temperature Li-Al/LiCl-KCl/FeS_2 Cells," J. Electrochem. Soc., 129(5), 925 (1982).

TABLE I

Peak Separation for Cathodic-Anodic Reaction Couples
(temp = 470°C)

Reaction Couples	Peak Separation	
	Eutectic	K-Free
I_a & I_c	0.50 V	--
II_a & II_c	0.21 V	0.15 V
III_a & III_c	0.36 V	--
IV_a & IV_c	0.18 V	--
V_a & V_c	0.15 V	0.15 V

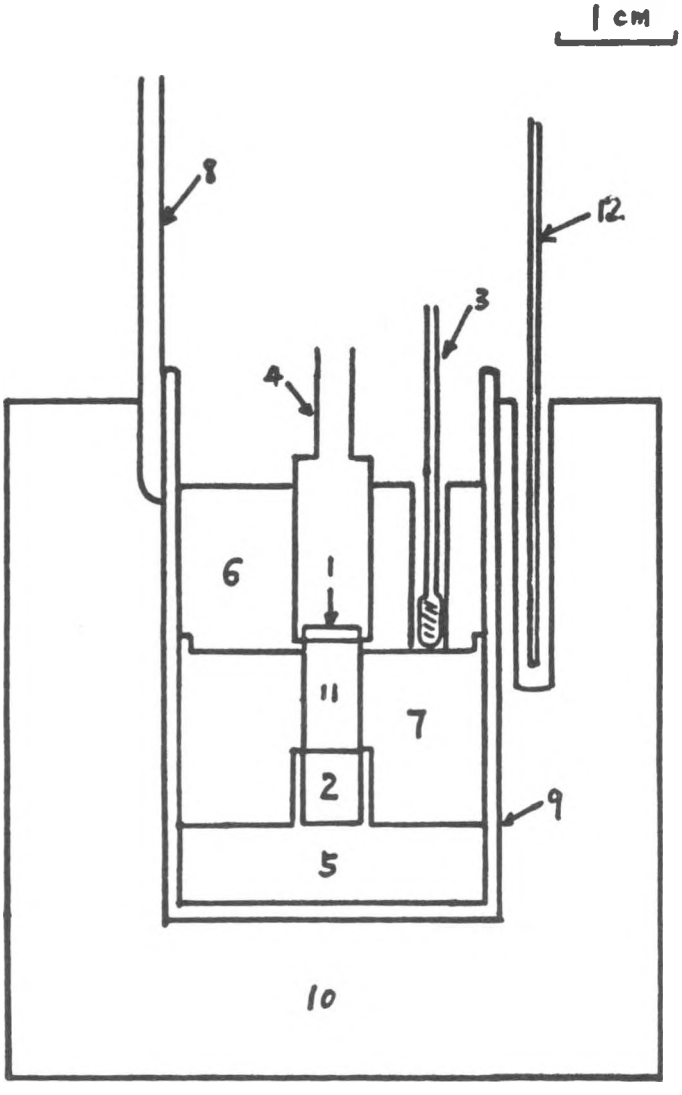

1. Fe disk electrode
2. Li-Si counter electrode
3. Li-Al reference electrode
4. Mo sleeve
5. stainless steel holder of counter electrode
6. boron nitride fixture 1
7. boron nitride fixture 2
8. counter electrode lead
9. stainless steel beaker
10. aluminum thermal mass
11. LiCl-KCl eutectic saturated with Li_2S
12. thermocouple

Fig. 1 Schematic diagram of a test cell.

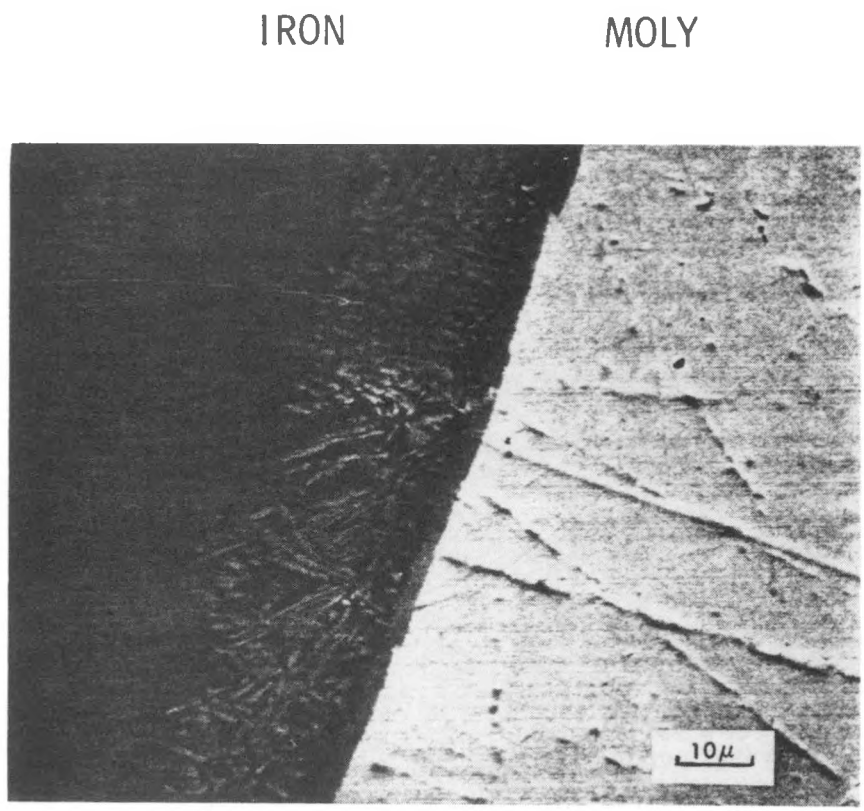

Fig. 2 The SEM picture of the planar Fe electrode at iron-molybdenum boundary (1000X).

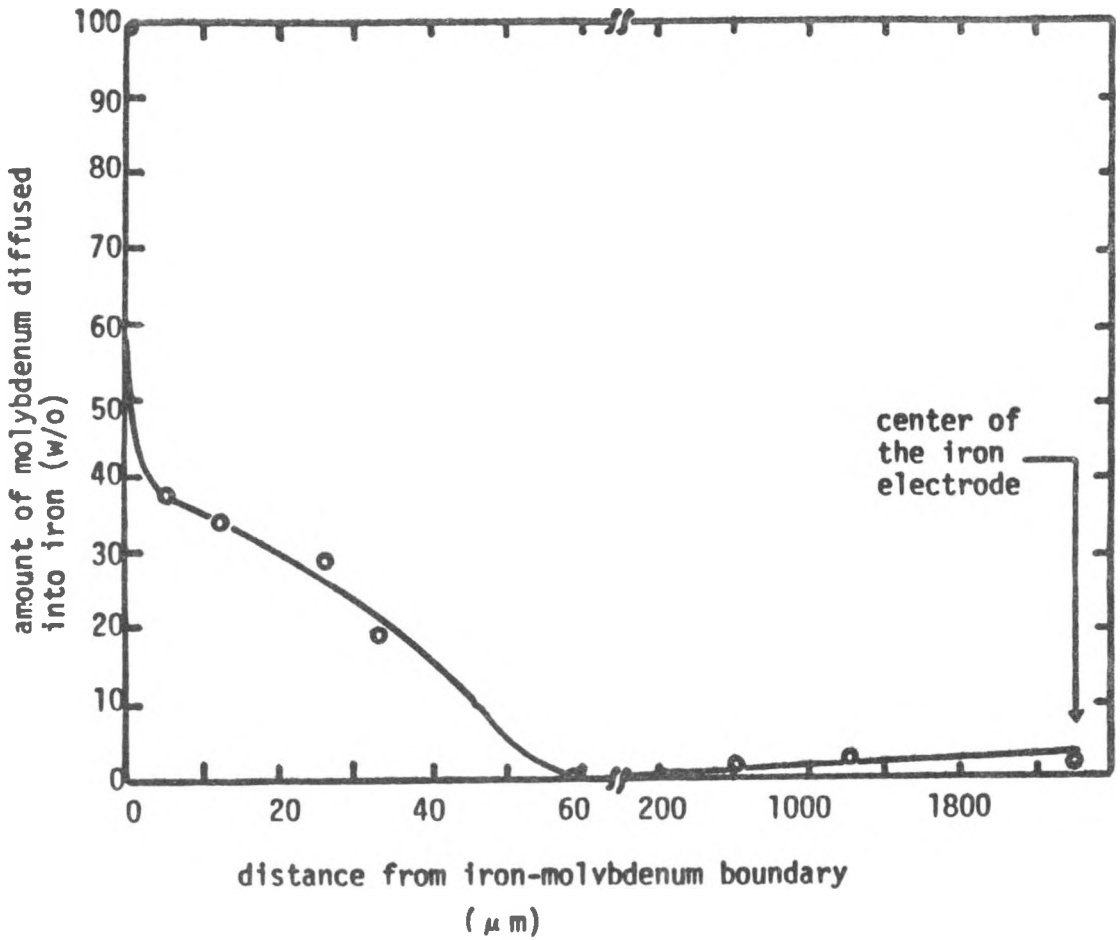

Fig. 3 The amount of molybdenum diffused into the planar Fe electrode, results obtained from microprobe studies.

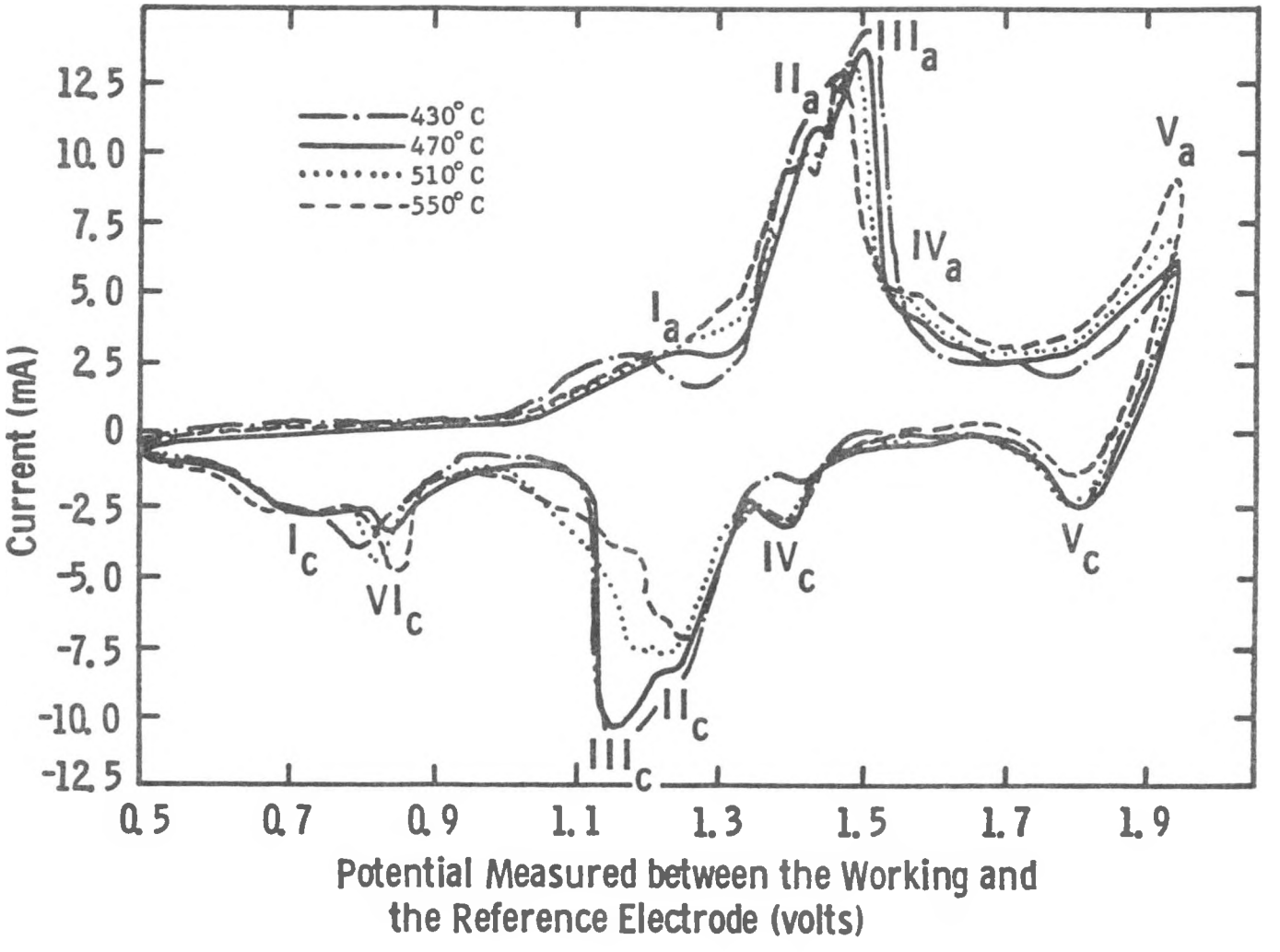

Fig. 4 The cyclic voltammograms obtained from the planar Fe electrode in LiCl-KCl eutectic saturated with Li_2S.
scan rate = 0.1 mV/sec, temperature = 430°, 470°, 510°, and 550° C.

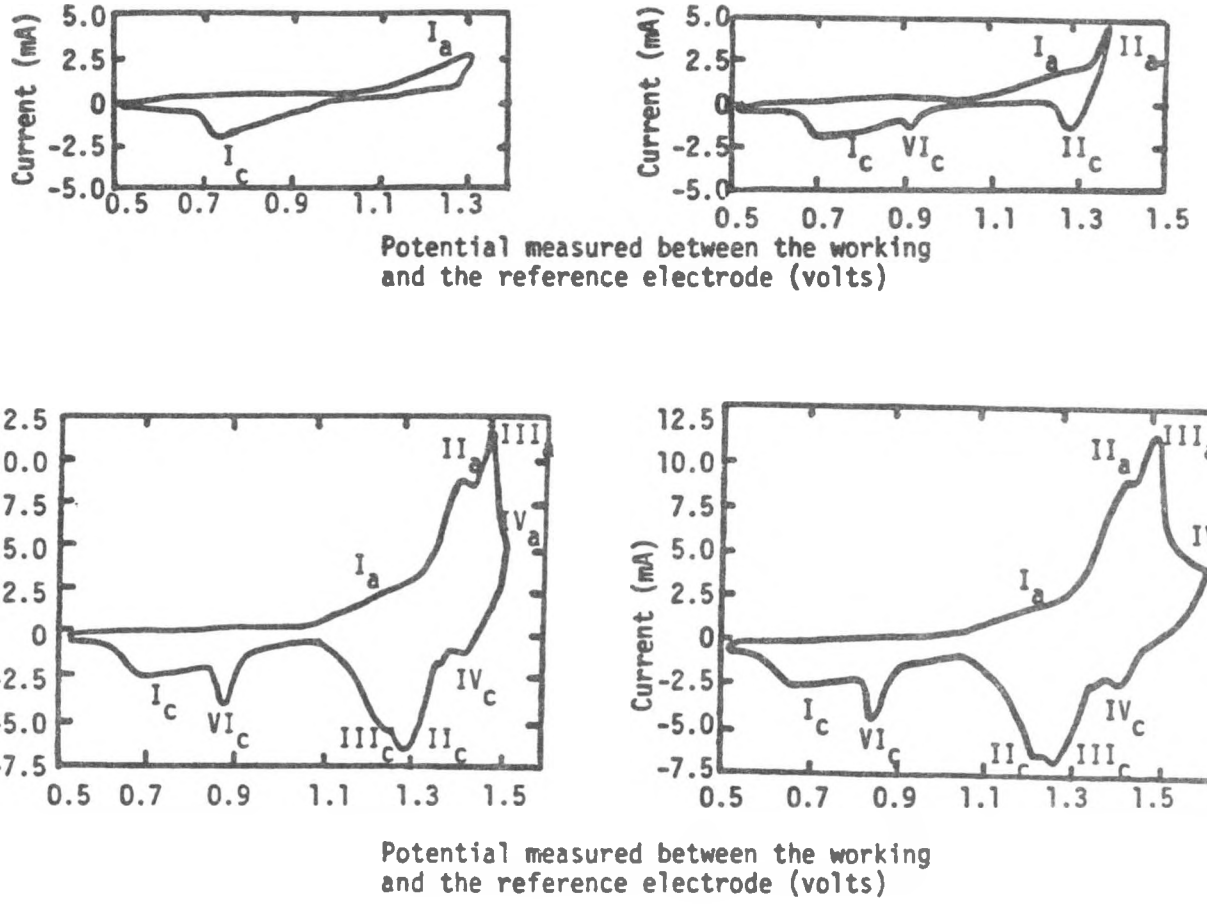

Fig. 5 The cyclic voltammograms obtained from the planar Fe electrode in LiCl-KCl eutectic saturated with Li_2S.
scan rate = 0.1 mV/sec, temperature = 510°C.

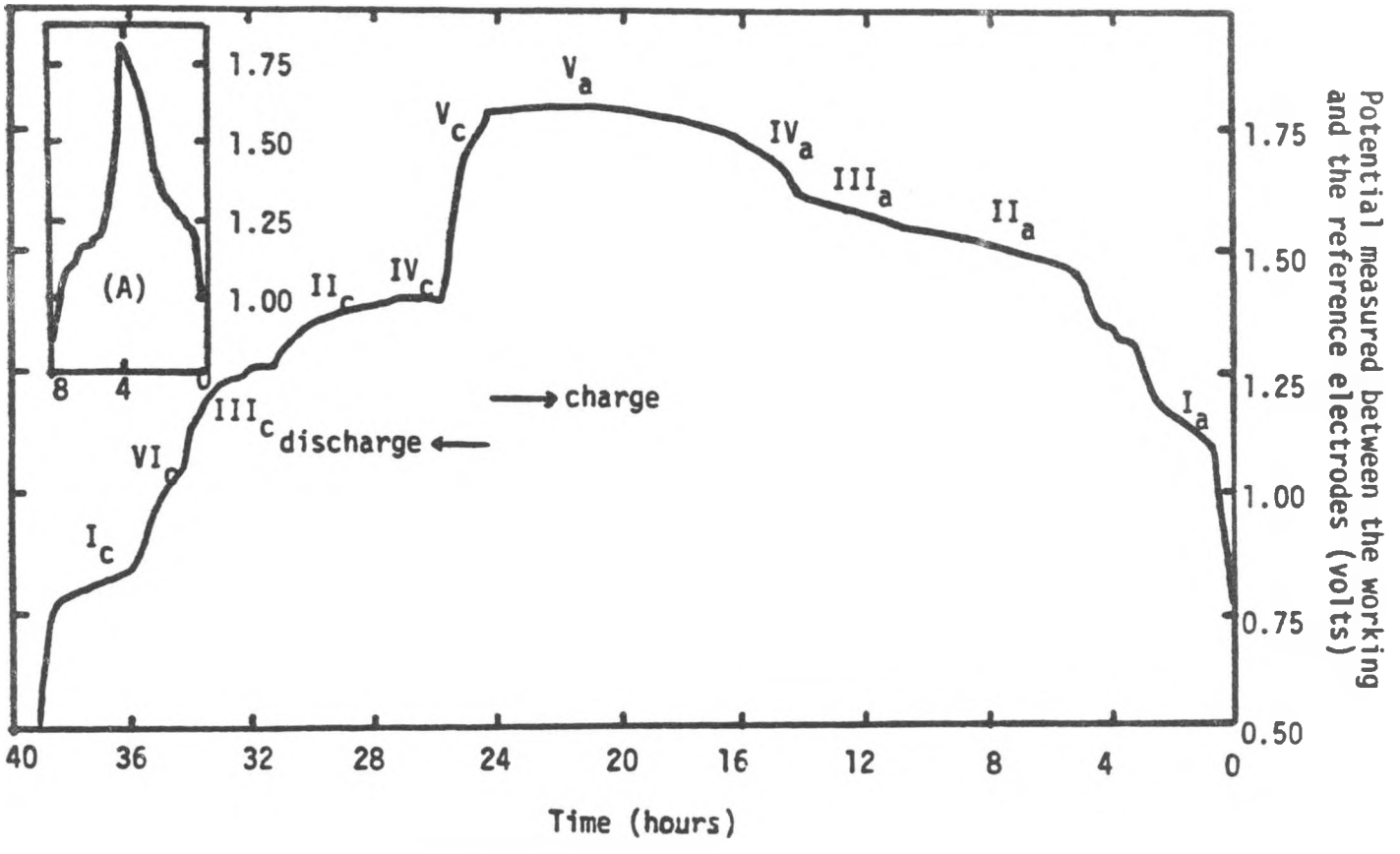

Fig. 6 The galvanostatic charge-discharge curves for the planar Fe electrode in LiCl-KCl eutectic saturated with Li_2S. current = 0.7 mA, temperature = 430°C.

6 (A) The galvanostatic charge-discharge curves for a pure molybdenum electrode in LiCl-KCl eutectic saturated with Li_2S. current = 0.7 mA, temperature = 430°C.

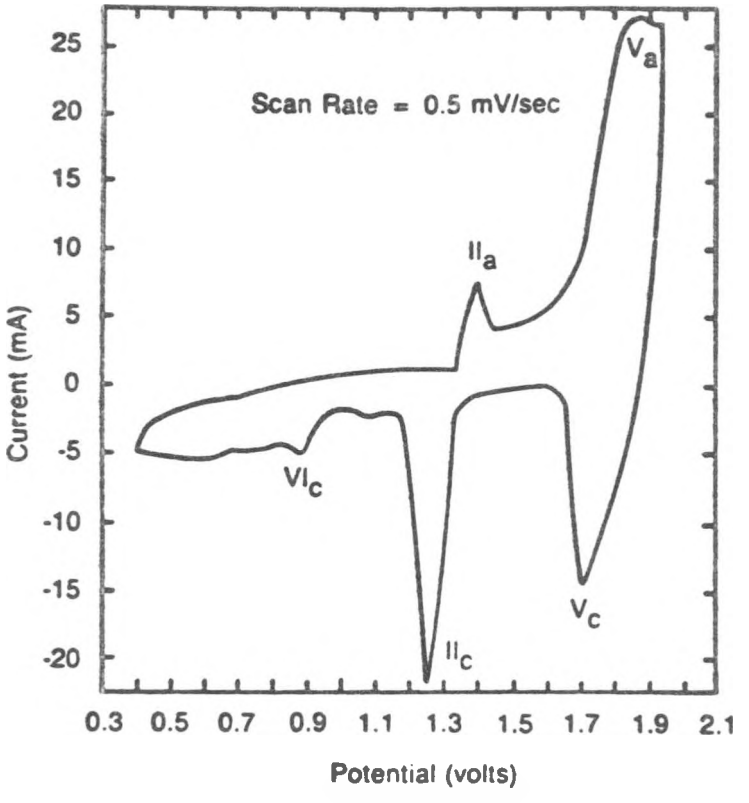

Fig. 7 Cyclic voltammograms obtained from the iron electrodes in the K-free electrolyte. Temperature = 470°C.

CAPACITY DECLINE OF IRON DISULFIDE ELECTRODES IN LITHIUM-ALLOY/METAL SULFIDE HIGH-TEMPERATURE CELLS

G. Barlow

Gould Inc.,
40 Gould Center,
Rolling Meadows,
Illinois 60008.

ABSTRACT

The lithium-alloy/iron disulfide couple has been considered for a molten-salt battery system for many years because of its high theoretical energy density. However, as a practical system it has failed to live-up to its early promise since there is a fairly rapid decay in the capacity of the upper-plateau discharge reaction. Acheiving a stable upper-plateau capacity is critical therefore, to further development of the Li-alloy/FeS_2 system for applications which require a long life battery.

It has been postulated that the rapid decline of the iron disulfide electrode upper-plateau capacity is primarily the result of sulfur loss due to thermal decomposition of the iron disulfide at typical cell operating temperatures of approximately 450C. The work discussed in this paper has been specifically directed towards determining whether or not the capacity loss is entirely thermally related and if so, how the problem can be overcome in a practical cell which can be operated at discharge rates in the C/6-C/3 range for extensive periods.

Thermal gravimetric and x-ray diffraction studies on pure FeS_2 and FeS_2/electrolyte mixtures in the temperature range 350C-600C, show that iron disulfide is thermally unstable. At temperatures above 500C the decomposition to pyrrhotite occurs in a few hours, below 400C however the results indicate that the decompositon is relatively slow and that it may take several thousand hours before FeS_2 is significantly decomposed.

In-cell experiments utilizing various alkali metal/halide electrolytes with melting points in the range 180-350C have shown that the rate of decline of the upper-plateau capacity is reduced when the cell operating temperature is lowered. However, the cell reaction kinetics are also much slower, particularly at 200C, so that cells have to be operated at lower current densities.

POWER PERFORMANCE OF LiAlSi/(FeNi)S_2 CELLS

Laszlo Redey
Argonne National Laboratory
9700 S. Cass Ave.
Argonne, IL 60439 USA

ABSTRACT

Half-cell and model-cell experiments have been conducted to investigate the electrochemical performance of (Fe-Ni)S_2 electrodes and Li-Al-Si/(Fe-Ni)S_2 cells. The electrodes, fabricated with 0.5- to 2-Ah theoretical capacity, have been investigated in both LiCl-LiBr-KBr and LiF-LiCl-LiBr electrolyte in the temperature ranges of 320 to 500°C and 450 to 500°C, respectively. Nickel-sulfide additive was found to improve the kinetics of the FeS_2 electrode. Power performance and charge acceptance of the cell improves to a great extent when Li_2S is used in excess of the stoichiometric amount required by the metal sulfide formation. The presence of lithium sulfide at the end of charge provides a unique overcharge protection mechanism.

EXPERIMENTAL TECHNIQUE

Half-cell and model-cell (a smaller-scale cell that closely simulates the behavior of the actual cell) experiments have been conducted to investigate the electrochemical performance of mixed iron-nickel sulfide, $(Fe_{1-m}Ni_m)S_y$ electrodes and $Li_x(Al_{0.5}Si_{0.5})/(Fe_{1-m}Ni_m)S_y$ cells. In these formulae, m is 0 to 1, and $\underline{x}$ and $\underline{y}$ refer to the compositions of the fully charged electrode materials. Positive electrodes have been investigated in the ranges of $\underline{y}$ = 1 to 2; in the model-cell experiments, $\underline{x}$ has been equal to 2. The composition of the cycled electrodes is specified by x and y at any point on any half-cycle curve on the basis of Faraday's law; consequently: $0 \leq x \leq \underline{x}$ and $0 \leq y \leq \underline{y}$. In this symbolism, $\underline{x}$, x, $\underline{y}$, y, and m indicate apparent atom ratios in the negative or positive active materials without referring to actual phases or compositions.

The electrodes, fabricated with 0.5- to 2-Ah theoretical capacity, have been investigated in both a 25% LiCl-37% LiBr-38% KBr low-melting electrolyte (compositions in mol %) and a 22% LiF-31% LiCl-47% LiBr all-Li^+-cation electrolyte; the temperature ranges of the investigations were 320 to 500°C and 450 to 500°C, respectively.

The electrodes in half-cell experiments were investigated in a cell described earlier [1]. The model-cell experiments were conducted in a test cell [2] that had 1.2-cm^2 electrodes and a BN-felt separator treated with MgO powder between them. The test cell was operated under both open or sealed conditions. The model cells and the test electrodes of the half-cell experiments were cycled galvanostatically with 25 to 400 mA/cm^2 current densities under various programs up to at least 50 cycles, and, in most cases, to hundreds of cycles.

Area-specific impedances as a function of time, ASR_t and $_iASR_t$, were measured by the current interruption/potential relaxation technique [3] and the high-intensity current pulsing method [4], respectively. The subscript t is the time after the current interruption in ASR_t and after initiation of the current pulse in $_iASR_t$. Area-specific peak power ($ASPP_t$) was calculated by the

$$ASPP_t = \frac{(E^\circ)^2}{4(_iASR_t)} \qquad \text{Eq. 1}$$

relationship. E° is the open-circuit cell voltage at a specified depth of discharge. This simple calculation of the $ASPP_t$ is acceptable because ASR_t was found to be almost independent of the applied pulse current density for a variety of high-temperature electrodes in both the previous [4] and the present experiments. Digital data acquisition and data analysis were used to find and represent relationships between experimental conditions and electrode/cell performance.

RESULTS AND DISCUSSION

Area-specific impedances of various investigated positive electrodes as measured during discharge are shown in Fig. 1. The area-specific impedance

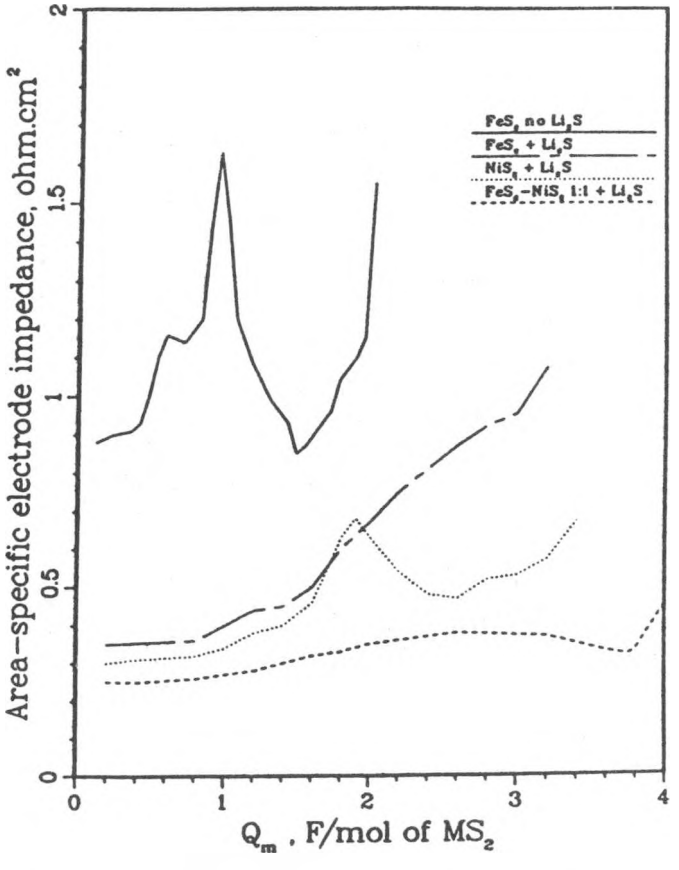

Fig. 1. Area-Specific Impedances (15-s values) of Metal-Sulfide Electrodes in All-Li^+-Cation Electrolyte at 475°C as Function of Utilization. In Fully Charged Condition, $Q_m = 0$.

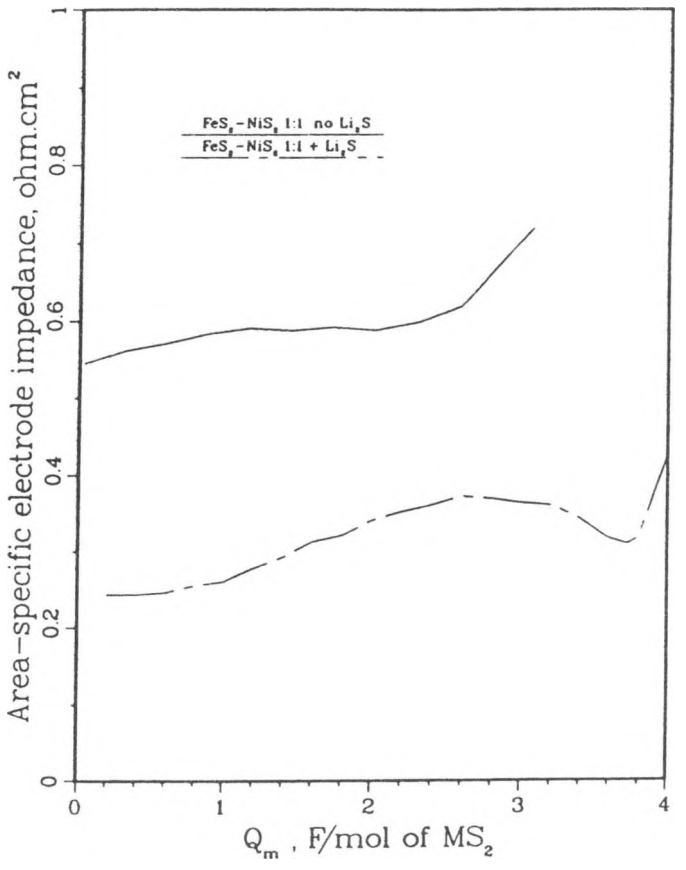

Fig. 2. Effect of Li_2S on 15-s Area-Specific Impedance of an FeS_2-NiS_2 (1:1) Electrode (All-Li^+-Cation Electrolyte, 475°C). In Fully Charged Condition, Q_m = 0.

vs. utilization diagrams give a good quantitative indication of the electrode performance. (In Figs. 1-3, utilization is expressed as a molar electrochemical quantity, Q_m, in faraday/mol of MS_2 units.) The area-specific impedance relates to the power capability of the electrode; and the range of Q_m embraced by any of the curves indicates the available capacity under the conditions of the discharge as specified by current density, cut-off voltages (both charge and discharge), temperature, etc. FeS_2 active material alone has high impedance and poor utilization. Furthermore, it shows very extensive variation of impedance. Lithium sulfide additive to FeS_2 (1:0.2 mol ratio) greatly decreases the impedance, especially in the "upper-plateau" region, and substantially extends the utilization. (Note that in Fig. 1 the upper-plateau region is at the low Q_m values; at complete charge, Q_m = 0.) The same effect of the Li_2S additive has been observed on the NiS_2 electrode. Addition of both Li_2S and NiS_2 to FeS_2 further decreases the impedance and increases utilization. In this case, the area-specific impedance is almost uniform along the whole span of the discharge (see bottom curve in Fig. 1). The uniformity of the impedance may result from the performance of the electrode in the high-impedance sections of one of the metal-sulfide components being boosted by the favorably low impedance of the other component in the same section and vice versa (a "mutually distributed current collector" effect.) At the present state of investigation, however, we can neither

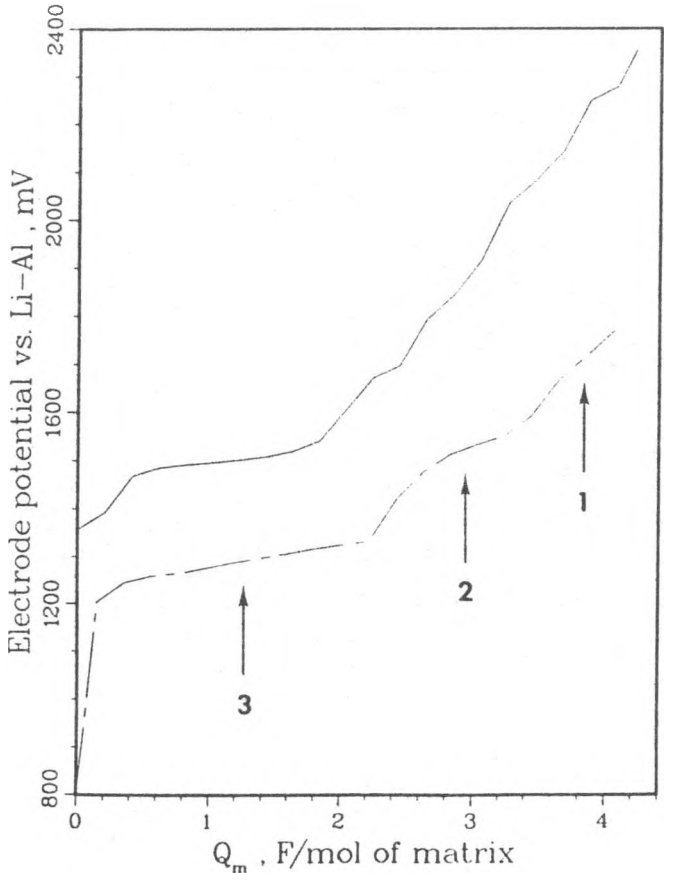

Fig. 3. Potentials vs. Li-Al of a Cycled FeS_2-NiS_2 (1:1) Electrode. Conditions of the Measurement: Li_2-S-Saturated All-Li^+-Cation Electrolyte, 475°C, 200 mA/cm², 0.8- and 2.35-V Cut-Off Potentials, 51st Cycle. Arrows Indicate the Middle of the Characteristic Discharge Plateaus. In Fully Discharged Condition, Q_m = 0.

exclude nor confirm the role of other effects, e.g., the role of multiple-sulfide-phase formations instead of (or parallel to) the simple physical effect of the mutually distributed current collector.

Figure 2 shows the impedances of the mixed FeS_2-NiS_2 electrodes both with and without excess Li_2S. The Li_2S additive lowers electrode impedance and extends utilization of the active material. When compared with those in Fig. 1, these two plots show that the very low impedance of the positive electrode was achieved by a synergetic effect of the mixed iron-nickel sulfides and the Li_2S additives.

Potentials of a cycled mixed FeS_2-NiS_2 (1:1) + Li_2S electrode (thickness: 4 mm; area loading: 0.924 Ah/cm² at Q_m=4) are shown in Fig. 3 on the Li-Al potential scale. In this figure, Q_m is equal to zero at the fully discharged state. The electrode was cycled with 200 mA/cm² current density between 0.8 and 2.35 V cut-off potentials. Even at this high current

density, the active material utilization is very good, as shown by the long span of Q_m on the discharge curve. The numbered arrows indicate the middle of the three characteristic sections of the discharge curve. Although the charge curve is more complex, it nevertheless indicates the very good charge acceptance of the electrode. In spite of the rather high charge cut-off potential, the Mo current collector showed no sign of corrosion even after 300 cycles.

The effects of electrolyte composition and temperature on the power performance of the mixed-sulfide electrode are summarized in Fig. 4 by two

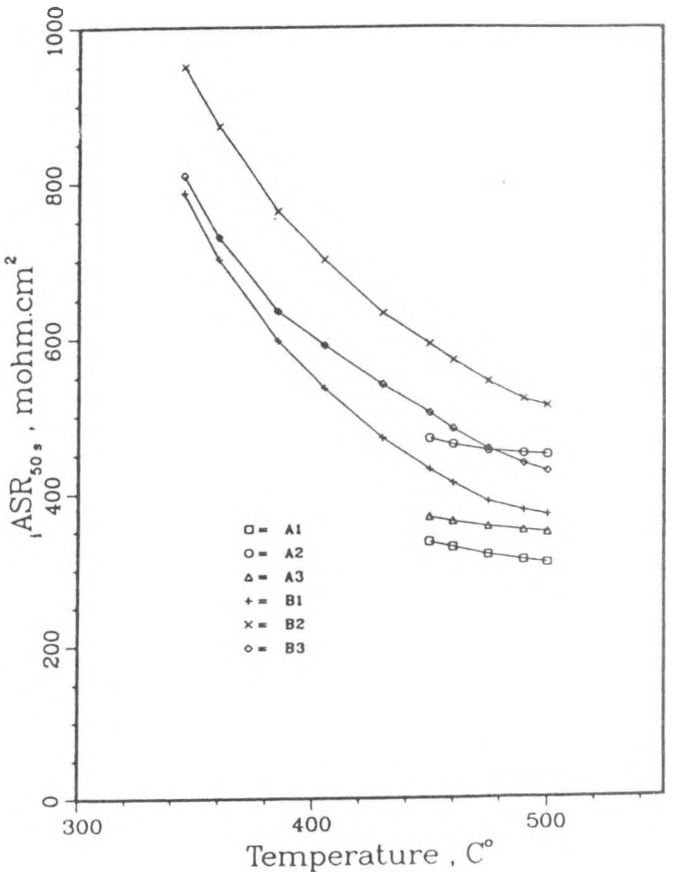

Fig. 4. Effects of Electrolyte Composition and Temperature on Area-Specific Impedance Measured in the 50th Second of 1 A/cm^2-Intensity Current Pulses. A: Li_2S-Saturated All-Li^+-Cation Electrolyte, B: Li_2S-Saturated Low-Melting Electrolyte: 1, 2 and 3 Refer to Approximate Utilizations of the Electrode as Indicated by the Arrows in Fig. 3.

families of plots. The power performance is characterized by the area-specific impedance ($_iASR_{50s}$) measured in long, high-intensity current pulses (1 A/cm^2, 50 s). Plots marked by A were measured in the all-Li^+-cation electrolyte, and those marked by B were measured in the LiCl-LiBr-KBr

electrolyte. For each electrolyte, the impedance values (shown as function of temperature) were measured at approximately the middle of the characteristic sections of the discharge curve, as indicated by the numbered arrows in Fig. 3. The effect of temperature is rather small in the all-Li^+-cation electrolyte, but the operational range is narrow because of the high melting point and the thermal stability problems of metal sulfides above 480°C. Although impedance substantially increases with decreasing temperature in the low-melting electrolyte, the ${}_iASR_{50\ s}$ = 600-800 mohm·cm² values indicate an acceptable performance even at 380°C. At 320° the ${}_iASR_{50s}$ values are higher than 1 ohm·cm². Thus, the practical operating temperature range is very broad in the low-melting electrolyte.

The synergetic effect of the mixed sulfides and the surplus of Li_2S provides an improvement in power output over a cell that utilizes FeS_2 or NiS_2 active material alone. Figure 5 shows the effect of the electrolyte

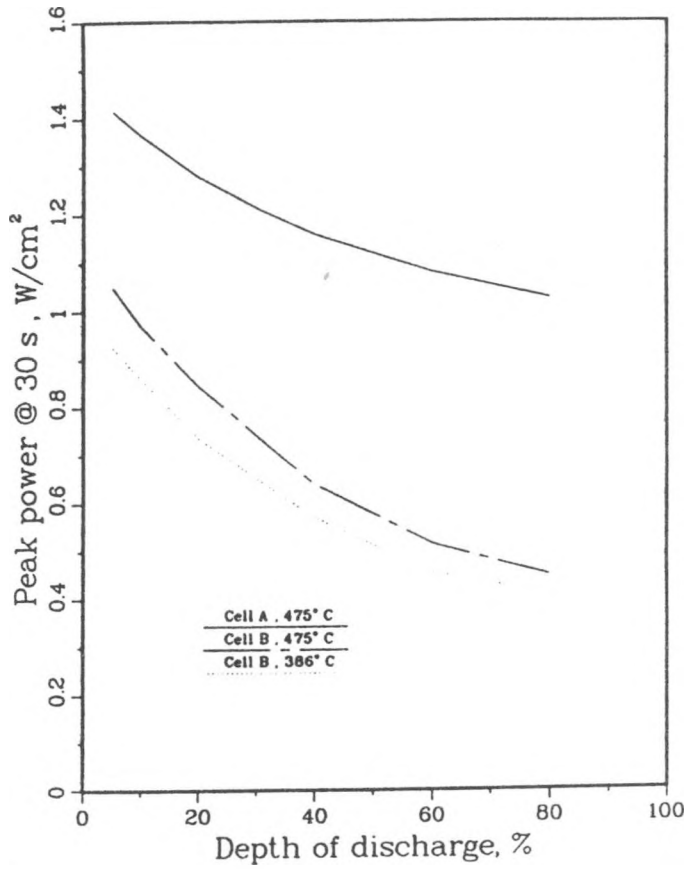

Fig. 5. Peak-Power Performance of LiAlSi/(FeNi)S_2 Cells in (A) All-Li^+-Cation and (B) Low-Melting Electrolytes

composition and temperature on power performance of the model cells. The sustained peak power at 30 s of a cell (m = 0.5, x = 2, and y = 2, all-Li^+-cation electrolyte) was measured as 1.4 W/cm² at 10% DOD and 1.1 W/cm² at 80% DOD. The all-Li^+-cation electrolyte and the higher temperatures favor better power performance. The improved power is also associated with higher rates

of charge or discharge; a typical eight-hour charge rate can be reduced to about one hour, and a typical four-hour discharge rate to less than one hour.

A sufficient quantity of Li_2S at the end of charge provides a unique, very effective overcharge-protection mechanism which is probably similar, in its effect, to that of the lead-acid battery. Overcharge protection in the cell may occur through a shuttle mechanism which lets the overcharge products react with each other without altering the general conditions of the active materials of the electrodes. In an experiment designed to test overcharge tolerance, a model cell performed with its original capacity and power capability in subsequent cycles after repetitive overcharges of 2-5 times the nominal capacity.

CONCLUSIONS

The kinetics of the iron sulfide electrode are significantly improved by the addition of nickel sulfide. Power performance and charge acceptance of the Li-Al-Si/(Fe-Ni)S_2 cell improve to a great extent when Li_2S is used in excess of the stoichiometric amount required by the metal sulfide formation. A sufficient quantity of Li_2S at the end of charge provides a unique overcharge protection mechanism.

ACKNOWLEDGMENT

This work was supported by the U.S. Department of Energy, Office of Energy Storage, under Contract W-31-109-Eng-38. The author is grateful to Drs. J. Ackerman and J. Battles of the Argonne National Laboratory for their encouragement and support.

REFERENCES

1. L. Redey and D. R. Vissers, "New Test-Electrode Design for Active Material Characterization," Extended Abstracts, 163rd Electrochem. Soc. Meeting, San Francisco, CA, Vol. 83-1, p. 69 (1983).

2. L. Redey, to be published.

3. L. Redey, D. R. Vissers, J. Newman, and S. Higuchi, "Electrode Characterization of LiAl/FeS Cells by Voltage-Loss Investigation," Proc. Symp. on Porous Electrodes: Theory and Practice, H.C. Maru et al., eds, The Electrochem. Soc. Inc., Pennington NJ, Vol. 84-8, p. 322 (1984).

4. L. Redey, "Characterization of Voltage Losses during High-Intensity Current Pulses in Reactive, Porous Electrodes of Molten-Salt Cells," Extended Abstracts, Symp. of Int. Soc. of Electrochemistry, Berkeley, CA, p. 811 (Aug. 5-10, 1984).

A STABLE IRON DISULFIDE SECONDARY CELL WITH LiCl-LiBr-KBr ELECTROLYTE

Thomas D. Kaun
Argonne National Laboratory
9700 S. Cass Avenue
Argonne, IL 60439

ABSTRACT

Results of innovations in the Li-Al/FeS_2 cell are reported. This cell incorporates two major changes from earlier cells of this type: (1) a novel electrolyte, 25 mol % LiCl-37 mol % LiBr-38 mol % KBr (m.p. 310°C) vs. 58 mol % LiCl-42 mol % KCl (m.p. 352°C) and (2) a high loading density (2.4 vs. 1.5 Ah/cm^3) for the FeS_2 electrode, which is then operated only on its higher voltage plateau (1.75 avg. V vs. LiAl). This cell design is designated "dense upper-plateau (U.P.) FeS_2 cell" to distinguish it from the conventional "two-plateau (T.P.) FeS_2 cell."

Prismatic bicells (24-48 Ah capacity) of 100-cm^2 separator area (BN felt) were fabricated for evaluating performance and cycle life. Cycle life testing was conducted at 397°C with a 4-h discharge rate (50 mA/cm^2) and 8-h charge rate (25 mA/cm^2). For these conditions, the first cell exhibited 89% utilization of the U.P. FeS_2 electrode capacity, and the voltage/capacity characteristics of the U.P. FeS_2 electrode continued to show virtually no change after 400 cycles (5400 h) of operation. The energy density of this U.P. FeS_2 cell is enhanced as a result of approximately 50% higher utilization of cell capacity and a 10% higher average discharge voltage at 50 mA/cm^2 than a comparable T.P. FeS_2 cell. Specific power at 80% depth of discharge (DOD) is also enhanced by approximately 100% because the cell voltage at that point in the discharge is about 0.3 V higher than that of the T.P. FeS_2 cell with much lower internal cell resistivity.

INTRODUCTION

Recent improvements in the Li-Al/FeS_2 cell have led to stable cycle life with a greater than 50% increase in specific energy and specific power over earlier FeS_2 cells. Earlier cells had unacceptably high capacity decline rates, 0.10 to 0.25% per cycle (1), which were due to sulfur migrating from the disulfide electrode into the separator region and depositing there as Li_2S (2). Approaches for reducing the capacity decline rates on the upper voltage plateau of the earlier cells also reduced cell performance.

The improved Li-Al/FeS_2 cell (3) has two major changes from earlier cells of this type: a novel electrolyte, 25 mol % LiCl-37 mol % LiBr-38 mol % KBr (4) (m.p. 310°C), rather than 58 mol % LiCl-42 mol % KCl (m.p. 352°C), and a higher loading density (2.4 vs. 1.5 Ah/cm^3) for the FeS_2 electrode,

which is then operated only on its higher voltage plateau (1.75 V vs. Li-Al). This "upper plateau" reaction can be written as:

$$FeS_2 + 2Li^+ + 2e^- \leftrightarrows Li_2FeS_2, \qquad [1]$$

although it is actually a series of three consecutive reactions (5). In this mode of operation, the electrode will be designated a dense, upper-plateau (U.P.) FeS_2 electrode. In a conventional "two-plateau (T.P.)" FeS_2 electrode, the lower-voltage (1.33 avg. V) reaction also is used. This reaction is:

$$Li_2FeS_2 + 2Li^+ + 2e^- \leftrightarrows 2Li_2S + Fe. \qquad [2]$$

The new electrolyte permits reduced operating temperatures of 380-425°C. Earlier cells with LiCl-KCl electrolyte were operated in a temperature range of 425-460°C.

EXPERIMENTAL

Prismatic bicells (24- and 48-Ah capacity) with separator area of 100 cm^2 (BN felt, Kennecott Corp.) were fabricated for evaluating performance and cycle life of the Li-Al/LiCl-LiBr-KBr/U.P.-FeS_2 system. The initial test cell duplicated earlier test cells used for evaluating the Li-Al/LiCl-KCl/T.P.-FeS_2 system (1). The electrodes (8.7 cm high x 6.3 cm wide) were contained behind perforated-sheet current collectors--molybdenum for the central FeS_2 electrode and 1008 steel for the two Li-Al electrodes.

The positive electrode contained FeS_2 with 15 mol % CoS_2 additive for a total theoretical capacity of 24- or 48-Ah (on the upper plateau). The slurry-formed negative electrodes (6) contained 53 at. % Li-Al alloy for 35- or 70-Ah capacity with 0.9-Ah/cm^3 loading density. Cells were assembled with a BN powder feedthrough seal. The electrolyte (Anderson Physics Lab.) is added to the cells in the molten state. Cells were subsequently operated in an argon glovebox.

Cycle-life testing at an 8-h charge rate and 4-h discharge rate (50 or 100 mA/cm^2) was controlled between voltage cutoffs of 2.05 and 1.25 V (IR included), respectively. A Ni/Ni_3S_2 reference electrode indicated working-electrode potentials during the deep-discharge cycling. Current interrupts of one-second duration were used to evaluate electrode and cell resistances. Power measurements were derived by integrating voltage at constant-current pulses (10-100 A) of 15-s duration.

RESULTS AND DISCUSSION

The Li-Al/LiCl-LiBr-KBr/U.P.-FeS_2 cell, which was cycle-life tested at 397°C, had at least 50% higher energy density than a Li-Al/LiCl-KCl/T.P.-FeS_2 cell of the same size (1), which was operated at 427°C. The voltage/capacity curves of these two cell types (each of approximately 24-Ah theoretical capacity) are presented in Fig. 1. Energy density at 50 mA/cm^2 for the U.P.-FeS_2 cell was enhanced as a result of an approximately 50% higher utilization of the capacity and a 10% higher average discharge voltage. The energy density at higher discharge rates, 100 and 150 mA/cm^2, showed even greater

improvement, with the utilization of capacity ranging from 82 to 75% at 397°C. The U.P.-FeS_2 cell is capable of an 82% utilization at 150 mA/cm² when operated at 427°C. Cell capacity at a discharge current density of 100 mA/cm² only slightly decreased as temperature was decreased from 427°C to 388°C. We also found good operability at temperatures as low as 380°C.

The 48-Ah cell tested the performance of doubly thick (8 mm) U.P.-FeS_2 electrodes. The utilization vs. discharge current density of the 48-Ah cell

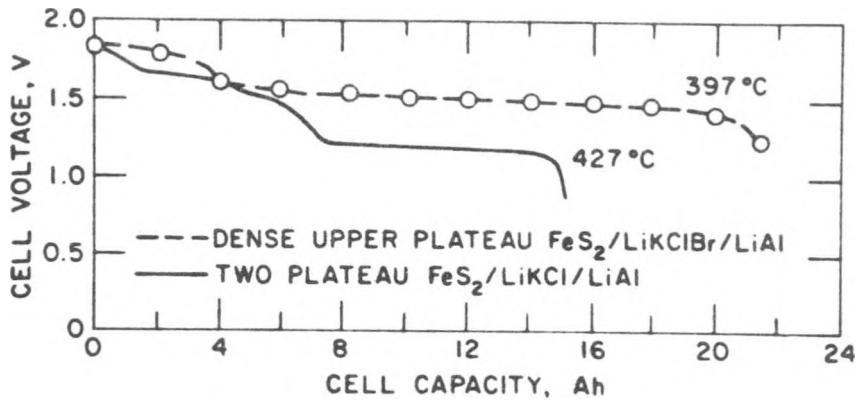

Fig. 1. Voltage/Capacity Curves at a Discharge Rate of 50 mA/cm².

matched that of the 24-Ah cell, as shown in Fig. 2. (High energy density of cells is developed from high utilization of thick electrodes.) At a discharge current density of 100 mA/cm², the thick-electrode U.P.-FeS_2 cell provided nearly a fourfold increase in energy storage with respect to separator area compared with that of the T.P.-FeS_2 cell; theoretical capacity was doubled and utilization was nearly doubled. (Tests with six cells of 1-Ah capacity confirmed these results.)

The 48-Ah cell demonstrated an outstanding combination of high energy and power density. The power density at 80% depth of discharge (DOD) was enhanced by at least 100% because of two factors. First, the cell voltage at 80% DOD was about 0.3 V higher than that of a T.P.-FeS_2 cell (see Fig. 1). Second, cell resistivity was lower for the dense U.P.-FeS_2 cell, ranging from 0.65 to 0.85 Ω-cm² for 5 to 80% DOD, respectively, compared with 1.2 to 1.6 Ω-cm² for the T.P.-FeS_2 cell. The higher voltage and lower resistivity of the U.P.-FeS_2 cell boost cell power density from 0.3 to 0.8 watts per square centimeter of separator area at 80% DOD.

The improved power and energy densities of the iron disulfide electrode at the reduced operating temperatures of 388 to 427°C are believed to be caused by two factors. One is improved electronic conductivity of the electrode. According to the Bruggeman equation (7)

$$Km = (1 - f)^{3/2} \qquad [3]$$

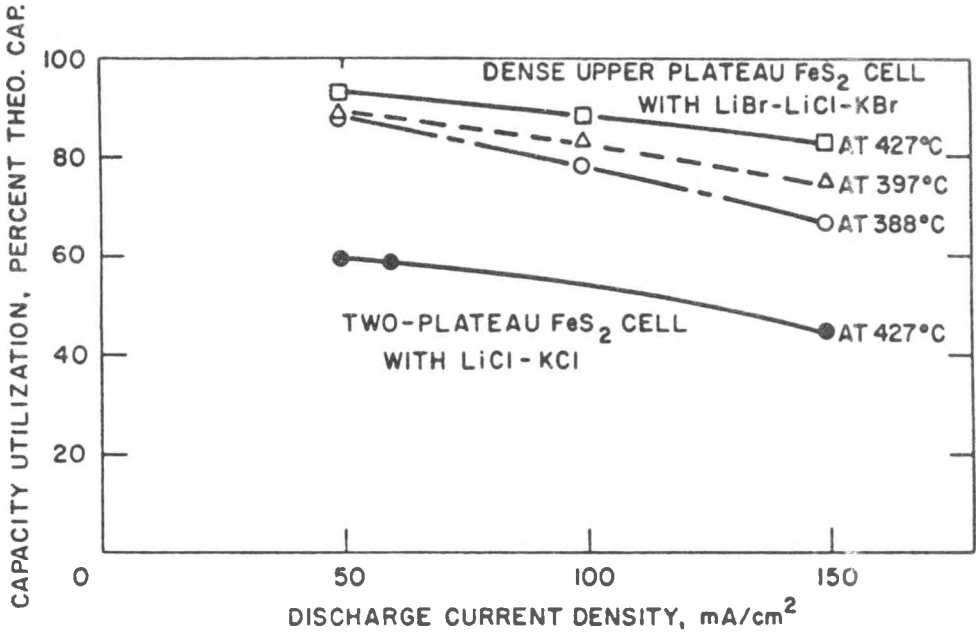

Fig. 2. Utilization vs. Discharge Current Density for Li-Al/FeS_2 Cells of 100 cm^2 Separator Area. The electrode thickness of the U.P.-FeS_2 cell was double that of the T.P.-FeS_2 cell.

where Km = bed conductivity/dense body conductivity and f = electrolyte fraction. Thus, the increased electrode loading density (from 32 to 50 vol %) doubles the electronic conductivity of the iron disulfide electrode. The second factor is an increased "dynamic range" with the LiCl-LiBr-KBr electrolyte. At 400°C, this electrolyte has a liquidus that extends over a Li^+/K^+ ratio of 1.25 to 2.6; for LiCl-KCl, the range is only 1.25 to 1.81. The broader liquidus for the LiCl-LiBr-KBr electrolyte would tend to alleviate salt crystallization; it has been postulated that the crystallization of LiCl-KCl impedes operation of molten-electrolyte cells at high current density (8).

The capacity utilization vs. cycle number for the U.P.-FeS_2 cell is shown in Fig. 3 (the coulombic efficiency of the cell is >99%). Its utilization is 89% at 50 mA/cm^2. The cell capacity has been nearly constant through more than 400 cycles and 5400 hours, and the cell voltage vs. capacity curve was little changed (as in Fig. 1) during this time. In this test, the cell was charged at 25 mA/cm^2 to a charge cutoff voltage of 2.05 V. These values are greater than those that could be used with the Li-Al/LiCl-KCl/T.P.-FeS_2 cell while maintaining stable capacity (1). Electrode potentials (vs. the Ni/Ni_3S_2 reference electrode) indicate that both electrodes, Li-Al and FeS_2, mutually attain full charge. The discharge capacity is voltage limited by the upper-plateau capacity of the positive electrode.

Apparently, both time-related and cycle-related capacity loss has been eliminated in this advanced cell. Considerable attention has been given to gaining an understanding of the mechanisms for capacity loss of FeS_2 in LiCl-KCl. Preto et al. (5) indicated that capacity loss for FeS_2 in LiCl-KCl

ACKNOWLEDGMENT

This work was supported by the U.S. Department of Energy, Office of Energy Storage under contract W-31-109-Eng-38. The author is grateful to M. F. Roche, J. E. Battles, and J. P. Ackerman for their support.

REFERENCES

1. F. J. Martino, W. E. Moore, and E. C. Gay, Argonne National Laboratory Report ANL-83-62, pp. 29-38 (1983).

2. J. E. Battles, F. C. Mrazek, N. C. Otto, Argonne National Laboratory Report ANL-80-130 (1980).

3. T. D. Kaun, J. Electrochem. Soc. 132, 3063 (1985).

4. A. G. Bergman and A. S. Arabadzhan, Russ. J. Inorg. Chem. (English Trans.) 8, 369 (1963).

5. S. K. Preto, Z. Tomczuk, S. Von Winbush, and M. F. Roche, J. Electrochem. Soc. 130, 264 (1983).

6. T. D. Kaun, U. S. Patent No. 4,358,513 (1983) and U.S. Patent No. 4,446,212 (1984).

7. D. A. Bruggemann, Ann. Physik 24, 636 (1935).

8. C. E. Vallet and J. Braunstein, J. Electrochem. Soc. 125, 1193 (1978).

9. D. Warin, Z. Tomczuk, and D. R. Vissers, J. Electrochem. Soc. 130, 64 (1983).

10. Z. Tomczuk and D. R. Vissers, Argonne National Laboratory Report ANL-83-62, pp. 18-21 (1983).

HEAT GENERATION IN LITHIUM-ALLOY, IRON DISULFIDE, HIGH-TEMPERATURE BATTERIES

H. F. Gibbard
Power Conversion, Inc.
495 Boulevard
Elmwood Park, NJ 07407

and

D. M. Chen
Anadigics, Inc.
35 Technology Drive
Warren, NJ 07060

ABSTRACT

Calorimetric measurements were made of the heat flow from an engineering-scale lithium-(aluminum, silicon)/iron disulfide cell with all-lithium-cation, molten-salt electrolyte during isothermal discharge at various currents. The discharge process was endothermic on the upper (FeS_2) plateau and exothermic on the lower (FeS) plateau. Measurements were made of the open-circuit potential of "pellet" cells as a function of state of charge and temperature. The temperature coefficient was positive on the upper plateau, and varied from 0.49 mV/K for fully charged cells to 0.74 mV/K for cells discharged by 30 to 50 percent of their actual capacity. On the basis of work performed at Argonne National Laboratory, these temperature coefficients should correspond to the reaction of FeS_2 to $Li_3Fe_2S_4$ and of $Li_3Fe_2S_4$ to $Li_{2+x}Fe_{1-x}S_2$, respectively.

INTRODUCTION

High-temperature lithium-alloy, iron sulfide batteries are under development for use in electric vehicles and in military applications requiring high specific energy and high volumetric energy density. Thermal management is an important aspect of the design of these batteries because of their high operating temperature and high energy density. The measurement of heat generation rates during cell discharge provides essential data for modeling and design of systems for thermal management of these batteries.

Chen and Gibbard[1] have reported calorimetric measurements and thermodynamic calculations of heat generation rates in LiAl/FeS cells. Recently we have been interested in the development of cells with higher energy densities. This paper describes results of calorimetric measurements of heat generation rates in Li-(Al, Si)/FeS_2 cells, where the replacement of FeS by FeS_2 yields a higher specific electrical capacity and a higher operating voltage.

EXPERIMENTAL

The high-temperature battery calorimeter used in previous measurements on FeS cells[1] was described by Hansen, et al.[2] The instrument was modified by the replacement of all silver-plated brass parts by nickel parts, and by strengthening the nickel-foil heaters and their leads. With these changes the calorimeter could be used for periods of several months at temperatures up to 500°C.

Initial attempts to measure the cell potential of, and heat flow from, iron disulfide cells with steel current collectors failed because of rapid corrosion and loss of upper-plateau capacity of the positive electrode. Accordingly, a cell incorporating molybdenum current collectors was fabricated. The prismatic cell contained three electrodes, each divided into two parts by a central sheet current collector. The thickness and width of the cell were 3.2 cm and 13.3 cm, respectively, which are the same as the dimensions of the FeS cells studied previously[1]. The height was 10.5 cm, which is half that of the FeS cells. The composition of the central positive electrode, by weight, was as follows: 65 percent iron disulfide, 6.7 percent molybdenum powder (added to enhance electronic conductivity), and 28.3 percent electrolyte. The composition of the electrolyte was 22.03 percent LiCl, 9.56 percent LiF and 68.41 percent LiBr. The composition of the two negative electrodes was 52 percent lithium-aluminum alloy (20.0 percent lithium), 13 percent lithium-silicon alloy (47.5 percent lithium), and 35 percent electrolyte. The total negative capacity, based on lithium content, was 185 Ah; the positive capacity, based on four-electron reduction of FeS_2, was 64.4 Ah. The separator was composed of 65 percent electrolyte and 35 percent magnesium oxide powder. Both sides of the positive electrode were covered by thin layers of yttria felt. All metal parts in electrical contact with the positive electrode were made of molybdenum.

RESULTS

The cell was cycled was subjected to seven cycles of charge at 4.0 A and discharge at 2-10 A at 450°C until its capacity to a lower cutoff voltage of 1.0 V stabilized at 50 Ah. Figure 1 shows the cell voltage plotted against

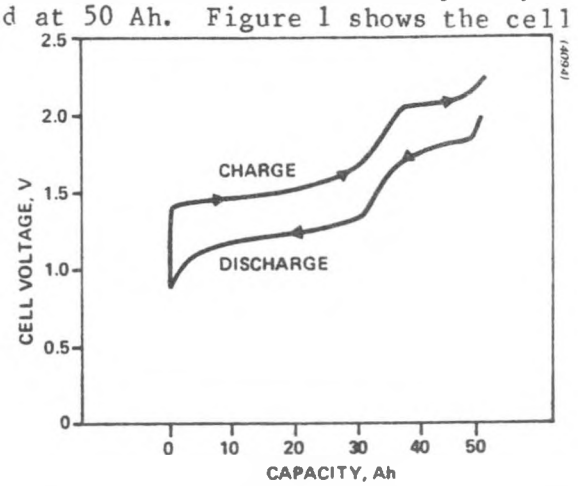

Fig. 1. Cell terminal voltage on the fifth charge-discharge cycle of an FeS_2 cell at 450°C.

capacity for a typical charge-discharge cycle. After showing good coulombic efficiency and two distinguishable voltage plateaus, the cell was placed in the high-temperature calorimeter for the measurement of heat generation.

The cell terminal voltage and heat generation rate for discharge at constant currents of 6,8, 10 and 12 A at 450°C are shown in Figures 2-5. In

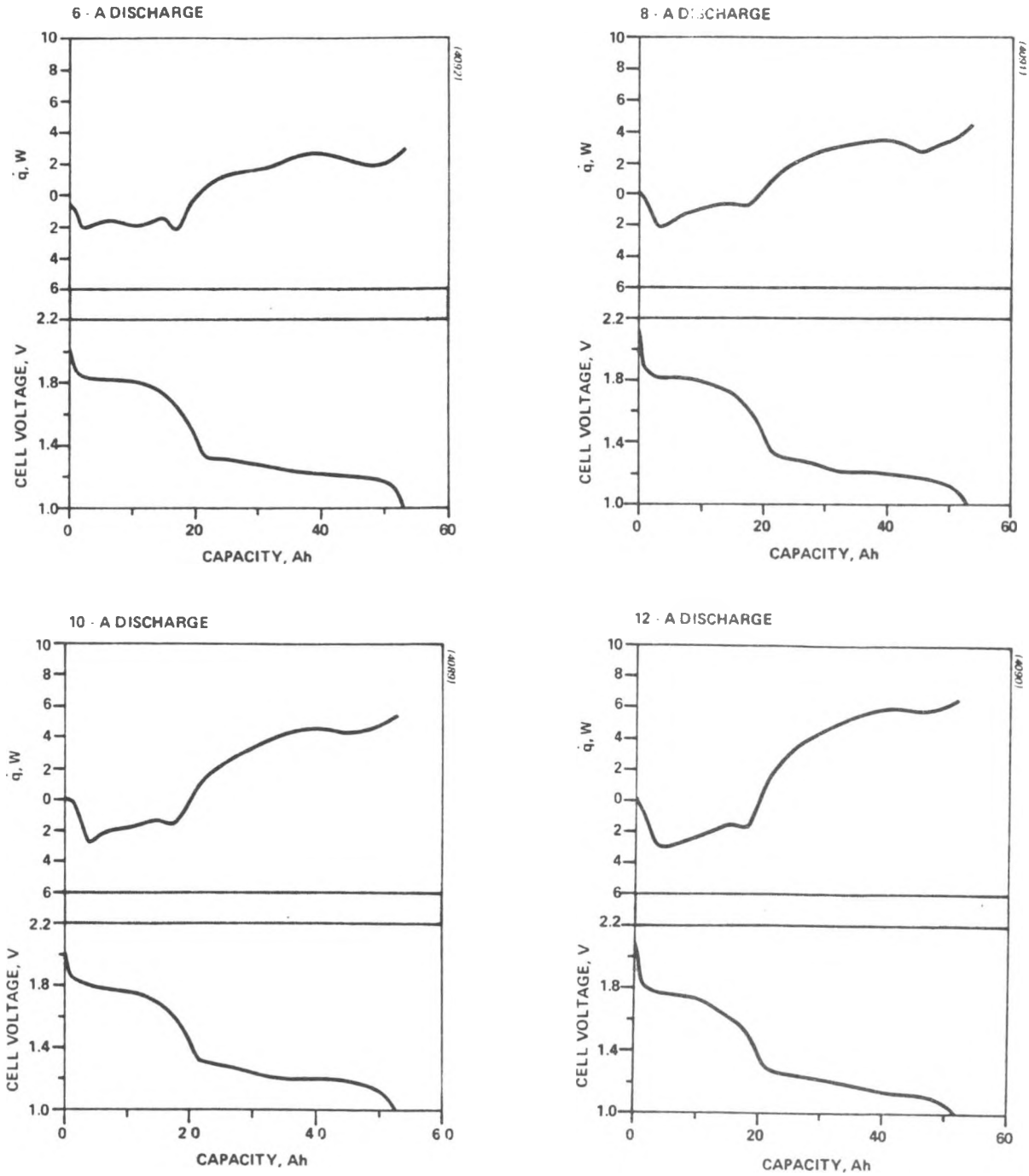

Figs. 2-5. Cell terminal voltage and measured heat generation rate during discharge at 450°C.

each case the discharge process is endothermic for the upper plateau and exothermic for the lower plateau. The average heat generation rate during discharge is nearly linear with discharge current, as shown in Figure 6.

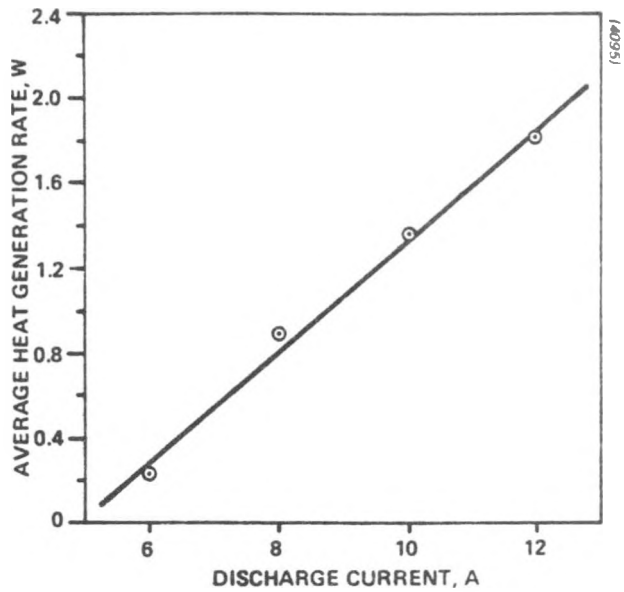

Fig. 6. Average heat generation rate as a function of discharge current.

DISCUSSION

Work at Argonne National Laboratory[3,4] has shown that the discharge of iron sulfide electrodes involves a complicated series of intermediate phases. Iron monosulfide in an electrolyte containing only lithium cations initially is reduced to Li_2FeS_2, which yields FeS on further reduction. In the presence of potassium ion in the electrolyte the reaction is further complicated by formation of the intermediate "J phase" ($LiK_6Fe_{24}S_{26}Cl$). We have shown the strong effects of electrolyte composition on the temperature dependence of the open-circuit voltage and on heat generation rates for FeS cells containing potassium ion[1] and for cells without potassium ion[5].

The discharge of iron disulfide electrodes is even more complicated. According to Tomczuk et al.[3], at low currents the discharge proceeds through a series of stages in which two or three solid phases coexist in the electrode. A fully charged electrode containing FeS_2, Fe_{1-x} and $Li_3Fe_2S_4$ exhibits a constant potential so long as all three phases are present. Discharge of the electrode yields another three-phase, constant-potential region containing $Li_3Fe_2S_4$, $Li_{2.2}Fe_{0.8}S_2$ and $Fe_{1-x}S$. Further discharge yields a material containing two phases of variable composition, $Li_{2+x}Fe_{1-x}S_2$ and $Fe_{1-y}S$, in which x and y tend to zero, with consequent variation of the electrode potential, as the discharge process proceeds. Depending on the initial electrode composition, it is possible to enter yet another three-phase field of small electrochemical capacity, containing Li_2FeS_2, FeS and Fe, before the last major constant-voltage array of phases appears. During the last stages of discharge Li_2S, Fe and Li_2FeS_2 are present.

The sequence of phase changes during the discharge of iron sulfide electrodes can be visualized by reference to the Li-Fe-S phase diagram shown in Fig. 7. Discharge of the FeS electrode would follow the dotted line HM,

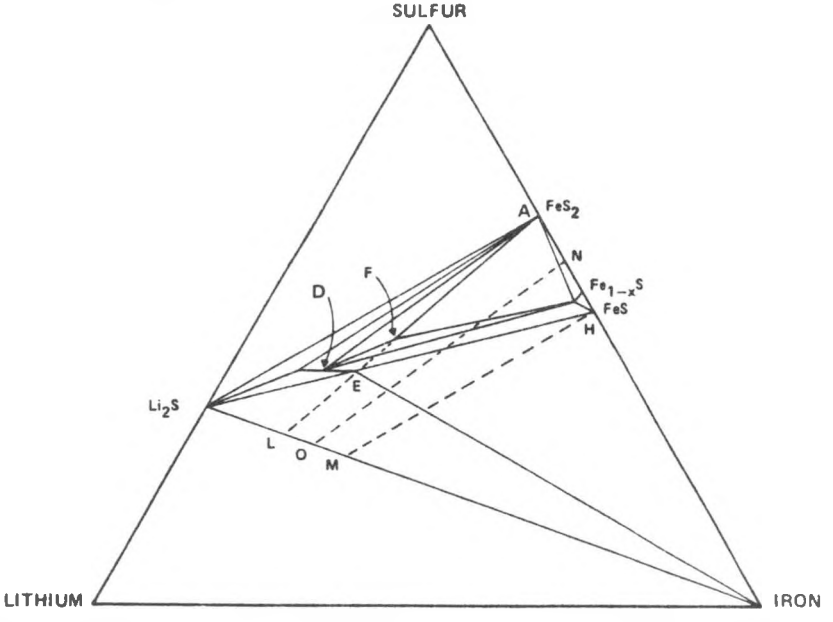

Fig. 7. Phase diagram of the Li-Fe-S system at 450°C (adapted from Tomczuk et al., Ref. 3). A, FeS_2. D, $Li_{2.2}Fe_{0.8}S_2$. E, Li_2FeS_2. F, $Li_3Fe_2S_4$.

while AL represents the hypothetical discharge process for a completely charged FeS_2 electrode. In practice, even at very low current the discharge process for an FeS_2 electrode would lie to the right of line AL, with the exact position dependent on the degree of conversion of FeS to the disulfide during charge. At practical currents the division between phase fields would not be sharp, and one or more nonequilibrium phases could be present until the end of discharge.

Evidence for the sequence of phase changes in the FeS_2 electrode comes not only from the phase diagram,[6,7] but also from metallographic examination of the phases present in partially discharged cells,[3] and from cyclic voltammetric measurements on laboratory cells[4]. In practical cells these phase changes are manifested by subtle changes in the slope of the discharge curve of terminal voltage plotted against time. At moderate to high discharge currents they may not show up at all.

Figs. 2-5 provide calorimetric evidence for the occurence of several phase changes in the iron disulfide electrode. From the original strip-chart traces of heat flow from the cell five regimes can be identified by marked changes in slope during discharge. We have attempted to correlate these changes with the phase changes predicted on the basis of the phase diagram, Fig. 7, and have been able to obtain a fairly close fit with the assumption that the discharge follows the line NO. This would be possible if the cell, initially assembled in the fully charged state, had lost upper-plateau capacity by the time the calorimetric measurements were made. Such capacity losses are common in FeS_2 cells, and are thought to be the result of loss of sulfur from the positive electrode, either through thermal decomposition or the formation of transient, soluble species during cycling. Since

nonequilibrium phases may be present, however, a quantitative comparison of the calorimetric results with the predictions from the equilibrium phase diagram is not justified without confirmation from metallographic or x-ray examination of electrodes from partially discharged cells.

A quantitative comparison is possible between the experimental results for heat flow and predictions based on measurements of the temperature dependence of the cell potential. We measured[8] the potential of "pellet" cells containing the same electrode formulations used in the engineering cell, as a function of temperature and state of charge. The thermodynamic relation for the rate of heat production $\dot{q}$ in an electrochemical cell is:

$$\dot{q} = I[-T(dE/dT) + E - V] \tag{1}$$

where I is current, taken positive for discharge, T is Kelvin temperature, E is cell potential, and V is the working cell voltage. Eq.(1) can be written

$$\dot{q} = I(E_H - V) \tag{2}$$

in terms of the enthalpy voltage E_H. From the measurements of potential at 450°C the temperature coefficient of emf is 0.0004926 V/K, and

$$\dot{q} = I(1.555 \text{ volt} - V) \tag{3}$$

for a fully charged cell. Fig. 8 shows the cell terminal voltage (continuous

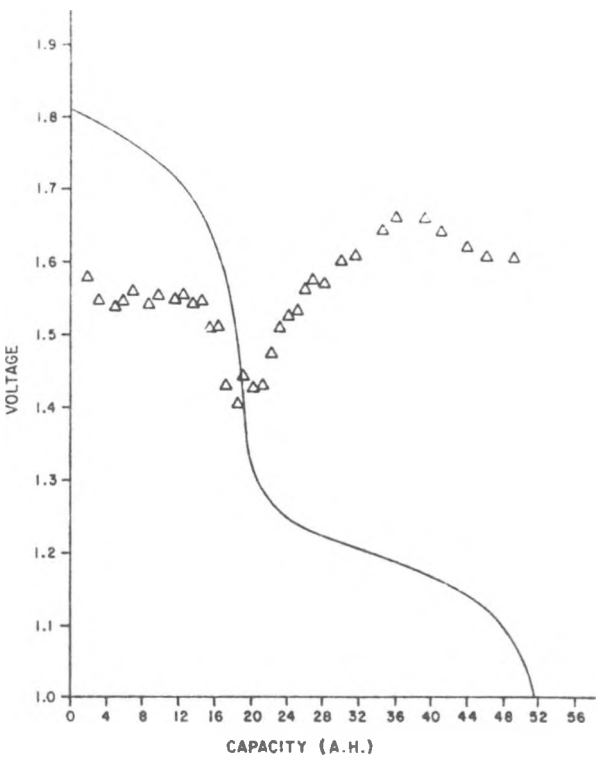

Fig. 8. Voltage (full curve) and enthalpy voltage (triangles) during discharge at 12 A at 450°C.

curve) and enthalpy voltage (triangles) computed from the calorimetrically determined heat flow and the terminal voltage using the equation

$$E_H = \dot{q}/I + V. \quad (4)$$

It may be seen that the agreement between the calorimetric heat and that predicted from emf measurements is within experimental error up to a delivered capacity of about 15 Ah. The electrochemical capacity of the highest-voltage phase group predicted from the phase diagram, $FeS_2 + Li_3Fe_2S_4 + Fe_{1-x}S$, is 37.5 percent of the total capacity of the electrode, assuming four-electron reduction to iron and lithium sulfide. This yields 19.5 Ah if the capacity is taken as the actual cell capacity and 24.2 Ah for the theoretical capacity of the positive.

After the first 15 Ah of capacity the enthalpy voltage rapidly declines. This is consistent with the onset of the second upper-plateau reaction, the enthalpy voltage for which is predicted from emf measurements to be 1.214 V. The electrochemical capacity of this phase group is only about 4 percent of the total capacity, and it is not surprising that the calorimetric heat failed to stabilize at the predicted value before the onset of the next cathodic reaction. It has not been possible to correlate the calorimetric results with the emf results quantitatively for the lower-plateau regime, but the results are in qualitative agreement in that both techniques show the discharge process to be exothermic.

CONCLUSIONS

The heat flow during the initial stages of discharge of a lithium-alloy, iron disulfide cell can be described in terms of the occurrence of a single electrochemical reaction and is consistent with the results with the results of measurements of emf as a function of temperature. In subsequent stages of the discharge reaction evidence was seen for an electrochemical reaction with a small electrochemical capacity and a large positive temperature coefficient of emf.

The fact that the discharge process is endothermic on the upper voltage plateau and exothermic on the lower plateau suggests (see Fig. 6) that a discharge current could be chosen at which the total, integrated heat during discharge vanishes. Although the discharge rate at which the average heat vanishes is rather low, about the C/10 rate, the test cell had high resistance because the molybdenum parts were held together mechanically and not welded. Practical cells, with greater upper-plateau capacity and lower I^2R resistive heats, should exhibit the same behavior at higher discharge rates. The low rate of internal heat generation of FeS_2 cells on discharge may simplify the construction of thermal management systems of large batteries, or those operated at high rates.

ACKNOWLEDGEMENT

This work was supported by the Assistant Secretary for Conservation and Renewable Energy, Office of Energy Systems Research, Energy Storage Division of the U.S. Department of Energy under Contract No. DE-AC03-76SF00098, Subcontract No. 4505810 with the Lawrence Berkeley Laboratory.

REFERENCES

1. D.M. Chen and H.F. Gibbard, J. Electrochem. Soc., 130, 1975 (1983).

2. L.D. Hansen, R.M. Hart, D.M. Chen and H.F. Gibbard, Rev. Sci. Instrum., 53, 503 (1982).

3. Z. Tomczuk, B. Tani, N.C. Otto, M.F. Roche, and D.R. Vissers, J. Electrochem. Soc., 129, 925 (1982).

4. S.K. Preto, Z. Tomczuk, S. von Winbush, and M.F. Roche, ibid., 130, 264 (1983).

5. D.M. Chen and H.F. Gibbard, Extended Abstract No. 352, The Electrochemical Society Fall Meeting, Detroit, October 17-21, Vol. 82-2, p. 566 (1982).

6. A.E. Martin, in "High Performance Batteries for Electric-Vehicle Propulsion and Stationary Energy Storage," Argonne National Laboratory Report ANL-78-94, p. 167 (1980).

7. A.E. Martin and Z. Tomczuk, "in High Performance Batteries for Electric Vehicle Propulsion and Stationary Energy Storage," Argonne National Laboratory Report ANL-79-39, p. 71 (1979).

8. D.M. Chen and H.F. Gibbard, "Fundamental Thermal Management Aspects of The Lithium Metal Sulfide Battery," Lawrence Berkeley Laboratory Report LBL-20026, July, 1985.

STABILITY OF A VITREOUS ELECTROLYTE FOR POSSIBLE USE IN HIGH-TEMPERATURE LITHIUM/SULFUR CELLS

Michael L. Smith,* Jack Winnick,†
Frank R. McLarnon and Elton J. Cairns

Applied Science Division
Lawrence Berkeley Laboratory
Berkeley, California 94720

ABSTRACT

A family of lithium-borate glasses has been identified by H. Tuller and co-workers at the Massachusetts Institute of Technology[1] as candidate electrolytes for use in high-temperature Li/S cells. Based upon screening tests, a glass composition (mol%) of 26% Li_2O-7% Li_2Cl_2-67% B_2O_3 was selected to exhibit an acceptable ionic conductivity of $3x10^{-3}$ $ohm^{-1}cm^{-1}$ at 400 °C, Tg = 475 °C, resistance to attack by S at 400 °C, and minimal attack by Li at 350 °C. A procedure was developed to form and seal glass tubes, and LiSn/glass/S cells were operated at various temperatures. It was possible to charge and discharge cells at current densities up to 70 mA/cm^2 (for 1-3 min) or 20 mA/cm^2 (for several hours) into the two-phase S-Li_2S_x region, but the electrolyte tended to fail when the cell was recharged from near the two-phase/single-phase boundary at ~73 mol% S. The charge-discharge curves also exhibited hysteresis effects, and a crystalline reaction layer was observed on the S side of the electrolyte tubes. X-ray diffraction analyses suggested that the reaction layer contained crystalline lithium-borate compounds, and static immersion tests showed that the glass was slowly attacked by polysulfides at the 400 °C cell operating temperature.

INTRODUCTION

The search for a reliable and efficient electrochemical energy storage system which could be used as an electric utility load-leveling device or as a power source for an electric vehicle has led to the investigation of several high-specific-energy systems which operate at temperatures where the electrolyte and/or the electrodes are liquids. One of these is the Li/S system on which research began as early as 1960 at Argonne National Laboratory.[2] The theoretical specific energy of the Li/S cell is 2700 Wh/Kg, and its potential at 400 °C is 2.18 volts. These values are sufficiently high to make the Li/S system an attractive candidate for meeting goals of high specific energy (200 Wh/Kg) and specific power (200 W/Kg) in practical cell hardware.

The earliest work on the Li/S system followed the approach of having molten electrodes in contact with molten-salt electrolytes. These efforts encountered difficult problems: (1) molten Li from the negative electrode was not retained by the current collector, and (2) the lithium polysulfides from the positive electrode were soluble in the electrolyte. The most typical solution to this problem has been to alloy the Li and to react the S with some non-participating materials; these approaches reduce the mobility and solubility of the electrode materials, but they also degrade the values of specific energy and power that can be realized. However, another solution

* Boeing Aerospace Co., Seattle, WA

† School of Chemical Engineering, Georgia Institute of Technology, Atlanta, GA

to these problems is to use a solid electrolyte in conjunction with molten electrodes. The solid electrolyte would act as a rigid barrier to contain both the metallic Li and the lithium polysulfides in their respective compartments. This solution has not been pursued extensively because of the lack of a suitably stable and conductive electrolyte. Recently there have been discoveries of fast-Li-ion conducting materials which show promising characteristics. The electrolyte used in this work is one of a family of vitreous lithium-borate materials, which exhibit Li-ion conductivity as high as $10^{-2}(\text{ohm-cm})^{-1}$ at 300 °C, with an activation energy of 0.46 eV.[1]

Among these fast-Li-ion conducting materials is the family of lithium-chloroborate glasses. The work reported here concentrated on one particular composition of lithium-chloroborate glass, which showed high ionic conductivity and was somewhat stable to Li attack.[3]

EXPERIMENTAL

The chemicals used to prepare the glass electrolyte were: 99.9% pure LiCl (Mallinckrodt), 99.9% pure Li_2O (Cerac), and 99% pure anhydrous B_2O_3 (Spectrum Chemicals Mfg. Corp.). The procedure to prepare the glass was as follows: first, ~40 grams of B_2O_3 was poured into a 100-ml Pt crucible and heated above 500 °C for several minutes to ensure that only anhydrous B_2O_3 remained. An accurate weight of B_2O_3 was then determined by subtracting the weight of the empty crucible. Next, the appropriate amounts of anhydrous Li_2O and LiCl were added to the crucible, which was then placed in a 950 °C furnace for 15-20 minutes. The crucible was removed from the furnace, and the molten glass was stirred with a Pt rod. The glass was then reheated for another 15-20 minute period, stirred, and then returned to the furnace for a final 20-30 minute heating period. After this sequence, the glass was either poured into a mold and made into discs or was blown into tubes. The glass was analyzed for Li, B and Cl content by atomic absorption spectroscopy. It was found to be lower in LiCl than expected, probably as a result of vapor being released from the melt at 800-1000 °C. The glass composition determined by atomic absorption was 7.3 mol% Li_2Cl_2, 25.7 mol% Li_2O and 67.0 mol% B_2O_3.

The mold for making the discs consisted of two 0.64 cm x 10 cm x 10 cm pieces of stainless steel stacked on top of one another. The bottom plate served as the base while the top plate, which had four 2.5-cm diameter holes drilled through it, served as the mold. After being allowed to cool, the discs were placed in a helium-atmosphere glove box. Care was taken never to handle the discs directly nor leave them in a moist environment longer than necessary. The formation of thin-walled tubes required that a glass-blowing technique be developed, which was complicated by the tendency of the glass to crystallize when reheated. The procedure for making these tubes was to place the Pt crucible full of molten glass (~1000 °C) in a pre-heated (700 °C) stainless-steel block, where it was allowed to cool until the viscosity of the glass was that of a heavy syrup. At this point, a flame-heated pyrex tube (10-mm OD) was dipped into the molten glass and gently stirred to ensure wetting of the pyrex by the molten glass. Once wetted, the tube was pulled up while blowing a steady pressure of air into the other end of the pyrex tube. This method resulted in thin-walled constant-diameter tubes which could be drawn to lengths of 10-60 cm. After cooling, the tubes were cut into lengths of ~10 cm, and one end was sealed over the flame of a bunsen burner. The final wall thickness of these tubes varied from 0.02 cm to 0.05 cm. Before being used as an electrolyte in an electrochemical cell, tubes were screened for structural weaknesses and flaws. Only the tubes which had uniform wall thicknesses and were free of air bubbles and crystals were used.

The S used for the positive electrode was obtained from AESAR and was reported to be 99.999% pure. The current collector was a 0.08-mm thick piece of cleaned Mo ribbon, around which 95% porosity graphite felt was packed tightly. The current collector filled the inside of the glass tube to a depth of ~3 cm. Enough S was loaded in the tubes so that when melted it would fill the voids in the porous graphite felt. The Mo ribbon was spot welded to a 0.25-mm diameter

Pt wire, and the glass was pinch-sealed around the Pt. The glass tubes were sealed inside a helium-atmosphere glove box by rapidly heating the glass to its softening point in an electrically-heated Mo coil and then gently pinching it closed with a pre-heated pair of needle-nose pliers. The temperature of the coil had to be sufficiently high to soften the glass in less than 5 seconds or the glass would crystallize. No attempt was made to evacuate the tubes during sealing, and tests showed that the tubes were able to withstand the excess internal pressure caused by heating to the normal operating temperature.

The negative electrode was a two-phase Li-Sn alloy. The Li and Sn were obtained from AESAR, and each was reported to be 99.9% pure. Because the negative electrode was a two-phase two-composition alloy, for a given temperature the cell potential was constant with respect to minor compositional changes. The LiSn electrode could, therefore, be used as a reference as well.

There were two types of experiments employed: the first type was to measure the change-in-voltage caused by a change in current, which was done at various states-of-charge. From these experiments, the pseudo-steady-state polarization could be determined as a function of current and state of charge. The second type of data resulted from measuring the cell voltage, while passing a constant current, as a function of time (or percent Li in the S electrode). This produced charge/discharge (capacity) curves.

RESULTS

Figure 1 is a plot of the pseudo-steady-state polarization η versus current density i for a typical cell. The curves represent data recorded at different states-of-charge and different rest conditions. The data for curve A were obtained when the cell was discharged for the first time, i.e. between 0.12 and 1.6 mol% Li. The data for curve B were taken when the cell was being recharged from curve A back to 0.9 mol% Li. Higher currents than those shown on the graph were passed but these caused the cell potential to climb very rapidly; this phenomenon was attributed to the formation of a S layer of the glass walls. Curve C represents data obtained by discharging the cell immediately following curve B, or between 0.9 and 3.9 mol% Li. The data for curve D were taken after discharging the cell at a rate of 28 mA (5.5 mA/cm^2) for 8 hours, which produced 17 mol% Li in the S electrode. Finally the set of points for curve D were taken by alternating every few minutes between charging and discharging, at ~18 mol% Li. At the conclusion of these experiments, the ohmic resistance was measured with an A.C. bridge and found to be 0.0025 $(ohm\text{-}cm)^{-1}$.

These tests revealed two significant characteristics of these Li/S cells. First, a comparison of curves A and D shows that the pseudo-steady-state polarization was higher when the cell was nearly fully charged than it was partially discharged. This is attributed to the low conductivity of nearly-pure S. Second, for a given state-of-charge, the pseudo-steady-state polarization was higher following a long discharge period than it was following either a significant relaxation period or period of charging. Comparison of A to C or D to E illustrates this trend. This phenomenon might be attributed to the formation of a reaction layer, which either blocks some of the active transfer area or reduces the glass ionic conductivity. The relaxation period and charging could have helped rid the glass of some of the reaction layer, and therefore decrease the polarization caused by the blocking film.

The contribution of ohmic resistance can be eliminated from the total polarization by subtracting the product of the total current and cell resistance from the total pseudo-steady-state polarization. Figure 2 is a plot of the IR-free overpotential versus current density for curves A and D in Figure 1. The shapes of these curves qualitatively resemble the shape expected for a cell which has a mass-transfer-limited current density i_{lim} ~23 mA/cm^2. However, the curves do not

quantitatively follow the expected shape. Therefore, the limiting current can not be solely attributed to mass-transfer phenomena, but rather, a combination of mass-transfer and other effects.

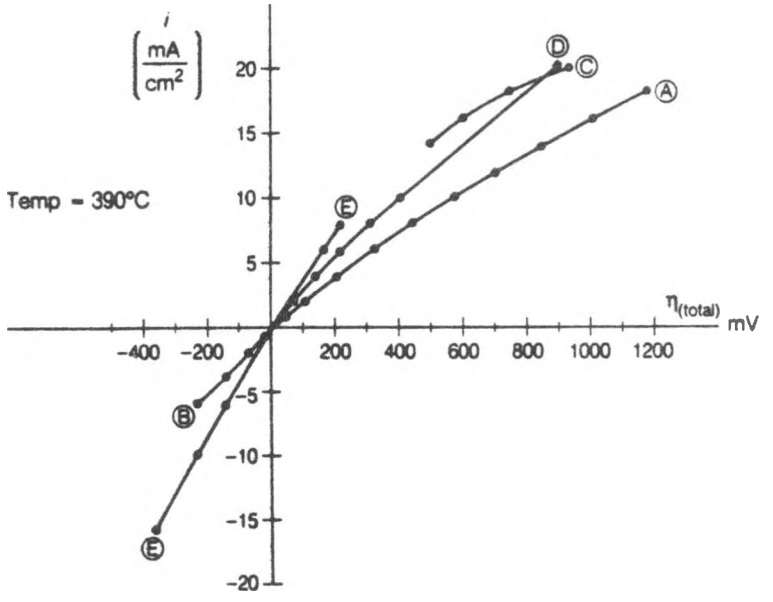

Figure 1. Pseudo-steady-state overpotential versus current density.

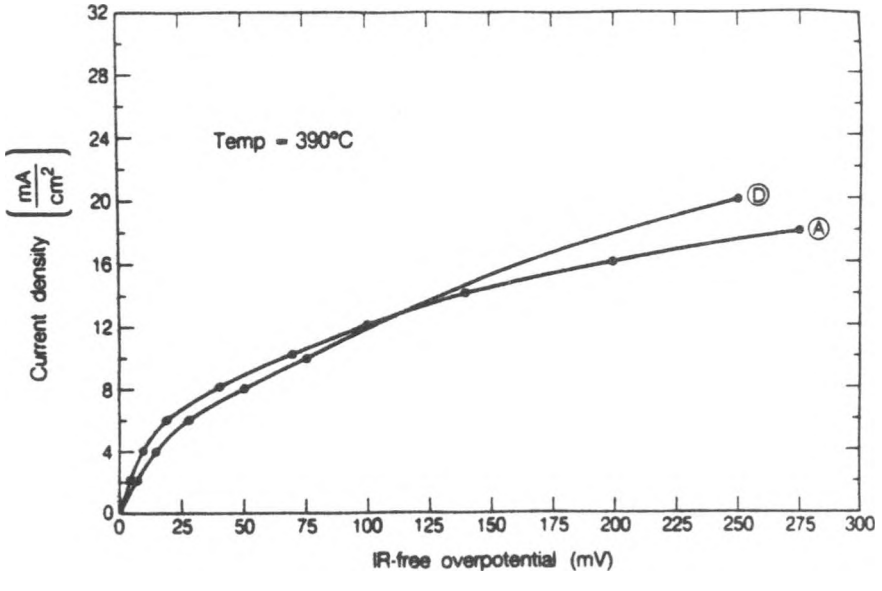

Figure 2. IR-free overpotential versus current density.

Charge-discharge cycle experiments were attempted with cells in both the fully-charged state and in a partially-discharged state. Figure 3 shows data from three cells for which galvanostatic discharges were initiated in the fully-charged state. Unfortunately, all three cells shorted before a complete cycle was obtained, and similar behavior was observed for every cell which was loaded with pure S. Some shorts were catastrophic and others were gradual, and they were the result of discharging the cells either too fast or too far. A cell which was discharged incrementally, with periods of rest separating the discharge periods, could be discharged farther that if it were discharged continuously. Also, the cells which were discharged at lower current densities could be discharged farther than those discharged at higher rates.

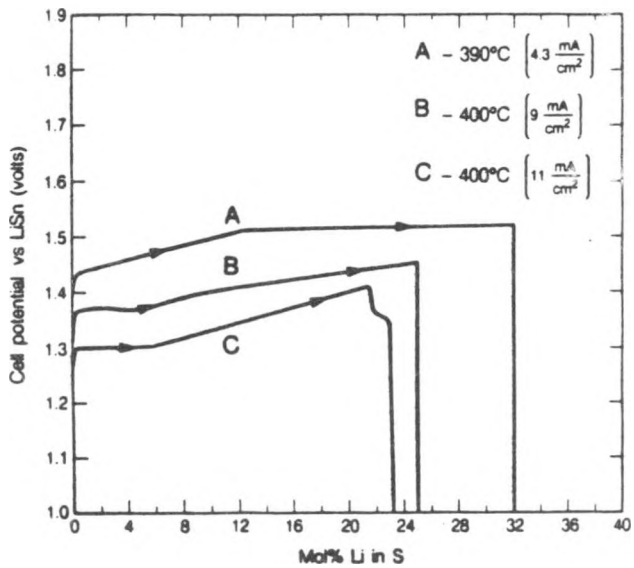

Figure 3. Galvanostatic discharge of three fully-charged cells.

The cells were also used to measure the solubility of Li (as a polysulfide) in S by monitoring the open-circuit cell potential as a function of quantity of Li titrated into the S compartment. The solubility limit was found to occur at 0.04 + 0.03/-0.01 mol% Li at 400 °C, in agreement with the value reported by Sharma.[4]

Figure 4 shows two plots: the first is current versus mol% Li, for a potentiostatic charge, and the second is voltage versus mol% Li, for a galvanostatic discharge. This cell was loaded in a partially discharged state, 23.8 mol% Li, and the open-circuit cell potential was 1.65 volts versus LiSn at 400 °C. The cell was first charged potentiostatically until the S electrode contained ~6 mol% Li, at which point the cell resistance rose to nearly 800 ohms. The high resistance is attributed to the formation of a layer of low-conductivity S. The cell was then discharged at a constant-current of 2 mA to 14 mol% Li, where it shorted.

After the failure of a cell, the glass tubes were examined and most were found to be coated with a yellowish-white reaction layer. Some of the reaction layer from a few of the tubes was removed, cleaned in CS_2 and methanol, and analyzed using an X-ray diffractometer. Figure 5 is an X-ray pattern from a powdered sample of the reaction layer of a typical cell, and Table 1 summarizes the compounds which could be identified. This X-ray pattern is very similar to those obtained from static immersion tests. There is strong evidence in the pattern for crystalline lithium chloroborate and lithium hydroxide, but when the glass was analyzed after being contacted with molten S, there was no evidence of any crystalline material. A significant finding was that there was a major peak at 35 degrees, which could not be confidently assigned to any known

compound. There are at least two lithium-borosulfide compounds known to exist, $Li_2B_2S_5$ and $LiBS_2$,[5] but for which the X-ray diffraction patterns are not available.[6,7] Table 2 is a partial list of potential reactions between lithium polysulfides and the lithium-chloroborate glass. Estimation of the X-ray patterns for these compounds, using data for analogous Na compounds, is likely to be rather unreliable because of the significant size difference of the Li and Na ions.

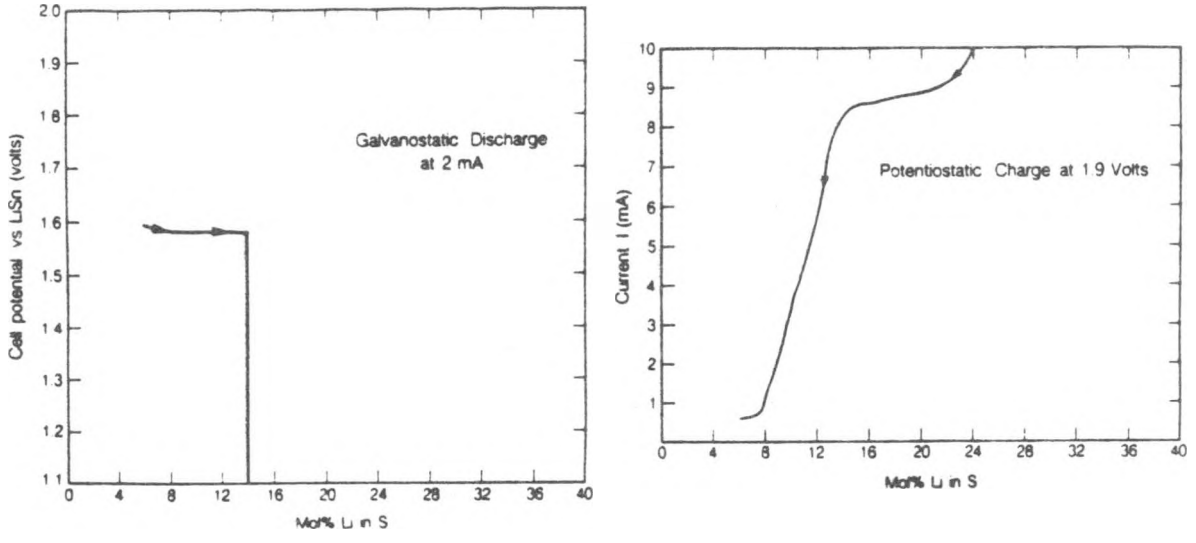

Figure 4. Potentiostatic charge and galvanostatic discharge versus mol% Li at 400 ° C.

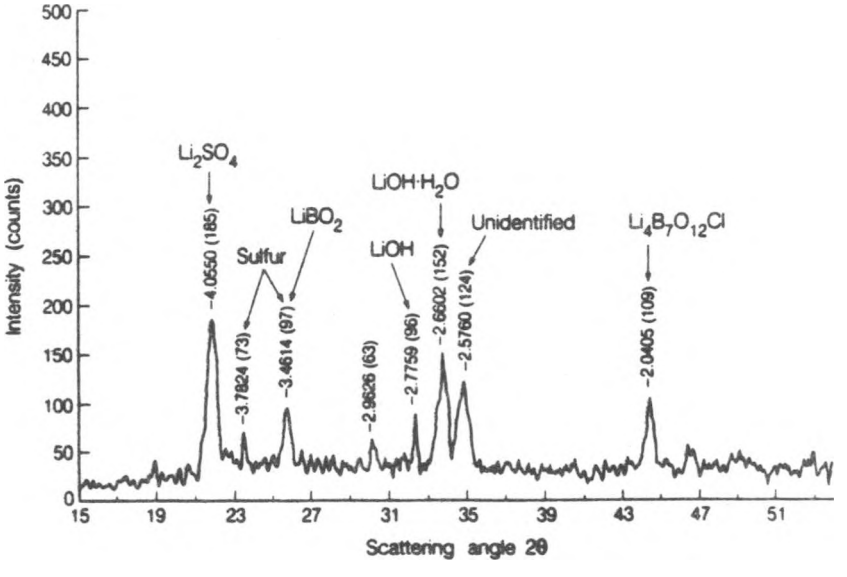

Figure 5. X-ray diffraction pattern for corrosion products in S-22 mol% Li_2S at 400 ° C.

Table 1. Summary of Possible Compounds in the Reaction Layer based on X-ray Diffraction Patterns.

Compound	d values	2θ values	Confidence	Comments
$Li_4B_7O_{12}Cl$	2.05_x 2.70_3 3.48_2	44.1 33.2 25.6	High	9.1 mol% $(LiCl)_2$ 27.3 mol% Li_2O 63.6 mol% B_2O_3
LiOH	2.75_x 4.35_4 2.51_2	32.5 20.4 35.8	Medium/High	Hydrated Li_2O
$LiOH{\cdot}H_2O$	2.67_x 2.70_5 2.44_5	33.5 33.2 36.8	Medium/High	Hydrated Li_2O
Li_2S	3.30_x 2.02_4 1.72_3	27.0 44.8 53.2	Medium/Low	Hygroscopic
Li_2SO_4	4.04_x 4.00_x 3.92_5	22.0 22.2 23.7	High	Caused by Contaminations
HBO_2	4.20_x 3.07_x 6.75_3	21.1 29.1 13.1	Low	Hydrated B_2O_3
$LiBO_2$	3.53_x 2.19_x 1.80_8	25.2 41.2 50.7	Medium	50% Li_2O 50% B_2O_3
Li_3BO_3	3.02_x 2.63_6 2.67_5	29.5 34.1 33.5	Medium	75% Li_2O 25% B_2O_3
Sulfur -#	3.89_x 2.73_7 3.12_3	22.8 32.8 28.6	Medium/High	Hexagonal
Sulfur -#	3.29_x 6.65_3 3.74_2	27.1 13.3 23.8	Low	Monoclinic
Sulfur -#	3.85_x 3.21_6 3.44_4	22.8 27.8 25.8	Medium/High	α-phase

Table 2. Partial List of Reactions Between Lithium Polysulfides and Lithium Chloroborate Glass.

$2Li_2S + 2B_2O_3 \rightleftarrows LiBS_2 + 3LiBO_2$
$2Li_2S + Li_4B_7O_{12}Cl \rightleftarrows LiBS_2 + LiCl + 6LiBO_2$
$(4Li_2S)\cdot S + 2Li_4B_7O_{12}Cl \rightleftarrows Li_2B_2S_5 + 2LiCl + 12LiBO_2$

DISCUSSION AND CONCLUSION

The attractiveness of using lithium-chloroborate glass as the electrolyte in a Li/S cell was supported by the observation that the glass was able to support current densities of 5-15 mA/cm^2 for 15-20 hours, or as high as 70 mA/cm^2 for 3-5 minutes. There appeared to be a limiting current at ~23 mA/cm^2. However, while the cells were being discharged, the glass apparently reacted with the lithium polysulfides, causing the cells to fail. These failures have been attributed to fractures in the glass, caused by one of two effects: volume mismatches between the glass and the reaction layer, and the reaction layer growing and blocking most of the cell's active area (which causes the remaining area to support a very high current density). Local current densities in excess of some critical value have been found to be responsible for failures of other solid electrolytes, e.g., the ceramic β''-alumina used in Na/S cells.[8]

The exact composition of the reaction layer could not be identified; however, it was clear that there were present some crystalline lithium-chloroborate compounds and possibly some lithium borosulfides. It is believed that discharging the cells does not cause formation of a reaction layer, but rather that discharging the cells accelerates such reactions. This is consistent with the idea that the lithium polysulfides were the attacking species. The reaction between the glass and the polysulfides would be accelerated during discharge, because the concentration of polysulfides near the glass wall would be greater than when the cells were being charged or at open-circuit. This conclusion is similar to some results reported for the Na/S system.[9]

RECOMMENDATIONS

The high ionic conductivity and workability of lithium-chloroborate glasses make them attractive candidates for use as electrolytes in Li/S cells. The conductivity is sufficiently high that during discharge in a Li/S cell, the ohmic potential drop would be only a small fraction of the open-circuit cell potential. However, there are significant problems which must be overcome: first, the glass needs to be made more resistant to Li attack; this problem is actively being worked by Tuller et al.[10-15] Recent findings show that some glasses may be stable to melts with Li activity as high as 0.08 at 380 °C. Second, the glass needs to be more resistant to attack by polysulfides. The first step to solving this problem should be to identify the compounds in the reaction layers. This would help to understand the attack mechanism and possibly indicate a method to stabilize the glass.

ACKNOWLEDGEMENT

This work is supported by the Assistant Secretary for Conservation and Renewable Energy, Office of Energy Storage and Distribution of the U.S. Department of Energy under Contract No. DE-AC03-76SF00098.

REFERENCES

1. D.P. Button, R.P. Tandon, H.L. Tuller and D.R. Uhlmann, J. Solid State Ionics *5*, 655 (1981).

2. E.J. Cairns and R.K. Steunenberg, "High Temperature Batteries", *Progress in High Temperature Physics and Chemistry,* **5**, 63, Pergamon Press, New York (1973).

3. M.L. Smith, F.R. McLarnon and E.J. Cairns, "Investigation of a Vitreous Electrolyte for Use in Lithium/Sulfur Cells," M.S. Thesis, University of California, Berkeley, CA (1985). Lawrence Berkeley Laboratory Report No. LBL-20737.

4. R.A. Sharma, J. Electrochem. Soc. **119**, 1439 (1972).

5. L. Gmelin, *Gmelin Handbuch der Anorganischen Chemie,* **19**, 12-15 (1981).

6. J.C. Rosso and M.M. Dubusc, *Chimie et Industrie-Genie Chimique,* **102**, 409-415 (1969).

7. V.H. Noth and G. Mikulaschek, *Zeitschrift fur Anorganische und Allgemeine Chemie,* **311**, 241-248 (1961).

8. A.V. Virkar, "Degradation of Na-Beta"-Alumina Electrolytes in Na-S Batteries," *Proceedings: DOE/EPRI Beta (Sodium-Sulfur) Battery Workshop V,* pp. 5-63 - 5-82, EPRI Report No. EM-3631-SR, (1984).

9. L.C. DeJonghe, "Solid Electrolyte Degradation: Problems and Solutions," *Proceedings: DOE/EPRI Beta (Sodium-Sulfur) Battery Workshop V,* p. 5-90, EPRI Report No. EM-3631-SR, (1984).

10. D.P. Button, L.S. Mason, H.L. Tuller, and D.R. Uhlmann, *Solid State Ionics,* **9 & 10**, 585-592 (1983).

11. H.L. Tuller, D.P. Button and D.R. Uhlmann, *J. of Non-Crystalline Solids,* **40**, 93-118 (1980).

12. D.P. Button, R.P. Tandon, H.L. Tuller, and D.R. Uhlmann, *J. of Non-Crystalline Solids,* **42**, 297-306 (1980).

13. D.P. Button, R. Tandon, C. King, M.H. Velez, H.L. Tuller and D.R. Uhlmann, *J. of Non-Crystalline Solids,* **49**, 129-142 (1982).

14. H.L. Tuller and M.W. Barsoum, *J. of Non-Crystalline Solids,* **73**, 331-350 (1985).

15. M.W. Barsoum, H.L. Tuller, and D.R. Uhlmann, *Extended Abstracts,* **84-2**, Electrochemical Society, Abstract #157 (1984).

SESSION C

RESEARCH AND DEVELOPMENT IN MOLTEN SALT SYSTEMS

Morning, April 18, 1986
Chairman, Robert Huggins
Vice Chairman, J. R. Selman

ELECTRODE KINETIC MEASUREMENTS OF VERY FAST REACTIONS: METAL DEPOSITION-DISSOLUTION IN MOLTEN HALIDES

Z. Nagy and J. L. Settle
Argonne National Laboratory
Chemical Technology Division
9700 South Cass Avenue
Argonne, Illinois 60439

ABSTRACT

Metal deposition–dissolution reactions in molten salts are very fast and difficult to investigate, as evidenced by large discrepancies in the reported exchange current densities. An error analysis of the d-c relaxation techniques was carried out, and it was determined that the measurement of the exchange current density can have a systematic error if the surface reaction rate is much faster than the diffusion rate. This systematic error will result in measured exchange current densities approximately equal to the largest exchange current density measurable under the given conditions. This systematic error can also result in fortuitously linear $\log i_o$ versus $\log C$ and $\log i_o$ versus $1/T$ plots, even when the results are grossly in error. A computer curve-fitting data evaluation coupled with a statistical sensitivity analysis is suggested to avoid these problems. The exchange current densities of iron, nickel and molybdenum were measured in LiCl–KCl eutectic melt at 450°C using an improved double pulse galvanostatic technique. Only that of iron could be measured reliably (1.7 ± 0.4 A cm^{-2} at 1.3×10^{-6} mol cm^{-3} Fe^{++} ion concentration); the nickel reaction is too fast to be measured (at least 5 A cm^{-2} at 1×10^{-6} mol cm^{-3} Ni^{++} ion concentration). The large discrepancies between these results and some results reported by earlier workers can be explained on the basis of the above described error analysis. It is concluded that past experiments resulting in large exchange current densities should be reexamined with improved measuring and data-evaluation techniques because it is possible that the reported values represent only the applicability limit of the measuring technique rather than the true exchange current density.

INTRODUCTION

Metal deposition-dissolution reactions are among the elementary processes occurring in high-temperature molten-salt batteries, such as the metal sulfide/lithium–aluminum batteries where iron and nickel are electrode materials of interest in a molten LiCl-KCl eutectic electrolyte. Measurements of the exchange current densities of these reactions by several investigators have yielded very poor agreement, as shown in Table I. Values differing by as much as three orders of magnitude have been reported,[1–9] with some values being in the range of hundreds of A cm^{-2}. Although these reactions are apparently very fast, they still can contribute to the overpotential of the battery electrodes because of the small metal ion concentration in the electrolyte due to the low solubility of the sulfides.[10]

Table I

Reported Exchange Current Densities in LiCl–KCl Eutectic Melt.

Metal	Metal ion Concentration (mol cm^{-3})	Temperature (K)	Exchange Current Density (A cm^{-2})	Method	Ref.
Nickel	1×10^{-6}	723	0.6	GDP	1
	1×10^{-5}	723	4.0		
	5×10^{-5}	723	13.0		
	7.7×10^{-6}	723	0.19	PS	2–4
	9.4×10^{-6}	723	0.22		
	2.0×10^{-5}	723	0.26		
	3.8×10^{-5}	723	0.30		
	6.0×10^{-5}	723	0.38		
	7.8×10^{-5}	723	0.42		
	3.66×10^{-6}	723	85.8	GDP	5
	7.80×10^{-6}	723	103		
	1.56×10^{-5}	723	177		
	3.42×10^{-5}	723	232		
	6.59×10^{-5}	723	376		
	2.9×10^{-6}	773	1.18	ACI	6
	2.6×10^{-5}	773	4.08		
	2.9×10^{-5}	773	4.10		
	2.4×10^{-4}	773	9.75		
	5.8×10^{-6}	773	4.7	GDP	7–8
	2.9×10^{-5}	773	9.3		
	5.8×10^{-5}	673	5.2		
	5.8×10^{-5}	723	9.1		
	5.8×10^{-5}	773	14.0		
	1.0×10^{-6}	723	>5.0	MGDP	9
Iron	2.1×10^{-6}	723	0.028	PS	3
	7.8×10^{-6}	723	0.041		
	4.0×10^{-5}	723	0.064		
	1.1×10^{-4}	723	0.077		
	2.9×10^{-6}	773	1.5	GDP	8
	5.8×10^{-6}	773	1.6		
	2.9×10^{-5}	673	1.0		
	2.9×10^{-5}	723	1.4		
	2.9×10^{-5}	773	3.0		
	1.3×10^{-6}	723	1.7	MGDP	9

Table I
(cont'd)

Notes: GDP = galvanostatic double pulse
PS = potential step
ACI = ac impedance
MGDP = modified GDP

THEORETICAL

In an effort to reconcile the large discrepancies in the reported exchange current densities, an error analysis was carried out for the experimental measuring techniques used in their determinations. Since dc relaxation techniques (potentiostatic or galvanostatic pulses) were used for most studies, they were chosen as the subject of this work. The limits of applicability of these techniques are known.[11–15] In these earlier studies, an applicability field was defined for each technique in terms of time constants for which the exchange current density is measurable with an error of less than 20%. However, no examinations were made to determine whether large errors occurring outside the field of applicability display any systematic behavior.

In the present investigation, it was found that if the electrode system falls outside the field of applicability, because the surface reaction is fast compared to diffusion to and from the surface (*i.e.*, the diffusional time constant is small), the exchange current density measurement can display a systematic error, resulting in a measured exchange current density approximately equal to the largest measurable exchange current density for the given conditions. This can result in exchange current densities whose values seem to fall within the field of applicability; furthermore, the dependency of the exchange current density on concentration and temperature can yield the expected linear functions, even though the measurement is grossly in error. This was found to be the case for all dc relaxation techniques (potentiostatic, galvanostatic, and coulostatic), using both the graphical and the computer curve–fitting data–evaluation methods. Some typical results of the calculations are shown in Figures 1-3.

The following method of calculation was used for the error analysis. Synthetic data were generated by (a) using the full analytical expression of the particular relaxation technique and (b) including random errors in the data sets. The exchange current density was then calculated from these data using the data–evaluation method under investigation, and this "measured" exchange current density was compared to the exchange current density used in the data generation. The error behavior did not always follow the potentially misleading type described above; under certain conditions the error was random and the measured exchange current density was widely scattered. Because of the potentially large number of calculations needed, no attempt was made to define the conditions under which the error becomes systematic. However, this is really immaterial; what is important, from a practical standpoint is that such behavior *can* occur.

It is concluded that experimental results giving exchange current densities near the edge of the applicability field of any dc relaxation technique should always be suspect, even if the expected concentration and temperature dependence is observed. It is not obvious from the experimental results when the range of applicability of a given technique is exceeded (especially when a graphical data–evaluation method is used) but there are

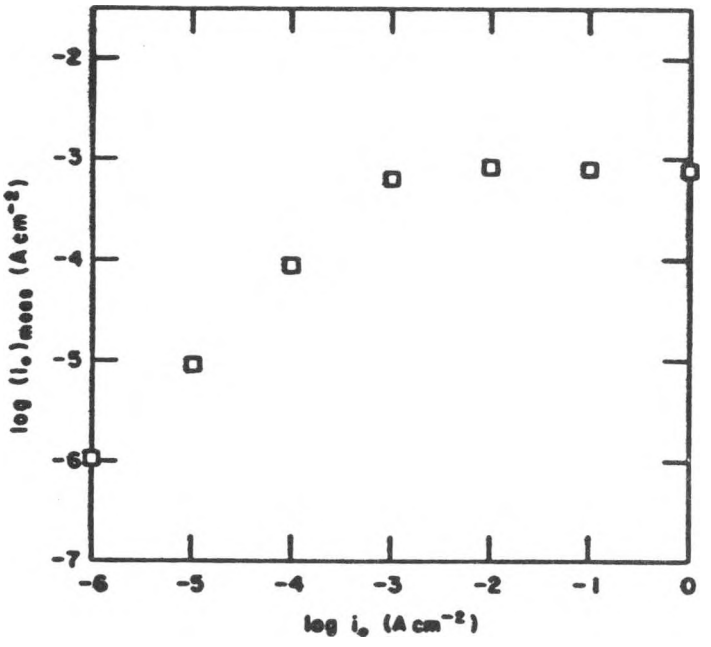

Fig. 1. Comparison of known and measured exchange current densities. Potential step technique, graphical data evaluation.

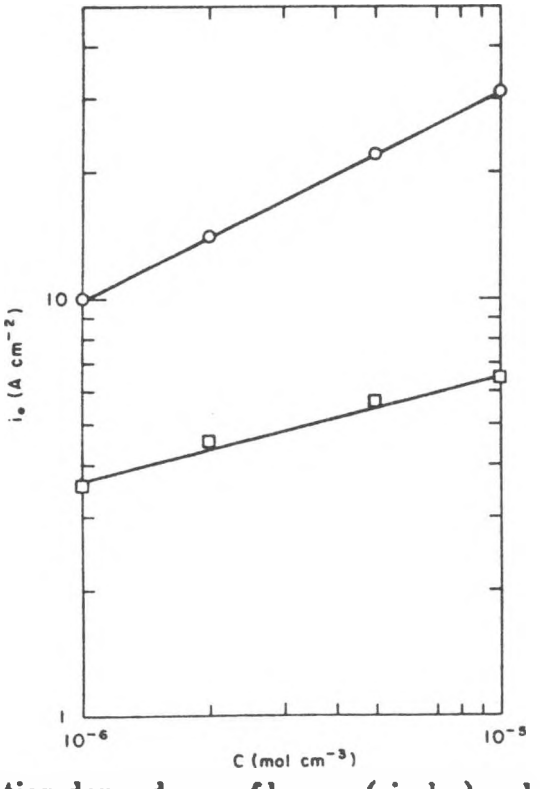

Fig. 2. Concentration dependence of known (circles) and measured (squares) exchange current densities. Double pulse galvanostatic technique, graphical data evaluation.

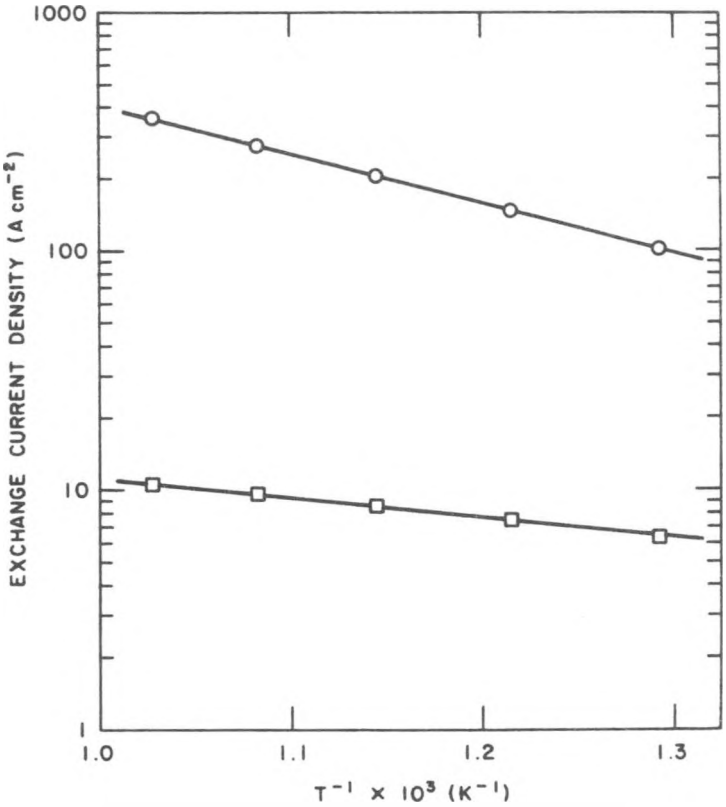

Fig. 3. Temperature dependence of known (circles) and measured (squares) exchange current densities. Single pulse galvanostatic technique, graphical data evaluation.

several techniques which can be used to extract information about the reliability of the data. Four such techniques are described below:

(a) A plot of the experimental data can often reveal possible problems. At short times, a plot of potential versus square root of time should be concave toward the time axis for the galvanostatic single pulse technique; a completely linear or convex plot indicates overwhelming diffusion control. Similarly, at short times, a plot of current density versus square root of time should be convex to the time axis for the potential step technique. For the coulostatic technique, a plot of logarithm of the potential versus time should be linear for a considerable time after the start of the experiment; the diffusional effects are serious when the plot curves soon after time zero. For the double pulse galvanostatic technique, a plot of potential at the potential minimum versus the square root of the prepulse length can be linear even when the results are grossly in error; a very large exchange current density and, consequently, the possibility of large error is indicated when negative intercepts are obtained on the potential axis. Unfortunately, none of these indicators is quantitative and borderline cases are difficult to decide.

(b) The measured system parameters can be used to calculate the time constants of the system and it can be located on the applicability diagram of the measuring technique. However, as demonstrated above, this method is not reliable when the measured parameters place the system near the border of the applicability field.

(c) The generation and evaluation of synthetic data was described in the above error analysis. When used properly, this is a powerful method to indicate the reliability of the parameters calculated from the experimental data. The measurement conditions have to be taken fully into consideration in the data generation (*e.g.*, rise time of pulses, error of all measurements, including the IR correction) and several data-sets should be generated by

varying the assumed exchange current density around the calculated value. The question is not only whether the parameters in question can be used to generate a data-set similar to the experimental one, but whether similar data-sets can also be generated using different parameter (*e.g.*, exchange current density) values, thereby indicating the insensitivity of the curve-fitting to that particular parameter. The generation of synthetic data-sets requires negligible programming effort and computing time compared to the curve-fitting calculations, and it is worthwhile to make such calculations a routine part of all data evaluations.

(d) Finally, a statistical sensitivity analysis can be carried out[16] by determining the covariance matrix of the parameters. This will indicate the information content of the experimental data with respect to the parameters. Results are reliable only if their standard deviation is small compared to the numerical value of the parameter (not more than a few percent). The last two methods, or a combination of them, should be used for very fast reactions, while for slower reactions the first two methods will suffice.

EXPERIMENTAL

The results of this error analysis guided our experimental work on the measurement of the deposition–dissolution kinetics of nickel, iron, and molybdenum in several halide melts. These melts were the eutectic mixtures of LiCl-KCl, LiCl-RbCl-$CaCl_2$, LiBr-KBr-CsBr, and NaCl-$NaAlCl_4$, containing 10^{-7} to 10^{-4} mol cm^{-3} of the chloride of the metal under investigation. The measurements were carried out in the temperature range of 175 to 550°C. The measurement methods used were dc relaxation techniques, mainly double pulse galvanostatic, but also single pulse galvanostatic and coulostatic techniques.

The measuring cell was essentially a thin layer cell containing two identical working electrodes separated by a 0.0125 cm gap. This design assures a low IR drop in the electrolyte, a uniform current distribution over the faces of the working electrodes, and a small inductive loop. The cell is shown in Figure 4; it has been described in more detail elsewhere.[17] The two identical working electrode arrangement gives an extended range where the linear current density–overpotential approximation can be used, thereby making the determination of the exchange current density more accurate.[18–19] The cell was immersed in molten salt contained in an open crucible at the bottom of a furnace well attached to a helium–filled glove box. The oxygen and moisture content of the helium were kept below 5 ppm by continuous gas purification. Most measurements were carried out using a digital transient recorder, resulting in about one order of magnitude decrease of the experimental errors as compared to an oscilloscope. A block diagram of the measuring circuit is shown in Figure 5. More details about the experimental procedure are given elsewhere.[9]

The data were analyzed using a multidimensional nonlinear least–squares curve–fitting method, which has shown to extend considerably the fields of applicability of all relaxation techniques.[11–15] As a result of (a) the use of a measuring cell especially designed for high temperature measurement of fast reactions, (b) the use of digital instrumentation, and (c) computer curve–fitting data analysis, we could measure exchange current densities generally about one order of magnitude larger, and under some conditions more than two orders of magnitude larger than was hitherto possible. An example of the results of the curve fitting data evaluation is shown in Figure 6.

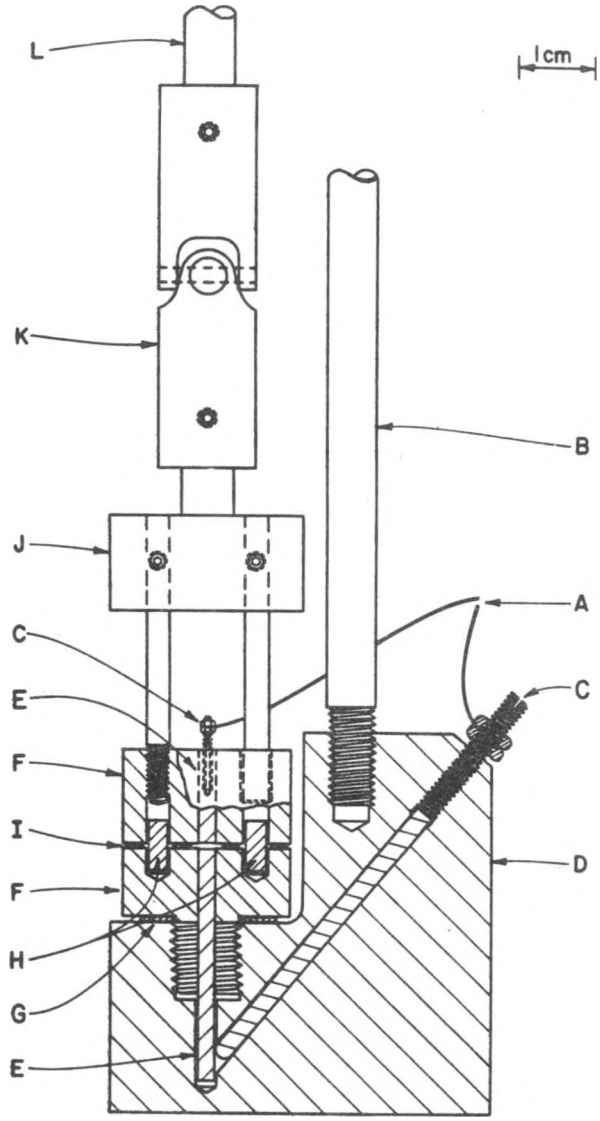

Fig. 4. Cell design. A–to coaxial electrical leads, B–steel support rod, C–metal electrode contacts, D–boron nitride housing, E–metal electrodes, F–boron nitride electrode holders, G–Grafoil gasket, H–metal alignment pins, I–metal spacer, J–steel adapter, K–steel universal joint, L–steel rod connecting to micrometer head.

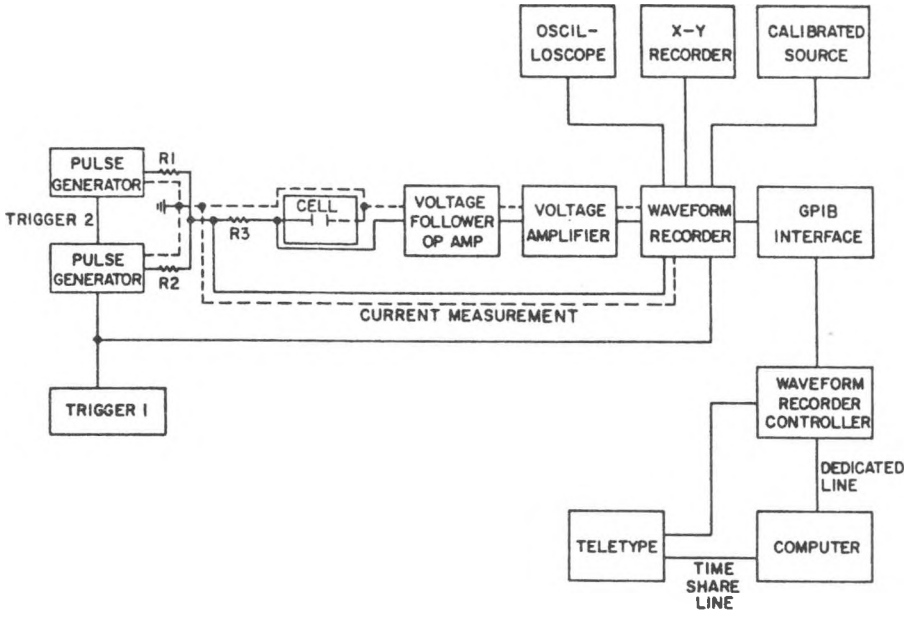

Fig. 5. Block diagram of the experimental setup.

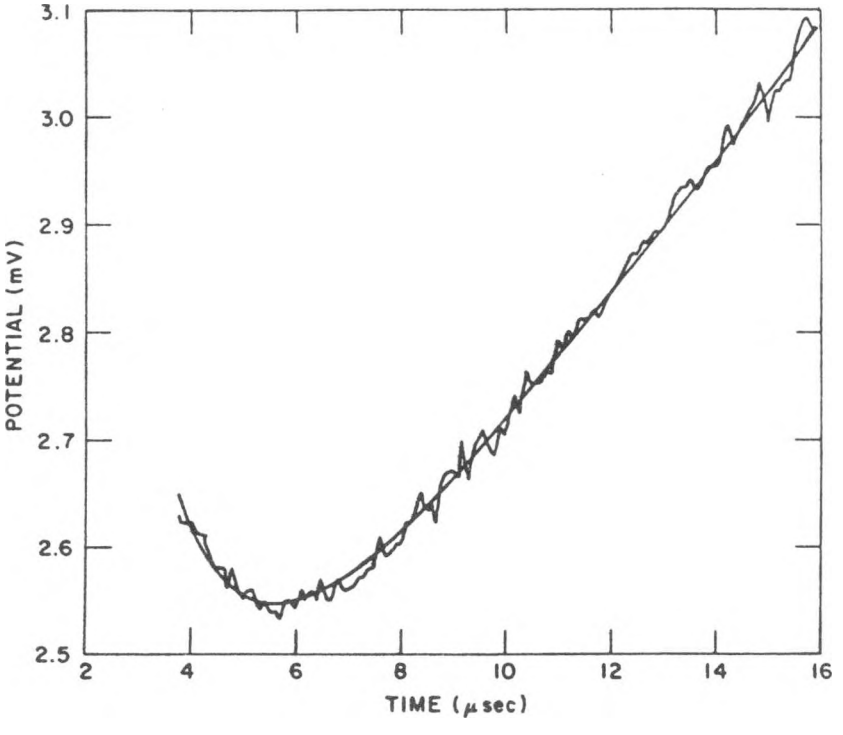

Fig. 6. An example of the galvanostatic double pulse relaxation curve together with the smooth curve generated by the computer curve-fitting data evaluation.

RESULTS AND DISCUSSION

Only in the LiCl-KCl eutectic melt at 450°C are there literature data available to compare to our results. In this melt, only the exchange current density of iron could be measured reliably (1.7 ± 0.4 A cm^{-2} at 1.3×10^{-6} mol cm^{-3} Fe^{++} ion concentration); the nickel reaction is too fast to be measured (at least 5 A cm^{-2} at 1×10^{-6} mol cm^{-3} Ni^{++} ion concentration), and the molybdenum results are unreliable because of melt decomposition. The large discrepancies between these findings and some results reported by earlier workers can be explained on the basis of the above described error analysis.

For the case of nickel, our minimum exchange current density of 5 A cm^{-2} at 450°C and at a nickel ion concentration of 1×10^{-6} mol cm^{-3} can be compared to the results of Boutellion *et al.*[2–4] who, for similar conditions, reported an exchange current density of about 0.1 A cm^{-2} using the potential step technique. Laitinen *et al.*[1] obtained approximately 0.5 A cm^{-2} using the double pulse galvanostatic technique with graphical data evaluation, and Haruyama *et al.*[7–8] reported values in the low A cm^{-2} range for the same technique. Boutellion *et al.* also used the double pulse galvanostatic technique[5] and reported values near 100 A cm^{-2}; however, these results are so far outside the field of applicability of the technique that they cannot be considered reliable. The error may have been caused by a nonlinear extrapolation technique to correct for the solution IR drop. A similar trend with measuring technique can be demonstrated for iron. Bouteillon[3] found an exchange current density near 0.01 A cm^{-2} with the potential step technique, while Haruyama *et al.* reported about 1 A cm^{-2} using the double pulse galvanostatic technique with graphical data evaluation.[8] Both of these values are lower than our 1.7 A cm^{-2}.

CONCLUSIONS

It can be concluded that reported exchange current densities are a strong function of the experimental techniques used for their measurement. The potential step technique with graphical data evaluation resulted in the lowest exchange current densities for both iron and nickel. The galvanostatic double pulse technique with graphical data evaluation gave considerably larger exchange current densities; this is in agreement with the fact that the latter technique can be used for much faster reactions than the potentiostatic measurement. Finally, our measurements, which were carried out with an improved double pulse galvanostatic technique, resulted in even larger exchange current densities. This conclusion is corroborated by the results of the error analysis described above in which it was found that a measured exchange current density may indicate only the limitation of the technique rather than the true exchange current density of the reaction when the latter is outside the field of applicability of the measuring technique. These results suggest that large exchange current densities reported in the literature should be reexamined using improved experimental and data–evaluation techniques to prove their validity.

ACKNOWLEDGMENT

This work was performed under the auspices of the Division of Materials Science, Office of Basic Energy Sciences, U.S. Department of Energy, under Contract W-31-109-Eng-38.

REFERENCES

1. H. A. Laitinen, R. P. Tischer, and D. K. Roe, *J. Electrochem. Soc.*, **107**, 546 (1960).
2. J. Amosse, J. Bouteillon, and M. J. Barbier, *C. R. Acad. Sci. (Paris)*, **C267**, 22 (1968).
3. J. Bouteillon, *Thesis*, University of Grenoble, Grenoble, France (1969).
4. J. Bouteillon and M. J. Barbier, *Electrochim. Acta*, **21**, 817 (1976).
5. J. Bouteillon, J. De Lapinay, and M. J. Barbier, *J. Chim. Phys.*, **71**, 346 (1974).
6. H. Numata and S. Haruyama, *J. Japan Inst. Metals*, **43**, 866 (1979).
7. A. Nishikata and S. Haruyama, *J. Japan Inst. Metals*, **47**, 198 (1983).
8. S. Haruyama, H. Numata, and A. Nishikata, Abstract No. I-102, p. 153, "Proceedings of the First International Symposium on Molten Salt Chemistry and Technology," Kyoto, Japan, April 20-22, 1983.
9. J. L. Settle and Z. Nagy, *J. Electrochem. Soc.*, **132**, 1619 (1985).
10. M. L. Saboungi, J. J. Marr, and M. Blander, *Met. Trans.*, **10B**, 477 (1979).
11. Z. Nagy, *J. Electrochem. Soc.*, **128**, 786 (1981).
12. Z. Nagy, *Electrochim. Acta*, **26**, 671 (1981).
13. Z. Nagy, *J. Electrochem. Soc.*, **129**, 1943 (1982).
14. Z. Nagy, *Electrochim. Acta*, **28**, 557 (1983).
15. Z. Nagy and J. T. Arden, *J. Electrochem. Soc.*, **130**, 815 (1983).
16. Z. Nagy *Electrochim. Acta*, **29**, 917 (1984).
17. Z. Nagy and J. L. Settle, in "Proceedings of the Fourth International Symposium on Molten Salts," M. Blander, D. S. Newman, M. L. Saboungi, G. Mamantov, and K. Johnson, Editors, Electrochemical Society Proceedings, Vol 84-2, p. 534, Pennington, NJ, 1984.
18. D. J. Kooijman, M. Sluyters-Rehbach, and J. H. Sluyters, *Electrochim. Acta*, **11**, 1197 (1966).
19. Z. Nagy, R. H. Land, G. K. Leaf, and M. Minkoff, *J. Electrochem. Soc.*, **132**, 2626 (1985).

THE CHEMISTRY AND ELECTROCHEMISTRY OF MOLYBDENUM PLATING FROM MOLTEN SALTS

S. H. White and U. M. Twardoch

EIC Laboratories, Inc.
111 Downey Street
Norwood, Massachusetts 02062

This paper is concerned with the synergism between solution chemistry and the electrode chemistry in electroplating molybdenum. However, before presenting the results from some basic studies, this specific area of materials processing will be placed in the context of electrolytic methods of materials fabrication for use in corrosive environments at elevated temperatures and high potentials. EIC has ongoing programs which are concerned with the development of electroplating refractory metals, in particular those in VIA, chromium, molybdenum, and tungsten from electrolyte operating below 500°C. These metals are of particular interest in view of their high melting points, hardness, and corrosion resistance, particularly at higher temperatures in oxygen free, or reducing environments and/or at high potentials which make them strong candidates as construction materials in new technologies of interest to this meeting[1]. The ability to electroplate and electroform these metals and their alloys is an important aspect of their successful application for corrosion and erosion protection.

Electrodeposition from molten salts has been successfully employed for the preparation of the more electropositive metals on a commercial scale. Successful processes, which include aluminum, magnesium, and alkali metals production, are operated when the cathode product is a liquid metal. On the other hand, titanium, tantalum, and niobium have been electrodeposited in dendritic form in large scale operations, but currently only tantalum is produced in commercial quantities in the Balke process. In contrast, electroplating of metals from molten salts has been less successful because the process requires a coherent deposit of metal with specified properties. This has restricted applications to aluminum and some transition metals. Electrolyte baths based upon molten alkali fluoride as solvent have been employed successfully with refractory metals. Table 1 summarizes the mean valencies of the refractory metal ions in solution, their reduction pathway and the temperatures at which the processes would need to be operated[2].

TABLE 1

SUMMARY OF THE ELECTROCHEMISTRY OF REFRACTORY METALS IN MOLTEN FLUORIDE MELTS

T°C	Element	Mean Valency	Reduction Sequence
-	Ti	-	$Ti^{3+} \rightarrow Ti$
700	Zr	4	$Zr^{4+} \rightarrow Zr$
700	Hf	4	$Hf^{4+} \rightarrow Hf$
600/800	V	3	$V^{3+} \rightarrow V$
600	Nb	4	$Nb^{4+} \rightarrow Nb^{+} \rightarrow Nb$
600/800	Ta	5	$Ta^{5+} \rightarrow Ta^{2+} \rightarrow Ta$
700/1000	Cr	3?	$Cr^{3+} \rightarrow Cr^{2+} \rightarrow Cr$
700	Mo	3.3	$Mo^{3+} \rightarrow Mo$
700	W	4.5	$W^{4+} \rightarrow W$

In the USA, only tantalum has been plated on a commercial scale. It is clear that the high temperatures required by the processes are detrimental to their application and commercialization. Efforts are being made to develop electrolytes which will enable lower temperature operations. This means moving away from the alkali fluoride solvents in favor of other alkali halide electrolytes[3]. The goals of the present work with molybdenum have been three fold:

(1) Develop the necessary understanding of the relevant molybdenum solution chemistry and electrodeposition processes.

(2) Develop lower temperature electrolytes for molybdenum plating.

(3) Explore the potentialities of pulse plating in these systems.

In the remainder of this paper, examples of results from these areas will be presented.

Molybdenum plating has been achieved in this work from LiCl-KCl and LiCl-CsCl eutectics at temperatures around 500°C. The results in Table 2 indicate that success has been achieved by using the pulse plating method. Where good deposits are obtained, the current efficiencies are high.

TABLE 2

PULSE PLATING OF MOLYBDENUM FROM ALKALI METAL CHLORIDE MELT AT 530°C

Pulsed Current (amps)	t_{off}/t_{on}	% Current Efficiency	Comments
0.3	90	85	Good Clean grey deposit.
0.3	90	89	Deposit flaked off substrate.
0.3	90	94	Grey deposit, some dendrites.
0.1	90	81	Grey deposit.
0.5	150	91	Grey deposit, adherent flakes and some dendrites.
0.3	90	50	Bright grey smooth deposit after washing.
0.3	90	77	Grey deposit, some flakes at three phase boundary.
0.3	90	90	Bright deposit.
0.9	90	88	Bright deposit.

Figure 1 shows that the deposit is coherent and uniform around the substrate indicating good throwing power. These results demonstrate that molybdenum can be deposited from chloride melts at temperatures around 500°C, considerably below those used previously[2,4] and offer an opportunity to develop a large scale process for molybdenum plating. The success of such a process will depend upon a number of factors which include the purity of the precursor material and solvent, the complex solution chemistry which will need to be quantified before the electrolyte can be optimized, and the development of the relationships between plating conditions and plate properties. Plating bath designers have considered the chemistry of the metal precursor in the electrolyte bath and the reduction pathway to metal. In addition, the details

of the early stages of metal formation on a foreign substrate are now recognized to be important. Molybdenum provides in interesting example of the synergism between the properties of solution and electrode chemistry. Such results to be discussed below strengthen the conviction that success in finding low temperature processes will arise out of a better understanding of the fundamental chemistry involved in these molten electrolytes.

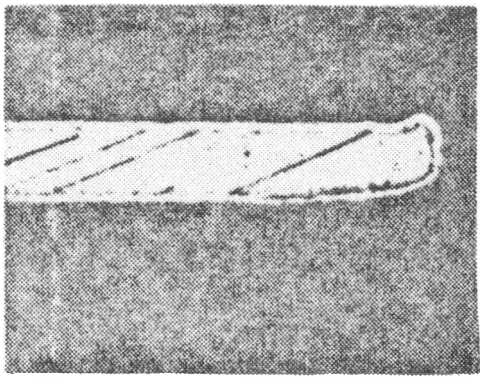

Fig. 1. Longitudinal section of nickel electrode plated with molybdenum at 50X magnification.

Molybdenum exhibits an extensive and complex solution chemistry in aqueous electrolytes which is still in the process of being characterized[5]. The same degree of detail is unavailable for fused salt solvents, and extrapolation from the properties of pure compounds can be misleading. As an example, the behavior of Mo(III) chloride dissolved in molten alkali chlorides is quite different from that expected on the basis of the properties of the pure compound. One of the requirements for further development of refractory metal plating, generally, is a better understanding and characterization of complexes of the various oxidation states of these metals in molten salts. Molybdenum forms a number of chloride complexes ranging from Mo(IV) through to Mo(II). It should be apparent that if Mo(IV) is chosen as starting material, the reduction pathway may well pass through these different oxidation states to metal which, might lead to poor control over the deposition process or failure to obtain any deposit since low oxidation state cluster compounds are rather difficult to reduce (see below results for $ZnCl_2$ melts).

Our present work has considered three solvents, LiCl-KCl, LiCl-CsCl, and $ZnCl_2$-KCl mixtures in an attempt to reduce the working temperature and to provide different environments in which molybdenum complex halide may form and be stabilized, e.g., it is known that large cations like caesium stabilize the dimer complex $Mo_2Cl_9^{-3}$ in aqueous solution. The results of the present studies may be summarized as follows. Solutions of K_3MoCl_6 in these solvents become stable in 24 to 48 hours after addition of this precursor. The electrochemical

studies show, particularly using cyclic voltammetry, that there is a strong temperature dependence of the electrochemical behavior. In addition, the electrochemical response is a function of the electrochemical observation time. The qualitative treatment of the voltammetric results in the alkali metal chloride melts support the earlier suggestion of Mellors and Senderoff[6] that in chloride melts, Mo(III) exists in solution in two different forms in dynamic equilibrium:

$$2MoCl_6^{-3} \rightleftarrows Mo_2Cl_9^{-3} + 3Cl^- \qquad [1]$$

Smirnov[7], on the basis of activation energies of diffusion measured in various alkali metal chlorides, suggested that the stability of the molybdenum (III) solution species was dependent upon the alkali metal cation. Differences in the voltammetric spectra for the different solvent compositions used in this work support this view, as do the results from potential step experiments described below. Under specific conditions of temperature and scan rate or current density, evidence was obtained which demonstrates that molybdenum deposition is possible and those results lead to the pulse plating work from these electrolytes. In contrast to the results in alkali chloride mixtures, the use of either the acidic or basic zinc chloride-potassium-chloride mixture does not lead to the deposition of molybdenum metal because of the formation of stable intermediate molybdenum (II) clusters in the available electrochemical window of these melts.

The electrocrystallization of molybdenum on to foreign substrates from chloride melts has been studied. Cyclic voltammetry, chronopotentiometry, and potential step measurements have provided the experimetnal evidence which shows that the formation of new metal phase from these electrolytes involves considerable overpotential. Figure 2 compares some results in the LiCl-CsCl electrolyte for the deposition of molybdenum on gold and platinum electrodes. It is clear that in neither case does the reduction process take place at the potential corresponding to the Mo(III)/Mo redox potential, but it has been shifted in a cathode direction by an amount dependent upon the substrate. In the case of the galvanostatic deposition of molybdenum on gold in LiCl-KCl, the potential time curve shows a significant initial overpotential followed by a distorted transition time. Simple calculations show that these effects are not due to uncompensated resistance in the electrolyte. Similar observations were reported by Senderoff and Mellors for both the chloride[6] and fluoride[8] melts at higher temperatures. Mellors and Senderoff[6] had related this overvoltage to the presence of the monomer/dimer equilibrium in solution. The present results suggest that not only is the monomer/dimer equilibrium involved, but that since different overpotentials are observed on the different electrodes then the actual nucleation process itself must also contribute to the total overpotential.

It will be demonstrated in an independent way that coupling of the solution equilibrium to the processes at the electrode surface takes place. Chronoamperometric studies lead to current time curves of the form shown in Figure 3. Such curves have been analyzed in terms of either a continuous nucleation/growth or an arrested nucleation/growth model in which the growth of nuclei is controlled by the spherical diffusion of the ions. Mathematical analysis of the potential step case[9] leads to simple relationships between the maximum current (i_m), the time at which the current becomes a maximum (t_m) and

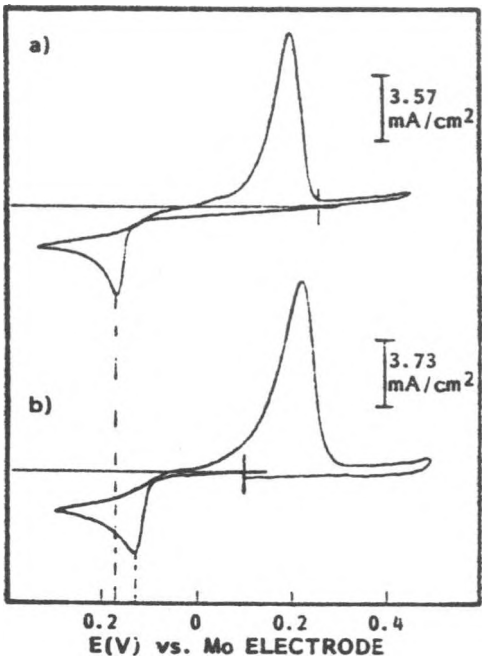

Fig 2. Cyclic voltammogram for the deposition of the molybdenum on gold (a) and platinum electrodes from molten LiCl-CsCl mixture containing 1.29 x 10^{-2} mol/kg of potassium hexachloromolybdate at 530°C. Scan rate, 0.02 V/s.

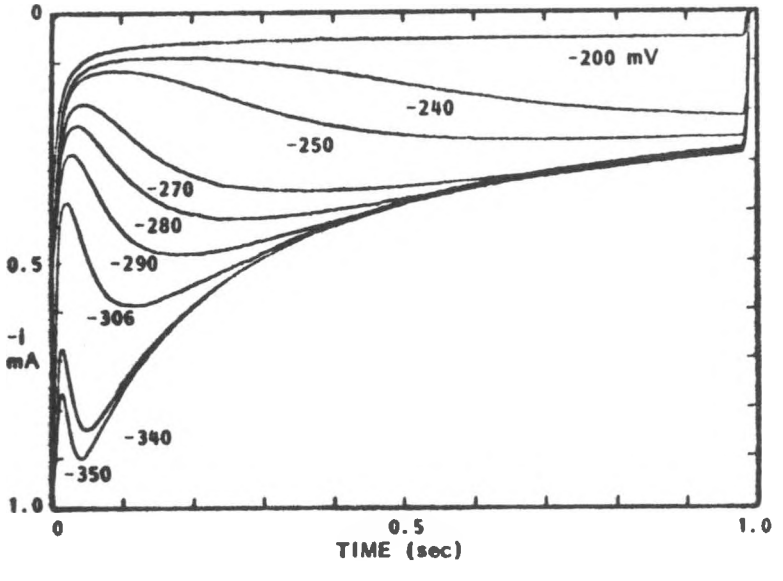

Fig. 3. Current time transients acquired at gold electrodes in different solvents for the reduction of Mo(III) at different overpotentials vs. Mo^{3+}/Mo. Au area 0.056 cm^2, 530°C LiCl-CsCl.

the solution properties of the electrolyte. At any given concentration, $i_m^2 t_m$ should be a constant which has a specific value determined by the nature of the nucleation process. In a typical situation for the electrolytes of our present work, a solution was used which contained 34 mM K_3MoCl_6, with a diffusion coefficient of molybdenum species of 6 x 10^{-6} $cm^2 sec^{-1}$. The theory then predicts that for progressive nucleation $i_m^2 t_m$ is 2.9 x 10^{-5} and for instantaneous nucleation $i_m^2 t_m$ is 1.8 x 10^{-5} $amps^2 sec$. Data obtained as a function of overpotential in the LiCl-KCl and in the LiCl-CsCl eutectics and normalized to a common electrode area compared in Figure 4.

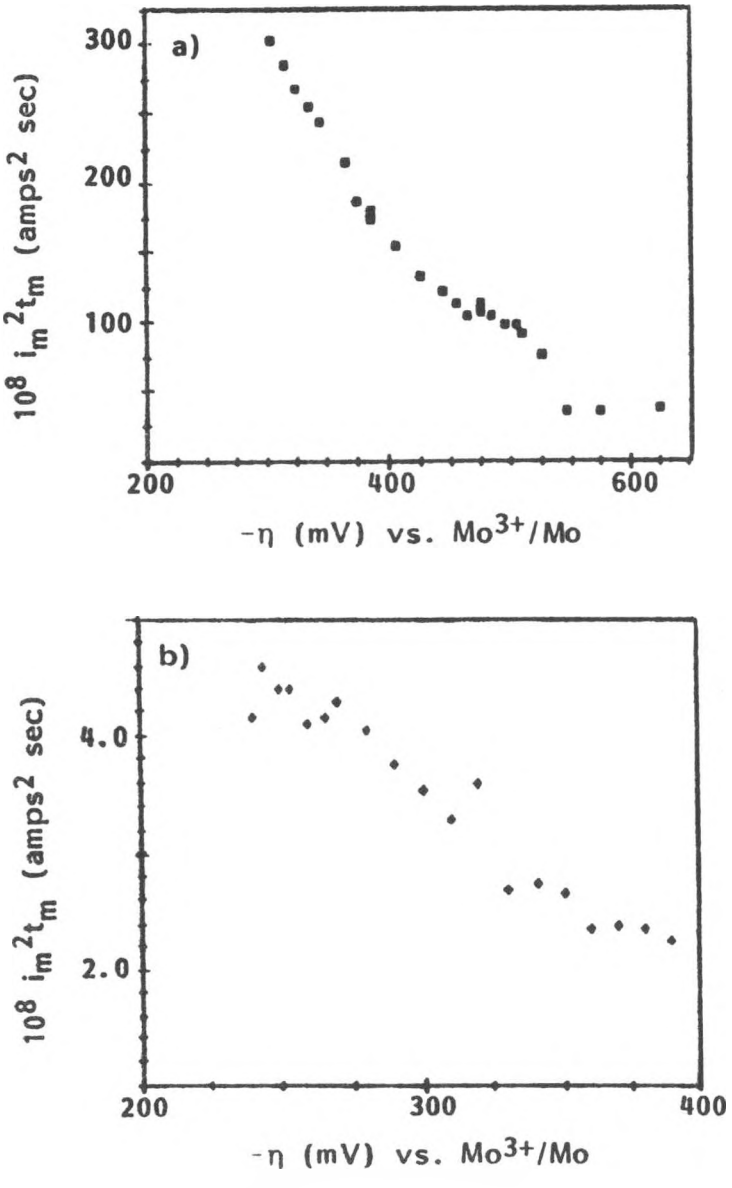

Fig. 4. Plots of $i_m^2 t_m$ versus applied overpotential for molybdenum deposition on a gold substrate in (a) LiCl-KCl at 450°C, (b) LiCl-CsCl at 530°C. Currents in (a) normalized to electrode area in (b).

It was found that for both solvents the product $i_m^2 t_m$ shows a dependence upon overpotential but that the changes with overpotential were markedly different. In the LiCl-KCl solvent, $i_m^2 t_m$ values are some two orders of magnitude greater than those in LiCl-CsCl solvent. Figure 5 illustrates the dependence of $i_m^2 t_m$ obtained at different overpotentials on the value of t_m in the LiCl-KCl. At the long times corresponding to low overpotentials, the magnitude of $i_m^2 t_m$ is close but below that predicted for progressive nucleation. As the overpotential is increased, then the value of $i_m^2 t_m$ rapidly decreases to a value almost ten times lower than that predicted for instantaneous nucleation on the basis of the solution properties. It must be concluded that some further feature modifies the growth of the nuclei formed on the electrode. These results are rationalized by considering that the surface concentrations of the electroactive species are controlled by the dynamics of the equilibrium between monomer and dimer (equation 1), which was suggested to account for the solution properties in LiCl-KCl. The temperature dependence of this equilibrium and the influence of solvent anion will need to be known before the solvent envisaged for low temperature chromium plating (3) can be assessed as solvents in molydenum plating baths. These results reinforce the importance of determining the basic chemical behavior prior to selecting electrolytes and designing pulse plating regimes for transition metal plating where unusual chemistry at the high temperatures is a characteristic.

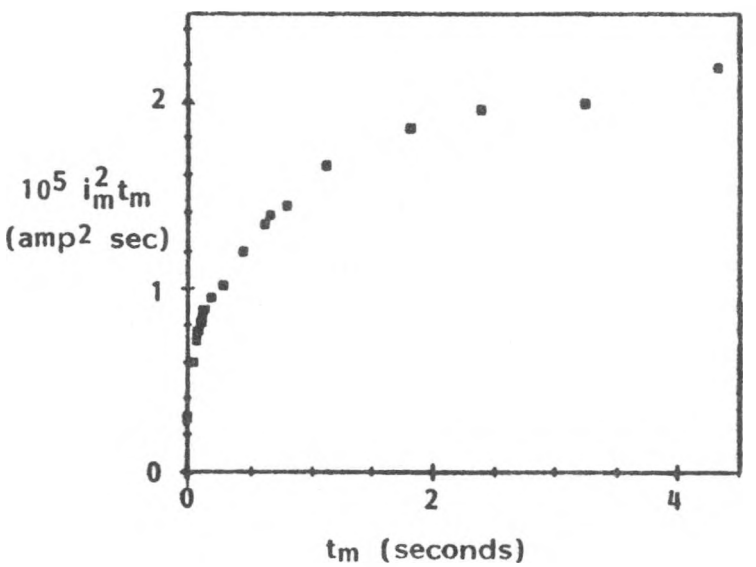

Fig. 5. $i_m^2 t_m$ from potential step as function of t_m for molybdenum deposition on gold at 450°C from K_3MoCl_6-LiCl-KCl solution.

Acknowledgments

This work has been supported by the Army Research Office under Contract No. DAAG29-82-C-0015 and by the National Science Foundation under Grant No. DMR-8360814.

References

1. E. J. Cairns and R. A. Muric, in Corrosion Problems in Energy Conversion and Generation, ECS, 1974.

2. D. Inman and S. H. White, J. Applied Electrochem., 8, 375 (1978).

3. S. H. White and U. M. Twardoch, submitted to J. Applied Electrochem. (1985).

4. G. W. Mellors and S. Senderoff, Canadian Patent 688,546 (1964).

5. F. A. Cotton and G. Wilkinson, Advanced Inorganic Chemistry, Interscience, 1980.

6. S. Senderoff and G. W. Mellors, J. Electrochem. Soc., 114, 586 (1967).

7. S. Senderoff and G. W. Mellors, J. Electrochem. Soc., 114, 556 (1967).

8. M. V. Smirnov, O. A. Ryzhik and G. N. Razantsev, Electrokhimiya, 1, 59 (1965).

9. G. Gunawardena, G. J. Hills, I. Montenegro and B. Scharifker, J. Electroanal. Chem., 138, 225 (1982).

CORROSION RESISTANT COATINGS FOR HIGH-TEMPERATURE SULFUR AND SULFIDE BATTERIES

D. C. Topor and J. R. Selman

Illinois Institute of Technology
Department of Chemical Engineering
Chicago, Illinois 60616

ABSTRACT

Electrochemical deposition of molybdenum and molybdenum carbide from a molten fluoride (FLINAK) bath at 750-850 °C has the advantage of producing dense, stress-free deposits. However, the level of water and hydrolysis products should not be in excess of 100 ppm, thus requiring the use of a dry, inert atmosphere room and a carefully devised drying procedure for the component salts. The electrochemical deposition was carried out in a 3-electrode cell using the potentiostatic mode with current densities 50 to 200 mA/cm^2 during 1 to 2 hours. The molten solvent contained potassium molybdate (5 to 6 w/o) for the deposition of Mo coating or sodium molybdate (4 to 6 w/o) and potassium carbonate (5 to 7 w/o) for Mo_2C coating deposition. The substrate material was low-carbon steel with a nickel interlayer. Both coatings showed good adherence, adequate thickness over edges and corners and a dense structure. Molybdenum and molybdenum carbide coatings exhibit quite similar behavior when cycled between representative anodic and cathodic polarization limits in Na_2S_3 melt at 300°C.

INTRODUCTION

Molybdenum and its compounds with carbon and sulfur are among the materials most suitable for protective coatings of positive current collectors in high-temperature sulfur or metalsulfide batteries, because of their excellent corrosion stability. Refractory metals posses unique combination of chemical and physical properties which have rendered them important in high-temperature structural material applications requiring corrosion resitance.[1]

The resistance of Mo in a sulfur-rich environment is excellent too and has led to a number of uses in different types of high-performance batteries. In $LiAl/FeS_2$ and $LiSi/FeS_2$ batteries as well as in the Na/S battery having metallic current collectors, molybdenum is used because is the only metal which allows high-utilization of the positive electrode reactants at the normal charge cut-off potential of 2.1 V.[2,3] During the recharging operation of the Na/S cell a sudden reduction of current density occurs which is caused in part by the formation of an insulating film of elemental sulfur. The resistance to corrosion when interfaced with polysulfide melt and exposed to wide range of potential drops, is a central

requirement for any current collector material. Therefore, the electrochemistry of the Na/S cell is concerned almost exclusively with the sulfur electrode.

In this work the optimal conditions are explored for producing molybdenum and molybdenum carbide coatings by molten salt electrodeposition onto a nickel/steel substrate. Also, the corrosion resistance of these coatings in polysulfide melt is tested.

BACKGROUND

Molybdenum.

The electrolytic preparation of molybdenum from alkali chloride melts was investigated by Senderoff and Brenner[4-6] and Senderoff and Mellors[7] with a view to the process of electrowinning, plating[8] and refining.[9] The temperature and the current density were the most important factors: higher temperatures (up to 900°C) and lower current densities were found to be beneficial for quality deposits of Mo. If sodium molybdate in a NaCl-KCl bath was used, it produced during electrolysis a black product (containing up to 77% Mo) dispersed through the melt.

An all-fluoride electrolyte process developed by Senderoff and Mellors[10-12] is the only one reported which has proved generally applicable to most refractory metal deposition as coherent coatings. The principal aspects of this process are similar to the all-chloride process. The molten bath is formed by the LiF-NaF-KF eutectic (FLINAK) mixed with an alkali hexachloro-molybdate. The Mo(III) species can also be produced in situ by reacting molybdenum haxafluoride gas with molybdenum powder dispersed in the melt. As a general rule the fluoride anion strengthens the anionic complex of the transition metals in molten fluorides, and the cation size and charge balance the stability of the complex.[13,14] The formation of a polynuclear molybdenum complex with fluoride ion is unlikely[15] due to the high activity of the "hard" F^- ion but other sources of irreversibility[16] may by the formation of insoluble intermediates or the low solubility of the lower fluorides of molybdenum. An insoluble intermediate may interfere with the normal growth of dendrites and thus continuous nucleation may occur at the electrode. Several review articles and papers on plating from various bath formulations have been published in recent years. [17-26]

Molybdenum carbide.

Fluoride solvent was also used to produce coherent coating of molybdneum carbide in a process similar to the molybdenum electrodeposition above-mentioned.[27] The electrolyte contained an alkali carbonate as the source of carbon. The electrolysis was operated at 800°C and 250 mA/cm^2. The Mo_2C deposition involves complicated surface chemistry: simultaneous reduction of carbonate and molybdenum complex, production of active carbon and molybdenum species able to react at certain sites on the electrode surface and the growth of a coherent, dense coating.

In earlier works, Weiss[28] and Suri et al.[29] used mixtures of alkali tetraborate and fluorides with alkali carbonates and molybdates (or MoO_3) to produce silvery crystals of Mo_2C however, no coherent coatings

were reported.

Corrosion in polysulfide melts.

The reaction mechanism of the sulfur-polysulfide electrode, despite considerable work carried out in several laboratories, particularly at the Ford Motor Company, Dearborn, Mich.[30], remains unclear as far as precise identity and concentration of melt species is concerned, as well as the effect of the formation of solid and liquid layers (semiconducting or nonconducting) at or near the electrode surfaces. In a review article Aikens[31] presented some recent advances in this field, along with the earlier well-established characteristics of the sulfur electrode.

The behavior of molybdenum in sodium tetrasulfide melt was investigated recently by Dobson, McLarnon and Cairns[32-34] using cyclic voltammetry and efforts were made to explain the observed results of cathodic sweeps.

EXPERIMENTAL

Instrumentation.

All plating experiments were carried out in an inert, dry atmosphere glove box (DRI-TRAIN 40-5 Glove Box, Vacuum Atmospheres Company, Hawthorne, Ca). The oxigen level was monitored by an oxygen analyzer (VAC Model AO-316C) and was maintained below 10 ppm. The moisture level, which was always maintained below 1 ppm, was monitored by a Sentry Hygrometer Panametrics Model 550. The box was provided with a stainless steel well attached to its floor and positioned in a Lindberg electrical furnace. A VAC DRI-COOL DK-3I refrigeration unit was used to force cold argon gas through a flexible hose to the top flange of the well penetrating inside the box as well as cooling the cover of the electrolytic cell.

The electrolytic cell assembly consists of a nickel 200 crucible positioned on a stand within the well, a cover with two heat shields and four holes for feed-through and one coaxial electrode, one Pt flag as quasi-reference and one chromel-alumel thermocouple. The electrodes and thermocouple passed through the holes of the cover into the well to reach the melt in the crucible. The cover holding these components can be moved into and out of the well respectively, before and after the electrolysis. The anode was a Mo rod of 6.3 mm dia; it was used as the central electrode of the coaxial electrode. Before immersion into the melt the anode was electropolished in a solution of phosphoric acid (55 vol %), sulfuric acid (25 vol %) and distilled water. Cylindrical cathodes of 3.1 mm dia and 4 cm length were cut from low-carbon steel rod and polished with 600 grit SiC paper.

The corrosion cell was made of Pyrex glass. During measurements it was connected to the inert and dry atmosphere of the glove-box. The cell cover made of Teflon was provided with Cajon Ultratorr connectors for the passage of the electrodes and thermocouple sheath. A vitreous carbon crucilbe was used to contain the polysulfide melt and served as the counter electrode. A BN lid, with a grafoil gasket and tight passages for sample and reference electrodes, was used to reduce the sulfur loss by vaporization from the crucible to insignificant levels. This loss was further reduced by overpressurizing the cell to 10 cm of water. The reference electrode was a solid Mo

rod of 3.1 mm dia, connected to the outer stainless steel tubing of the coaxial electrode. Before use it was electropolished to expose a clean and smooth surface to the melt. The sample rod was screwed into a hole made in the central Mo electrode of the coaxial electrode. A small Hoskins Model FD 101 electric furnace was used to fuse the polysulfide and maintain it at the working temperature.

The i-E curves were obtained using a PAR 173 Potentiostat-Galvanostat equipped with PAR 179 Digital Coulometer and a PAR 175 Universal Programmer. The voltammetric transients were recorded with a Houston Instrument Omnigraphic 2000 X-Y recorder and/or a Nicolet Explorer II storage oscilloscope.

Materials.

FLINAK (LiF-46.5 mol%, 29.24 w/o; NaF-11.5%, 11.71 w/o; KF-42.0 mol%, 59.05 w/o) "polarographic" grade purchased from Anderson Physics Laboratory, Champaign, Ill., was used as solvent. All salts used in the bath formulation were 99+ percent purity anhydrous products. The solid salts were dried at 200°C, under 0.1 torr pressure. NaF, LiF, FLINAK, Na and K carbonates were found to lose less than 0.5 w/o during two hours of individual drying. Only the alkali molybdates (Cerac 99.9%) showed a 3 w/o loss. All dried compounds were stored in the glove-box. Molybdenum and nickel were purchased from Materials Research Corporation, Orangeburg, N.Y. The sodium trisulfide was supplied by Prof. G. J. Janz of Rensselaer Polytechnic Institute, Troy, N.Y.

Electrode preparation.

To improve the adhesion of Mo to substrate an interlayer of a metal close to Mo in the electromotive force series in FLINAK is necessary, e.g. nickel. Before plating with Ni the steel rods were electropolished in a solution of concentrated HCl (25 vol%) and glycerin (75 vol%), washed in water and acetone, and dried. A Ni strike was plated from a Watts bath at 55°C and 0.3 A/cm^2. Each cathode substrate was then screwed into a long stainless steel rod connected directly to the outer stainless steel tubing of the coaxial electrode.

Coating procedure.

100 g FLINAK were used as solvent and 4 to 6 g of molybdate were added to form the electrolyte composition for Mo plating. To plate Mo_2C, additions of 4 to 6 g molybdate and 5 to 7 g carbonate were used. Each of these mixtures was poured into a 100 ml nickel crucible and placed in the furnace well. The temperature was slowly raised to 700°C. One to two hours were necessary after melting to produce a clear melt. During this period some black residue was formed on the melt surface, probably due to the carbon from organic contaminants. It later reacted wiht the oxide present in the melt, leaving a clean surface. At the same time a small amount of black powder accumulated on the bottom but the bulk of the melt remained clear.

The melt was further purified by pre-electrolysis between graphite electrodes at 1.5 V until the current dropped to a low constant value. A chemical analysis of bath composition was made after several electrodeposition experiments using the atomic absorption spectrophotometric method. These

analyses indicated almost 50% reduction of molybdenum concentration; in the case of the bath for carbide deposition the carbonate concentration decreased to one half of that of molybdate, the latter remaining practically unchanged. If the concentration of oxygenated salts was increased, the melt lost its clear appearance and the cooler parts of the cell were covered with a yellow to violet condensate. The "self-regulated" bath compositions were preserved by using molybdenum metal as soluble anode and adding 2 to 3 g of carbonate to replenish the carbonate loss during carbide plating. The carbonate amount was designed to overcompensate for the carbon expected to be used up in a 4-electron reduction step for 0.01 equivalents of charge passed.

After electrolysis the electrodes were ultrasonically freed of ahderent frozen melt and weighed to determine current efficiency. The deposit composition was determined by X-ray diffraction. Coatings which appeared sound were further examined by scanning electron microscope.

Corrosion procedure.

Both types of coatings were exposed to polysulfide melt at 300°C to test their stability and behavior under various polarization conditions. A pure solid Mo metal electrode was also used to establish the "normal" behavior of this melt, under identical conditions.

Selected coatings of Mo and Mo_2C were mounted on the central Mo rod of the coaxial electrode, introduced into the corrosion cell, and assembled cell attached to the argon/vacuum line. Dry argon gas from glove-box was bled in the cell after several evacuations. The temperature of the cell was slowly raised to 300°C and the coaxial electrode lowered into the melt after loosening the ultratorr connector. The cell was allowed to equilibrate until the open circuit voltage, monitored by a digital voltmeter, reached a stable value. This value, usually 15-20 mV, was selected as zero potential of the potentiostat during the i-E curve recording. All potentials were measured versus the Mo/MoS_2/melt electrode formed after more than 5 hours of contact between the melt and the Mo rod used as reference electrode. After collecting the desired data during several days, the electrodes were removed from the melt, the cell fanned and transferred to the glove-box. Both reference and sample electrode were ultrasonically freed from frozen melt in acetone, washed, dried and weighed.

RESULTS AND DISCUSSION

Coating deposition.

The material commonly used for electrochemical deposition of metals from molten halides is predominantly the halide of the metal to be plated, since a high miscibility exists between inorganic compounds having a common anion. For the dissolution of a metal salt with a different anion the strength of interaction between solute cation and solvent anion is important. If there is a complex formation, the solute stability is enhanced but the complex stability varies strongly with the oxidation state of the metal. For example, in molten chlorides disproportionation and polymerization reactions of lower valence states are important phenomena. Such reactions however, are not observed in the case of molten fluorides, since F^- anion is known to

stabilize the solution. Use of molybdate as solute in FLINAK involves a slightly different solution chemistry: because F^- ion is more electronegative than O^{2-} ion and is present in large excess the probable Mo-species may be a molybdenum-fluoride complex. This assumption was corroboarted by the i-E behavior upon addition of molybdate, since the latter resulted in a substantial increase of current at -0.2 V vs. the Pt quasi-reference electrode, indicating that the solute is electroactive. (Figure 1)

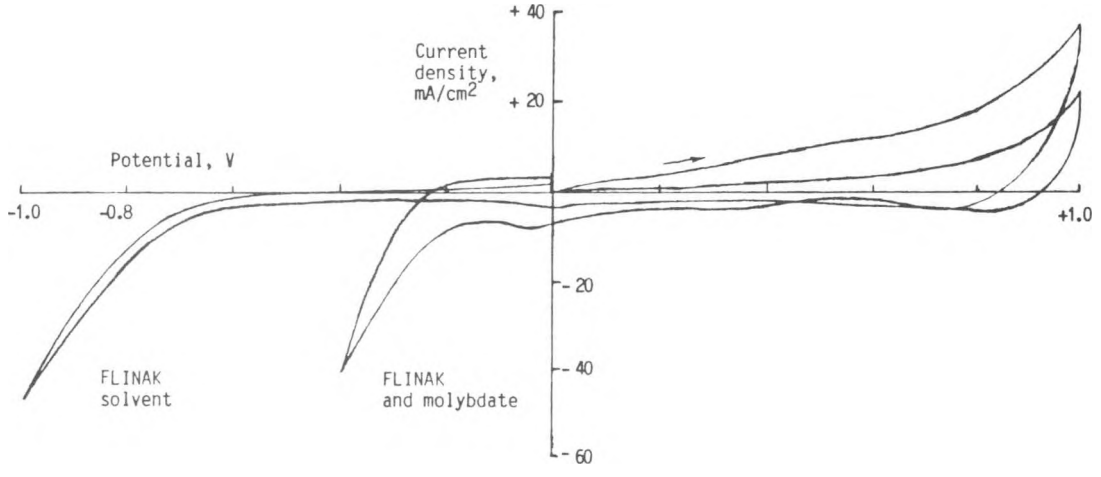

Figure 1. Cyclic voltammogram of FLINAK solvent and its mixture with K_2MoO_4 (6.4 w/o) at 800°C. WE and CE: Graphite Ultra F (7.2 cm^2 area).

Molybdenum coatings were obtained at relatively low current densities of 20-50 mA/cm^2, at 780°C with maximum 21% current efficiency. A Mo coating thickness of 6 μm was deposited in 55 minutes with 1000 C total electric charge passed. In the system FLINAK-tungstate the tungsten fluoride complex was reduced in two steps to produce W coatings with 10% current efficiency.[35] In Figure 2 a SEM micrograph of Mo coating is shown, which illustrates the high quality of the growth of angular crystals on a more dense pore-free substructure.

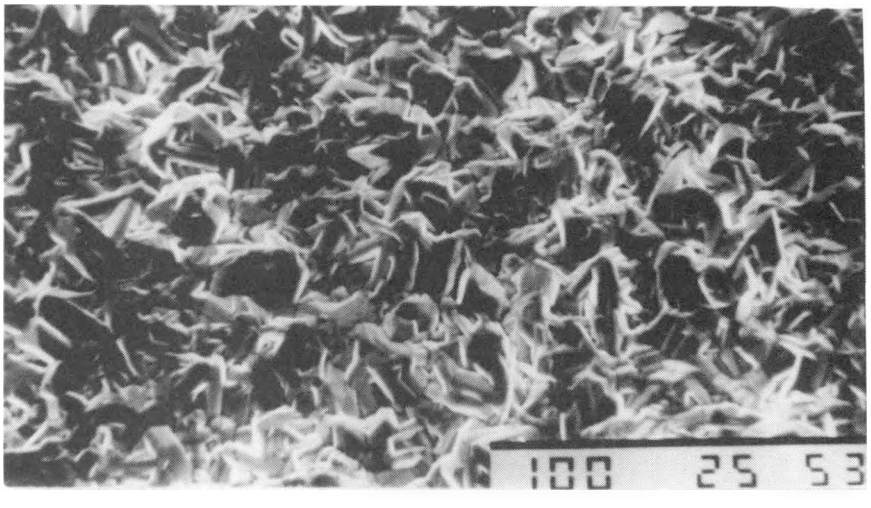

Figure 2. SEM micrograph of molybdenum coating.

High quality molybdenum carbide coatings were obtained at 60-160 mA/cm^2 and 860°C with 45% current efficiency. This efficiency may be considered quite satisfactory in comparison with 30-50% values reported by Stern and Gadomski[36] for tungsten carbide deposition. The SEM micrograph of a Mo_2C coating exhibits the same features as the Mo coating, indicating a dense coverage of substrate. (Figure 3)

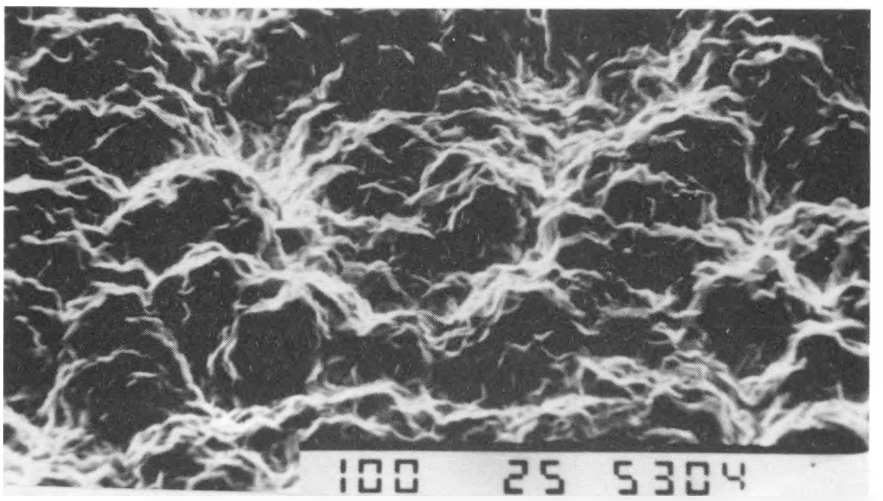

Figure 3. SEM micrograph of molybdenum carbide coating.

The formation of Mo_2C was confirmed by X-ray diffraction which clearly pointed out the formation of alpha-phase with some preferential orientation. (Figure 4)

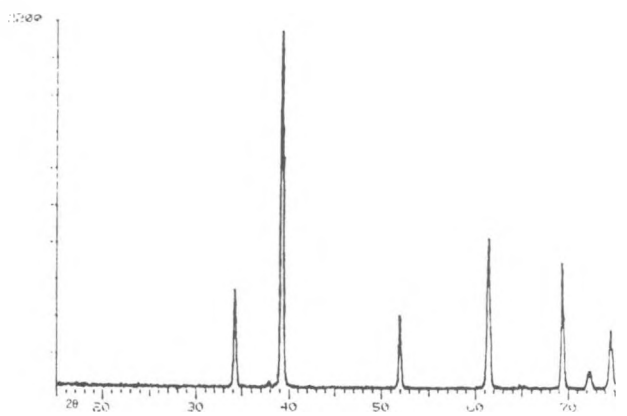

Figure 4. X-ray diffraction spectrum of Mo_2C coating.

Corrosion testing.

A comparative investigation of Mo and Mo_2C behavior was conducted in order to asses carbide stability in the polysulfide melt. As pointed out earlier, Mo exposed to this melt at temperatures above 300°C produces a passivating layer of sulfide which dissolves very slowly in the melt. Under dynamic conditions the static corrosion characteristics are strongly

modified as less conducting films on the electrode surface are formed. Nevertheless, as a simulation of real behavior in a Na/S cell, cycling the sample between representative anodic and cathodic polarization limits is more appropriate than other kinds of corrosion experiments.[37] Na_2S_3 melt at 300°C was selected as the test melt and it was supposed that Mo_2C would be rapidly attached.[30] This melt composition (67 w/o S) is in the one melt region of the phase diagram, corresponding to 100% discharge depth of a Na/S cell.[38]

Mo and Mo_2C exhibit quite similar behavior, as illustrated by the voltammograms in Figure 5. In the inset is reproduced a cyclic voltammogram for Mo recorded by Dobson, McLarnon and Cairns[39].

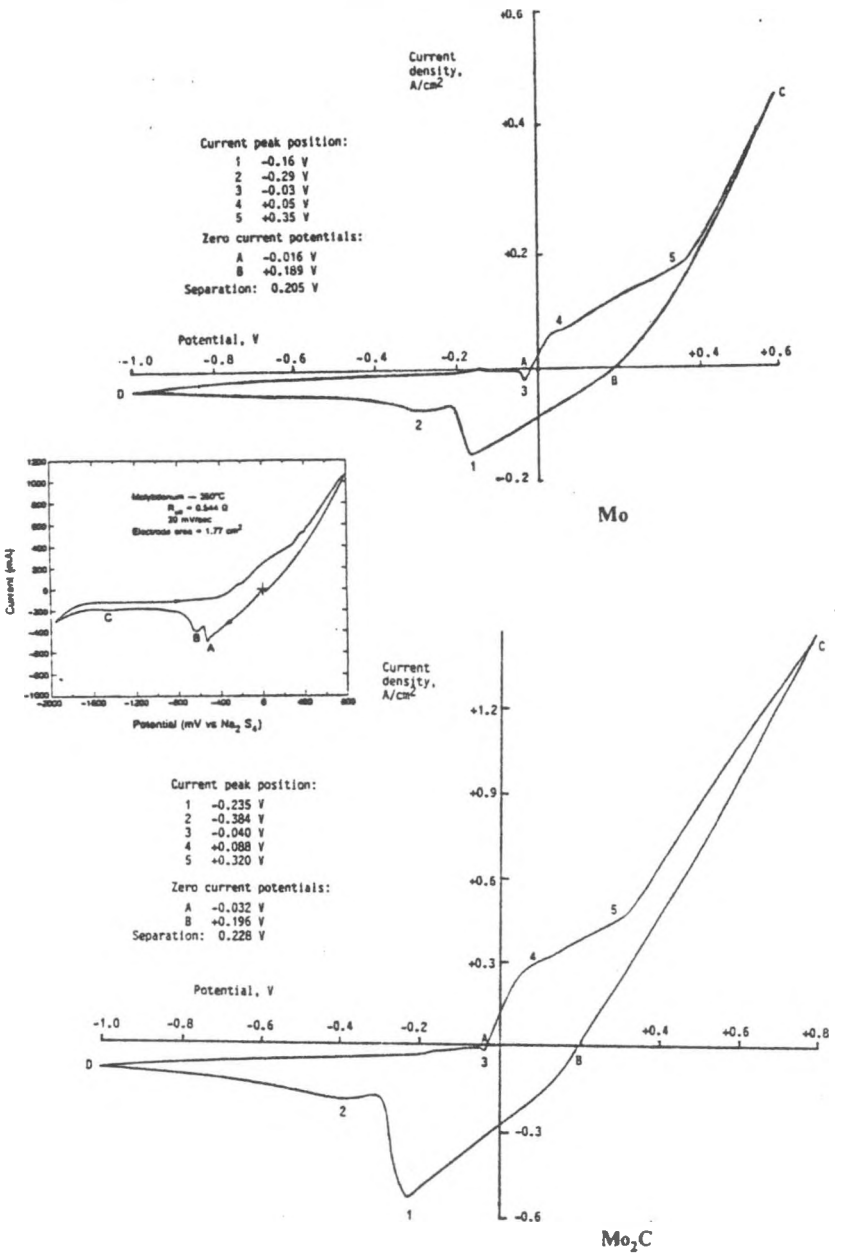

Figure 5. Cyclic voltammograms at Mo and Mo2C electrodes in Na_2S_3 melt at 300°C. Sweep rate 20 mV/s.

In both i-E curves the principal first cathodic peak which is labeled 1, satisfies the linearity of i_p vs. $v^{1/2}$, but sharp transitions suggest significant deviations from the usual diffusion-controlled curves obtained in the absence of a solid film at the electrode surface. Only near the equilibrium potential of the melt is the electrode reaction a diffusion-controlled redox process. It has been conjectured[31] that the nature of the electrode surface exerts an important effect on the oxidation of polymeric sulfur to elemental sulfur. If one considers the anodic part of both cyclic voltammograms recorded at low sweep rates, Mo_2C seems to behave (Figure 6) as a

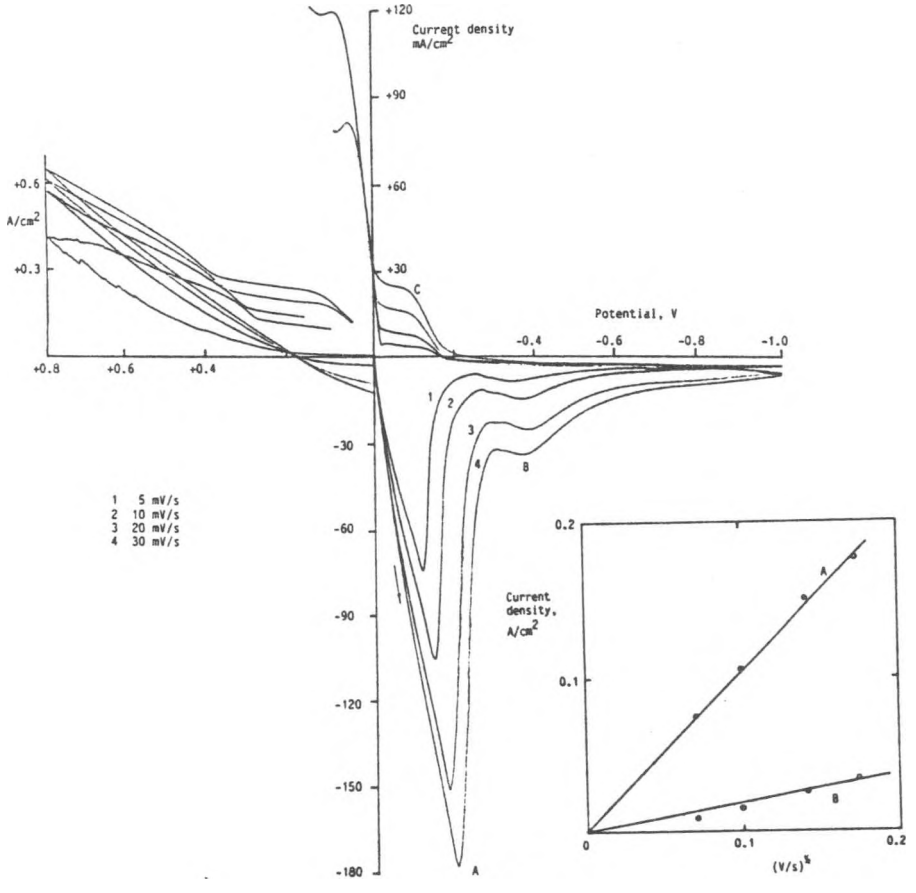

Figure 6. Cyclic voltammogram at Mo_2C electrode in Na_2S_3 melt at 300°C. Inset i_p vs. $v^{1/2}$ plot.

"molybdenum" as well as a "carbon" electrode: a linear increase of current with applied voltage (anodic to +0.35 V) takes place as for molybdenum (Figure 7) but "vitreous carbon" behavior occurs when the removal of liquid sulfur film by the melt (unsaturated in sulfur) leads to the apparition of a large peak. (Figure 8).

On the cathodic side, the "bump" labeled peak 2 in Figure 5, was attributed to some reorganization inside the sodium disulfide film[39] or to melt-metal interaction within this layer in the case of molybdenum.[33] By increasing the sensitivity 10 times when recording the cathodic region of the molybdenum electrode, this peak was shown to have a structured shape

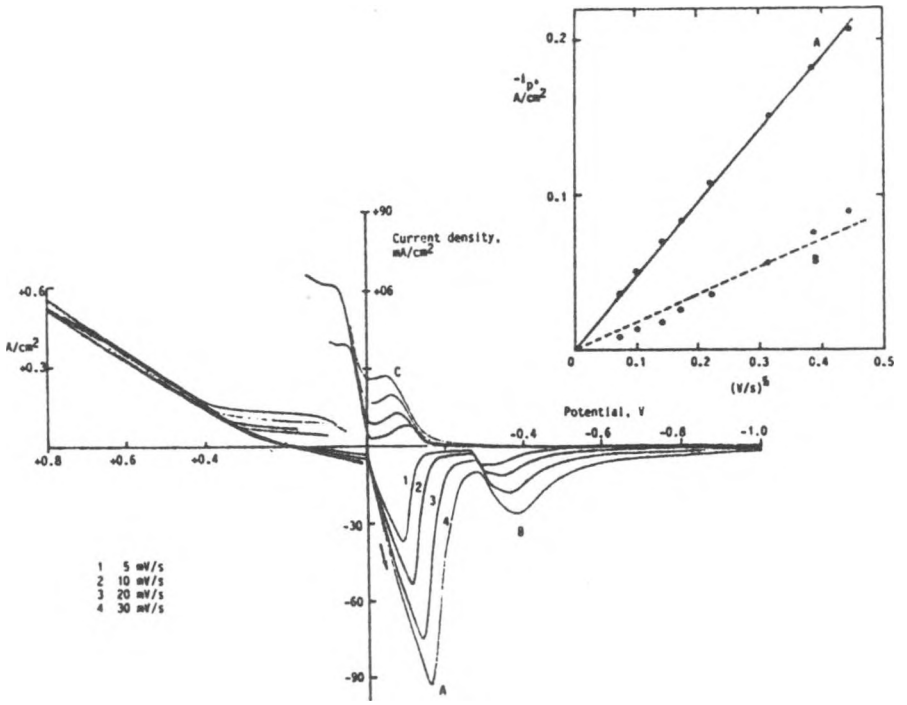

Figure 7. Cyclic voltammogram at Mo electrode in Na_2S_3 melt at 300°C. Inset i_p vs. $v^{1/2}$ plot.

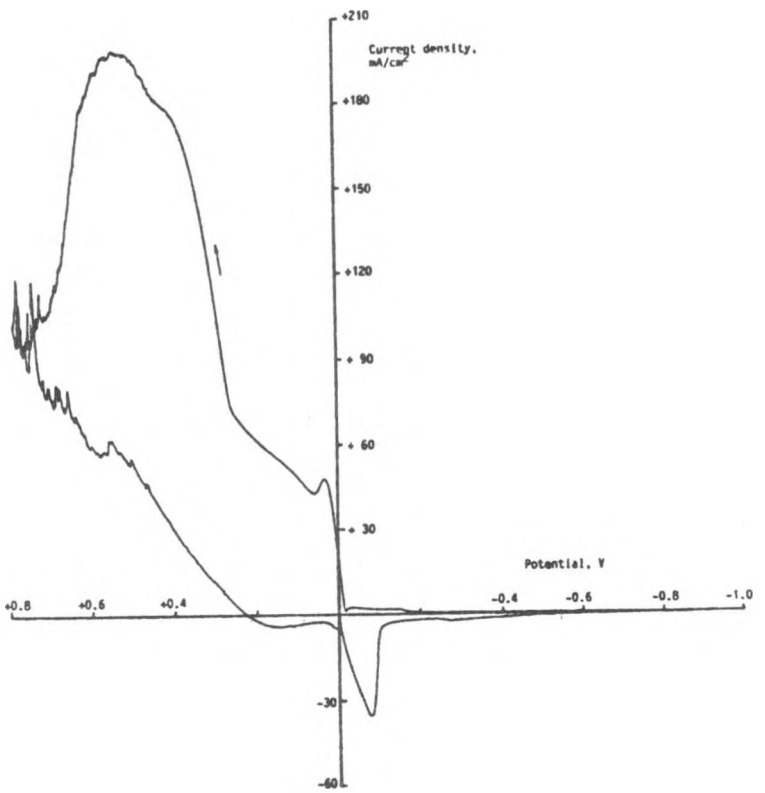

Figure 8. Cyclic voltammogram at Mo_2C electrode in Na_2S_3 melt at 300°C. Sweep rate 2 mV/s.

(Figure 9). This result deserves further attention.

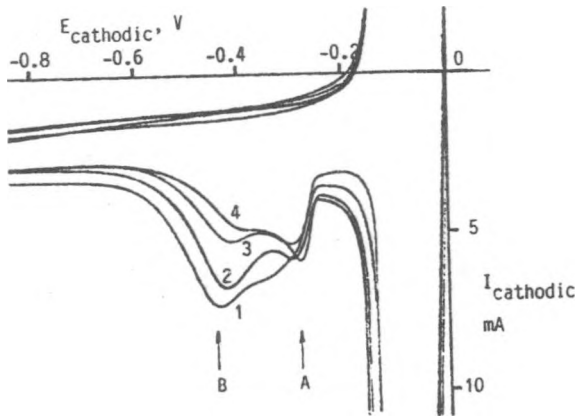

Figure 9. Cyclic voltammogram at Mo electrode in Na_2S_3 melt at 300°C. Structured shape or peak 2. 1 to 4 consecutive sweep cycles.

The investigation of molybdenum carbide behavior in sodium tetrasulfide melt using an improved corrosion cell is now under way.

Acknowledgment

This work was supported by the U.S. Department of Energy, through the Lawrence Berkeley Laboartory, Berkeley, Ca. (Project #4529210).

REFERENCES

1 T.E. Tietz and J.W. Wilson, "Behavior and Properties of Refractory Metals", Stanford University Press, Stanford, 1965.

2 J.L. Sudworth, Chap. 6 in "Electrochemical Power Sources. Primary and Secondary Batteries", M. Barak ed., IEE London, 1980.

3 J.E. Battles et al., in "Corrosion Problems in Energy Conversion and Generation", C.S. Tedmon ed., TES, Corrosion Division, Princeton, N.J., 1974.

4 S. Senderoff and A. Brenner, J.Electrochem.Soc., 101(1954)16.

5 S. Senderoff and A. Brenner, J.Electrochem.Soc., 101(1954)28.

6 S. Senderoff and A. Brenner, J.Electrochem.Soc., 101(1954)31.

7 S. Senderoff and G.W. Mellors, J.Electrochem.Soc., 114(1967)556.

8 S. Senderoff and J.R. Labrie, J.Electrochem.Soc.,102(1955)77.

9 D.E. Couch and S. Senderoff, Trans.Metal.Soc.AIME, June (1958) 320.

10 G.W. Mellors and S. Senderoff, Can. Pat. #688,546 (1964).

11 G.W. Mellors and S. Senderoff, in "The University of Pittburgh Conference on the Application of Fundamental Thermodynamics", G.R. Fitterer ed., Gordon and Breach, N.Y., 1966.

12 S. Senderoff and G.W. Mellors, J.Electrochem.Soc.,114(1967)586.

13 S. Senderoff, G.W. Mellors and P. Bertz, Ann.N.Y.Acad.Sci.,79(1960)878.

14 G.W. Mellors and S. Senderoff, in "Electrochemistry", H. Friend and F. Gutman eds., Pergamon Press, London, 1954, p. 578.

15 P.G. Dudley, D. Inman and S.H. White, 2nd Intern.Symp. "Molten Salts", Pittsburgh, Pa., 1978, p. 29.

16 S. Senderoff and G.W. Mellors, Science,153(1966)475.

17 R.S. Sheti, in "Advances in Surface Coating Tehcnology", London, 1978, p. 153.

18 D.R. Sadoway, Molten Salt Bull.,#28(1985)17.

19 F. McCawley, J.Electrochem.Soc.,116(1969)1028.

20 J. Koger, US Pat. #3,783,014 (1974).

21 A.N. Baraboshkhin, Tr.Inst.Elektrokhim.Ural.Filial Acad.Sci USSR, #15(1970) 51; #18(1982)87; Zasch.Metal.,17(1981)371; Fiz.Khim.Elektrokhim. Raspl.Sol.Shlak.,2(1969)212.

22 K. Kikiro, Trans.Jap.Inst.Met.,26(1985)198.

23 J.M. Penato, N. Debrouwer and CI.Mathieu, Fr.Demande #2,514,375 (1981).

24 A.K. Suri and C.K. Gupta, J.Less Comm.Met.,31(1973)389.

25 N.Q. Minh, J.Metals,37(1985)28.

26 Z. Guang-Wen and W. Chai-Tong, 3rd All-China Conference on Molten Salt Chemistry and Electrochemistry, May, 1985.

27 K.H. Stern, US Pat. #4,430,170 (1984).

28 G. Weiss, Ann.Chim., Ser. 12,Vol.1(1946)446.

29 A.K. Suri, T.K. Mukherjee and C.K. Gupta, J.Electrochem.Soc.,120(1973)622.

30 F.A. Ludwig, in "Research on Electrodes and Electrolytes for the Ford Na/S Battery"AER-73-07199, 1975 and subsequent reports ending 1978.

31 D.A. Aikens, Chap. 4 in "The Sulfur Electrode", R.P.Tischer ed. Academic Press, N.Y. 1983.

32 J.C. Dobson, F.R. McLarnon and E.J. Cairns, TES Ext. Abstr., #99, 83-2(1983)

33 J.C. Dobson. F.R. McLarnon and E.J. Cairns. 7th Battery and Electrochemical Contractors Conference, Crystal City, Va.,1985, p.79.

34 J.C. Dobson, F.R. McLarnon and E.J. Cairns, TES Ext. Abstr.,85-2(1985)86.

35 M.L. Deanhardt and K.H. Stern, TES Ext. Abstr., #437(9184).

36 K.H. Stern and S.T. Gadomski, 4th Intern.Symp. "Molten Salts", San Francisco, Ca., 1983, p. 611.
37 H.S. Wroblowa et al.,in "Proc DOE/EPRI Beta Na/S Battery Workshop V, EPRI EM-3631 SR, Dec. 1984, p. 6.
38 R. Knoedler and W. Bansemir, J. Appl.Electrochem.,15(1985)387.
39 R.P. Tischer and F.A. Ludwig, in Adv.Electrochem.Electrochem.Eng., H. Gerischer and C.W. Tobias eds., Vol. 10, J. Wiley and Sons, N.Y., 1977.

Techniques for Electrodeposition of Metals from Molten Salt Systems*

R. Varma, T. Vargas, H. Shimotake,+
K. Koyama,‡ and G. Hope
Chemical Technology Division
Argonne National Laboratory
Argonne, IL 60439

Molten salt offers an alternative to aqueous electrolyte for the electrodeposition of metals. Refractory metals not platable from aqueous electrolyte can be electroplated from molten salt solutions. Metal coatings obtained from molten salt are stress-free, crack-free, nonporous, and strongly adherent to the substrate. Another obvious advantage is the ability to produce hydrogen-free coatings. However, metal deposits from molten salts are prone to be dendritic unless precautions are taken.

A common electrolytic medium known as FLINAK (46.5 mol % LiF-11.5 mol % NaF and 42.0 mol % KF) has been used for the state-of-the-art electrodeposition of refractory metals (i.e., Ti, Zr, Hf, V, Nb, Ta, Cr, Mo, and W). The distinct advantage of the FLINAK process is that it can achieve metalliding (i.e., surface alloying of the depositing metal with the host metal during the electroplating). Nevertheless, the use of FLINAK is sometime restricted because the plating process is conducted at high temperatures (700-900°C) and the mechanical properties of the substrate may be adversely affected. Also, the fluoride melts are highly corrosive.

Lower temperature chloride melts deserve close consideration. The advantages, such as their noncorrosive nature as well as lower temperature of operation, may be useful in developing commercial processes. [Such saltsystems provide a suitable alternative electrolyte for electrodepostion of refractory metals.] The electrodeposition of chromium and molybdenum will be analyzed here in some detail. The deposition from LiCl-KCl eutectic has been known to produce large crystal grains in the case of chromium deposition; for molybdenum, deposits of that metal along with subhalide of the metal occurs during plating from chloride melts. These and other problems in plating Cr and Mo from chloride melts will be analyzed and solutions suggested.

The advantages of pulse plating regimes and forced mass transport, for grain growth in the electrodeposition of chromium from LiCl-KCl-$CrCl_2$ melt will be examined. Results of recent studies conducted at ANL for the improvement of morphological characteristics of chromium electrodeposits obtained from the LiCl-KCl (eutectic) will be presented. The results obtained so far indicate that the combined use of forced mass transfer and nucleating pulse in conjunction with current reversal pulsing are beneficial towards achieving some control over crystal grain growth.

The role of additives such as Rb^+, Ba^+ and Cs^+ species to prevent deposition of molybdenum subhalide and help to produce smooth and choerent molybdenum deposits from KCl-LiCl (eutectic)-$MoCl_3$ solution at 600°C will also be examined.

---

*This work was supported by the U.S. Department of Energy, Office of Energy Storage under Contract W-31-109-Eng-38.
Present addresses: +Amoco Corporation, P. O. Box 400, Naperville, IL 60566.
‡Department of Metallurgy and Material Science, Himeji Institute of Technology, 2167 Shosha, Himeji 671-22, Japan.

Future Directions in Molten Salt Research as it Relates to Energy Storage

Elton J. Cairns
Lawrence Berkeley Laboratory, and
University of California
Berkeley, CA 94720

The future directions for molten salt research relevant to electrochemical energy storage may be discussed in several categories, which are found to be in rather different states of maturity.

The thermodynamics of the relevant molten salt electrolyte systems and the various electrode systems under serious consideration are in the best state of any of the topics discussed here. Many phase diagrams of interest (and potential interest) for molten-salt electrolytes have been measured and calculated. In general, the calculated diagrams agree very well with the measurements, giving confidence that computations, together with only a few measurements can yield high-quality phase diagrams for multi-component alkali-halide systems. The phase diagrams for solid electrodes are generally more complicated and less predictable, but many of them have been measured with good accuracy. Also, the activities of the relevant components have been measured, yielding the essential thermodynamic information. This general topic of electrode and electrolyte thermodynamics is in an adequate state of development. For the future, it is to be expected that more sophisticated thermodynamic models and computational methods will provide for more powerful tools to be used in the estimation of the properties of more complex systems.

Techniques for the study of the molecular structure and speciation in molten-salt electrochemical systems are being developed, but are still in their infancy. This field suffers from a low level of effort, combined with the inherent difficulty of performing high-precision experiments in situ at elevated temperatures and (usually) in controlled atmospheres. Raman spectroscopy and UV-visible absorption spectroscopy have shown success for the study of the bulk electrolyte phase; extension of Raman to electrode surfaces is an important goal. Perhaps infrared spectroscopy for electrode surfaces can also be developed. Other techniques such as photothermal deflection spectroscopy are candidates. Ultimately, scanning-tunneling microscopy may be feasible for studying the structure of electrode surfaces in-situ, and on an atomic scale.

The study of the kinetics and mechanisms of electrode reactions has been following the lead of work in ambient-temperature systems. Steady-state techniques have been in use for some time. Transient techniques are finding wider use. Voltage-sweep methods are most common, followed by potential-step and current-step methods. Recent improvements in pulse and double-pulse methods have been made, improving the accuracy available for fast reactions.

As more is learned about the details of operation of the various electrodes that comprise the systems of interest, it becomes more important to

have available sophisticated mathematical models for electrodes and complete cells. These models, appropriately implemented on computers, can provide for new levels of understanding with regard to the complex interactions among the many variables in practical porous-electrode systems. They can also be used as design tools, helping to meet specific performance goals, while reducing the need for large numbers of experiments. The recent advances in computer speed, memory size, and cost reduction provide a major opportunity to advance the contributions that can be made by modeling. The future is certain to provide more detailed and powerful models of electrochemical cells, including models with the capability of providing information about the behavior of rechargeable cells undergoing many charge-discharge cycles.

New materials can be expected to continue to set the pace for the development of advanced electrochemical energy conversion systems. They will play a central role in setting the limits of the performance and life capabilities of new and existing systems. New materials and new processes can also be expected to play key roles in reducing the cost of new systems in order to compete in the marketplace. Both active materials and the (inactive) materials of construction for cells can either prevent or enable the success of any electrochemical system. Too often, adequate attention to materials problems has been left until last in the R&D cycle. In the future, an earlier appreciation of materials development is expected. More sophisticated methods of materials synthesis and quality control will be necessary. It is likely that electrochemical methods for the preparation of special high-performance materials will be used to a greater extent in the near future.

There is now a window of opportunity for new, high-performance batteries to be developed and enter various markets -- before other advanced systems are developed. If this opportunity can be used successfully, then a strong competitive position will be established for molten-salt batteries. If not, then the development of a marketable battery will be much more difficult, because the new battery will be called upon to displace a competing system which is already established. Based on current research results, it appears feasible to develop a molten-salt battery capable of 200 W/kg, 200 W-h/kg, 500+ deep cycles, and at least 2 years operating life, with a cost acceptable for specialty applications. These cells are very robust, can resist many thermal cycles, have a good packing density, and require only simple temperature control.

The aggressive development of a high-performance molten-salt battery should be a high-priority goal, if we are to meet our battery needs. If the U.S. doesn't develop such a system first, we will be importing it from another country! Let's not waste this opportunity!

This work is supported by the Assistant Secretary for Conservation and Renewable Energy, Office of Energy Storage and Distribution of the U.S. Department of Energy under Contract No. DE-AC03-76SF00098.

Distribution for ANL-86-40

Internal:

J. P. Ackerman
J. D. Arntzen
J. E. Battles (25)
M. Blander
R. L. Breyne
T. O. Brun
L. Burris
A. A. Chilenskas
C. C. Christianson
W. DeLuca
A. K. Fischer
F. Y. Fradin
E. C. Gay
D. R. Hamrin
J. E. Harmon
C. E. Johnson
T. D. Kaun
V. M. Kolba
M. L. Kyle
R. A. Lewis
R. F. Malecha
F. J. Martino
W. E. Miller
F. C. Mrazek
Z. Nagy
P. A. Nelson
E. G. Pewitt
R. B. Poeppel
J. B. Rajan
L. Redey
M. F. Roche
M.-L. Saboungi-Blander
W. W. Schertz
J. L. Settle
J. A. Smaga
M. J. Steindler
S. Susman
Z. Tomczuk
J. P. Unik
R. Varma
D. R. Vissers (25)
S. Vogler
R. W. Weeks
ANL Patent Dept.
ANL Contract File
ANL Libraries
TIS Files (5)

External:

DOE-TIC, for distribution per UC-94cb
Manager, Chicago Operations Office, DOE
V. H. Hummel, DOE/CH
W. R. Frost, DOE/CH
J. Purcell, DOE/CH
Chemical Technology Division Review Committee Members:
  R. G. Wymer, Oak Ridge National Lab.
  E. B. Yeager, Case Western Reserve U.
E. Adler, Hughes Aircraft Co., El Segundo
E. Aiello, Research Institute Library, The University of Chicago
D. M. Allen, Wright-Patterson AFB, OH
J. Ambrus, Naval Surface Weapons Center, Silver Spring, MD
F. Anson, California Institute of Technology, Pasadena, CA
J. Appleby, Electric Power Research Institute, Palo Alto, CA
W. J. Argersinger, Jr., The University of Kansas, Lawrence, KS
B. A. Askew, Los Altos, CA
K. F. Barber, Div. of Electric and Hybrid Propulsion, USDOE
G. Barlow, Gould Inc., Rolling Meadows, IL
R. W. Barnes, Lithium Corporation of America, Gastonia, NC
T. R. Beck, Electrochemical Technology Corp., Seattle, WA
K. J. Bell, Oklahoma State University, Stillwater, OK
D. N. Bennion, Brigham Young University, Provo, UT
J. Birk, Electric Power Research Institute, Palo Alto, CA
C. F. Bonilla, Columbia University, New York, NY
T. G. Bradley, General Motors Corp., Warren, MI
W. Brandt, University of Wisconsin, Milwaukee, WI
J. Braunstein, Oak Ridge National Laboratory, Oak Ridge, TN
J. O. Brittain, Northwestern University, Evanston, IL
J. J. Brogan, Div. of Energy Utilization Research, USDOE
E. W. Brooman, Battelle Memorial Institute, Columbus, OH
P. J. Brown, Division of Electric and Hybrid Propulsion, USDOE
B. D. Brummet, McGraw-Edison Co., Bloomfield, NJ

K. R. Bullock, Johnson Controls, Inc., Milwaukee, WI
D. M. Bush, Sandia National Laboratories, Albuquerque, NM
B. L. Butler, Science Applications International Corp., San Diego, CA
P. Butler, Sandia National Laboratories, Albuquerque, NM
E. S. Buzzelli, Westinghouse Electric Corp., Pittsburgh, PA
E. J. Cairns, Lawrence Berkeley Laboratory, Berkeley, CA
R. P. Clark, Sandia National Laboratories, Albuquerque, NM
M. Classen, Eagle-Pitcher Industries, Inc., Joplin, MO
A. R. Cook, International Lead Zinc Research Organization, New York, NY
S. Dallek, Naval Surface Weapons Center, Silver Spring, MD
L. DeJonghe, Lawrence Berkeley Laboratory, Berkeley, CA
D. L. Douglas, Electric Power Research Institute, Palo Alto, CA
E. Dowgiallo, Div. of Electric and Hybrid Propulsion, USDOE
R. E. Dueber, Aeronautical Laboratories, Wright-Patterson AFB, OH
A. E. Dukler, University of Houston, Houston, TX
J. Dunning, General Motors Research Laboratory, Warren, MI
M. Eisenberg, Electrochimica Corporation, Menlo Park, CA
J. Evans, Lawrence Berkeley Laboratory, Berkeley, CA
W. J. Frea, Michigan Technological University, Houghton, MI
J. H. B. George, George Consulting International, Inc., Concord, MA
F. Gibbard, Power Conversion, Inc., Elmwood Park, NJ
J. Giner, Giner, Inc., Waltham, MA
G. Goodman, Globe Battery Div., Johnson Controls, Inc., Milwaukee, WI
R. S. Gordon, Ceramatec, Inc., Salt Lake City, UT
H. Grady, Foote Mineral Company, Exton, PA
S. Grass, Boeing Aerospace Company, Seattle, WA
G. Greenberg, Electric Vehicle Battery Technology, Stamford, CT
K. Grothaus, Sandia National Laboratories, Albuquerque, NM
R. Guidotti, Sandia National Laboratories, Albuquerque, NM
N. Gupta, Ford Motor Co., Dearborn, MI
N. Hackerman, Rice University, Houston, TX
G. L. Hagey, Div. of Advanced Energy Conversion Systems, USDOE
J. Hampton, Barnett TVA, Chattanooga, TN
U. J. Hansen, Indiana State University, Terre Haute, IN
R. Hudson, Eagle-Picher Industries, Inc., Joplin, MO
R. A. Huggins, Stanford University, Stanford, CA
V. Jalan, Electrochemical, Inc., Woburn, MA
S. James, Naval Weapons Center, Silver Spring, MD
G. J. Janz, Cogswell Laboratory, Rensselaer Polytechnic Institute, Troy, NY
H. Jensen, C&D Power Systems Div., Allied Corp., Plymouth Meeting, PA
R. E. Jones, Office of Conservation, USDOE
F. Kalhammer, Electric Power Research Institute, Palo Alto, CA
P. Kaspar, San Francisco Operations Office, USDOE
A. C. Khandkar, Ceramatec, Inc., Salt Lake City, UT
R. S. Kirk, Div. of Electric and Hybrid Propulsion, USDOE
K. W. Klein, Electric Energy Systems Division, USDOE
J. LaGrone, San Francisco Operations Office, USDOE
W. Lambert, San Francisco Operations Office, USDOE
J. J. Lander, Air Force Aero Propulsion Laboratory, Wright-Patterson AFB, OH
A. R. Landgrebe, Energy Storage and Distribution Division, USDOE
C. A. Levine, Dow Chemical Company, Walnut Creek, CA
J. E. Linehan, Marquette University, Milwaukee, WI
P. S. Lykoudis, Purdue University, West Lafayette, IN
G. Mamantov, University of Tennessee, Knoxville, TN
Marquette University, Department of Chemistry, Milwaukee, WI
K. L. Matson, PSE&G Research Corp., Newark, NJ

F. McLarnon, Lawrence Berkeley Laboratory, Berkeley, CA
R. M. Meighan, C&D Power Systems Div., Allied Corp., Plymouth Meeting, PA
Michigan Technological University, Houghton, MI
N. R. Miller, United Nuclear Industries, Inc., Richland, WA
R. W. Minck, Ford Aerospace & Communications Corp., Newport Beach, CA
K. E. Mueller, White Oak Laboratory, Silver Spring, MD
R. H. Muller, Lawrence Berkeley Laboratory, Berkeley, CA
R. A. Murie, General Motors Technical Center, Warren, MI
G. Murphy, Iowa State University, Ames, IA
D. Newman, Bowling Green State University, Bowling Green, OH
J. S. Newman, University of California, Berkeley, CA
J. Nowabilski, Union Carbide Co., Tonawanda, NY
L. G. O'Connell, Electric Power Research Institute, Palo Alto, CA
P. G. Patil, Office of Vehicle & Engine R&D, USDOE
E. A. Peretti, University of Notre Dame, Notre Dame, IN
P. Pierini, Dow Chemical Company, Walnut Creek, CA
D. Plymale, Albuquerque Operations Office, USDOE
G. W. Preckshot, University of Missouri, Columbia, MO
R. K. Quinn, Sandia National Laboratories, Albuquerque, NM
R. Rightmire, Standard Oil of Ohio, Cleveland, OH
R. A. Rizzo, Johnson Controls, Inc., Milwaukee, WI
P. N. Ross, Lawrence Berkeley Laboratory, Berkeley, CA
H. Rosson, The University of Kansas, Lawrence, KS
S. Ruby, Div. of Energy Utilization Research, USDOE
A. J. Salkind, Rutgers Medical School, Piscataway, NJ
A. Sammels, Aurora, IL
C. K. Sanathanan, University of Illinois, Chicago, IL
W. Schaefer, Commonwealth Edison, Maywood, IL
T. Schneider, Electric Power Research Institute, Palo Alto, CA
R. I. Schoen, National Science Foundation, Washington, DC
J. R. Schorr, Battelle Columbus Laboratories, Columbus, OH
H. J. Schwartz, NASA Lewis Research Center, Cleveland, OH
J. Q. Searcy, Sandia National Laboratories, Albuquerque, NM
J. R. Selman, Illinois Institute of Technology, Chicago, IL
A. Sesonske, Purdue University, West Lafayette, IN
H. Shimotake, Amoco Research Center, Naperville, IL
R. W. Shivers, Div. of Energy Utilization Research, USDOE
J. A. Shropshire, Exxon Research and Engineering Co., Linden, NJ
R. Singleton, U. S. Bureau of Mines, Washington, DC
W. Spindler, Electric Power Research Institute, Palo Alto, CA
R. K. Steunenberg, Naperville, IL
R. L. Strombotne, U. S. Dept. of Transportation, Washington, DC
P. Symons, Palo Alto, CA
R. Szwarc, General Electric Co., St. Petersburg, FL
L. Thaller, NASA Lewis Research Center, Cleveland, OH
C. W. Tobias, University of California, Berkeley, CA
D. Topor, Illinois Institute of Technology, Chicago, IL
A. A. Uchiyama, Jet Propulsion Laboratory, Pasadena, CA
University of Maine, Prof. in charge of Chem. Engineering, Orono, ME
J. V. Vinciguerra, Eagle-Picher Industries, Inc., Joplin, MO
J. B. Wagner, Arizona State University, Tempe, AZ
W. Walsh, Naperville, IL
S.-C. Wang, General Motors Research Laboratory, Warren, MI
R. D. Weaver, Electric Power Research Institute, Palo Alto, CA
S. A. Weiner, Ford Motor Co., Dearborn, MI
C. E. Weinlein, Johnson Controls, Inc., Milwaukee, WI

S. White, EIC Laboratories, Inc., Norwood, MA
B. W. Wilkinson, Michigan State University, East Lansing, MI
F. Will, General Electric Co., Schenectady, NY
J. Withrow, Chrysler Corp., Detroit, MI
T. Wydeven, NASA Ames Research Center, Moffett Field, CA
N. P. Yao, Clarendon Hills, IL
R. Zalosh, Factory Mutual Research, Norwood, MA
G. Benninger, Powerplex Technologies, Inc., Downsview, Ontario, Canada
Biblioteca Sede Central, Comision Nacional de Energia Atomica, Buenos Aires, Argentina
J. O. B. Carioca, Nucleo de Fontes Nao Convencionais de Energia da UFCE, Fortaleza-Ceara, Brazil
C.-H. Cheng, Atomic Energy Council, Taipei, Taiwan, Republic of China
Chloride Technical Limited, Manchester, England
S. Das Gupta, The Electrofuel Manufacturing Co., Toronto, Ontario, Canada
W. Fischer, Brown, Boveri & CIE.AG, West Germany
K. Fujimiya, University of Tokyo, Tokyo, Japan
M. T. Herbert, National Radiological Protection Board, Chilton, England
H. Hjuler, Technical University of Denmark, Denmark
Japan Atomic Energy Research Institute, Tokai-mura, Japan
I. W. Jones, Chloride Silent Power, Ltd., Astmoor, Cheshire, England
L. Kemmerich, Kernforschungszentrum Karlsruhe GmbH, Karlsruhe, Germany
H. Kodowaki, GS Japanese Storage Co. Ltd., Kyoto, Japan
Korea Advanced Energy Research Inst., Technical Information Division, Korea
K. Kurita, Hitachi, Ltd., Tokyo, Japan
S.-S. Lee, The Korea Advanced Institute of Science and Technology, Seoul, Korea
K. Matsuda, Inst. of Physical and Chemical Research, Yamato-machi, Japan
R. Nordberg, Sahlgren's Hospital, Goteborg, Sweden
L. Pearce, Admiralty Materials Laboratory, Holten Heath, England
J. P. Pompon, Compagnie Generale d'Electricite, Laboratoires de Marcoussis, Marcoussis, France
J. A. Sabato, Comision Nacional de Energia Atomica, Buenos Aires, Argentina
N. Saratchandran, Bhabha Atomic Research Centre, Bombay, India
F. M. Stackpool, Chloride Silent Power, Ltd., Astmoor, Cheshire, England
J. Sudworth, Beta Research & Development Ltd., Sinfin, Derby, United Kingdom
D. F. Tessier, Alcan International, Kingston, Ontario, Canada
E. Voss, Varta Batterie A.G., Kelkheim, Germany
T. Wallin, Royal Institute of Technology, Stockholm, Sweden
F. Weigel, Institut fuer Anorganische Chemie der Universitat Munchen, Germany